ON THE MECHANICAL PROPERTIES OF NOVEL METALLIC GLASS ARCHITECTURES: A MOLECULAR DYNAMICS INVESTIGATION

SARA ADIBI

NATIONAL UNIVERSITY OF SINGAPORE
2014

ON THE MECHANICAL PROPERTIES OF NOVEL METALLIC GLASS ARCHITECTURES: A MOLECULAR DYNAMICS INVESTIGATION

SARA ADIBI
(M.SC., (Hons) ISFAHAN UNIVERSITY OF TECHNOLOGY, IRAN)

A THESIS SUBMITTED
FOR THE DEGREE OF DOCTOR OF PHILOSOPHY

DEPARTMENT OF MECHANICAL ENGINEERING
NATIONAL UNIVERSITY OF SINGAPORE

2014

Declaration

I hereby declare that the thesis is my original work and it has been written by me in its entirety. I have duly acknowledged all the sources of information which have been used in the thesis. This thesis has also not been submitted for any degree in any university previously.

Sara Adibi
August 2014

Acknowledgement

I would like to express my gratitude to all people who supported me during the course of my study at the National University of Singapore (NUS) and Institute of High Performance Computing (IHPC).

First and foremost, I would like to express my profound appreciation and sincere thanks to my advisors, Prof. Shailendra Joshi and Dr. Paulo Sergio Branicio for their endless and superb support of my PhD study and research. I would like to express my heartfelt thanks to Prof. Joshi. I have been really impressed by his attitude and his efforts in providing a positive and encouraging environment in his research laboratory. I sincerely appreciate his patience and confidence towards his students. From our interaction, I have gained profound understandings, knowledge and awareness of both scientific and technical aspect of the research. I must give my special thanks to my advisor Dr. Paulo Branicio. He was indeed a private tutor providing me with constant and invaluable advices, directions, and new viewpoints and taught me from the first day I joined IHPC. Dr. Branicio was beside me in every step of doing this project. I am very grateful to his kind support of my project and to the many discussions we have had on the field of molecular dynamics simulations and writing scientific articles. Thank you for being so patient with me in every step.

I also would like to thank my friends and colleagues at NUS, in particular Mr. Balaji Selvarajou, Mr. Amir Hossein Sakhaei, Mr. Saeid Arabnejad, Mr. Kartikey Joshi, Dr. Habib Pouriayevali, Dr. Ramin Aghababaei, Dr. Jing Zhang, Dr. Mostafa Jamshidian, Mr. Nader Hamzavi and Dr. Sunil Rawat for the enjoyable discussions and their encouragement.

I also would like to give my warmest thanks to Neha, Maryam, Behnaz, Elham, Shahrzad, Maedeh, Alisha, Marjan, Khatereh, Taiebeh and all my dear friends

in Singapore. They helped me stay sane trough difficult days of my PhD journey. Their support and care helped me overcome setbacks and stay focused on my graduate study. I greatly value their friendship and I deeply appreciate their belief on me.

Many thanks also go to the A*STAR Computational Resource Centre (ACRC) and IHPC for their support for the use of their high performance computing facilities, and for being so efficient and friendly in handling our administrative issues, and many thanks to all the staff and students of IHPC for their friendship.

I also want to express my appreciation to the laboratory officers of Applied Mechanics lab at NUS, Mr. Chiam Tow Jong, Mr. Joe Low Chee Wah, and Mr. Alvin Goh Tiong Lai, for their pleasant support.

I would also like to acknowledge research scholarship support from A*STAR under Singapore International Graduate Award (SINGA).

Last, but not least, I would like to thank my family for their love, support, inspiration, and dedication. Completing a doctoral thesis research is an extensive undertaking requiring sacrifices and broad support from family. It would have certainly been impossible to bring this work to fruition without the support of my beloved parents and my brother. My parents have been constantly supporting me throughout the life, ignited the desire to learn and to deeply appreciate science and knowledge. Indeed, they shaped my life, motivated me, and endlessly supported me beyond what I can express by words. Their prayer was what sustained me thus far. I also would like to give my special thanks to my brother for all his help and support to me from an early age.

Dedication

To my dear parents (Safa and Akbar),

for making it possible to embark on this journey

&

for their love, endless support and encouragement all through the way

List of Contents

Summary

Metallic glasses (MGs) are interesting materials with a disordered liquid-like structure and metallic solid-like properties. In recent years, the prospect of realizing MG architectures with superior mechanical properties has attracted a lot of attention. The primary objective of this thesis is to perform comprehensive molecular dynamics (MD) simulations of conventional MG and engineered MG architectures, called Nanoglasses (NGs), in order to gather detailed insight into the mechanical properties and deformation mechanisms of these materials. In the first part of this work, we perform large-scale MD simulations to investigate the mechanical behaviour and deformation mechanisms of $Cu_{64}Zr_{36}$ MG nano-scaled cylindrical specimens (nanopillars) under tensile loading. The objective here is to systematically analyse the role of applied strain-rate and geometric characteristics of the specimen on their strength and failure response. The results reveal that with increasing strain-rate the macroscopic failure transitions from brittle (shear bands) to ductile (necking) mode. Further, specimens with smaller aspect ratio (length/diameter) fail at larger strains than their larger aspect-ratio counterparts. The latter is a consequence of the storage of a larger amount of elastic energy that enables fully propagating shear bands immediately following the macroscopic yield. In addition, results show that surface imperfections are essential to explain the experimentally observed tendency for necking at smaller diameters. While simulations with smooth nanopillar surfaces show failure by shear band propagation at any diameter, simulations with defective surfaces show clear size effects with failure by necking for diameters below 50 nm and by shear banding for larger diameters. In the second part of the thesis, we simulate novel NG architectures that are engineered to

improve the stability of plastic deformation of MGs. Using MD simulations, we investigate in detail the mechanical behaviour of $Cu_{64}Zr_{36}$ NGs over a range of glassy "grain sizes". The architectures are generated using Voronoi tessellation in a procedure that qualitatively mimics the structure produced by the experimental synthesis route. Our results show that NGs exhibit a transition from localized deformation in the form of a single dominant shear band to a near homogeneous plastic deformation with decreasing grain size. This occurs because the interfacial regions (grain boundaries) act as preferred channels of plasticity, causing generation of an interconnected motif of shear bands that depends on the microstructure grain size. Further, we demonstrate the effects of alloy composition on the structural and mechanical properties of CuZr NG films with grain sizes ranging from 3 to 15 nm. These results also confirm the localized to near-homogeneous transition of plastic deformation with decreasing grain size at all compositions. An important highlight of the composition study is that the transition grain size depends on the alloy composition. A comprehensive structural analysis of NGs indicates that the differences in the mechanical behaviour as a function of composition are rooted at the distinct statistics of the prominent atomic Voronoi polyhedra. In addition, it is also influenced by the thickness of glass-glass interface (GGI) and the consequent fraction of atoms at interfaces for a given average grain size. Furthermore, the composition dependence of the mechanical behaviour in NG follows that of the parent conventional MG, i.e. a stronger MG will generate a stronger NG. On the other hand, the intrinsic tendency of homogeneous deformation below the transition grain size is not affected by composition. We further study the role of microstructural topology in the failure behavior of NGs.

We simulate $Cu_{64}Zr_{36}$ NG nanopillars with three-dimensional grain structure and grain sizes in the range of 3- 20 nm under uniaxial tension. The results reveal that the degree of deformation homogeneity and correspondingly the induced ductility is dependent on the grain size and structure, and the connectivity of the GGI network. The three-dimensional grain structures in NG nanopillars prevent the formation of one dominant localized shear band path along NG interface. The results indicate that NG nanopillars exhibit necking and induced plasticity at all grain sizes in addition to the transition to near-homogeneous flow at small grain sizes.

List of Tables

List of Figures

List of Abbreviations

2D	Two-dimensional
3D	Three-dimensional
BDT	Brittle-to-Ductile Transition
BMG	Bulk Metallic Glass
CE	Continuum Elasticity
CFD	Continuum Fluid Dynamics
CN	Coordination Number
DFT	Density Function Theory
DPR	Deformation Participation Ratio
EAM	Embedded Atom Method
FEM	Finite Element Method
FI	Full Icosahedron
FIB	Focused Ion Beam
GB	Grain Boundary
GGI	Glass-glass interface
LRO	Long-range order
MC	Monte Carlo
MD	Molecular Dynamics
MG	Metallic Glass
NG	Nanoglass
PBC	Periodic Boundary Conditions
SB	Shear Band
SC	Shear Cluster
SRO	Short-Range Order
STZ	Shear Transformation Zone
TEM	Transmission Electron Microscopy
VP	Voronoi Polyhedral

Part I

INTRODUCTION

1. Introduction

1.1 Background

Metallic glasses (MGs) constitute an intriguing class of metallic materials. They were first produced in 1960 by rapid quenching of metallic liquids at very high cooling rates of ~10^6 K/s (Klement et al., 1960). At such cooling rates, atoms may not get sufficient time to reorganize themselves into a crystalline state leading to an amorphous atomic structure. Absence of long-range order (LRO) in such structures naturally eliminates common crystalline defects such as dislocations and grain boundaries (GBs). Owing to the absence of LRO and defects, MGs exhibit some mechanical characteristics that are distinct from their crystalline counterparts (Boudreaux and Frost, 1981; Cyrot-Lackmann, 1980; Greer, 1995; Salimon et al., 2004; Telford, 2004; Zhang et al., 2004). In particular, they generally possess higher strength, hardness, elasticity, and elastic energy storage capacity compared to their crystalline counterparts.

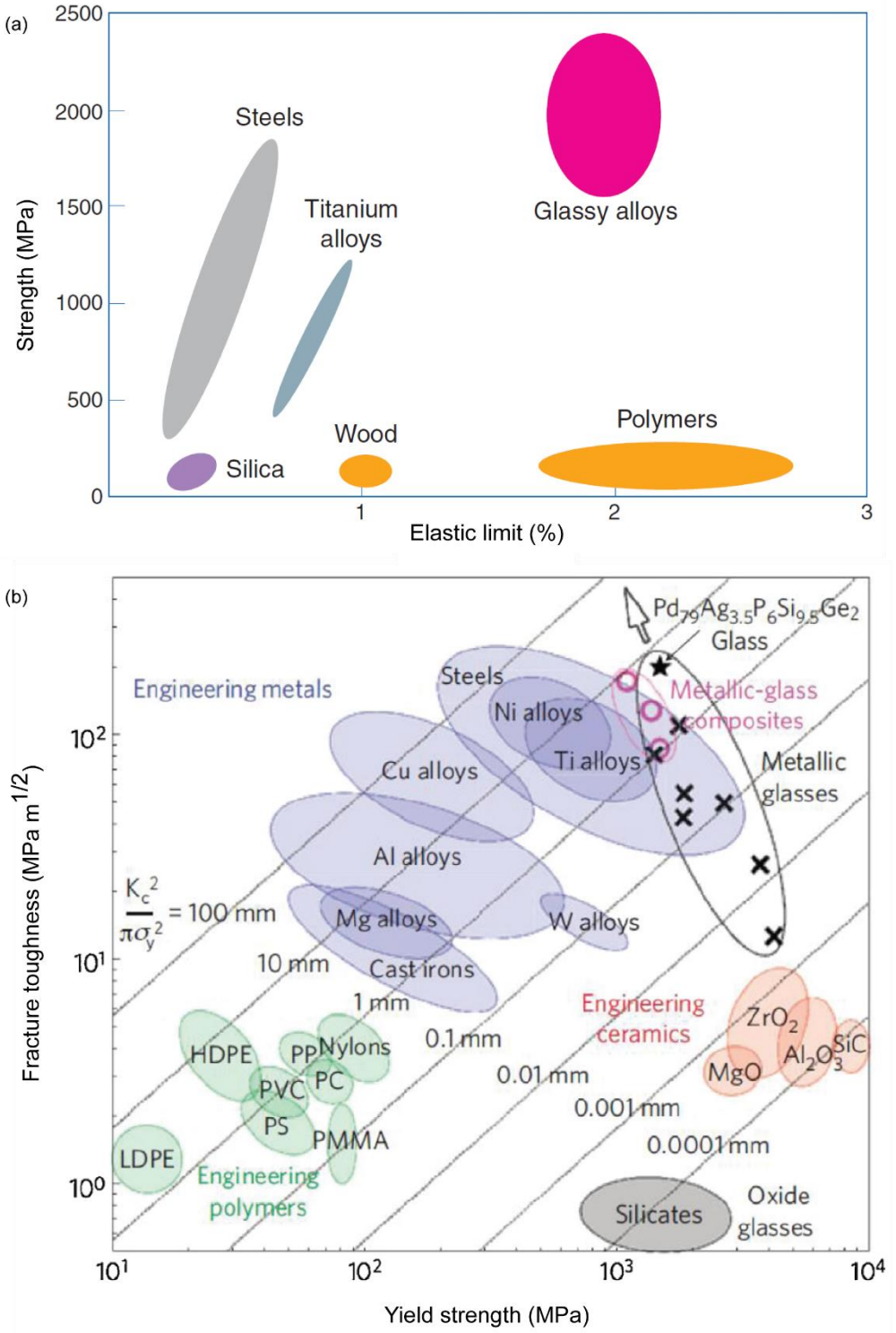

Figure 1-1 Comparing MG properties with different materials according to their (a) strength and elastic limit. Reprinted with permission from (Telford, 2004) © 2004 Elsevier Ltd, (b) yield strength and fracture toughness. Reprinted with permission from (Greer et al., 2013) © 2013 Elsevier B.V.

Fig 1-1 compares the strength, elastic limit, yield stress and fracture toughness of MGs based on multiple representative materials. For some particular compositions, MGs may also possess high corrosion resistance and interesting magnetic properties (Greer and Ma, 2007; Schuh et al., 2007; Shan et al., 2008; Yavari et al., 2004). Due to such outstanding combination of properties, MGs are subject of intense investigation (Chen et al., 2011; Cheng et al., 2009b; Liu et al., 2011; Shan et al., 2008; Sharma et al., 2009; Wessels et al., 2011) and are considered ideal candidates for structural applications, such as high performance sport equipment, electronics, medicine, defence, aerospace and fine jewellery industry (Liu et al., 2014; Miracle et al., 2008; Telford, 2004).

The Achilles' heel of MGs, which prevent their widespread use as a structural material, is their lack of global plasticity (Schuh et al., 2007). In a broad sense, MGs are similar to ceramics in that they exhibit negligible ductility when deformed beyond their strength limit. Unlike crystalline metals, which usually exhibit large macroscopic plasticity, MGs fail rather catastrophically via propagation of runaway shear bands (SBs) (Argon, 1979; Falk and Langer, 1998). Recent experimental and computational studies have shown evidence that this limited plasticity is intrinsically dependent on their atomic structure, which is dictated by their composition and processing conditions (Bruck et al., 1994; Cheng et al., 2008b; Duan et al., 2006; Fan et al., 2000; Lewandowski, 2001; Şopu et al., 2011a). For a given MG composition, the mechanical behaviour can be altered considerably by the change in the processing history such as using different cooling rates or annealing times (Khonik et al., 2008; Lind et al., 2006; Murali and Ramamurty, 2005; Ramamurty et al., 2002; Shi and Falk, 2006; Wu et al., 2007b). These alterations likely originate from

changes in the topology of the atomic structure, which results in changes in the atomic Voronoi statistics (Hufnagel and Brennan, 2003; Mauro et al., 2011). For instance, presence of high fraction of certain atomic Voronoi polyhedral (VP) has been identified as a key structural feature in CuZr MGs compositions that controls not only the yield strength and the elastic properties, but also the initiation of shear localization and the intrinsic (lack of) plasticity (Cheng et al., 2009a; Cheng et al., 2008b; Wang et al., 2008). Over the last decade, a major body of research has focused on improving the plasticity of MGs (Hofmann et al., 2008; Jang et al., 2011; Kim et al., 2011; Wu et al., 2007a; Zhao et al., 2010). Fig. 1-2 illustrates three methods of improving MG ductility. Amongst these, insertion of nanocrystalline inclusions (figs 1-2a and b) (Hays et al., 2000, 2001; He et al., 2002; Hofmann et al., 2008; Shi and Falk, 2008) and pre-deformation of samples (figs 1-2c and d) (Cao et al., 2010; Lee et al., 2010; Scudino et al., 2010) have shown to improve the tensile ductility of MGs. These methods result in a pattern of uniformly distributed multiple SBs in the MG volume that carry plasticity thereby increasing the overall ductility of the sample during tensile deformation. An alternative approach not based on changes in composition or pre-processing was proposed and may significantly increase the ductility of MGs (Jing et al., 1989). In this approach (figs 1-2e and f), fine MG powder is consolidated by cold compression generating what is called a *nanoglass* (NG). The inherent glass-glass interfaces (GGIs) in an NG were shown to have structural similarities to SBs (Fig. 1-2g) (Ghafari et al., 2012b; Gleiter, 2008; Ritter et al., 2011). They

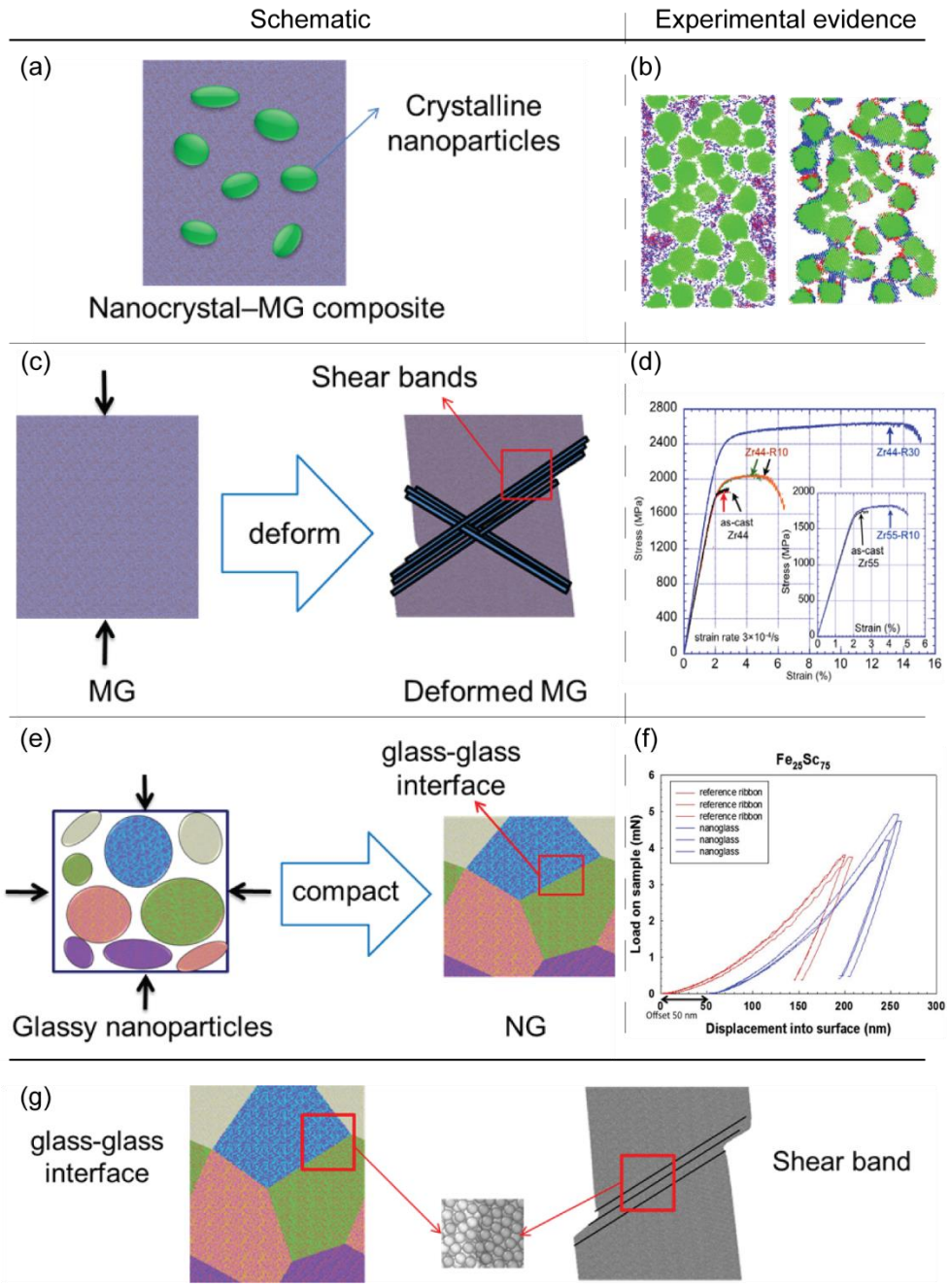

Figure 1-2 Some approaches to improve the ductility of MGs. (a , b) Nanoinclusion, (b) Atomic configurations during the compression test of MG-composite at 0% and 10% strain. Reprinted with permission from (Shi and Falk, 2008) © 2007 Acta Materialia Inc. (c , d) pre-deformation, (d) Compressive stress–strain plots of as-cast and differently cold rolled Zr44 showing the improvement of intrinsic plasticity upon cold rolling of brittle BMGs at room temperature. Reprinted with permission from (Lee et al., 2010) © 2010 Acta Materialia Inc. (e , f) Nanostructured MG (NG), (f) Load-displacement curves of nanoindentation test for the $Fe_{25}Sc_{75}$ NG and the BMG ribbon. Reprinted from (Franke et al., 2014). (g) Similarity of NG interface and SB in MG.

exhibit lower short range atomic order (SRO) and higher atomic Voronoi volume when compared to the glassy grains and arguably can act as a favourable channel for plasticity (Ritter et al., 2011; Şopu et al., 2011a).

Recent trends aimed at miniaturization have brought to the fore an interesting size effect in MGs. It has been reported that reducing the MGs specimen size below a critical length scale induces non-negligible plastic deformation (Chen et al., 2011). For instance, Greer and co-workers (Jang and Greer, 2010; Jang et al., 2011) reported a transition from a strong-but-brittle to a stronger-and-ductile state simply by size reduction of MGs in the sub-micrometre regime. While such a size-dependent characteristic in MG provides attractive avenues, its mechanistic underpinning is still elusive and remains an active topic of investigation (Jang and Greer, 2010; Kuzmin et al., 2012; Lee et al., 2007a; Magagnosc et al., 2013; Schuster et al., 2008; Wu et al., 2009c).

The remaining of the present chapter briefly reviews the history of MGs, proposed mechanisms underlying their deformation, and recent views on their failure mechanisms. The chapter is closed by introducing NGs as a promising method to enhance MGs' ductility.

1.2 A Brief History of Metallic Glasses

The history of MGs began with the synthesis of the first binary MGs ($Au_{80}Si_{20}$) by Klement and colleagues at Caltech in 1960 (Klement et al., 1960). They applied a rapid quenching method to cool the material from 1600 K to room temperature at the rate of ~10^6 K/s. The high cooling rate method used, melt spinning, to form the amorphous structure limit the size of the final MG samples to the order of microns with a thin ribbon or film shape. To commercialize MGs,

new techniques such as vapor deposition (Greer, 1995), solid state amorphization reactions (Eckert et al., 1988), and amorphization by high energy radiation (Cahn and Greer, 1996) have been developed. In addition, different alloy compositions were investigated to find materials with low cooling rate, which could allow the production of increased specimen sizes.

MGs with dimensions in the order of millimeters are referred to as bulk MGs (BMG). Chen and colleagues made amorphous spheres of the ternary system of Pd-Ag-Si, Pd-Cu-Si, and Pd-Au-Si at cooling rates of 10^2 K/s to 10^3 K/s (Chen and Turnbull, 1969). The first BMG sample synthesized in laboratory conditions was based on ternary Pd-Cu-Si alloy (Chen, 1974). The synthesis process comprised rapidly quenching a molten alloy in a fused quartz capillary by submerging it into water. This procedure resulted in samples with sizes up to 1 ~ 3 mm. The first commercialized MG called Metglas, was successfully made by Libermann and Graham (Liebermann and Graham, 1976), and later was widely used in low loss power distribution transformers. In the early 1980s, glassy ingots of $Pd_{40}Ni_{40}P_{20}$ with a diameter of 5 mm were produced by Turnbull's research group through a slower cooling rate of 1 K/s (Drehman, 1982). Then, this group synthetized the largest BMG to that date with a casting thickness of 1 cm and using the method of processing in a boron oxide flux (Kui et al., 1984). However, the expensive cost of Pd metal limited industrial application of this material and its commercialization.

In the late 1980s, Inoue and his colleagues in the Tohoku University discovered several multicomponent alloy systems with lower critical cooling rates, such as Mg-, La-, Zr-, Fe-, Ti- and Ni-based alloy systems (Inoue, 2000). They produced aluminum MG with $La_{55}Al_{25}Ni_{20}$ composition which has been

widely used in the aerospace industry (Inoue et al., 1990). Johnson and Peker developed a high performance five element BMG alloy named Vitreloy1, with a chemical composition of $Zr_{41.2}Ti_{13.8}Cu_{12.5}Ni_{10}Be_{22.5}$ and used it in a NASA project (Peker and Johnson, 1993). This amorphous alloy can be fabricated through a slow cooling rate of 1K/s, and cast in sizes up to 10 cm. Producing samples of this Zr-based BMG family does not require any special processing treatment, and can be synthesized by conventional casting methods.

So far, the combination of a great majority of common metals has been used to produce MGs. Table 1-1 summarizes the characteristic properties and potential applications of a representative group of MGs (Greer et al., 2013). For further detailed review on MGs, please refer to (Greer, 1995; Inoue and Takeuchi, 2002; Johnson, 1999).

Table 1-1 Representative MGs with their characteristic properties and potential applications (Greer et al., 2013).

MGs	Characteristic properties	Potential applications
Zr-Ti-Cu-Ni-Be	High glass-forming ability and stability	Molding, sporting goods, structural components
Fe-Co-Zr-Si-C	Soft ferromagnetism	Transformer cores
Co-Si-P-Fe-Ni	High hardness and wear resistance	Coatings
Ce-Al-Cu	Low glass-transition temperature	Metallic plastics
Pd-Ag-P-Si-Ge	High strength-toughness combination	Damage-tolerant materials
Mg-Zn-Ca	Biodegradable	Bone implants

1.3 Deformation Behavior of MG

Chen and Wang (Chen and Wang, 1970) were one of the first to quantify the mechanical properties of MGs. They conducted tensile tests on a rolled-quenched foil of Pd–Si based MGs and demonstrated higher strength (near theoretical value), lower Young's modulus, and smaller permanent elongation of MGs compared to their crystalline counterpart. Masumoto and Maddin

(Masumoto and Maddin, 1971) performed a comprehensive study of the mechanical behavior of MGs. They conducted a tensile test on MGs over a broad range of temperatures and strain rates. Their results established the high strength and brittleness of MGs. They observed deformation lines associated with surface steps and SB based cracks in MG samples under bending. They estimated the thickness of the deformation lines to be ~20 nm, consistent with most of the current observations of SBs thickness by transmission electron microscopy (TEM). Leamy and colleagues (Leamy et al., 1972) studied the shear nature of plastic deformation in MGs and demonstrated that samples failing in tensile test show significant shear deformations without any sign of tensile crack. The failure observed occurred at the maximum shear stress plane at ~45° with respect to the tensile axis. Evidence of structural disordering in SBs was shown by Pampillo and colleagues (Pampillo et al., 1972). They also showed that the chemical potential of the material is different in the SB relative to the bulk. Polk and Turnbull (Polk and Turnbull, 1972) suggested that the deformation in MGs could be localized or homogeneously distributed along the sample depending on the strain rate. (Spaepen, 1977) sketched the deformation mechanism map for MGs revealing the effect of temperature and strain rate on the deformation transition from a homogeneous manner to a localized manner (cf. Fig. 1-3). The two forms of deformation, homogeneous and localized, are discussed in the following subsections:

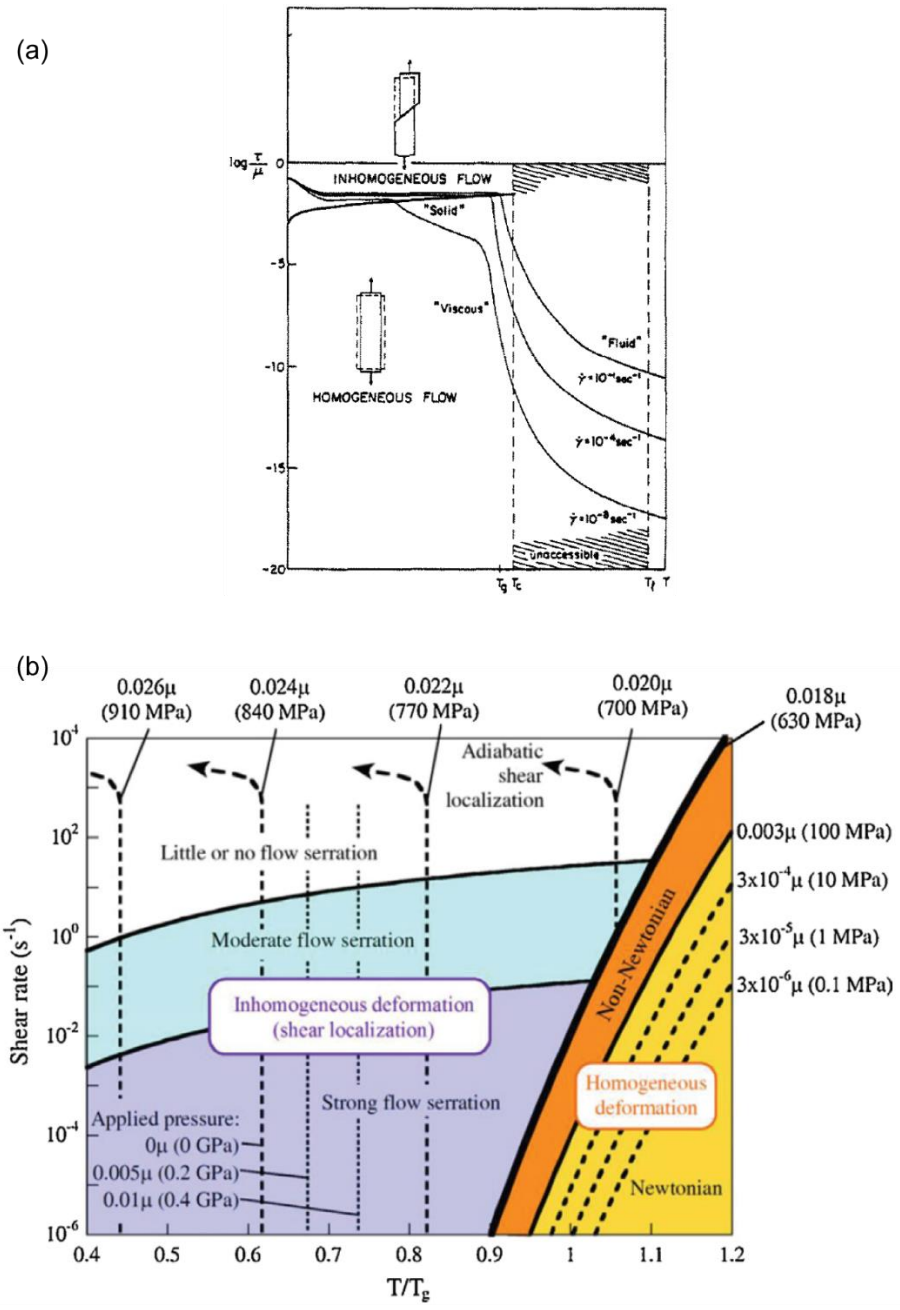

Figure 1-3 Deformation mechanism map for MGs. (a) Various mode of deformation in MGs. Reprinted with permission from (Spaepen, 1977) © 1977 Published by Elsevier Ltd. (b) Deformation dependence of MGs on temperature and strain rate. The actual stress values given in the map are for a specific glass, but are expressed more generally in terms of the shear modulus μ. Reprinted with permission from (Greer et al., 2013) © 2013 Elsevier B.V.

1.3.1 Homogeneous Deformation

The characteristic property that governs plastic flow in MGs is the atomic scale excess free volume. As seen in Spaepen's deformation mechanism map

(Spaepen, 1977), at high temperatures MGs may undergo homogeneous deformation leading to large strains. For an amorphous metal, homogeneous deformation results from the gradual emergence of viscous flow as temperature increases. Particularly when an equilibrium between structural disordering and ordering is instantly reached, a steady-state homogeneous flow is obtained. Spaepen's atomic viewpoint asserts that this stage corresponds to equilibrium between the nucleation and annihilation of free volume (Spaepen, 1977). Commonly, the plastic flow of MGs depends on the deformation strain rate as well (Bletry et al., 2004; Lu et al., 2003; Reger-Leonhard et al., 2000). At low stress levels, the flow is Newtonian and MGs may undergo nearly ten-fold deformation (Kawamura et al., 1999). Increasing the strain rate causes non-Newtonian flow, reducing the deformability of the MG (Nieh et al., 2002; Nieh et al., 2001).

Another form of homogeneous flow in MGs is known as the non-steady-state flow. In this scenario, initially the generation and annihilation terms in free volume evolution are not balanced, although the deformation is still homogeneous. The initiation of the plastic deformation is reflected by a stress overshoot in the stress-strain relationship, which is followed by a stress softening. The stress drop continues until the annihilation and generation of free volume reach equilibrium, beyond which the stress-strain response manifests as a plateau (Lu et al., 2003).

1.3.2 Inhomogeneous Deformation

Inhomogeneous deformation in MGs occurs at high stresses and low temperatures through shear banding (Johnson and Samwer, 2005; Schuh et al., 2004). SB formation is a result of strain localisation caused by softening through

localized accumulation of free volume (Donovan, 1989; Li et al., 2003; Liu et al., 2005a). One interpretation suggests that the free volume accumulation within SB leads to a local reduction in the viscosity (Wright et al., 2001). An alternative interpretation is the local adiabatic heating within the SB (Chen et al., 1994; Leamy et al., 1972; Lewandowski and Greer, 2006; Liu et al., 1998; Zhang et al., 2011). These results imply that the rise in temperature in SB is a result, rather than a cause, of shear banding in MGs.

At room temperature, shear banding resulting in dominant localization is the main reason of low plasticity and catastrophic failure in MGs under compression and tension (see Fig. 1-4) (Zhang et al., 2003). Therefore, it is essential to thoroughly understand the initiation and propagation of SBs in order to describe the observed inhomogeneous deformation in MGs and tackle the challenging problem of brittle failure prevention.

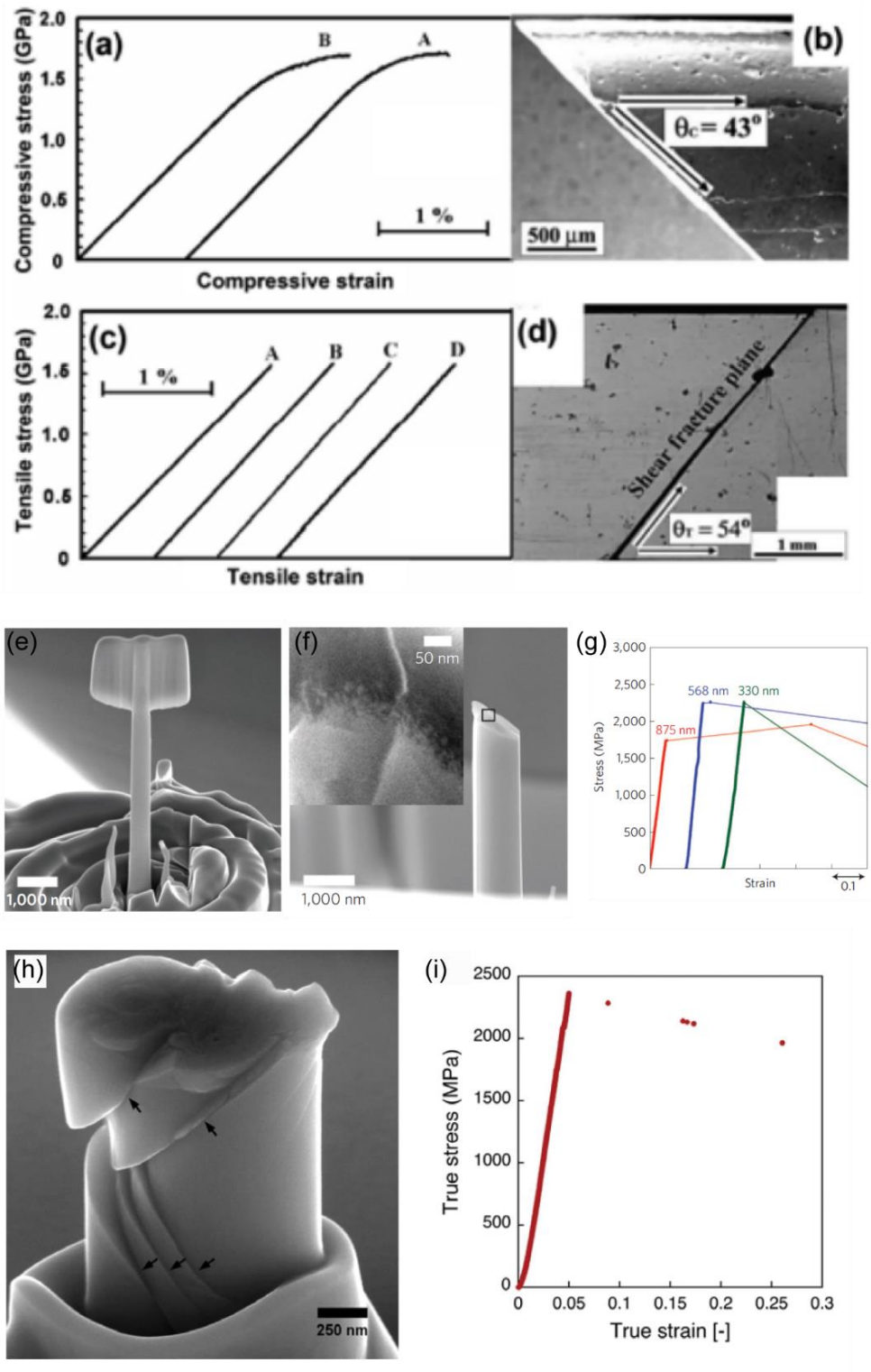

Figure 1-4 Brittle failure of the MG under uniaxial (a,b) compression, and (c,d) tension. Only limited plasticity can be achieved due to sudden fracture along a major SB. Reprinted with permission from (Zhang et al., 2003) © 2002 Acta Materialia Inc.. (e,f,g) MG nanopillar failure under tension. Reprinted with permission from (Jang and Greer, 2010) © 2010, Rights Managed by Nature Publishing Group, (h,i) Compressed MG nanopillar deformed through a shear banding process (indicated by arrows). Reprinted with permission from (Jang et al., 2011) © 2010 Elsevier Ltd.

1.3.3 Atomistic Deformation Mechanisms

In crystalline materials, plastic deformation is largely facilitated by dislocations, which are the most common linear defects (Dieter and Bacon, 1988). In contrast, the absence of crystalline structure in MGs results in plastic deformation that is mediated by local atomic rearrangement (shear transformation) (Argon, 1979; Falk, 1999; Falk and Langer, 1998; Schuh et al., 2007; Srolovitz et al., 1983). A shear transformation is an inelastic process, which releases stored elastic energy stored in the system under the action of shear stress. Shear transformation includes a cluster of atoms that undergo deformation in a more profuse way than its surrounding matrix. The local region containing these atoms is referred to as the shear transformation zone (STZ) (Falk and Langer, 1998). Two widely accepted models of atomistic deformation in the MGs are (i) the free volume model (Spaepen, 1977; Steif et al., 1982) and (ii) the STZ model (Argon, 1979). The free volume model is based on a similar concept for conventional glasses and liquid (Cohen and Turnbull, 1959; Polk and Turnbull, 1972) in that the evolution of a state variable (the free volume) determines the strain evolution in the MG. It is formally defined as the average excess atomic volume in a material relative to an ideally ordered structure. Under shear loading, free volume is formed (i.e. system experiences dilatation) by forcing the atoms to jump into smaller interstitial spaces in their immediate neighbourhood. A series of these discrete atomic jumps induce deformation in the MG. The macroscopic plastic flow under the pure shear loading is a result of the net forward atomic movements in the direction of applied stress (Fig. 1-5a). The STZ model is akin to the free volume model in terms of the atomistic description with the exception that an STZ is a cluster comprising ~ 100 atoms

that forms the deformation unit (Heggen et al., 2005; Mayr, 2006; Reger-Leonhard et al., 2000). Fig. 1-5b illustrates the STZ deformation mechanism under shear stress.

Both mechanisms are thermally activated with comparable activation energy around tens of $k_B T_g$, where k_B denotes the Boltzmann constant and T_g is the glass transition temperature (Polk and Turnbull, 1972; Spaepen, 1977).

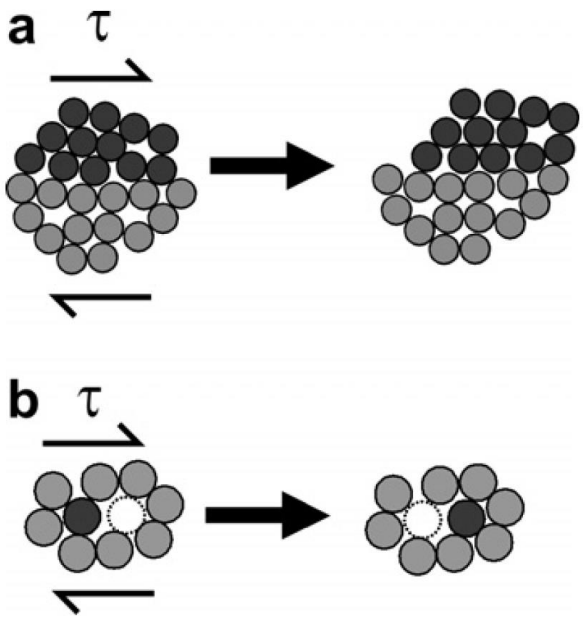

Figure 1-5 Two dimensional Schematic illustration of (a) shear transformation zone (STZ) deformation mechanism, and (b) a local atomic jump (free volume deformation mechanism). Reprinted with permission from (Schuh et al., 2007) © 2007 Acta Materialia Inc..

1.4 Fracture Behavior of MG

Due to characteristic amorphous structure of MGs, their fracture behaviour in many cases resembles that in oxide or silicate glasses. This does not imply that fracture of MGs is always brittle; in some cases, ductile fracture is observed (Hess et al., 2011; Xi et al., 2005). Although some MGs exhibit a comparable level of toughness to the crystalline materials, the ductile fracture in MGs is

usually different from that in the crystalline materials. This difference is due to the lack of dislocation based plasticity. Fracture is considered to be ductile in the case of large plastic deformation. The fracture surface morphology in the ductile fracture shows a vein pattern, as shown in Fig. 1-6 (Xi et al., 2005). In contrast, brittle fracture occurs with limited plasticity and usually exhibits a relatively flat surface with fine vein patterns (Xi et al., 2005).

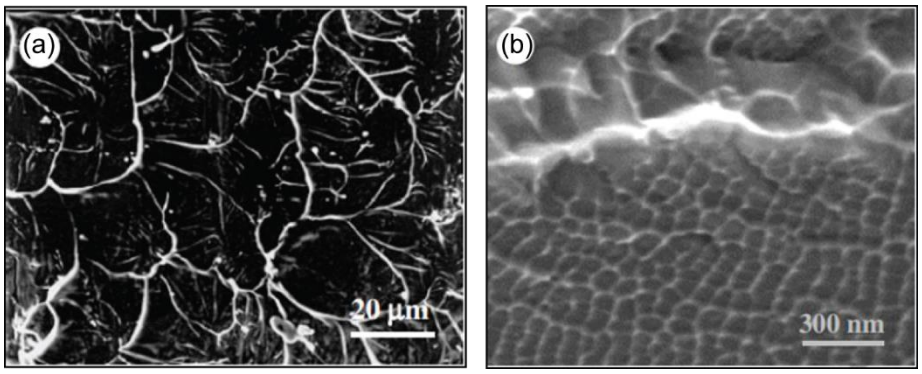

Figure 1-6 Scanning electron microscopy of fracture surface of the (a) ductile MG, showing the characteristic vein pattern. (b) brittle MG, in which the vein pattern can only be observed at a large magnification. Reprinted with permission from (Xi et al., 2005) © 2005, American Physical Society.

Studies on a large number of MGs revealed that the fracture energy is correlated to the elastic properties (Lewandowski, 2001). More specifically, studies indicate that MGs with Poisson's ratio (υ) greater than ~ 0.4 tend to show high fracture energy and fail plastically. MGs with smaller Poisson's ratios, in contrast, exhibit brittle fracture. In terms of the shear modulus (μ) and bulk modulus (B), MGs with $\mu/B < 0.4$ are tough, while those with $\mu/B >$

0.43 are brittle[1] (Lewandowski et al., 2005), illustrated in Fig. 1-7. MGs with a low value of μ show poor resistant to plastic shear deformation, while a large value of B indicates strong resistance to the dilatation necessary for mode-I crack propagation.

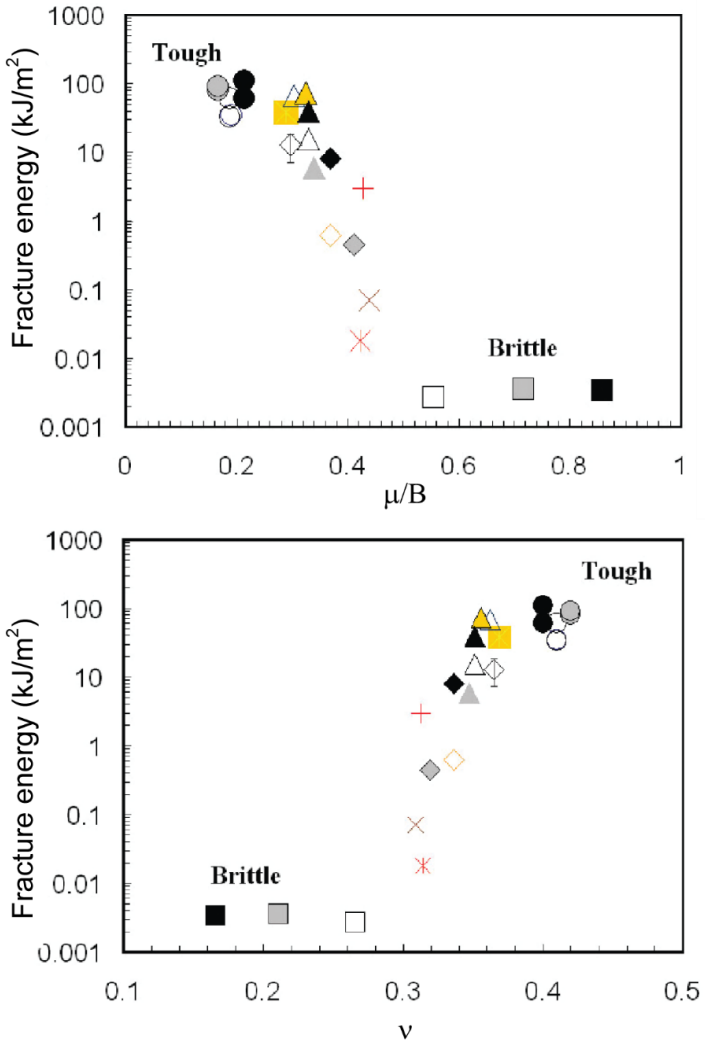

Figure 1-7 Variation of the fracture energy with (a) bulk-to-shear modulus ratio, (b) Poisson's ratio. Both shows sharp brittle-to-ductile fracture transition at a critical value. Reprinted with permission from (Lewandowski et al., 2005) © 2005 Taylor & Francis.

[1] Poisson's ratio υ and the modulus ratio μ/B are inversely related by $\mu/B = (3(1-2\upsilon))/(2(1+\upsilon))$ revealing a competition between the shear and dilatation.

1.5 Effects of Loading Rate and Temperature

Temperature and strain rate play important roles in the deformation of MGs (Cao et al., 2013; Greer et al., 2013; Spaepen, 1977). The mechanism map introduced by Spaepen (Spaepen, 1977) delineated homogeneous and inhomogeneous deformation regimes at high and low temperatures, respectively. (Lu et al., 2003) systematically studied the deformation behavior of Vitreloy 1 ($Zr_{41.2}Ti_{13.8}Cu_{12.5}Ni_{10}Be_{22.5}$ BMG) across a broad range of strain rates and temperatures, and demonstrated that the dependency of BMG alloys on strain rate reduces with decreasing the ambient temperature. Extensive experimental studies at room temperature on a variety of BMGs indicate a rather rich landscape of strain rate sensitivity. BMG alloys may exhibit positive, negative or no strain rate sensitivity depending upon its composition (e.g. Table 1-2).

Table 1-2 Selected literature on strain rate effect on BMGs.

Negative rate sensitivity	$Pd_{40}Ni_{40}P_{20}$ (Mukai et al., 2002a) $Zr_{38}Ti_{17}Cu_{10.5}Co_{12}Be_{22.5}$ (Xue et al., 2008) Zr/Hf (Gu et al., 2003) Dy_3Al_2 (Sergueeva et al., 2004)
Positive rate sensitivity	$Ti_{45}Zr_{16}Ni_9Cu_{10}Be_{20}$ (Zhang et al., 2007) $Ti_{40}Zr_{25}Ni_8Cu_9Be_{18}$ (Ma et al., 2009) $Nd_{60}Fe_{20}Co_{10}Al_{10}$ (Liu et al., 2005b)
No effect	Vitreloy1 (Bruck et al., 1996; Lu et al., 2003)

Due to the lack of crystalline structure in BMGs, conventional theories of rate sensitivity for crystalline materials cannot be applied directly to amorphous alloys. There are several alternative plausible hypotheses regarding the influence of strain rate on the yield stress (Cao et al., 2013; Liu et al., 2005b; Ma et al., 2009; Nieh et al., 2002; Xiao et al., 2003; Zhang et al., 2007). Early

room temperature studies on Vitreloy 1 indicate rate insensitive behaviors over a wide range of strain rates (Bruck et al., 1996; Lu et al., 2003; Zhang et al., 2007). On the other hand, experiments on other BMG compositions (e.g. PdNi based or Zr based) indicate that many of them exhibit negative strain rate sensitivity (Gu et al., 2003; Mukai et al., 2002a, b; Sergueeva et al., 2004; Xue et al., 2008). Intriguingly, these negative rate sensitive materials exhibit rather different failure mechanisms despite of the identical strain rate sensitivity trends. It has been seen that in Zr-based materials, the serrated flow that is common at quasi-static strain rates is suppressed at high strain rates (Xue et al., 2008); this contributes to initiation of a single SB. Theoretical analyses show that catastrophic fracture occurs when the critical plastic shear strain exceeds a certain threshold value (Xue et al., 2008). Creation of multiple SBs accommodates the critical strain and delays the occurrence of the fracture. When the generation of multiple SBs is reduced at high strain rates, major SBs dominate and quickly reach the critical strain value causing failure much earlier from a macroscopic perspective, this results in a decrease in the yield stress. For BMGs with negative strain rate sensitivity, other than Zr-based compositions (Gu et al., 2003; Mukai et al., 2002a, b; Sergueeva et al., 2004), a high strain rate initiates multiple SBs. Micro-scale SBs initiate well below the quasi-static yield stress. These micro-SBs do not propagate at low stresses. However, under dynamic loading, the rapid generation of heat within SBs becomes significant in their evolution leading to specimen failure immediately following the initiation of minor SBs; this decreases the yield stress at high strain rates and accounts for the negative strain rate sensitivity (Gu et al., 2003; Mukai et al., 2002a, b; Sergueeva et al., 2004).

In comparison, Ti-based BMGs have been shown to exhibit positive rate sensitivity (Ma et al., 2009; Zhang et al., 2007). This is attributed to a different cluster structure of Ti-based alloys compared to other alloys where locally ordered icosahedral nuclei are embedded in the amorphous matrix (Park et al., 2005). The existence of a micro-crystalline structure also contributes to the positive strain rate effect of Ti-based BMG alloys. Another material with positive rate sensitivity is $Nd_{60}Fe_{20}Co_{10}Al_{10}$; this feature is also attributed to the cluster structure of this material (Liu et al., 2005b). Further experimental studies are required to elucidate the mechanism underlying strain rate sensitivity in BMGs.

1.6 Sample Size Effect

Shi and colleagues (Shi, 2010; Shi and Falk, 2006) conducted a series of MD simulations on MG nanowires and demonstrated that small samples exhibit more resistance to shear localization. In another study, Kuzmin et al. (Kuzmin et al., 2012) demonstrated that the yield strength is generally independent of sample size. However, recent nano-scaled experiments by Jang and Greer (Jang and Greer, 2010), and Wang et al. (Wang et al., 2012) reveal that MGs exhibit the “smaller is stronger" phenomenon. Moreover, several recent experimental investigations indicate an intriguing brittle-to-ductile transition (BDT) in the failure mode upon specimen size reduction (Chen et al., 2013; Guo et al., 2007; Jang and Greer, 2010; Tian et al., 2013). *In-situ* tensile experiments (Guo et al., 2007; Jang and Greer, 2010) on Zr-based MG nano-scale specimens indicate a BDT at specimen diameter of about 100 nm. More recent experiments (Tian et al., 2013) also report a similar transition at ~80 nm in nanoscale tensile

experiments on $Cu_{49}Zr_{51}$ MG. Similar experimental and atomistic simulation results from different MG tensile tests (Chen et al., 2013; Li and Li, 2005, 2006, 2008; Luo et al., 2010) suggest that the BDT phenomenon in nanoscale MG is ubiquitous rather than material specific. Table 1-3 summarizes key studies elucidating the size effect on the deformation and failure mechanisms in various MGs. For further discussion, the reader is referred to the reviews by Greet et al. and Greer and de Hosson (Greer et al., 2013; Greer and De Hosson, 2011).

Table 1-3 Size effects on MG deformation experiment/MD simulation (Greer et al., 2013; Greer and De Hosson, 2011).

Authors	MG composition	Size (nm)	Loading	Deformation & failure
(Kuzmin et al., 2012)	Zr-based	90-600	Compression	Distributed deformation below 150 nm
(Kuzmin et al., 2011)	Al-based	110-900	Compression	Distributed deformation below 300 nm
(Deng et al., 2011)	Cu51Zr49	200	Tension	Homogeneous elongation
(Chen et al., 2011)	Cu-based & Zr-based	70-645	Compression	BDT Transition at 125 nm (taper free)
(Jang and Greer, 2010)	Zr-based	100	Tension	Necking (transition from SB to homogeneous deformation at 400 nm)
(Luo et al., 2010)	Al-based	< 20	Tension	Homogeneous elongation and necking
(Yavari et al., 2010)	Zr-based	250-300	Compression	Distributed deformation
(Bharathula et al., 2010)	Zr-based	200	Compression	Distributed deformation + shear-banding
(Wu et al., 2010)	Zr-based	150	Compression	Multiple SBs
(Cao et al., 2009)	Cu-based & Zr-based	93-645	Compression	Intermittent shear banding
(Cheng et al., 2009a)	Cu-based & Zr-based	100	Compression bending	Intermittent shear banding
(Shan et al., 2008)	$Cu_{46}Zr_{47}Al_7$	300	Compression	Intermittent shear banding
(Volkert et al., 2008)	$Pd_{77}Si_{23}$	140	Compression	Intermittent shear banding
(Lai et al., 2008)	Zr-based	700 & 1000	Compression	Shear banding
(Wu et al., 2008a)	Zr-based	3000-	Compression	Malleable to brittle transition at 3000 nm
(Guo et al., 2007)	Zr-based	100	Tension	Necking (metal-like ductility (25%) at 100 nm)

(Schuster et al., 2007)	Pd-based	250	Compression	Multiple SBs
(Cao et al., 2009)	$Cu_{64}Zr_{36}$	27	Compression	Shear-banding
(Cheng et al., 2008a)	$Cu_{64}Zr_{36}$	8	Tension	Necking
(Shi, 2010)	$Ni_{50}Nb_{50}$	5-20	Tension	>7.5 Shear banding & <5 Necking
(Li and Li, 2006)	$Ni_{40}Zr_{60}$	13.6	Tension	Necking

1.7 Ductility Enhancement in MGs

Since brittle failure of MGs occurs by accumulation of shear displacement along one dominant SB, one way to improve ductility is to restrict the propagation of individual SBs and instead distribute the plastic strain over an array of multiple SBs. Several approaches have been proposed to achieve this in practice. In the following sections we review them and briefly discuss a few promising ideas.

1.7.1 Geometrical Constraint

One approach to enhance tensile ductility in MGs is to impose geometrical constraints on SB propagation. For instance, coating a thin layer of film onto the bulk MG may provide effective constraint on the MG deformation mode by confining the propagation of SBs into the substrate/film interface thereby enhancing their ductility (Choi and Hong, 2009; Chu et al., 2012) (e.g. Fig. 1-8).

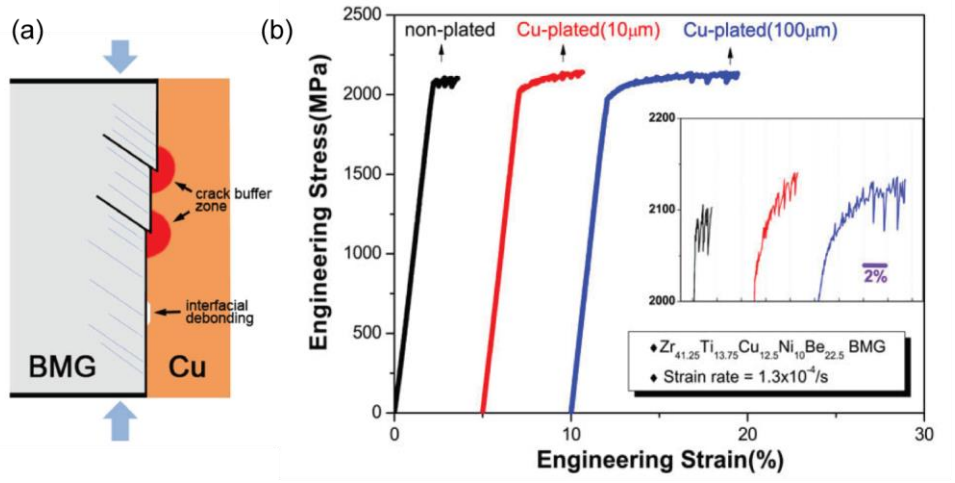

Figure 1-8 Enhancing ductility of the BMG by Cu coating. (a) Schematic illustration of the enhancing mechanism, (b) Stress-strain responses of non-plated and Cu-plated BMG with thin and thick Cu-plated layers. Reprinted with permission from (Choi and Hong, 2009) © 2009 Acta Materialia Inc.

Another technique is to induce a stress gradient (Wu et al., 2008b). This stress gradient introduces local stress concentration, resulting in the formation of multiple SBs that effectively impart ductility, as shown in Fig. 1-9.

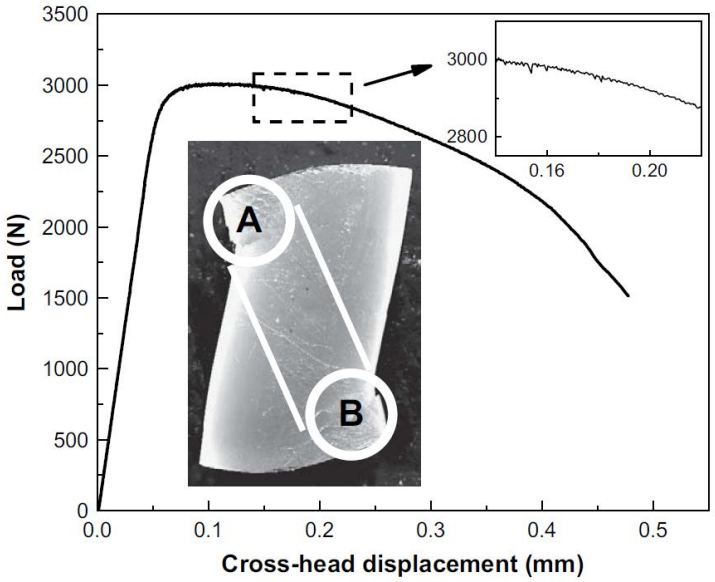

Figure 1-9 Enhanced ductility of the BMG by artificially creating a stress gradient (monoclinic geometry). Reprinted with permission from (Wu et al., 2008b) © 2008 Elsevier Ltd.

Other geometrical constraints to improve ductility are generated through rolling or bending (Pampillo, 1975), laminated composites in which layers of ductile metals alternate with layers of MGs (Alpas and Embury, 1988; Leng and Courtney, 1991), and porous MGs with randomly distributed pores (Brothers and Dunand, 2006; Wada et al., 2005).

1.7.2 MG Composites

A promising approach toward ductile MGs is via synthesizing composite architectures comprising amorphous matrix and crystalline inclusions. The crystalline phase facilitates initiation of a large number of SBs and inhibit the propagation of individual SBs. Examples of introducing crystalline phases into the amorphous matrix include partial devitrification of an MG, forming *in-situ* MG composite through precipitation of the crystalline phases during solidification and produce ex situ composites by adding second phase particles into a melt (Dong et al., 2011; Schroers and Johnson, 2004; Zhang et al., 2005). For instance, a BMG with soft dendrite inclusions exhibits substantial ductility, as shown in Fig. 1-10 (Qiao et al., 2009). During deformation, significant stress concentration develops around the second-phase particles. This initiates the formation of multiple SBs as the yield criterion is met easily around these particles.

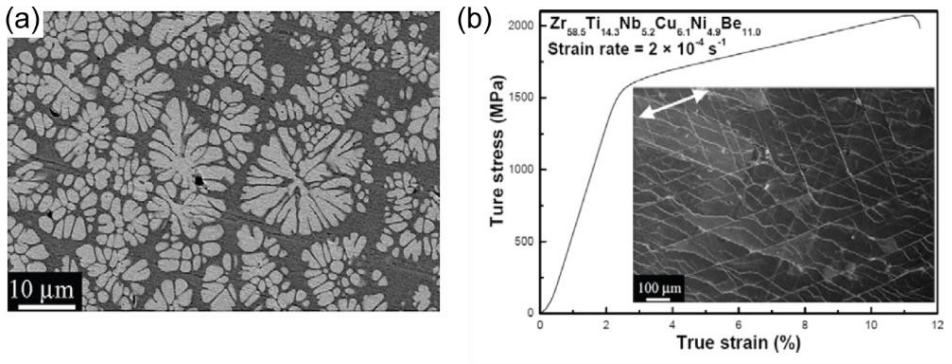

Figure 1-10 (a) Scanning electron microscopy of the Zr-based BMG composite with dendrite crystalline phases. (b) Corresponding strees-strain curve showing substantially improved plasticity. The inset shows the deformed MG composite. Reprinted with permission from (Qiao et al., 2009) © 2009 Published by Elsevier Ltd.

1.7.3 Nanoglasses

NGs are MGs with a nanoscale glassy poly-grained structure. They suggest a potential route toward significantly increasing the ductility of traditional MGs while retaining high strength (Gleiter, 2008, 2009; Jing et al., 1989). NGs are synthesized by consolidation of ultrafine MG powder (Gleiter, 1991) produced, for example, by inert gas condensation (Jing et al., 1989). Their microstructures comprise bulk glassy regions connected by grain boundary (GB)-like interfacial regions (see Fig. 1-11) that possess distinct amorphous structure compared to the bulk regions. The GGIs of NGs possess a reduced density relative to the density of the glassy grains.

In the past few years, NGs with various chemical compositions, such as Au−Si, Au−La, Fe−Si, La−Si, Pd−Si, Ni−Ti, Ni−Zr, and Ti−P, have been synthesized by inert gas condensation (Gleiter, 2008). The stability of the induced interfaces in NGs has been demonstrated for different compositions (Fang et al., 2012; Franke et al., 2014; Ghafari et al., 2012a; Jing et al., 1989; Witte et al., 2013; Wu et al., 1999). Motivated by this development,

considerable research effort is being pursued toward studying the effect of GGIs on the mechanical properties of MG (Albe et al., 2013; Fang et al., 2012; Gleiter, 2008; Ritter et al., 2011; Sopu et al., 2009; Şopu et al., 2011a).

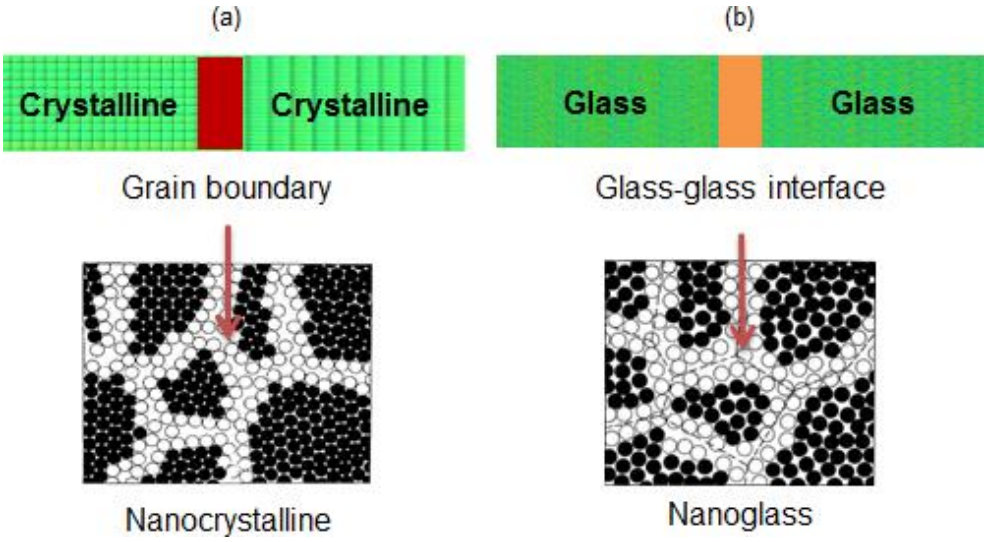

Figure 1-11 Analogy between microstructure of (a) nanocrystalline materials and of (b) NGs.

Preliminary experiment (e.g. Fig. 1-12) (Fang et al., 2012) and modelling investigations of NGs have indicated their superior performance in terms of ductility than their conventional MG counterparts (Albe et al., 2013; Ritter and Albe, 2012; Ritter et al., 2011; Şopu et al., 2011a). Using molecular dynamics (MD) simulations, Sopu et al. (Şopu et al., 2011a) show that the GGIs act as preferred regions for the formation of SBs. This suggests that manipulating the size of nanoscale glassy grains in MG could pave way to achieve high ductility. For further review on NGs, the reader is referred to the reviews by Gleiter et al. (H. Gleiter, 2014).

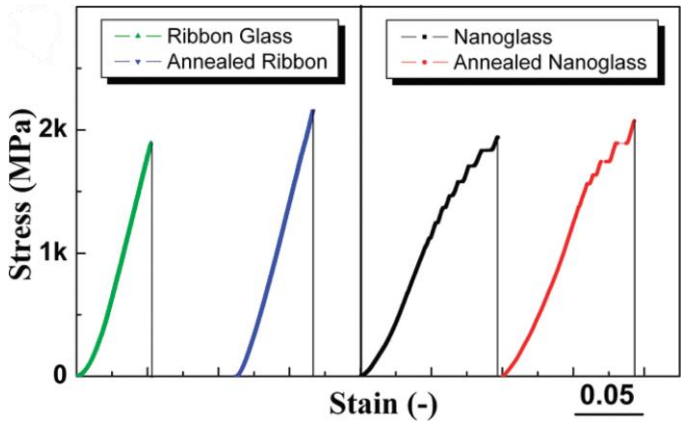

Figure 1-12 Microcompression on MG and NG micropillars (2 μm in diameter and 5 μm in height). Glassy ribbon exhibits brittle fracture at ~ 5% and ~1900 and ~2200 MPa for the as-prepared and annealed states. NG, in the as-consolidated state yields at ~ 1250 MPa, then shows nonlinear plastic flow followed by a fracture stress of ~ 1950 MPa, comparable to the ribbon glass. Reprinted with permission from (Fang et al., 2012) © 2012, American Chemical Society.

In a very recent work, the mechanical properties of $Sc_{75}Fe_{25}$ NG nanopillars were investigated by in situ tensile and compression tests in a transmission electron microscope (Wang et al., 2014). It was reported that the 400 nm diameter NG nanopillars exhibit a 15% plastic strain under uniaxial tension and failure by necking. As discussed by the authors, this is an outstanding plastic deformation ability with unprecedented tensile plasticity among MG samples of similar sample sizes (Wang et al., 2014). Figure 1-13 shows the stress strain curve and deformation snapshots of the NG and MG during tensile loading. It shows that the NG deformed like a ductile material and exhibit significant plasticity (Wang et al., 2014).

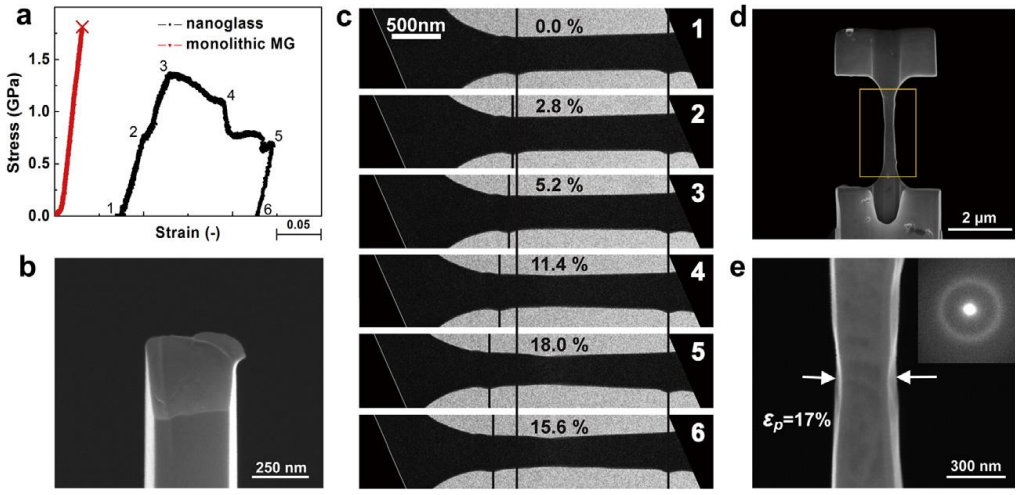

Figure 1-13 (a) The tensile stress–strain curves of $Sc_{75}Fe_{25}$ NG and monolithic MG; (b) Sample of the monolithic MG after tensile loading; (c) snapshots of the deformation of NG nanopillar during tensile loading ; (d,e) Samples of NG after tensile deformation. The inset of (e) shows the corresponding selected-area diffraction pattern. Reprinted with permission from.(Wang et al., 2014) © 2014 Acta Materialia Inc.

1.8 Motivation

While the foregoing discussion is by no means comprehensive, it serves as a short preamble that highlights some of the key areas in the field of mechanics of MGs. It essentially helps to set the objectives of the present work. From the perspective of this author, some of the unexplored or poorly explored aspects in the mechanics of MGs are:

i. While there exists a wealth of literature on the mechanical properties of MGs, a definitive understanding of size effect, geometry, and loading rates on the mechanical properties and deformation mechanisms of MG remains elusive.

ii. While experimental studies indicate competition between SB and necking in the failure of MG nanopillars, the origin of this competition

is not well defined. Likewise, the possible role of extrinsic effects such as specimen geometry on the BDT in the nano-scaled regime has not been explored.

iii. While NGs appear to be promising MG micro-architectures, there are very few studies focused on characterizing the mechanical behavior of NGs as a function of specimen and microstructural sizes. To enable a systematic design approach towards engineered NG architectures for strength and ductility, an in-depth understanding of the effect of glassy grain size and the GGIs on the mechanical properties of NG is necessary. It is reasonable to postulate that apart from the grain size, the properties of NGs will also depend on the composition and processing conditions. Moreover, it was demonstrated that the presence of GGIs in NG architectures helps achieve enhanced ductility compared to the parent MG. However, it is not known how these GGIs are structurally different from those of the grains.

iv. So far, MD simulations of NGs have focused on bulk systems with a columnar arrangement of grains. It is of interest to investigate the interaction between extrinsic (specimen geometry) and intrinsic (grain size and topology of grains) effects on the mechanics of NGs.

MD simulations provide a useful approach to gain detailed insight into the strength and failure mechanisms in MGs and NGs, especially in nano-scaled systems. Therefore, MD is the tool of choice for this work.

1.9 Objectives

With the summary in the preceding section setting the motive, we describe here the objectives pursued in this work. The overarching objective of this thesis is to investigate in detail the nexus between the mechanical characteristics and deformation mechanisms of nano-scaled MGs and NGs using large-scale MD simulations. The specific objectives of this work are:

- To investigate the extrinsic effects due to specimen size, aspect ratio and applied strain rate on the deformation behavior of nano-scaled MGs.
- To investigate the role of geometric imperfections on the failure mechanisms in nano-scaled MG samples.
- To map the effect of composition and microstructure on the strength and failure response of NGs.
- To examine the role of microstructural topology in the failure behavior of NG nanopillars.

To meet these objectives, we choose CuZr MG as our model system. To perform MD simulations, post-processing, and visualisations in this work we choose the Large-scale Atomic/Molecular Massively Parallel Simulator (LAMMPS) (Plimpton, 1995) and the Open Visualization Tool (OVITO) (Stukowski, 2010) packages.

1.10 Thesis outline

The thesis is organized as follows:

Chapter 2 introduces the MD method. This chapter provides an overview on different interatomic potentials, initial conditions, boundary conditions, and ensembles used in the simulations.

Chapter 3 covers the MD simulation of $Cu_{64}Zr_{36}$ MG nanopillars under tensile loading. Using geometrically smooth specimens, we elucidate the effect of sample diameter and aspect ratio as well as loading strain rate on the stress-strain characteristics and failure modes. We then investigate the effect of surface imperfection on the transition of the failure mode in MGs.

Chapter 4 presents an MD investigation of the uniaxial tensile deformation and failure characteristics in NG architectures. The behaviors of NG architectures are compared with the conventional MG counterparts. We further study the effect of alloy composition and grain size. In particular, we quantify the statistics of atomic VP at grains and GGIs, GGI thickness, and the fraction of the bulk and interfacial regions as a function of NG composition and grain size.

Chapter 5 summarizes the effect of grain size on the ductility and failure of the NG nanopillars. The NG nanopillars with 3D grain structures are studied under uniaxial tension, and the failure mechanisms are investigated and discussed.

Finally, Chapter 6 summarizes our key findings, and enumerates a number of ongoing and future directions in this field.

2. Methodology

2.1 Computational Materials

Within recent years, modelling of materials has developed and established as a thriving research field with unique capacities that interfaces theory and experiments. Numerical modelling and simulation serves as a powerful tool to predict empirical data and reproduce experimental conditions in order to acquire comprehensive details about the physical structures and phenomena. Fig. 2-1 classifies material phenomena into four distinct length- and correspondingly, temporal-scales: electronic structure, atomistic, microstructure, and continuum. The scale spanning from ten to a thousand angstroms is referred to as the atomistic scale. Among several alternatives the MD method is particularly well developed for this scale (Allen and Tildesley, 1989; Kohn and Sham, 1965). The significant feature of atomistic simulations is that with recent advances in computing techniques and hardware, it is possible to simulate systems with

large number of atoms (currently in excess of 10^9) (Yip, 2005) or to perform simulations for extended times (currently in the range of several microseconds to seconds) (Yip, 2005). That provides freedom to investigate a wide range of challenging problems that were previously intractable. For instance, the challenging simulations reported in this thesis on MGs and NGs are only possible because of these recent developments.

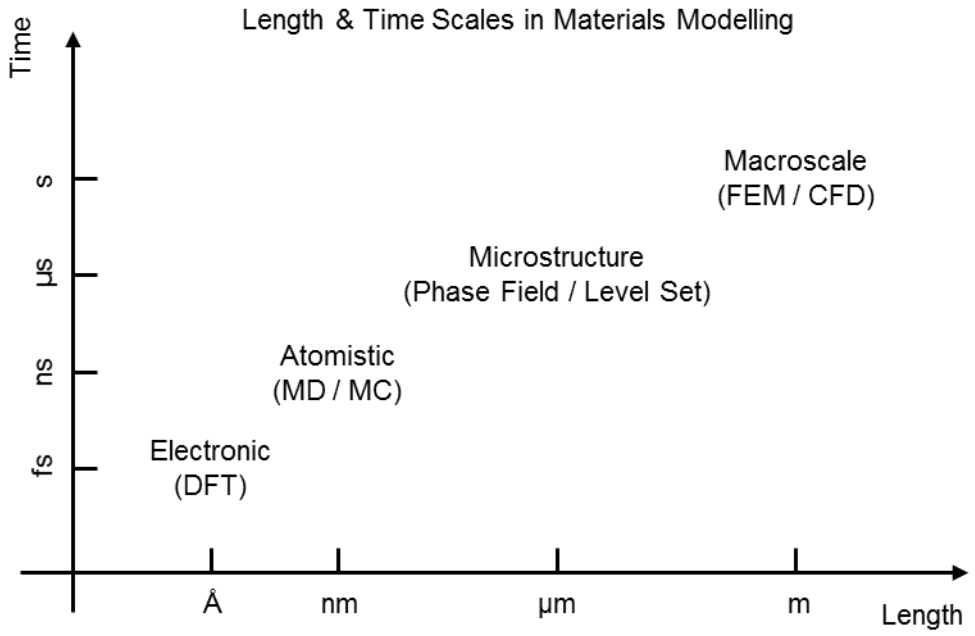

Figure 2-1 Length scales in material modelling. Basic understanding and prediction lie in microscopic levels, while, many application in the physical world take place in micron scale and higher (Finite element method (FEM), Continuum fluid dynamics (CFD)).

2.2 Molecular Dynamics Method

MD is a powerful and versatile atomistic simulation method (Allen and Tildesley, 1987; Haile, 1997; Hoover, 1988; Li, 2005; Li et al., 2008; Raabe, 2004). In its core MD is a simulation technique that predicts the trajectories of a system of N interacting particles in the space-time. The atomic trajectories are

determined based on numerical integration of the Newton's equations of motion. In its classical formulation, forces between atoms are determined based on a specific interatomic potential, which empirically represents the sub-scale interatomic interactions. The equations of motion are solved numerically for a given set of boundary and initial conditions. Macroscopic thermodynamic properties can be obtained from the time evolution of the system using statistical mechanics, e.g. elastic constants as a function of temperature, diffusivity, thermal conductivity, etc. Non-equilibrium dynamic properties may also be evaluated following the atomistic trajectories, e.g. fracture propagation, plasticity, shock waves, etc.

Fig. 2-2 describes a simplified algorithm for an MD simulation, which comprise the following steps:

- Describe the initial positions ($\mathbf{r}$) and velocities ($\boldsymbol{v}$) of atoms.
- Calculate the forces ($\boldsymbol{F}$) on each atom which includes the forces between atoms and external forces such as gravity and electric fields. Calculate the acceleration on each atom ($\boldsymbol{a} = \boldsymbol{F}/m$).
- Integrate the Newton's equation of motion employing an appropriate finite-difference scheme, i.e. calculate the updated position and velocity of each atom after a small time interval (δt) based on the calculated acceleration.
- Repeat the previous two steps until thermodynamic equilibrium is reached and thermodynamic average quantities are calculated. Alternatively, for non-equilibrium simulations, continue until the desired phenomenon is characterized.

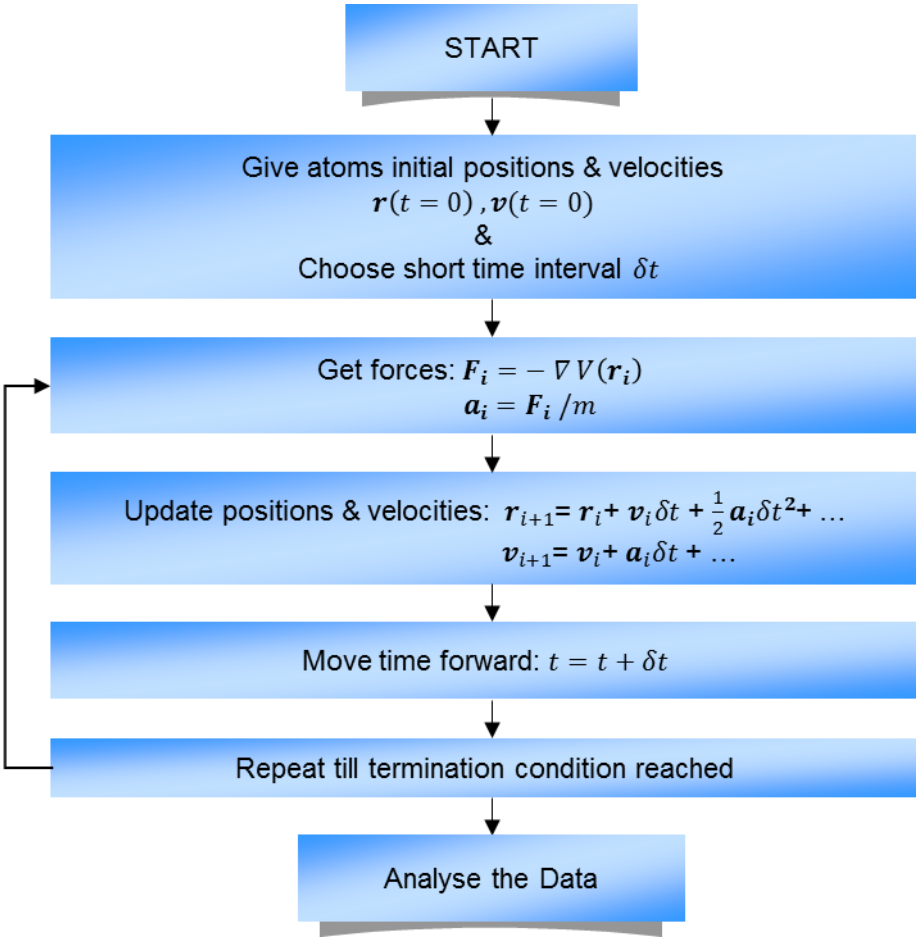

Figure 2-2 Illustration of the MD algorithm. V is the interatomic potential, $\boldsymbol{r}$ position of atom, $\boldsymbol{v}$ velocity of atom, $\boldsymbol{a}$ acceleration of atom, and $\boldsymbol{F}$ interaction force exerted on atoms. t is time and δt time interval in numerical integration.

The basic algorithm for MD simulations generates equilibrium configurations in the NVE ensemble (constant number of particles, volume, and energy). However, different algorithms can be used to perform simulations in different ensembles such as NVT (constant number of particles, volume, and temperature), NPT (constant number of particles, pressure, and temperature), and $N\sigma T$ (constant number of particles, stress, and temperature). In addition, during MD simulations, properties are calculated and saved during runtime along with the trajectory of the particles. In summary, some of the key

components in every MD simulation are: Boundary and initial conditions, choice of ensemble and algorithm to integrate the equations of motion, and the choice of properties to be calculated (Li, 2005).

In recent times, MD has emerged as a powerful approach to predict materials behaviour including failure mechanisms at the nanoscale (Branicio et al., 2010; Branicio et al., 2008; Murali et al., 2011; Ritter et al., 2011; Shekhar et al., 2013). In order to fully take advantage of the possibilities offered by MD simulations on nanoscale material modelling one should keep in mind its capabilities and limitations. Some of the most important items to be addressed are the size of the systems that can be simulated, the interatomic potential to be used, and the time scale involved in the simulations. All these points are very relevant for this work on MGs, therefore we discuss them in detail.

(i) *System size*. The computational resources and hardware storage limit the size of the samples that can be handled by MD simulations. Recent advances in parallel computer processing and the increasing availability of efficient parallel computer systems and larger storage facilitates make it possible to simulate systems with million to billion atoms (Branicio et al., 2010; Branicio et al., 2008; Shekhar et al., 2013; Zhang et al., 2008). This allows MD simulations of such immense sample sizes with realistic boundary conditions. For instance, recent MD simulation of nanopillars with diameter larger than 50 nm are reported in the literature (Gu et al., 2012). Those simulations are particularly interesting because the simulated systems are also accessible in experiments, and hence allow a direct comparison of simulation and experimental results. That is an

ideal situation since the experimental data at nanoscale is commonly challenging to analyze. On the other hand, predictions of large-scale MD simulations need experimental validation since the calculations are usually done at conditions different from those where the interatomic potentials were fit.

(ii) *Interatomic potential*. Many interesting physical phenomena in materials, such as failure, plastic deformations, and fracture propagation, require large systems with very large number of atoms and often require long simulation times. Using semi-empirical interatomic potentials in MD simulations allows fast calculations of the total energy and interatomic forces facilitating the modelling of such processes (Delogu, 2009; Lao et al., 2012; Li and Li, 2008; Murali et al., 2011; Wu, 2006; Yip, 2005). However, the accuracy of MD simulations depends directly on the accuracy of the interatomic potential. Therefore, the choice of the interatomic potential for a given material has to be done judiciously. In addition, the bulk of the computational time in MD is spent calculating forces based on the interatomic potential chosen. A complex interatomic potential, even though maybe more accurate, may severely limit the total simulation time. Thus, choosing an appropriate interatomic potential plays a key role in allowing or not an MD simulation to be performed and in predicting accurate nanoscale properties.

(iii) *Simulation time*. The temporal resolution in MD is set by the atomic vibration frequency, which is in the order of picoseconds. As a result, the time step to be used in MD is usually in the fs scale. In practice that

limits the total amount of simulation time to the ps – ns range, since usually no more than several million steps can be simulated in reasonable computing time, even using very high efficient and large computer systems. Consequently, the usual rates in MD are very large and orders of magnitude faster than common experimental rates. For example, in preparing MGs very high cooling rates are adopted in MD simulation (~ 10^{10} Ks^{-1}) compared to the conventional (high) quenching rates used in experiments (~ 10^{1}-10^{6} Ks^{-1}). Such high cooling rates may result in some artefacts in MGs such as higher free volume than in real MGs, which could produce qualitatively different results. Another example is the high strain rate required to deform samples to non-negligible macroscopic strains. MD simulations are usually performed at high strain rates (> 10^{7} s^{-1}) while typical experimental loading rates range between ~ 10^{-4}-10^{4} s^{-1} (Kato et al., 1997). Given the importance of the effects of strain rates in the results, we discuss them in detail in Chapter 3.

Despite these limitations, MD is becoming an invaluable tool to predict and to understand experimental results on mechanical and structural properties of nanoscale MG (Cao et al., 2009; Cheng et al., 2008a; Greer et al., 2013) and NGs (Albe et al., 2013; Ritter and Albe, 2012; Ritter et al., 2011; Şopu et al., 2009; Şopu et al., 2011a).

2.2.1 Initial and Boundary Conditions

It is essential to specify appropriate initial conditions before starting an MD simulation. Typically positions and velocities must be specified. In addition, one may want to also specify the exact thermodynamic values of pressure, stress tensor, temperature, etc. Some of choices of initial conditions:

(i) The atoms are located in equilibrium crystal lattice positions and velocities are assigned with random values within a given range;

(ii) Atoms are placed in random positions based on a desired density and velocities are assigned null value;

(iii) Atoms positions follow a pre-determined structure, e.g. an MG amorphous structure, and velocities are assigned by Maxwell-Boltzmann distribution to give a defined temperature.

Initial atomic positions depend on the type of the system, its current state, and the objective of the simulation. Initial atomic positions in crystalline systems are usually placed at their equilibrium lattice positions defined by the crystal system and the material density. An amorphous system may be prepared by melting an initial crystalline system and quenching the resulting equilibrium molten state to low temperatures where the diffusion is negligible and the structure stable. Initial velocities are usually assigned by a well-defined Maxwell-Boltzmann distribution of values defined by a given temperature. The velocities are adjusted to eliminate global linear and angular momenta.

In addition to initial conditions, it is also necessary to define appropriate boundary conditions to be applied during the MD simulations. Given the huge computational cost of simulating large systems, periodic boundary conditions (PBC) are widely used in MD simulations of bulk systems. After a given system size is defined to represent the significant features of interest in the system, the

system is enclosed in a fully periodic cell. The rationale of using PBC is that it allows the accurate simulation of bulk properties using a relatively small system. It avoids having to deal directly with surfaces and having to define a system finite dimension explicitly. An MD simulation cell with PBC is repeated in all three independent direction in order to properly account for force calculation and atoms migration (diffusion). Thus, when an atom cross an MD cell boundary, an exact duplicate of that atom enters the cell trough the opposite face (see Fig. 2-3). In other words, PBC considers no physical walls around the central computational cell boundary, leading to a constant number of atoms in the entire system over time (Allen and Tildesley, 1989; Allen and Tildesley, 1987). If actual surfaces are required, e.g. to investigate fracture initiation from a notched surface, it can be readily applied by introducing vacuum in the MD simulation cell along the direction where surfaces are needed (Allen and Tildesley, 1989; Allen and Tildesley, 1987).

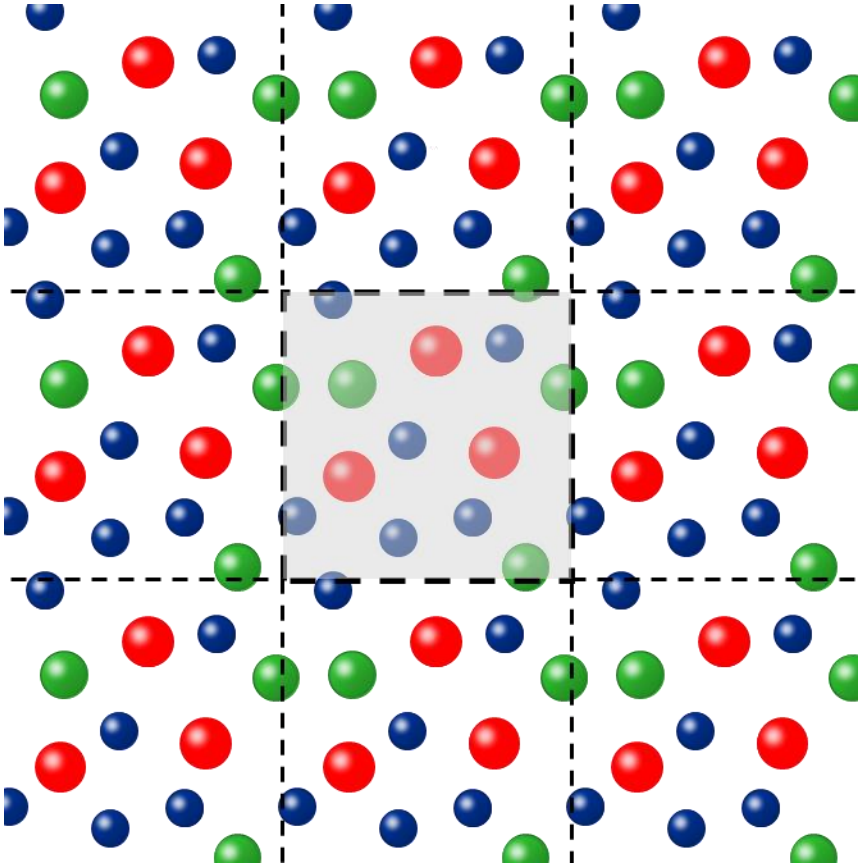

Figure 2-3 Periodic boundary conditions in MD shown schematically in 2D. The simulation cell (shaded) is infinitely repeated in each direction. When an atom leaves the MD cell its periodic image enters from the opposite side of the cell.

2.2.2 Interatomic Potential

The interatomic potential describes interaction between particles in the system and is the backbone of MD simulations. The fidelity of an MD simulation depends on how well the interatomic potential model describes a real system (Li et al., 2008). It is a function of the particles position in the system and represents the potential energy for the system in a specific atomic configuration. In general, the interatomic potential can be written as a summation of one-body, two-body, and higher order interactions, as formulated in Eq. 2-1 (Li et al., 2008):

$$v = \sum_{i} v^{(1)}(\boldsymbol{r}_i) + \sum_{j>i} v^{(2)}(\boldsymbol{r}_i, \boldsymbol{r}_j) + \sum_{k>j>i} v^{(3)}(\boldsymbol{r}_i, \boldsymbol{r}_j, \boldsymbol{r}_k) + \cdots \quad 2\text{-}1$$

In Eq. 2-1, the first term represents the one-body interaction, which depends on the absolute atomic positions and denotes the effects of external force fields, such as gravitational or electrostatic. The second term shows the energy due to the pair-wise particle interactions. A typical example of the tow-body potential is the Lennard-Jones (LJ) potential (Jones, 1924). The third term in the equation, gives the three-body interaction. An example of the three-body potential is the Tersoff potential, which considers a sum over groups of three atoms, considering the angle between them (Tersoff, 1988). Tersoff potential is widely used in various applications such as in silicon, carbon, and germanium systems (Ansari et al., 2014; Dürr and Höfer, 2013; Lee and Lu, 2014; Mahmoudinezhad and Ansari, 2013; Park et al., 2014; Tersoff, 1988). The other following terms in the equation are interactions between more than three atoms also known as many-body interactions. Embedded atom method (EAM) potential (Foiles et al., 1986) is an example of a many-body potential in that the electron density is calculated over a sum of the contribution of surrounding atoms. Because the EAM describes accurately metallic bonding, it is one of the most widely used interatomic potentials used to simulate metals and metallic alloys.

2.2.2.1 EAM Method

The EAM is a many-body potential specifically designed to describe metallic bonding (Foiles et al., 1986). The rationale behind this method is that each atom is embedded in a host electron gas created by all surrounding atoms. The embedded energy is determined by the local electron density that each atom is immersed in

(Nørskov and Lang, 1980). The total EAM energy is represented by the following expression:

$$E = \sum_{i} F_i \left[\sum\nolimits_{j \neq i} f_j \left(r_{ij} \right) \right] + \frac{1}{2} \sum_{i,j} \phi_{ij}(r_{ij}) \qquad 2\text{-}2$$

where r_{ij} is the distance between atoms i and j, and $f_j\ (r_{ij})$ is the contribution to the electron density at a site i due to the neighbouring atom j. Hence, the sum over f_j is the measurement of the local electron density. F_i is an embedding energy associated with the energy required to place atom i in the electron cloud environment. ϕ_{ij} is a pair-wise potential function representing the residual pair interactions.

The EAM method has been widely applied in studying grain boundaries, fracture and defects and other material processes in metals and metallic alloys (Cheng and Ma, 2011; Greer and De Hosson, 2011; Wu et al., 2012; Wu et al., 2013; Wu et al., 2011). In this work, the atomic interactions in CuZr MG and NG systems are calculated using an EAM potential fitted to CuZr properties (Cheng et al., 2008a).

2.2.3 Statistical Ensembles

An ensemble is a collection of the possible microstates with identical macroscopic properties of the thermodynamic system. Each statistical ensemble is characterized by a set of conserved thermodynamic quantities such as: volume (V), energy (E), temperature (T), and pressure (P). The choice of the ensemble is based on the desired experimental condition. An excellent reference for detailed understanding of statistical ensembles is (Allen and Tildesley, 1989;

Haile, 1997; Li, 2005; Raabe, 2004; Yip, 2007). Here, we give a very brief account of typical ensembles adopted in MD modelling.

2.2.3.1 Microcanonical Ensemble (NVE)

The microcanonical ensemble (NVE) is the most commonly used statistical ensemble in MD simulation because of its convenience and simplicity. In this ensemble, the system of N atoms is considered to be isolated from the surrounding environment and the total energy is conserved. Other thermodynamic quantities such as P, T, and chemical potential (μ) fluctuate around their average values at equilibrium. In the thermodynamic limit as $N \rightarrow \infty$, the relative fluctuation goes to zero as they are proportional to $1/\sqrt{N}$, and the microcanonical ensemble becomes equivalent to the canonical (NVT), grain canonical (μVT), isobaric (NPE) and other ensembles. However, the equilibrium states of these ensembles are not equivalent for a finite system, in particular small systems. That is one of the reasons that MD simulations should be done in systems of at least 1,000 atoms, in order to keep fluctuations low, allowing accurate calculation of equilibrium properties.

Although the NVE emsemble is the most convenient choice in MD, it is often not the most desirable since most experiments are done at constant temperature (T) and/or pressure (P). Fortunately, the *NVT* and *NPT* ensembles can be readily be used in MD by choosing appropriate methods. There are several approaches to conduct MD at constant T. The most popular is the one introduced by Nose (Nosé, 1984) and later generalized by Hoover (Hoover, 1985). In this method,

the constant T is achieved by coupling the momenta of the atoms to an external heat bath.

2.2.3.2 Canonical Ensemble (NVT)

In the canonical ensemble, N, V and T are conserved. In this ensemble, the system is thermally coupled with a heat reservoir to maintain constant T while E is allowed to fluctuate. There are many thermostat methods that allow the addition and removal of energy from MD systems approximating the NVT ensemble. The most popular techniques are direct velocity rescaling, the Nose-Hoover thermostat (Nosé, 1984), Nose-Hoover chains, the Berendsen thermostat (Berendsen et al., 1984), the Andersen thermostat (Andersen, 1980) and Langevin dynamics (Lemons and Gythiel, 1997; Schlick, 2010).

2.2.3.3 Isothermal-Isobaric Ensemble (NPT)

In the NPT ensemble a mechanical coupling is introduced to the system, which allows the system to maintain N, P and T. In other words, the NPT ensemble has heat bath (thermostat) and barostat (Parrinello and Rahman, 1980; Rahman, 1964).

2.2.4 Computation of Physical Properties

The thermodynamic state of the system is defined by a few parameters. The equation of state may be used to express other thermodynamic properties. For a given system in equilibrium, any thermodynamic quantity is given by definition as the average of its value on all the possible states of that ensemble. Given the

prohibitively large number of possible configurations of a system of any finite size at finite temperature in MD the thermodynamic quantities are calculated based on time averages following the Ergodic theorem, which in the MD context means that the ensemble average is identical to the time average of instantaneous values for a large enough simulation time (Li, 2005; Yip, 2007). Therefore, in MD any microscopic measure of a thermodynamic property $\mathcal{A}$ is the average of the instantaneous value of that property over time:

$$\mathcal{A} = \langle \mathcal{A} \rangle_{time} = \frac{1}{N_{step}} \sum_{i=1}^{N_{step}} \mathcal{A}(\mathrm{t}_i) \qquad 2\text{-}3$$

where $\langle\ \rangle$ indicates the average of the property, N_{step} is the number of simulation time steps used in the equilibrium average, and $\mathcal{A}(\mathrm{t}_i)$ the instantaneous property at time step t_i. Ideally, this average should be performed for the maximum number of time steps possible. However, in practice most averaged thermodynamic properties converge to a very accurate value in no more than 50,000 steps.

Various thermodynamic quantities, such as internal energy, temperature, and pressure are computed by simply averaging the correspondent instantaneous quantities over the phase-space trajectory. For example, the thermodynamic temperature (T) may be obtained in terms of the average kinetic energy $\langle K \rangle$ using the equipartition theorem:

$$T = 2\,\langle K \rangle / 3Nk_B \qquad 2\text{-}4$$

Where k_B is the Boltzmann constant. The thermodynamic pressure can be calculated from the Virial theorem:

$$PV = Nk_BT + \frac{1}{3}\langle \sum_{i=1}^{N} r_i \,.\, f_i \rangle \qquad 2\text{-}5$$

where f_i is the force on atom i, and r_i represents atomic position.

However, some thermodynamic variables (e.g. entropy and free energy) cannot be commutated from equations similar to equations 2-3, 2-4 and 2-5, and require more sophisticated methods to be calculated.

2.2.5 Computation of Mechanical Properties

MD simulations provide the characterization of structural, mechanical, and dynamic properties of a system of particles in solid, liquid, or gas state. For instance, elastic constants and bulk modulus of the crystal system can be obtained by calculation of equilibrium lattice constant and cohesive energy of the system (Li, 2005; Yip, 2007). Once the equilibrium lattice constants are determined, other elastic constants of the crystal in addition to the bulk modulus can be calculated. Other elastic constants besides bulk modulus can be computed by imposing a strain on the crystal and monitoring the changes of potential energy (Li, 2005; Yip, 2007). In practice, it is easier to extract the elastic constant information from the stress-strain relationship. The slope of the stress-strain curve gives the elastic constant. The stress of the simulation cell can be computed by averaging the Virial stress of atoms.

2.2.5.1 Virial Stress

The Virial stress provides a measure of the mechanical stress in the atomic scale. Using the Virial theorem, the internal stress tensor for an atomic system can be written as (Branicio and Srolovitz, 2009; Tsai, 1979):

$$\sigma_{\alpha\beta} = \frac{1}{\mathrm{V}} \langle \sum_{i} \left[m_i v_i^{\alpha} v_i^{\beta} + r_i^{\alpha} f_i^{\beta} \right] \rangle \qquad 2\text{-}6$$

where α and β are Cartesian indices and $\langle\ \rangle$ indicates the time average. The forces f_i contain only the internal contributions due to the particle interaction in the system. Engineering stress can be computed as the average atomic stress in the system based on the Virial stress definition. For simplicity, the initial (undeformed) volume of the system may be used in the averaging process based on the assumption that the density of the system is not significantly altered during deformation.

For some problems, one is interested in the local-stress distribution rather than the total stress. A major difficulty arises from the fact that atomic level stress is not well defined, as stress unlike force is inherently related to the assumption of continuity and requires volumetric averaging. Nonetheless, in MD simulations, variations of the stress over length scales of a few atomic bonds is usually sufficient. Then, one can define a quantity that reasonably extrapolate the continuum definition of stress to atomistic length scales by making a local average of the stress around nano-scale regions of space following the original Virial definition of Eq. 2-6.

2.2.5.2 Local Atomic Von Mises Shear Strain

Atomic local shear strain is a quantitative interpretation of strain localization at the atomic level (Shimizu et al., 2007). This parameter can be calculated to quantify the generation and development of local plastic deformation in the system. Since strain is a relative measure (Jinghan Wang, 1995) two atomic configurations (the reference and the current) are needed to compute the local

strain. The transformation matrix $\boldsymbol{J}$ is defined to best map these two configurations.

$$\{\boldsymbol{X}_{ji}^{0}\} \rightarrow \{\boldsymbol{X}_{ji}\} \quad \forall j \in N_i \tag{2-7}$$

$\boldsymbol{X}^0$ and $\boldsymbol{X}$ in Eq. 2-7, are row vectors which present the reference and current separations between atoms i and j, respectively, N_i is the total number of nearest neighbours of atom i in the current configuration and j is one of the nearest neighbours of atom i. $\boldsymbol{J}_i$ is determined by minimizing Eq. 2-8 (Shimizu et al., 2007):

$$\sum_{j \in N_i} \left| \boldsymbol{X}_{ji}^{0} \boldsymbol{J}_i - \boldsymbol{X}_{ji} \right|^2 \tag{2-8}$$

The Lagrangian strain matrix is then calculated as (Eq. 2-9):

$$\eta_i = \frac{1}{2} \left(\boldsymbol{J}_i \boldsymbol{J}_i^{T} - \boldsymbol{I} \right) \tag{2-9}$$

then the local von Mises shear invariant is commutated as

$$\eta_i^{Mises} = \sqrt{\eta_{xy}^2 + \eta_{xz}^2 + \eta_{yz}^2 + \frac{\left(\eta_{xx} - \eta_{yy}\right)^2 + \left(\eta_{xx} - \eta_{zz}\right)^2 + \left(\eta_{yy} - \eta_{zz}\right)^2}{6}} \tag{2-10}$$

In Eq. 2-10, x, y and z are Cardinal components. η_i^{Mises} is a good measure of local inelastic deformation (Shimizu et al., 2007).

2.2.6 Molecular Dynamics Packages

Multiple open source packages are commonly used for MD simulation, such as LAMMPS (Plimpton, 1995), DL POLY (Smith and Forester, 1996; Smith et al., 2002), Moldy (Refson, 2000), IMD (Roth et al., 2000), NAMD (Nelson et al., 1996), Gromacs (Berendsen et al., 1995), CHARMM (Brooks et al., 1983) and AMBER (Pearlman et al., 1995).

In the present work, all MD simulations are carried out with LAMPPS. LAMMPS is an open source package with highly scalable algorithms to perform parallel MD simulation on large computing clusters of different architectures. This feature allows the simulation of massive systems with million to billion atoms. LAMPPS has a library of interatomic potentials to perform MD simulation for solid-state materials, soft matters, coarse grained and mesoscale systems (Plimpton, 1995). LAMPPS have been widely used in the simulation of large-scale MG systems (Cao et al., 2009; Cheng et al., 2009a; Cheng and Ma, 2011; Greer et al., 2013; Greer and De Hosson, 2011; Şopu et al., 2011a).

2.2.6.1 Visualization tools

In order to gain more scientific insight into a physical system and physical phenomena, it is very useful to visualize and analyse the atomic configuration of the system. Power visualization techniques play a key role in this work. Their task is to translate atomic coordinates from simulations into a meaningful graphical representation that enables insightful interpretation of the atomic mechanisms. There are several packages designed for visualization of atomistic structures generated by MD, such as OVITO (Stukowski, 2010), Atomeye (Li, 2002), and VMD (Humphrey et al., 1996). Here, we perform all atomistic visualizations using the open-source visualization tool OVITO. In addition to visualization, it provides analysis tools to handle large-scale atomistic database produced by MD simulations.

2.3 Modelling Mechanical Properties

In our work, MD simulations of CuZr are performed based on the EAM potential of Cheng et al. (Cheng et al., 2008a) in the NVT and NPT ensembles using LAMMPS (Plimpton, 1995). A time step equal to or smaller than 5 fs is applied to integrate the equations of the motion.

To investigate the deformation mechanisms in CuZr MG and NGs, we performed strain-controlled uniaxial tensile loading tests on nanoscale samples. That means that during the deformation the sample is continuously stretched uniaxially at a constant engineering strain rate. The other two dimensions of the system are adjusted that enforce zero stress producing truly uniaxial loading conditions. PBC is applied in the loading direction. The boundary conditions in the two other direction depend on the specific system simulated. In MG and NG reference bulk systems PBC is applied in one direction (short MD cell dimension) while the other is let free to allow surface generation of defects. In cylinder samples, free surface is used in two lateral directions. During the loading, the temperature is maintained at 50 K by using a Nose-Hoover thermostat.

Engineering stress is calculated as the averaged atomic Virial stress definition using the initial volume of the undeformed system. The generation and evolution of local inelastic deformation in the system is quantified using the atomic local von Mises shear strain η^{Mises}. Visualization of the structures is done using OVITO. Ddetails on the specific procedure followed to construct each simulation model and details about the loading conditions are discussed in the methodology part of each chapter.

2.4 Modelling of Metallic Glasses

Unlike the well-defined long-range order that is inherent to crystalline metals, the atomic arrangement in amorphous alloys is characterized by short-to-medium range order. CuZr MG alloys have very specific amorphous structure with a well-defined medium range order (Cheng and Ma, 2011; Wang et al., 2008). In order to prepare and characterize CuZr glass models in this work we use specific procedures as described in the next subsections.

2.4.1 Preparation of the MG by Melting and Quenching

The most popular method to prepare an MG is by fast quenching of the molten alloy. Fig. 2-4 shows the glass formation behavior of a $Cu_{64}Zr_{36}$ alloy model. Cooling down the molten alloy below its melting temperature with sufficiently high cooling rate will bring the molten alloy into a supercooled state, which has an amorphous structure (Ritter et al., 2011). With further decrease of temperature, the supercooled melt forms a glass. Fig. 2-4 exhibits a gradual and almost linear change in the volume throughout the whole cooling procedure. At a specific temperature, known as the glass transformation temperature T_g, the rate of volume change decreases sharply (see Fig. 2-4). The curvature at T_g is a sign of glass formation. T_g is not a true thermodynamic parameter of a second order phase transition since it depends on experimental conditions, particularly the cooling rate (Duan et al., 2005). A rapid cooling rate in the cooling procedure prevents nucleation of the crystalline phase. Thus, the molten alloy can be cooled down below melting temperature without crystallization, resulting in a glass structure. Faster cooling rates results in a shorter time for the

atoms to relax, and leads to a higher T_g and distinguished amorphous structures (Duan et al., 2005). Since the MG is in a metastable state its atomic structure is constantly changing with time. The lower the temperature the lower is the diffusivity and the change in the glass structure. In order to perform the simulations in a stable MG structure we perform all simulation at T = 50 K.

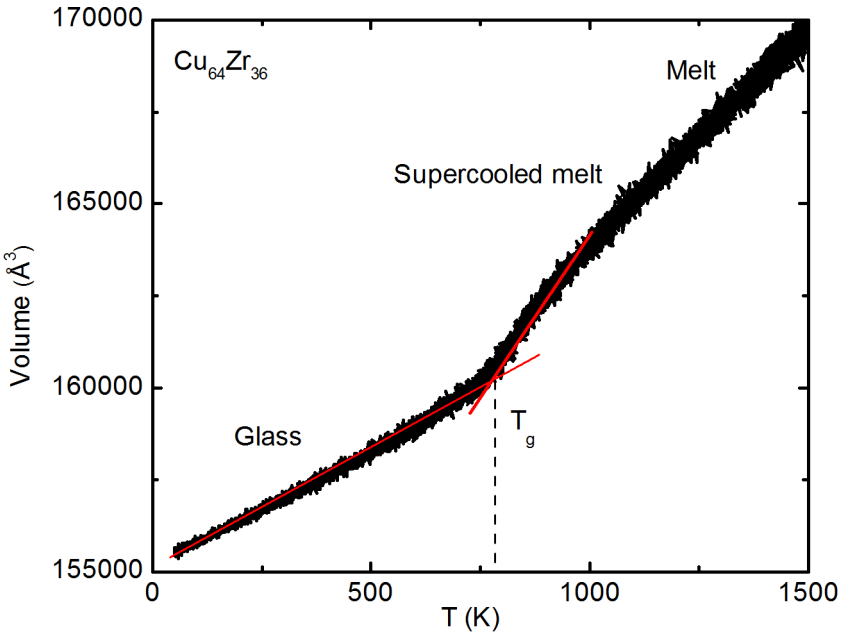

Figure 2-4 Volume as a function of temperature for $Cu_{64}Zr_{36}$ during MG generation by quenching of the liquid state.

2.4.2 Radial Distribution Function (RDF)

The structural features of a material can be characterized by calculating various correlation functions, the simplest of which is the radial distribution function (RDF). The RDF describes the relative density of pairs of atoms at given distances in a material and is particularly used to describe the structure of liquids and amorphous structures. By definition the RDF gives the probability of finding a pair of atoms at a given distance r. Since it is a spherically symmetrical function, it is independent of orientation. The RDF can be express as:

$$g(r) = \frac{V}{N^2}\langle \sum_i \sum_{j \neq i} \delta(r - r_{ij}) \rangle \qquad 2\text{-}11$$

Where N denotes the number of atoms in the system, V is the volume, i and j are atoms indices which run over all N atoms, and r_{ij} is the distance between the pair of atoms i and j.

Fig. 2-5 shows the partial RDF plot of a $Cu_{64}Zr_{36}$ MG structure model, which shows broad peaks corresponding to the amorphous structure. The second peak of the functions splits into two sub-peaks. This is a well-known characteristic feature of the glassy state (Wendt and Abraham, 1978). The split in the second peak is a sign of short-range atomic order formation in the glassy regime (Heck et al., 2013).

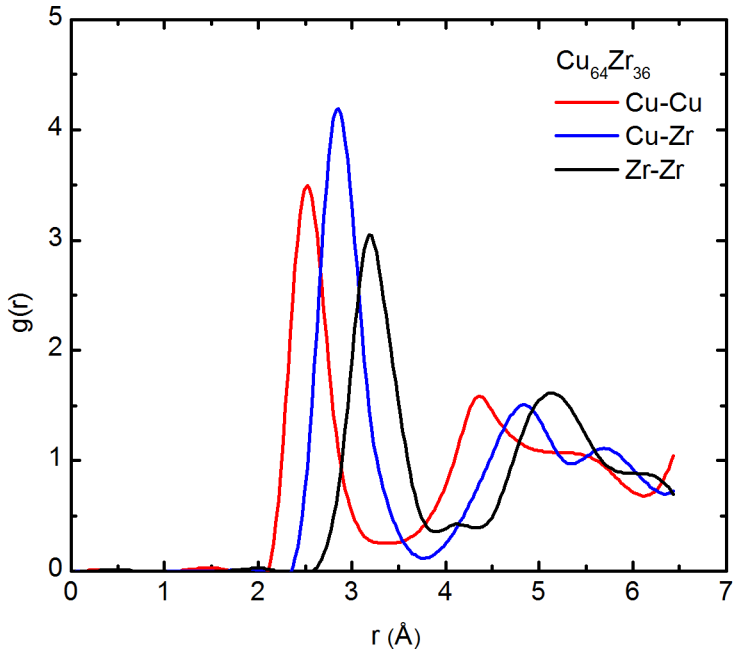

Figure 2-5 Radial distribution function of $Cu_{64}Zr_{36}$ for Cu-Cu, Cu-Zr, and Zr-Zr pairs at T = 50 K.

2.4.3 Structural Analysis Based on the Voronoi Tessellation

One of the commonly used techniques to characterize the structure of liquids and glasses is the Voronoi tessellation method (Cheng and Ma, 2011; Huang et al., 2010; Sheng et al., 2006). In this technique, the amorphous sample is analyzed based on the characteristic VPs generated by the local structure around at each atom. The kind and the volume of VPs is a signature of the SRO of the amorphous alloy. The specific VPs found in CuZr alloys as a function of composition will be quantified in detail in Chapter 4.

Finney (Finney, 1970) describes in detail the essence of the Voronoi polyhedron analysis. For a given atom in a set, take the bisect plane perpendicular to the vector between that atom and one of its adjacent atoms. Repeat the process for all the atoms in the neighborhood of the given atom. The VP associated with the atom is then defined as the smallest polyhedron formed from these bisects planes, so that no plane crosses the formed polyhedron. This polyhedron, hence, defines the region of space closer to the given atom than to any other atom in the set given. Fig. 2-6a demonstrates a two dimensional illustration of the lines connecting neighbor atoms and their bisect planes. The network of VP completely fills the space. The network of VPs uniquely determines the coordinates of the atoms in the system. Thus, the lattice of the atoms can be replaced by their equivalent set of VPs. This transforms the problem of packing spheres into packing polyhedra (Finney, 1970). The atomic coordination number (CN) can be determined by using the Voronoi tessellation method, which also characterizes the local atomic environment (Sheng et al., 2006). A common Voronoi polyhedron index, which is used here, is given by:

$C < n_3, n_4, n_5, n_6, \ldots >$ which indicates that C is the central atom of the Voronoi polyhedron that has n_i faces with i edges, and $\sum_i n_i$ is the total CN of C.

The Voronoi tessellation method is widely applied to study the structure of various amorphous materials such as organic materials, ceramics, and in particular, MGs (Cheng and Ma, 2011; Huang et al., 2010; Sheng et al., 2006) (Ritter and Albe, 2012; Şopu et al., 2011a). An example of the Voronoi tessellation analysis of MG is the work by Cheng and Ma (Cheng and Ma, 2011). They identified the most prominent VPs in several representative MGs, as shown in Fig. 2-6b. In particular, the full icosahedra (FI) centred at Cu are reported to be the most important polyhedron for $Cu_{64}Zr_{36}$ (Cheng and Ma, 2011; Ding et al., 2014). An FI which is also named Dodecahedron as shown in Fig. 2-6c is a polyhedron which has 12 faces with 5 edges and Voronoi index $< 0,0,12,0 >$ (Cheng et al., 2008a). This Voronoi polyhedron is the key structural feature in amorphous CuZr alloys which exhibits high packing density (Lee et al., 2007b) and high shear resistance (Cheng et al., 2008a).

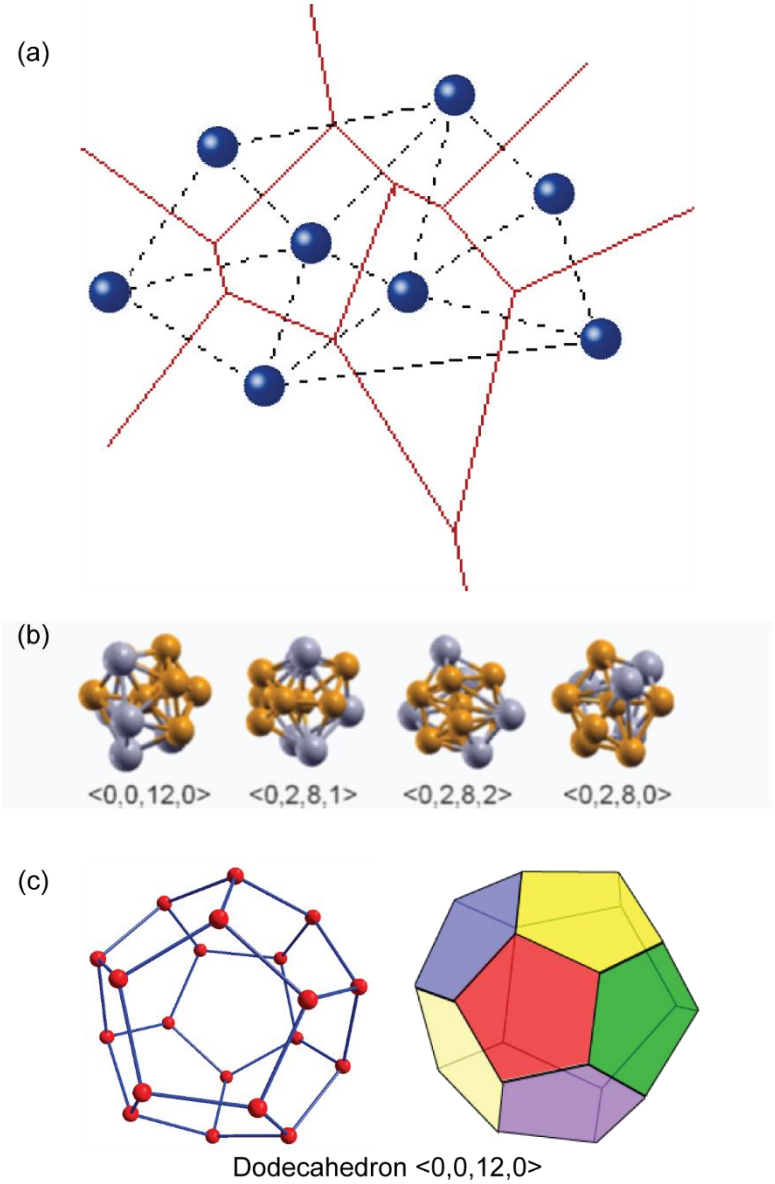

Figure 2-6 Voronoi tessellation method. (a) Construction of two-dimensional Voronoi polygon. (b) Several representative Cu-centered Voronoi polyhedral (orange balls for Cu and gray balls for Zr). Reprinted with permission from (Cheng and Ma, 2011) © 2010 Elsevier Ltd. (c) Full icosahedron (Dodecahedron) polyhedron.

Part II

METALLIC GLASSES

3. Effects of Size, Strain Rate, and Geometric Imperfections on the Mechanical Properties and Deformation Mechanisms of Nano-scaled Metallic Glass Specimens

3.1 Background

The prospect of improving the mechanical properties of MGs by modifying their fundamental deformation mechanisms has attracted much attention in recent years. In particular, literature reports indicate that nanoscale samples of MGs can behave rather differently than their bulk counterparts (Chen et al., 2011; Chen et al., 2013; Greer and De Hosson, 2011; Jang et al., 2011; Kumar et al., 2011; Kuzmin et al., 2012; Tian et al., 2013; Wang et al., 2012; Wu et al., 2010). Intriguingly however, rather than unequivocally clarify the nature of failure in MGs, experiments (Bharathula et al., 2010; Cao et al., 2009; Chen et al., 2010; Chen et al., 2011; Chen et al., 2013; Cheng et al., 2007; Dubach et al.,

2009; Greer and De Hosson, 2011; Guo et al., 2007; Hofmann et al., 2008; Jang and Greer, 2010; Jang et al., 2011; Kumar et al., 2011; Kuzmin et al., 2012; Kuzmin et al., 2011; Louzguine-Luzgin et al., 2010; Luo et al., 2010; Nakayama et al., 2010; Schuster et al., 2007; Schuster et al., 2008; Shan et al., 2008; Tian et al., 2013; Volkert et al., 2008; Wang et al., 2012; Wu et al., 2009a; Wu et al., 2009b; Wu et al., 2008a; Wu et al., 2009c; Wu et al., 2010; Xie and George, 2008; Yang et al., 2011a; Yang et al., 2010; Yang et al., 2011b; Zheng et al., 2007) and simulations (Delogu, 2009; Li and Li, 2005, 2006, 2008; Shi, 2010) on nanoscale MG structures exhibit contrasting results. These reports indicate either brittle failure via localized SBs or ductile necking. Moreover, several recent experimental investigations indicate an intriguing BDT in the failure mode upon specimen size reduction (Chen et al., 2013; Guo et al., 2007; Jang and Greer, 2010; Tian et al., 2013). For a better understanding of the intrinsic failure of MGs, it is important to characterize how the deformation mechanisms in nano-scaled MG specimens evolve with specimen dimensions. Further, it is important to investigate if and how does the presence of geometric imperfections affect the failure characteristics as a function of the specimen size. With those objectives in mind, we perform comprehensive MD simulations of nano-scaled circular cylindrical MG specimens (nanopillars) to provide detailed insights into the intrinsic mechanical properties and deformation mechanisms in this class of material. We analyze the effect of specimen size (diameter and aspect ratio) on the mechanical response under uniaxial tensile loading. In order to gain detailed understanding on the effect of applied deformation loading, we perform MD simulations for these specimens over nearly three orders of magnitude of strain rate. A major highlight of this Chapter

is the detailed investigation of the role of surface geometric imperfections on the tensile instability and failure mode. To that end, we perform MD simulations on MG nanopillars with imperfections in the form of single and multiple circular notches carved along the specimen circumference. In particular, we investigate the effect of specimen size relative to the notch size in the mechanical response of the nanopillars. We demonstrate that specimen size and surface imperfections are parameters that can effectively modulate the macroscopic characteristics of MG nano-scaled specimens.

3.2 Methods

We perform large-scale MD simulations of $Cu_{64}Zr_{36}$ cylindrical MG nanopillars with diameters from 5 to 100 nm. The nanopillar samples have an aspect ratio (length/diameter) ranged from 2.5 to 50. Samples are deformed by applying a constant tensile engineering strain rate ($\dot{\varepsilon}$) in the range of 10^7 s^{-1} to 4×10^{10} s^{-1}. MD simulation set up and the interatomic potential used in the simulations are the same as that described in section 2.3.

3.2.1 Constructing MG Nanopillars

Fig. 3-1 shows a schematic of the MD procedure to generate the cylindrical MG nanopillars. In constructing the MG sample, a representative volume element (RVE) of $Cu_{64}Zr_{36}$ crystalline structure of dimensions $5.5\times5.5\times5.5$ nm^3 with

about 10,000 atoms[2] with PBC along all three dimensions, is first equilibrated at 2000 K (higher than the 1400 K melting temperature of $Cu_{64}Zr_{36}$) for 0.2 ns. Subsequently, the system is quenched to 50 K at a cooling rate of 10^{10} Ks^{-1}, while maintaining zero external pressure.[3] The bulk samples are then constructed by multiple replications of the final relaxed cubic MG system. The samples are further annealed for 0.5 ns at a temperature near the $Cu_{64}Zr_{36}$ glass transition temperature (T_g) of 800 K. This value is in agreement with experimentally reported values of T_g for $Cu_{64}Zr_{36}$ (Cheng et al., 2008a; Duan et al., 2005).

[2] The RVE comprising of cubic cell of roughly 10,000 atoms is used to make the simulation computationally tractable. By using a suitable RVE and replication one can conveniently generate large BMG systems with good structural quality (Cao et al., 2009; Cheng and Ma, 2011). Further, to remove possible artifacts, the system was relaxed near the glass transition temperature for 500 ps. Similar procedure is commonly reported in the literature (Cao et al., 2009; Cheng and Ma, 2011; Gu et al., 2014).

[3] The effects of different cooling rates in the resulting structure have been investigated extensively (Cheng et al., 2008). The cooling rate used in the generation of the MG samples in this thesis is consistent with that widely used in previously reported MD simulation of MGs (Cao et al., 2009; Şopu et al., 2011) and predict mechanical behaviors consistent with those found in experiments.

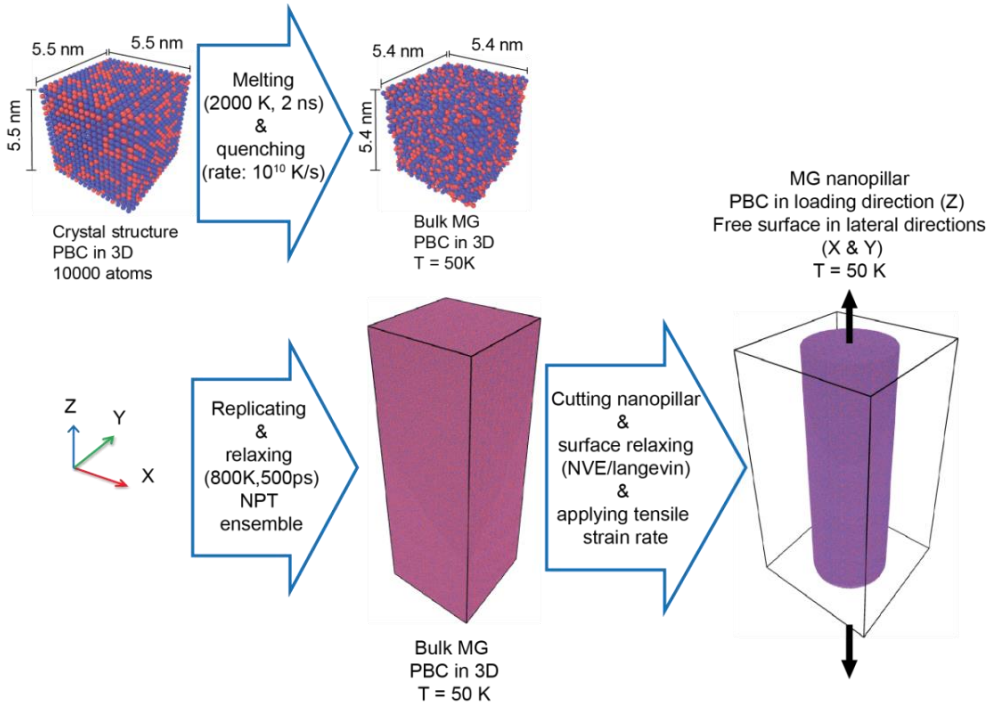

Figure 3-1 Schematic of the procedure to generate MG nanopillar models.

Finally, the bulk samples are cooled to 50 K and relaxed for 0.04 ns at zero external pressure. This method is similar to those applied previously in the literature (Adibi et al., 2013; Cao et al., 2009). Nano-scaled specimens of different diameters are *carved* from the final large bulk MG system. Free surfaces are relaxed using Langevin dynamics for 0.02 ns. In the case of notched specimens, a 1 nm deep U-shaped notch is introduced along their circumference. Residual stress along the specimen axial direction (*z* direction) is relaxed using the NPT (constant number of particle, pressure, and temperature) thermodynamic ensemble for 0.02 ns before applying deformation loading. Samples are simulated under uniaxial stress condition with PBC by applying constant strain rate loading along the axial *z* direction while maintaining traction

free conditions in the *x* and *y* directions. During the loading the temperature is maintained at 50 K.

Prior to discussing the role of geometry and imperfections, it is important to articulate the role of applied strain rate on the failure mode. In the following subsection, we briefly present the observations of the study on the effect of applied strain rate on the manner in which nano-scaled MG specimens fail. These observations enable us to adopt a reasonable range of strain rates that avoid strong strain rate effects and allow us to investigate the intrinsic mechanical deformation mechanisms of nano-scaled MG specimens as a function of specimen size and geometric imperfections.

3.3 Strain Rate Effect

Previous studies have reported that the mechanical behavior of nanoscale structures may be strongly influenced by high strain rates typically applied in MD simulations (Branício and Rino, 2000; Cao et al., 2013; Koh et al., 2005; Rupert, 2013; Tsuzuki et al., 2011; Wen et al., 2008). Applied strain rates in MD simulations are typically several orders of magnitudes higher than most experimental conditions, which are usually quasi-static. The high loading rates in MD simulations are necessitated by the high computational expense in capturing sufficiently large strains leading to plasticity and failure while resolving atomistic time-scales. However, to obtain results that are not qualitatively influenced by strain rate and can be compared with relevant experiments, it is useful to obtain information on the limiting strain rate below which such effects are minimal. To that end, we first report the effect of strain rate on the failure mode by performing tensile simulations of MG specimens (*d*

= 15 nm and aspect ratio, ξ = 13 and ξ = 50) over a wide range of strain rate, $10^7\ s^{-1} \leq \dot{\varepsilon} \leq 4\times10^{10}\ s^{-1}$.

The results shown in Fig. 3-2a, indicate that the higher the strain rate, the higher are the yield stress and strain to failure. For $\dot{\varepsilon}$ values up to $10^9\ s^{-1}$, the specimens fail abruptly, as demonstrated by the sudden drop of stress from the yield point. However, for $\dot{\varepsilon} > 10^9\ s^{-1}$, the gradual drop in the stress beyond the peak at the yield point indicates smooth graceful failure (figs 3-2b-d). Fluctuations in the stress-strain curves for high strain are caused by the strong oscillatory breathing mode (a vibration mode) in the specimens along the radial direction. Figs 3-2b-i indicate the different deformation modes that occur as a function of strain rate. At strain rates below ~ $4\times10^8\ s^{-1}$, the MG nanowires fail by nucleation and propagation of a dominant SB. However, at higher strain rates the deformation mode gradually transitions to necking (figs 3-2d-f). Note that beyond a threshold strain rate the number of necking regions increase with increasing strain rate. The effect of strain rate on the number of necks can be explained using the Grady-Kipp model (Kipp and Grady, 1985), which invokes the role of inertia in description of this failure mode (See Appendix A). The deformation mode finally transitions to continuous viscous flow from $\dot{\varepsilon} \sim 10^9\ s^{-1}$ to $\dot{\varepsilon} \sim 10^{10}\ s^{-1}$.

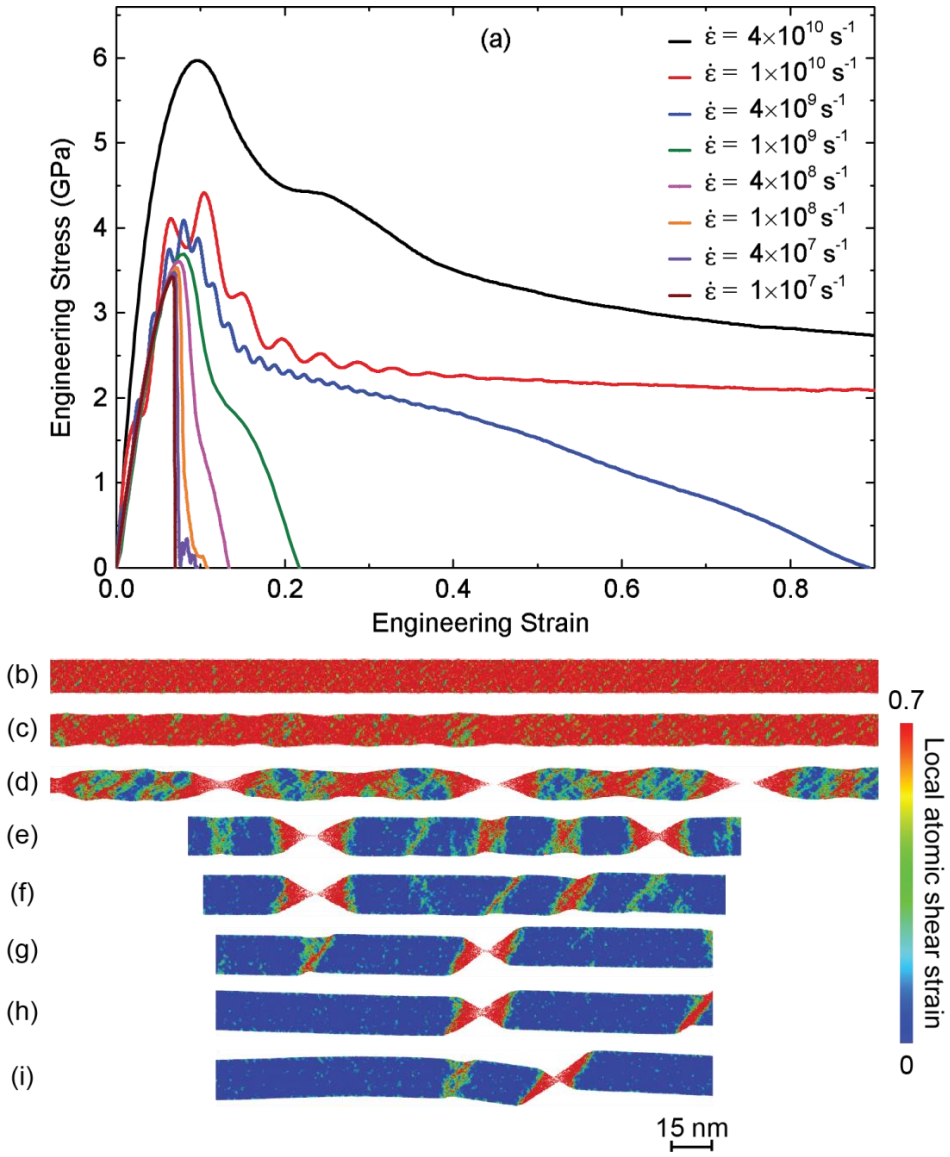

Figure 3-2 Strain rate effects on the deformation of MG nanopillars. (a) Stress-strain curves for nanopillars deformed with strain rates from 10^{7} s^{-1} to 4×10^{10} s^{-1}, (b)-(i) Illustrations of the nanopillars, in decreasing strain rate order, at failure or at strain 0.9 in the case of strain rate equals or higher than 4×10^{9} s^{-1}. Nanopillars are coloured according to the calculated local atomic shear strain. All nanopillars have a diameter of 15 nm and aspect ratio, ξ = 13.

In summary, the results indicate that strain rates up to 4×10^{8} s^{-1} do not have a strong effect on the failure mode and the MGs fail via SB evolution, which is similar to the experimentally observed failure mode at quasi-static rates of loading. Guided by these observations, we use a constant engineering strain rate of 4×10^{7} s^{-1} in the remainder of this work, unless otherwise specified.

Having understood the role of applied loading rate, we now discuss the effects of specimen geometry (diameter and length) and geometric imperfections.

3.4 Effect of Specimen Aspect Ratio

Consider a nano-scaled MG cylindrical specimen of length l and diameter d, giving an aspect ratio $\xi = l/d$. Fig. 3-3 shows the effects of ξ on the stress-strain responses and deformation mechanisms of nano-scaled MG specimens under uniaxial tension. Fig. 3-3a shows the overall engineering stress (σ)-engineering strain (ε) curves with d = 15 nm and ξ in the range of 2.5 to 50, which are subjected to tensile loading. As can be seen from Fig. 3-3a, the yield stress (peak stress) and the corresponding yield strain (strain at peak stress) ε ~ 0.07 are independent of the ξ. This yield strain is related to the formation of a dominant localization, indicating that the localization event is independent of the ξ, irrespective of the nature of localization. Further, over the range of the ξ considered here there exists an abrupt drop in the stress $(\Delta\sigma)$ at the yield strain. As depicted in Fig. 3-3a inset, this $\Delta\sigma$ depends on the ξ such that the larger the aspect ratio the bigger is the stress drop. As may be expected, it tends to saturate above a certain ξ, because the minimum stress after the collapse reaches zero indicating complete material separation. At smaller aspect ratios $(2.5 \leq \xi \leq 10)$ the stress drops are smaller and the specimen tends to recover leading to a more gradual failure. This is the case because the $\Delta\sigma$ is related to the amount of elastic energy that transforms to kinetic energy during SB propagation. By increasing the specimen length, the total stored elastic energy

increases correspondingly and therefore, the kinetic energy that is available to drive the propagation of a localized SB across also increases.

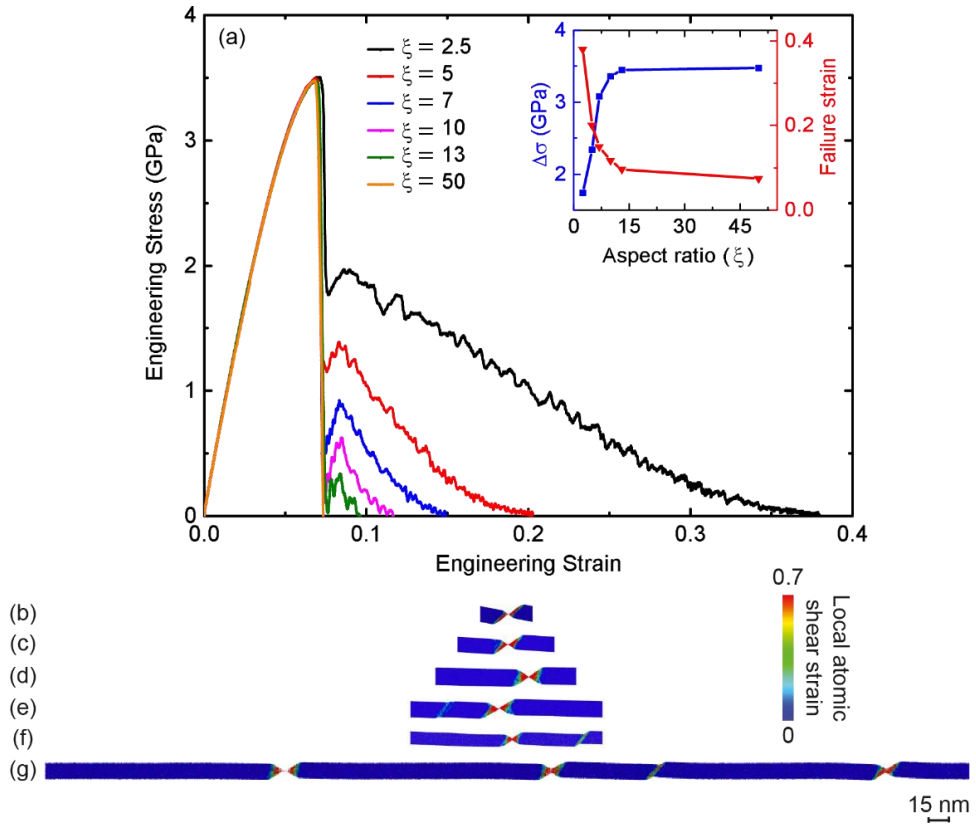

Figure 3-3 Aspect ratio effect of the MG nanopillars. (a) Stress-Strain curves for nanopillars with aspect ratio from 2.5 to 50, inset stress drop and failure strain of MG nanopillar with different aspect ratios. (b)-(g) Illustration of the deformed nanopillars simulated highlighting the failure mode, in increasing aspect ratio order. Nanopillars are coloured according to the calculated local atomic shear strain. All nanopillars have a diameter of 15 nm and are deformed at 4×10^{7} s^{-1} tensile loading.

Defining failure strain as the strain at which complete material separation occurs, we conclude that the smaller the ξ the larger is the failure strain. This can be understood considering that the high aspect ratio specimens are able to store more elastic energy for a given strain enabling the full propagation of SBs across the pillars at the yield point. It implies that higher ξ provide sufficient stored energy to fully develop localized SB activities into fully SB that span

across the systems once the SB initiation is reached. As it can be seen in Fig 3-3 the plastic strain at failure is zero for $\xi \sim 13$ and above what implies a threshold strain value at total failure for the nanopillars. The saturation of the failure strain above $\xi \sim 13$ is expected assuming a SB aligned perfectly at 45° with the nanopillar axis.

The results reveal that the length of the specimen determines the amount of energy, which is available to drive plastic deformation to failure, which is consistent with the recent studies (Volkert et al., 2008; Wu et al., 2012). Indeed, (Wu et al., 2012) made a similar observation in single crystal copper nanowires in that the length of specimen related to the amount of stored elastic energy causing a change in the failure mode from brittle to ductile. They indicated that, short copper nanowires fail via a ductile mode, while long wires exhibit extreme shear localization and abrupt failure (Wu et al., 2012). Consistent with the observations on crystalline Cu nanowires, in the present work the aspect ratio of an MG nano-scaled specimen determines the amount of stress drop at the yield point and its final failure strain.

Figs 3-3b-g illustrates the deformation mechanism of the MG specimens at failure for different aspect ratios indicating that for all aspect ratios, the specimens fail by SB propagation. More than one SB may form provided the aspect ratio is higher than a certain threshold. Here, the length scale between two localized SB is ~ 13 times the specimen diameter, which is well captured by the Grady-Kipp model (Kipp and Grady, 1985) (see Appendix A).

3.5 Effect of Specimen Diameter

Fig. 3-4 displays the effect of specimen diameter on the deformation of MG nanopillars. Fig. 3-4a shows the stress-strain curves for specimens with diameters in the range d = 15 nm to d = 50 nm, keeping $\xi = 2.5$. As shown in this figure, in the range considered here, the diameter does not have any direct effect on the peak stress and failure strain of the specimens. As discussed earlier, the stress does not reach zero at the sudden drop because of two reasons: (1) the small aspect ratio ($\xi = 2.5$) and (2) the specimens are deformed at a constant strain rate rather than a constant rate of load increase. Figs 3-4b-e show the atomic configuration of specimens coloured according to their local atomic shear strain at failure strain. The deformation mode in all the cases is due to the SB propagation. From these and the preceding results, we deduce that in defect-free nano-scaled MG specimens, it is the aspect ratio and strain rate that determine the failure mechanism of nano-scaled MG specimens and the diameter or the length alone does not play any significant role.

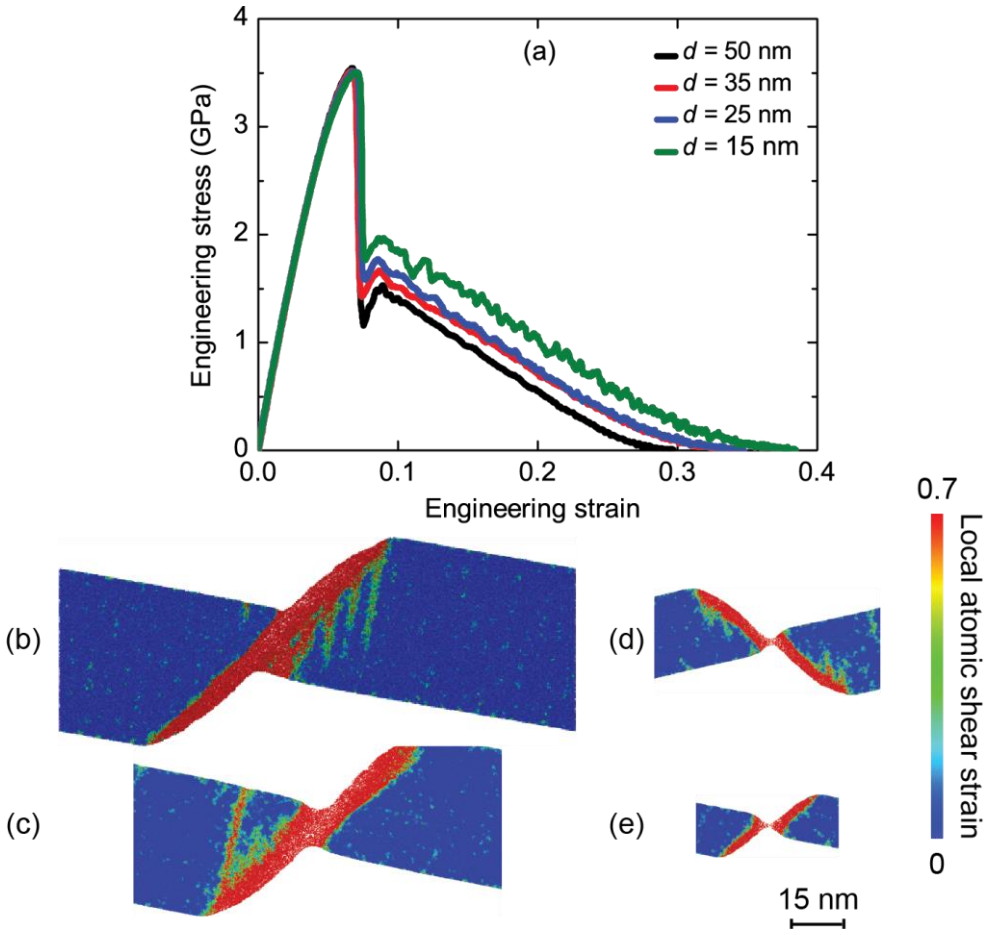

Figure 3-4 Lack of diameter effects on the deformation of MG nanopillars. (a) Stress-Strain curves for nanopillars with diameter from 15 nm to 50 nm showing similar curves. (b)-(e) Illustrations of the deformed nanopillars at failure indicating shear banding failure for all diameters. Nanopillars are coloured according to the calculated local atomic shear strain. All nanopillars have an aspect ratio of 2.5 and are deformed at 4×10^{7} s^{-1} tensile loading.

It is interesting to note here that while our simulations until now predict catastrophic failure via shear banding at all specimen diameters (at a fixed aspect ratio), a number of recent experiments show evidence of transition from SB to necking (also referred to as brittle-to-ductile transition) in nanoscale MG specimens with dimensions of ~100 nm or smaller (Chen et al., 2011; Chen et al., 2013; Guo et al., 2007; Jang and Greer, 2010; Jang et al., 2011; Tian et al., 2013; Wang et al., 2012). In other words, while experiments indicate a size effect in failure, MD simulations, on idealized defect free models, suggest a

size-independent mode of failure with no observable transition from SB to necking. Some theories have been proposed to explain the enhancement of ductility at smaller length-scales in MG. These include: (i) interaction between structural and free volume diffusion length-scales (Wang et al., 2013); (ii) competition between crack propagation stress and stress for homogeneous flow (Jang and Greer, 2010), or (iii) interaction between the plastic zone size ahead of stress concentration and the specimen size (Greer et al., 2013; Tian et al., 2013). To the best of our knowledge, these have not been evaluated in a detailed manner so far. In the following subsection, we take a simple, yet elegant recourse driven by practical situation in order to uncover a size effect in SB-necking transition. In particular, we demonstrate that in the presence of geometric imperfections the diameter plays an important role in determining the failure mode, thereby producing a clear size effect.

3.6 Role of Surface Geometric Imperfections

In the build up towards our hypothesis that imperfections may serve as effective generators of the observed BDT in nano-scaled MG specimen, we compare the evolution of plastic deformation of a smooth 100 nm diameter specimen ($\xi = 2.5$) loaded in uniaxial tension to that of a deeply notched specimen of similar diameter (notch root radius $a = 15$ nm). Fig. 3-5 shows that while the smooth specimen localizes into thin SB the notched specimen shows a discernibly distinct plasticity evolution. Although SBs emanate at the notch in the incipient stages, the plastic flow develops in the neck region homogeneously leading to

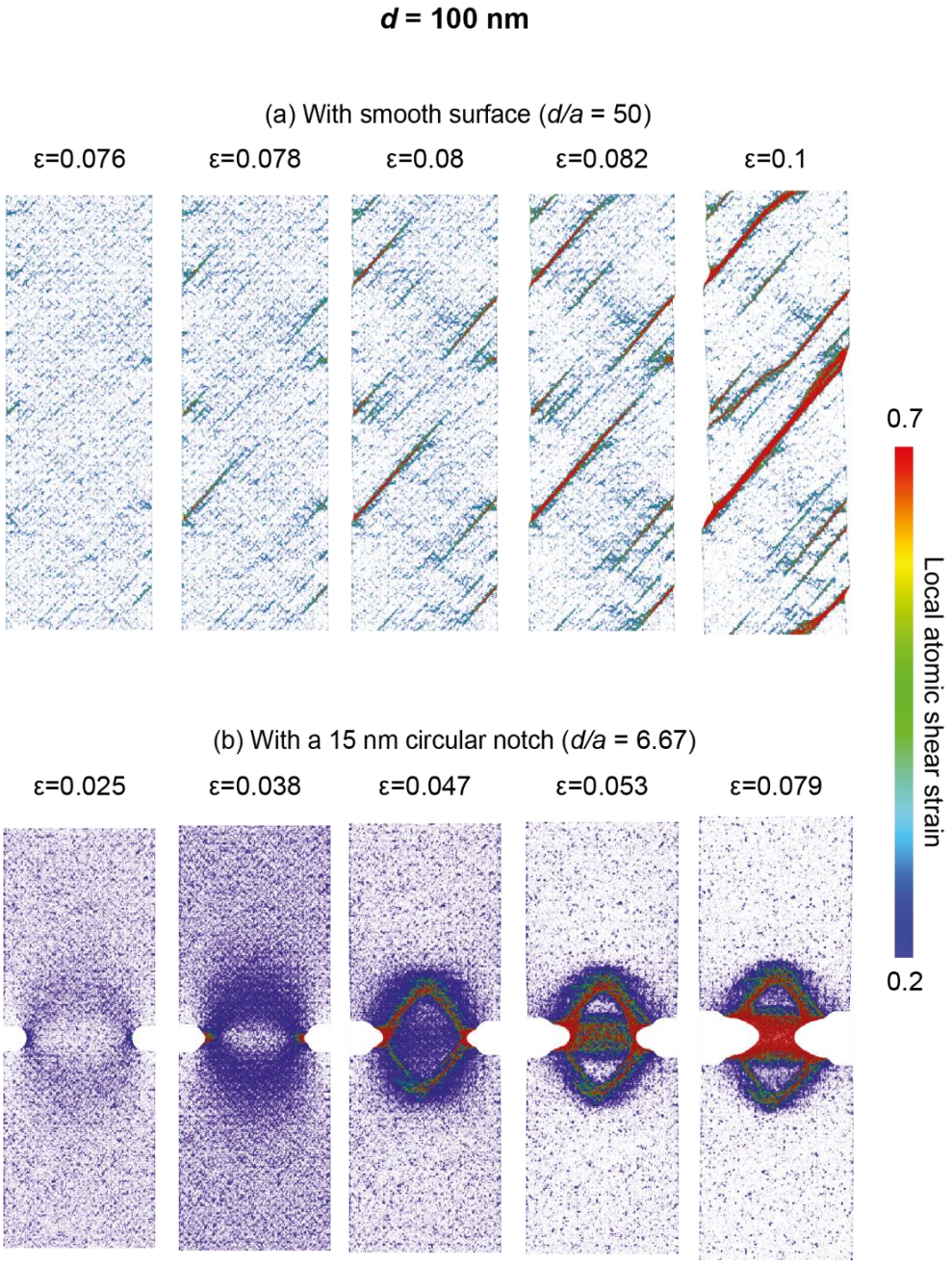

Figure 3-5 Shear band to necking transition in failure mode of 100 nm diameter MG nanopillars with smooth and notched surface, respectively. Nanopillars are coloured according to the calculated local atomic shear strain. In 100 nm nanopillar with 15 nm U-shape notch (b) only atoms with local atomic shear strain higher than 0.05 are shown. Nanopillars are deformed at 10^8 s^{-1}. a is represented as a surface roughness in smooth nanopillar and as a notch deep in nanopillar with U-shape notch.

suppression of localized SB. Notably, this phenomenon is similar to the recent experimental observation of (Wang et al., 2013). It is well known that geometric imperfection such as a blunt notch can produce a size effect in the Mode-I

fracture toughness (K_c) of MGs. Insightful experiments by (Flores and Dauskardt, 2001) indicate a linear increase in the toughness with $\sqrt{a}$, where a is the notch-root radius. Using a sophisticated constitutive model, (Henann and Anand, 2009) show that a large elasto-plastic deformation theory coupled with dilatational effects predicts this dependence. These and similar investigations motivate a somewhat different interpretation of the experimentally observed SB to necking transition in nano-scaled MG. Real nano-scaled MG specimens do not possess atomically smooth surfaces. Often, surface roughness is dictated by processing steps adopted in specimen preparation (Bharathula et al., 2010; Luo et al., 2010; Nakayama et al., 2010; Schuster et al., 2007; Shan et al., 2008; Volkert et al., 2008; Wu et al., 2009c). Typically, such nano-scale cutting processes generate surface roughness in the order of 1-3 nm (Ali et al., 2002). Although the magnitude of the roughness seems small, it may affect the mechanical behavior of nano-scaled specimens, since a surface imperfection is a potential source of stress concentration and stress triaxiality (Henann and Anand, 2009; Murali et al., 2013). On the other hand, our idealized defect free MD specimens carved from bulk samples using sharp cuts are atomically smooth and possess surface roughness in the order of few angstroms[4]. Therefore, it is natural to ask: how would nano-scale specimens behave with the introduction of surface geometric imperfections mimicking real scenario in a simulated condition? In the following subsections, we answer this and related questions through extensive MD simulations on MG nano-specimens

[4] We estimate the roughness by measuring the distance from peak to bottom of valleys in the atomic landscape of a representative surface region.

mimicking notched and rough surfaces. Later, we also discuss the observed behaviors on the basis of mechanistic principles.

3.6.1 Plastic Deformation of Smooth and Notched Nano-specimens

As a starting point, it is useful to consider an idealized scenario where a single surface imperfection exists in the form of a circular notch of certain root radius. This assumption allows access to well-known results based on the elasto-plastic theory in understanding the stress fields that exist ahead of a notch and relate them to the observed localization phenomena. Therefore, we first consider specimens with the same diameters and aspect ratio as in the preceding section, but introduce a single U-shaped notch along their circumference. To be consistent with the magnitude of the surface roughness in experimental MG nano-specimens, the notches here are 1 nm deep (h) and 1 nm wide (a), see Fig. 3-6. We call these as N_1 notches in the remainder discussion.

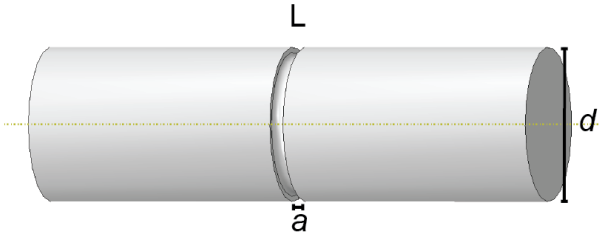

Figure 3-6 Schematic illustration of the cylindrical nanopillars with a surface defect composed of a U-shape notch along the whole circumference of the nanopillars to represent surface defect in the pillar. The U-shape notch used here is 1 nm deep and 1 nm wide and mimics the typical surface roughness found in experimental MG nanopillars.

We perform MD simulations on both MG specimens, with smooth and notched surfaces. To capture the effect of specimen size range over which the BDT could possibly occur, we consider d ranging between 5 - 100 nm while keeping the

aspect ratio $\xi = 2.5$. All the simulations are performed under constant strain rate $\dot{\varepsilon} = 4 \times 10^7\ s^{-1}$, except for the specimens with d = 100 nm, which are loaded[5] at $\dot{\varepsilon} = 1 \times 10^8\ s^{-1}$.

Fig. 3-7 illustrates the primary result of the simulations. It shows the plasticity evolution in the two main categories of nano-scale specimens under consideration: (i) Smooth specimens (figs 3-7a,c,e,g,i,k,m) – these are specimens with 5 nm ≤ d ≤ 100 nm possessing a natural surface roughness ~0.2 nm, and (ii) Imperfect specimens (figs 3-7b,d,f,h,j,l) – these are specimens (10 nm ≤ d ≤ 100 nm) with a pre-induced N_1 notch (Fig. 3-6). In all the cases, the atoms are colored according to the value of the local atomic shear strain and for clarity, only atoms with local atomic shear strain larger than 0.2 are shown. To highlight the deformation mode the specimens are not shown in the same length scale. The result reveals the effect of a surface imperfection on the manner in which localization occurs as a function of specimen diameter. In the case of smooth specimens (figs 3-7a,c,e,g,i,k,m) shear banding induced localized failure is the characteristic mode of failure in the diameter range 100 nm ≥ d ≥ 10 nm. For d = 10 nm (Fig. 3-7k), we observe a mixed failure characteristic that arguably is a combination of SB propagation and necking, resulting in a somewhat diffuse SB. Interestingly, for d = 5 nm there is a transition from shear banding to a well-defined necking (Fig. 3-7m). However, note that this transition regime 5 nm ≤ $d \leq 10$ nm in the case of smooth specimens is well

[5] A higher strain rate is used in this case because of the prohibitive computational cost involved in simulating ~134 million atoms system for extended simulation time enough to characterize its failure mode. However, the strain rate is still in the range where it is expected to introduce mild effects on the failure mode (cf. Section 3.3).

below those reported in experiments (Chen et al., 2011; Chen et al., 2013; Guo et al., 2007; Jang and Greer, 2010; Jang et al., 2011; Tian et al., 2013; Wang et al., 2012). Notwithstanding this quantitative difference, we keep in mind the occurrence of this transition in smooth specimens and return to this observation in the subsequent discussion.

Figs 3-7b,d,f,h,j,l show the evolution of plastic deformation for specimens (10 nm $\leq d \leq$ 100 nm) with N_1 surface imperfection. For specimens with d = 100 nm and 50 nm, failure develops in the form of sharp SB, akin to the corresponding smooth case. As expected, the SBs emanate ahead of the notch root at ~45° to the nanopillar axis. However, the scenario changes appreciably with decrease in specimen diameter (50 nm $\geq d \geq$ 15 nm). Comparing the characteristics of localization in the notched specimens (figs 3-7d,f,h,j) with those of the smooth specimens (figs 3-7c,e,g,i) over this diameter range, we see that the notched nano-scaled specimens exhibit a clear transition in failure mode from SB to necking. The specimen with d = 25 nm indicates a transition size with characteristics of a mixed failure mode in that it has a strong signature of necking but also shows a shear offset typical of an SB. At d = 15 nm, however, the specimen localizes into a neck with no signs of shear offset. The results explicitly show that a BDT occurs as a function of diameter by the presence of a surface notch in the nano-scaled regime.

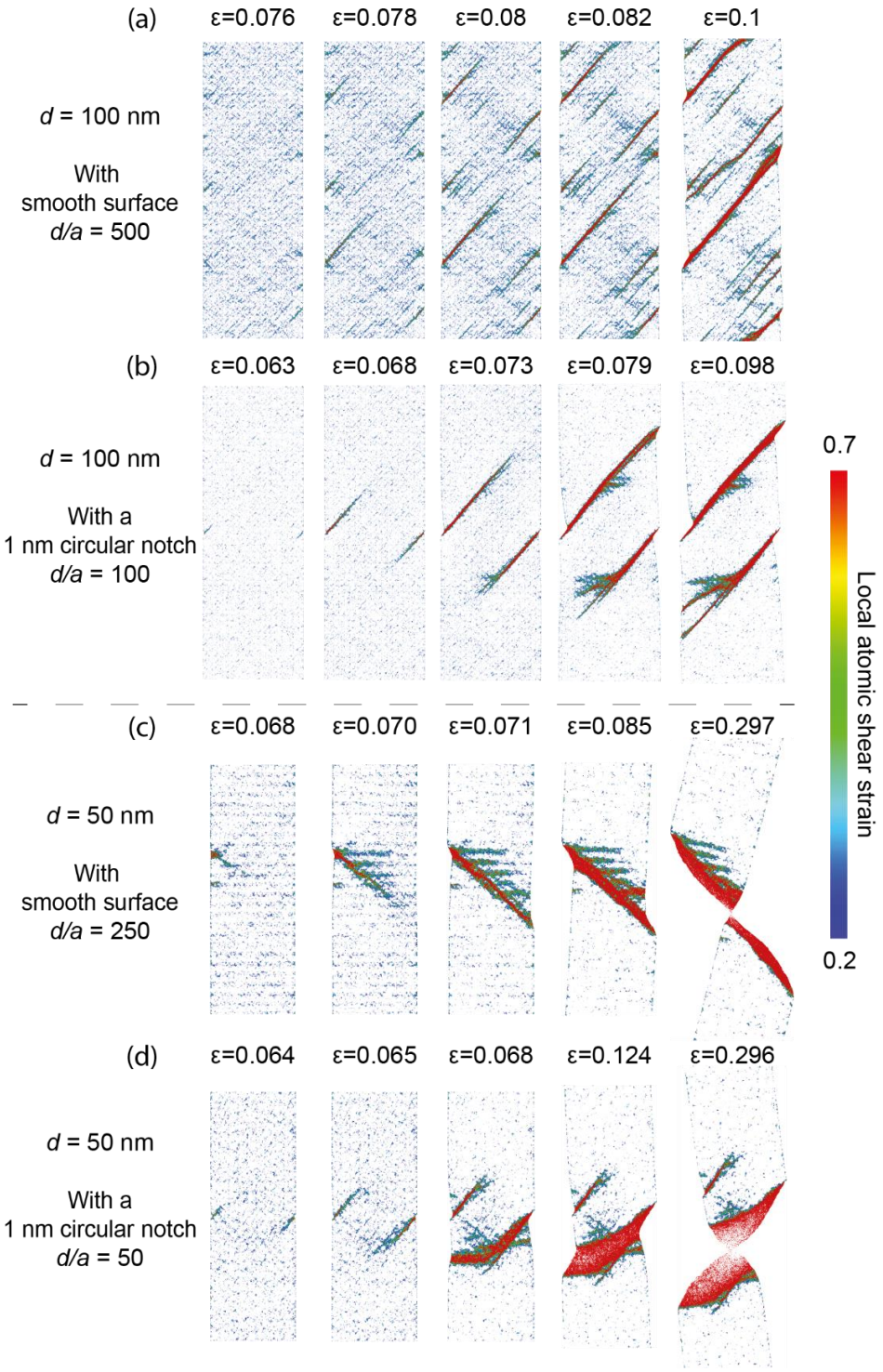

Figure 3-7 Diameter effects on the deformation and failure mode of MG nanopillars with smooth or notched surfaces. Nanopillars are coloured according to the calculated local atomic shear strain. Only atoms with local atomic shear strain higher than 0.2 are shown. Nanopillars have a diameter from 5 nm to 100 nm and are deformed at 4×10^{7} s^{-1}. 100 nm nanopillar with smooth surface and 1 nm U-shape notch (a and b) are deformed at 10^{8} s^{-1}. a is represented as a surface roughness in nanopillars with smooth surfaces and as a notch deep in nanopillars with U-shape notch.(continued)

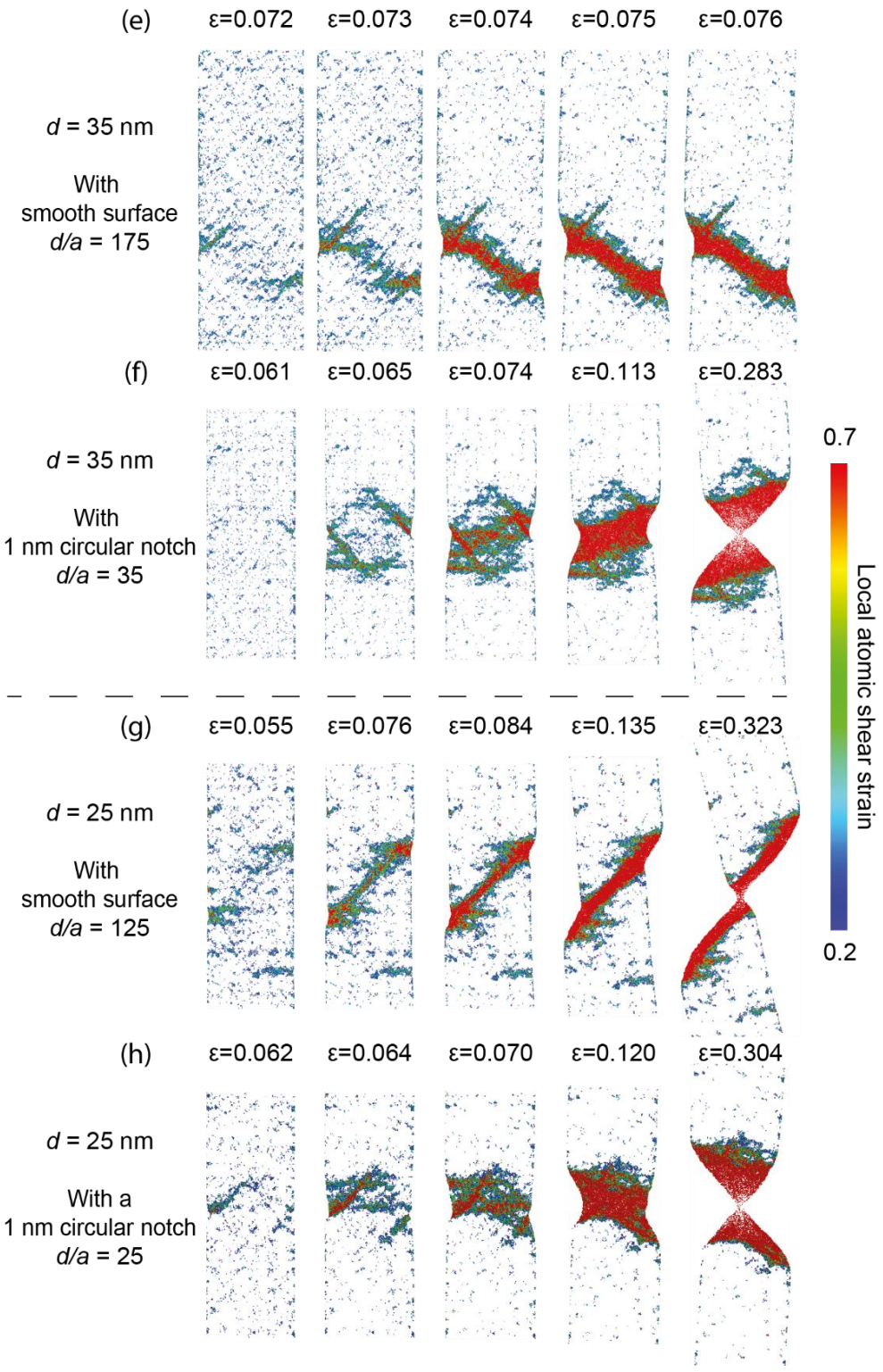

Figure 3-7 Diameter effects on the deformation and failure mode of MG nanopillars with smooth or notched surfaces. Nanopillars are colured according to the calculated local atomic shear strain. Only atoms with local atomic shear strain higher than 0.2 are shown. Nanopillars have a diameter from 5 nm to 100 nm and are deformed at 4×10^{7} s^{-1}. a is represented as a surface roughness in nanopillars with smooth surfaces and as a notch deep in nanopillars with U-shape notch.(continued)

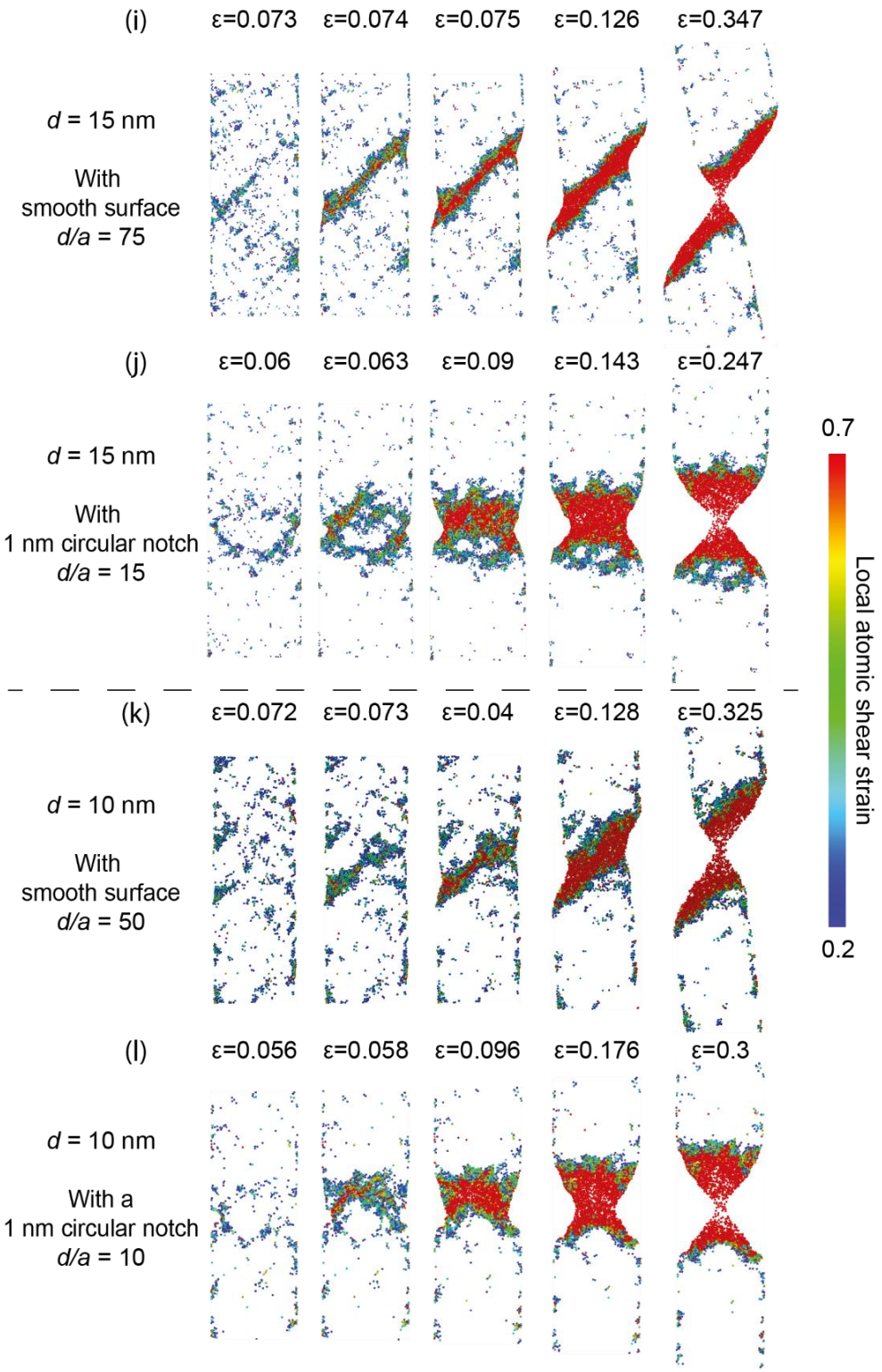

Figure 3-7 Diameter effects on the deformation and failure mode of MG nanopillars with smooth or notched surfaces. Nanopillars are coloured according to the calculated local atomic shear strain. Only atoms with local atomic shear strain higher than 0.2 are shown. Nanopillars have a diameter from 5 nm to 100 nm and are deformed at 4×10^{7} s^{-1}. a is represented as a surface roughness in nanopillars with smooth surfaces and as a notch deep in nanopillars with U-shape notch.(continued)

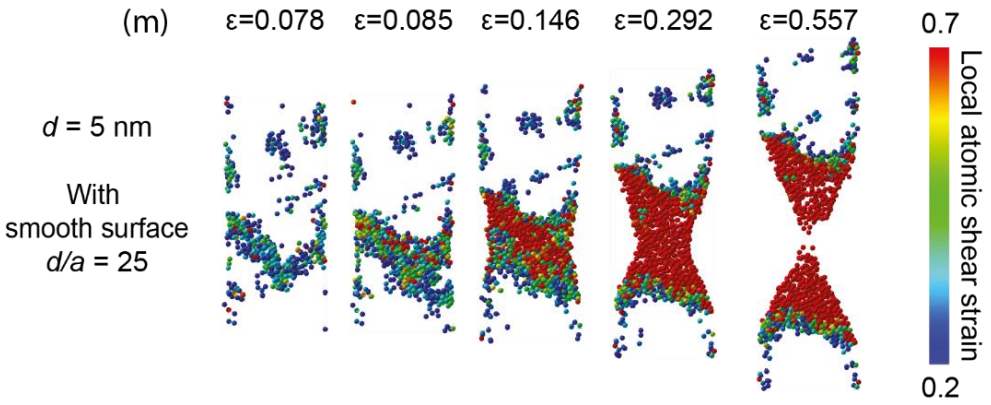

Figure 3-7 Diameter effects on the deformation and failure mode of MG nanopillars with smooth or notched surfaces. Nanopillars are coloured according to the calculated local atomic shear strain. Only atoms with local atomic shear strain higher than 0.2 are shown. Nanopillars have a diameter from 5 nm to 100 nm and are deformed at 4×10^{7} s^{-1}. a is represented as a surface roughness in nanopillars with smooth surfaces and as a notch deep in nanopillars with U-shape notch.

3.6.2 Necking Failure in Notched Specimens

The observations from Fig. 3-7 suggest that the transition from SB to necking below a critical specimen size should always occur in experiments on MG nano-specimens since it is reasonable to assume that surface imperfections of the order a ~ 1-3 nm would be ubiquitous. Note that in the figure, we also report the ratio d/a. Here, we indistinguishably assume a to represent the characteristic magnitude of the surface roughness in the case of smooth specimens. The results indicate that for CuZr nano-specimens the BDT occurs at a critical ratio d/a ~ 25. Remarkably, the same critical aspect ratio also seems to hold even in the case of smooth specimens (figs 3-7a,c,e,g,i,k,m). While the specific reasons of this critical ratio is not probed in detail here, it provides a basis for the observed necking for d = 5 nm (Fig. 3-7m) for smooth specimens without resorting to a different argument. The threshold d/a ratio also explains the experimentally observed BDT reported in several independent investigations (Chen et al., 2013; Guo et al., 2007; Jang and Greer, 2010; Tian et al., 2013).

The MD simulations suggest that, for CuZr MG nano-specimens, as long as the ratio d/a is equal to or smaller than ~ 25 one should observe necking. For larger ratios, nucleation and propagation of a localized SB is likely to be the failure mode. This prediction is in excellent agreement with a wide range of experiments that show failure by necking, by SB propagation or a BDT (Bharathula et al., 2010; Chen et al., 2011; Chen et al., 2013; Cheng and Ma, 2008; Deng et al., 2011; Jang and Greer, 2010; Jang et al., 2011; Kuzmin et al., 2011; Luo et al., 2010; Nakayama et al., 2010; Schuster et al., 2007; Shan et al., 2008; Tian et al., 2013; Volkert et al., 2008; Wang et al., 2012; Wang et al., 2013; Wu et al., 2009c; Yavari et al., 2010). Therefore, our results clearly indicate that the presence of surface imperfections (such as nano-scale roughness, notches, undulations, or flaws) in the surface of the nano-scaled specimens would induce a BDT in MG below a certain critical diameter dictated by the magnitude of the surface imperfection.

Fig. 3-8 compares experimentally reported failure modes in nano-scaled MG specimens under tensile loading with those observed in this work as a function of d/a ratio. In the figure, a mixed failure behavior that includes both SB-like and necking-like phenomena are grouped under the "mixed failure" and named "transition" regime. The trend displayed in Fig. 3-8 points out that a BDT occurs at the threshold ratio d/a within the range of 25 to 50.

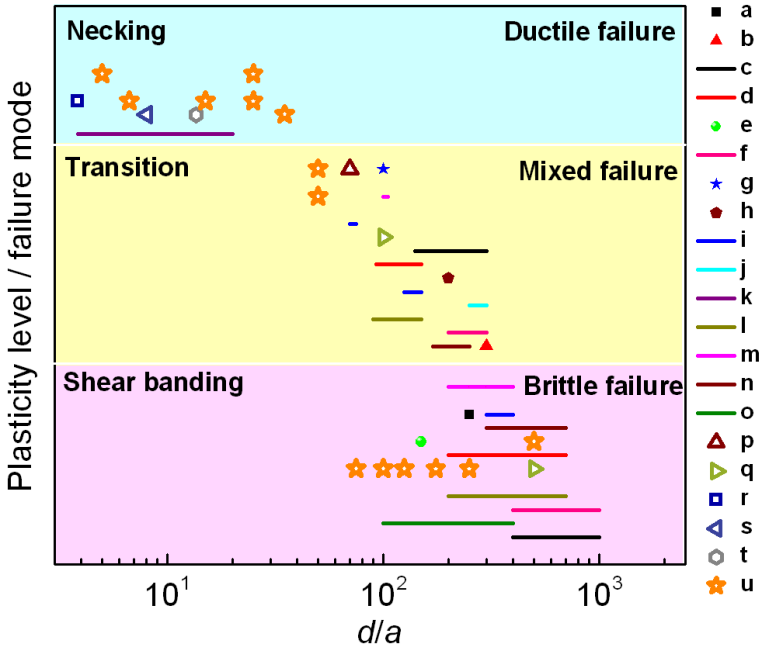

Figure 3-8 Plasticity level / failure mode map vs. *d*/*a* in the reported literature and the current work. (a(Schuster et al., 2007), b(Shan et al., 2008), c(Volkert et al., 2008), d(Nakayama et al., 2010), e(Wu et al., 2009c), f(Bharathula et al., 2010), g(Jang and Greer, 2010), h(Deng et al., 2011), i(Chen et al., 2011), j(Yavari et al., 2010), k(Luo et al., 2010), l(Kuzmin et al., 2011), m(Jang et al., 2011), n(Wang et al., 2012), o(Wang et al., 2012), p(Tian et al., 2013), q(Chen et al., 2013), r(Wang et al., 2013), s(Cheng and Ma, 2008), t(Li and Li, 2006), u: this work).

One should note that nano-scale MG specimens might possess additional surface properties that influence their mechanical behavior and failure mode. For example, specimens fabricated by FIB may have their surface state modified compared to the bulk by virtue of changes in the local atomic structure and composition due to ion implantation. Such changes may also influence the deformation characteristics at small length-scales. Recently, (Chen et al., 2013) investigated the possible effects from FIB by performing tensile loading experiments on $Ni_{80}P_{20}$ MG nano-specimens fabricated using FIB versus those prepared via template electroplating. Their results show BDT failure by size reduction in both cases, although FIB nano-specimens exhibit more ductility,

likely due to the less relaxed surface state that may enable profuse activation of diffuse SBs. Nonetheless, the size dependent ductility in case of electroplated MG specimens in their work is worth noting and must be driven by mechanisms other than irradiation induced effects. If we assume that specimens fabricated by template electroplating have surface roughness in the same order as those fabricated by FIB (TEM images in (Chen et al., 2013) suggest mean roughness ~1 nm), based on the present results, we should expect a similar size-dependent BDT.

While the notched specimens with 1 nm notch root radius exhibit size-dependent BDT, we recall that the simulations of smooth specimens also reveal necking, albeit at much smaller diameter ($d \approx 5$ nm) (cf. Fig. 3-7m). For this diameter and $a \sim 0.2$ nm (atomic scale surface roughness for smooth specimen) $d/a \approx 25$, which is similar to the transition ratio in the case of notched specimens. Following this argument, one should have brittle failure by SB at any diameter if the surface roughness can be eliminated. In fact, recent MD simulations suggest that this assumption may be true. The surface roughness in MG nano-specimens can be nearly eliminated if they are generated using simulated casting (Shi, 2010). Atomic roughness level using this method is virtually non existent, since all surface atoms are located at the mathematically defined casting surface. Tensile loading simulations of specimens generated by simulated casting indicate no transition in the failure, which occurs via SB in all cases, even at $d \leq 5$ nm (Shi, 2010).

Our argument that it is only the d/a ratio that drives this transition might tend to suggest that such a transition may also be plausible at larger diameters

(microns or even mm) provided the notches or imperfections are large enough so that the d/a ratio condition is satisfied. However, this may not be necessarily true as the underlying mechanistic principles indicate that there may be another inherent material length-scale that mediates the transition. This length-scale is the thickness of the SB (t), which is typically in the range of few nm for most MGs. We defer the mechanics aspect of the transition until Section 3.6.3.

While the results show clearly the effects of a notch in the failure of the MG nanopillars, it is worthwhile to consider why the presence of a notch in a rather brittle material could possibly induce ductility. Ordinarily, the presence of surface imperfections or flaws in a brittle material causes catastrophic brittle failure. One may then expect that the presence of a notch in an MG sample would prematurely induce brittle failure by SB propagation, with resulting strength reduction. However, recent MD simulations have shown that this behavior does not apply to MG. Numerical results on CuZr MG thin films demonstrate that the material is rather insensitive to the presence of flaws (Sha et al., 2013) and SBs are activated and fail the material at the same ultimate tensile stress as that in samples without notches. The only noticeable effect of the notch was in the localization of the failure point. The initial stress concentration induced by notches generates a plastic deformed region close to the yield point that eventually releases the stress concentration explaining the flaw insensitive strength. Our MD simulations show a similar phenomenon. Plastic deformation is generated ahead of notches in the specimens thereby releasing the stress concentration. The presence of a plastically deformed region ahead of a crack in a bulk MG have also been reported experimentally (Flores

and Dauskardt, 1999). If this plastic zone size, say p, is comparable to the specimen diameter, it promotes stable necking. On the other hand if $p \ll d$, the same plastically deformed region becomes a source for SB initiation and propagation. Therefore, one can think of the observed notch induced ductility in MG nanopillars resulting in its necking also as a consequence of the inherent MG flaw insensitiveness.

3.6.3 Stress State in Notched Specimens

To investigate the relationship between the BDT and d/a ratio, we perform three-dimensional finite element simulations of notched specimens based on linear elastic analysis. A linear elastic analysis is deemed reasonable here, because we are interested in evaluating the stress state leading up to the yield condition. Fig. 3-9a plots the stress intensity ($\frac{\sigma_{zz}}{\sigma_{\infty}}$, where σ_{zz} is the local normal stress and σ_{∞} is the average stress, in the loading direction) as a function of the normalized specimen size measured along the centreline of the notch for various d/a ratios. As expected, for all d/a ratios the stress intensity is significantly higher at the notch root and decays toward the centre. Further, at any given location between the two notch roots, smaller d/a ratio produces higher stress intensity. Notably, for $d/a < 25$ the stress intensity is greater than 1 over the entire cross-section length. In part that is one of the reasons for the pronounced necking observed for small d/a, since the induced stress intensity confines the deformation to the cross section region, where the stress conditions are favourable. Even though the analysis of the stress intensity explains the localization of the deformation, since it defines the region where the local stress

will overcome the strength of the material, it does not accounts for the lack of SB generation and propagation. In particular, it does not indicate the reason for the BDT. To understand the relative importance of the stress state in driving SB versus initiating a neck, we plot the stress triaxiality, defined as $T = \sigma_h/\sigma_e$, where σ_h is the hydrostratic stress and σ_e is the von Mises equivalent stress. Fig. 3-9b shows the variation of T between the notch roots for different d/a ratios. For $d/a \geq 25$, the high hydrostatic (tensile) stress is largely restricted in the immediate vicinity of the notch root and is lower than the Mises stress $(0.65 \leq T \leq 0.7)$. However, for $d/a < 25$, the peak triaxiality increases dramatically while also shifting closer toward the center of the specimen between the notch roots. Further, the overall triaxiality along the centreline joining the notch roots also increases with decreasing d/a. While these results are qualitative in nature and based on linear elasticity, they provide indicators on the possible reasons for the transition with decreasing diameter. Given the higher σ_e compared to σ_h in the notched region $(T < 1)$, it is likely that the initial plasticity may occur by shear rather than by void growth.

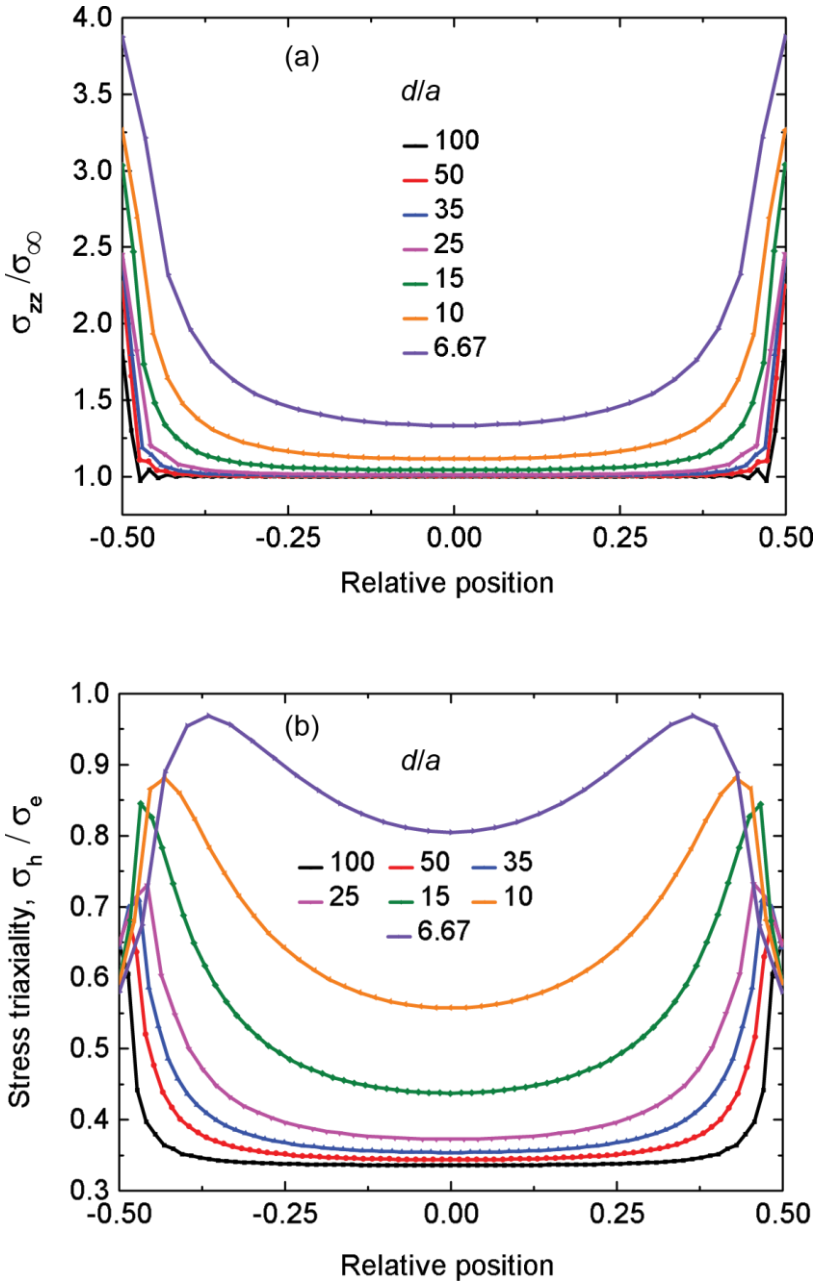

Figure 3-9 Stress state in nanopillars with U-shape circular notch. (a) Stress intensity $\left({}^{\sigma_{zz}}/_{\sigma_{\infty}}\right)$ as a function of the normalized specimen size measured along the centreline of the notch for various *d*/*a* ratios. (σ_{zz} is the local normal stress and σ_{∞} is the average stress, in the loading direction) (b) Stress triaxiality ($T = \sigma_h/\sigma_e$) as a function of the normalized specimen size measured along the centreline of the notch for various *d*/*a* ratios. (σ_h is the hydrostratic stress and σ_e is the von Mises equivalent stress). *x*-axis shows the position along the path located in the middle of the nanopillars normalized by (d-2a).

Having said that, it is the magnitude of these stresses that will ultimately decide the preferred mode of localization. This gives rise to two scenarios: (i)

$\sigma_h > \sigma_c$; but $\sigma_e < \sigma_y$, where σ_c is the critical cavitation stress and σ_y is the uniaxial yield strength, or (ii) $\sigma_e > \sigma_y$; but $\sigma_h < \sigma_c$[6]. In the first scenario, void nucleation and growth will drive the instability in regions where the cavitation stress is exceeded leading to failure via necking. While this is possible, the second scenario is more likely because typically $\sigma_y < \sigma_c$ (Henann and Anand, 2009). If this occurs, then one would expect the incipient plasticity to occur via localized SB emanating from the notch root. This is certainly confirmed in our MD simulations for large $d/a > 35$ ratios. On the other hand, a rather interesting case presents itself if one considers that SB also happens to be the preferred mode of incipient plasticity at smaller d/a ratios. The basis of such a scenario occurring are the observation in Fig. 3-7 for so-called transition d/a ratio ~25 and to some extent, d/a ~ 35 as well), which indicate a mixed localization phenomenon of diffuse SB and necking. Then, it would be of interest to ask as to how an SB would transition to a neck. We postulate a possible mechanism for such a transition. It can be shown that the stress state within an SB (oriented at an angle $\theta \sim 45°$ to the horizontal axis) under global tensile loading is that of hydrostatic tension (Murali et al., 2013). This occurs due to the fact that the material within the SB is softer than the material that sandwiches it. Further, a hydrostatic tensile stress state also persists ahead of a notch root, i.e. at $\theta = 0°$ (Henann and Anand, 2009). The actual magnitudes of hydrostatic stresses along these two paths may depend on the specific material parameters, but it may be reasonable to assume that the hydrostatic tension in

[6] Note that the condition $\sigma_e > \sigma_y; \sigma_h > \sigma_c$ would be trivial as the material would preferably start to yield by shear given that $T < 1$.

the SB may be higher than that along $\theta = 0°$ (Murali et al., 2011). Then, if the hydrostatic tension in the SB exceeds cavitation stress, it would lead to nucleation of voids within the SB as well. Here, the length-scales of interest are: d, a, t and l, where $l = \left(K_c/\sigma_y\right)^2$ is the plastic zone size. If the thickness (t) of the SB and the plastic zone size are comparable to or greater than the structural length-scales then the hydrostatic tensile stress induced cavitation would tend to prevail over the notched region. Experiments and simulations indicate that the typical SB thickness prior to failure is in the range of 20-30 nm (Greer et al., 2013), while a rough estimate (for CuZr MG) gives, $l \approx 100 - 300$ μm. We conjecture that when $d/a \sim t/a$, one should observe a transition to necking

The observable amount of stress triaxiality for $d/a < 25$ across the whole cross section and in particular, close to the notch tip points out to the reason why the BDT occurs at this particular d/a ratio.

3.6.4 From Notches to Surface Imperfections: Effect of Distribution of Imperfections

To simulate the effect of imperfections along the whole surface of the nanopillars (surface roughness), we performed additional simulations that are based on: randomly distributed circular notches of full circumferential extent. We show that even minute, but ubiquitous surface imperfections/roughness play an important role in determining the macroscopic failure mode of MGs at the nano-scale through their interactions with material and structural length-scales.

Figure 3-10 shows the schematics of the rough specimens. For comparison, the schematics of the smooth and notched specimens are also shown. In the case

of rough specimens, circumferential notches of characteristic dimension $0 \leq a \leq 2$ nm were introduced (see Fig. 3-10). We considered specimens with $15 \leq d \leq 25$ nm. In all the cases, the initial length to diameter ratio was kept fixed at 2.5.

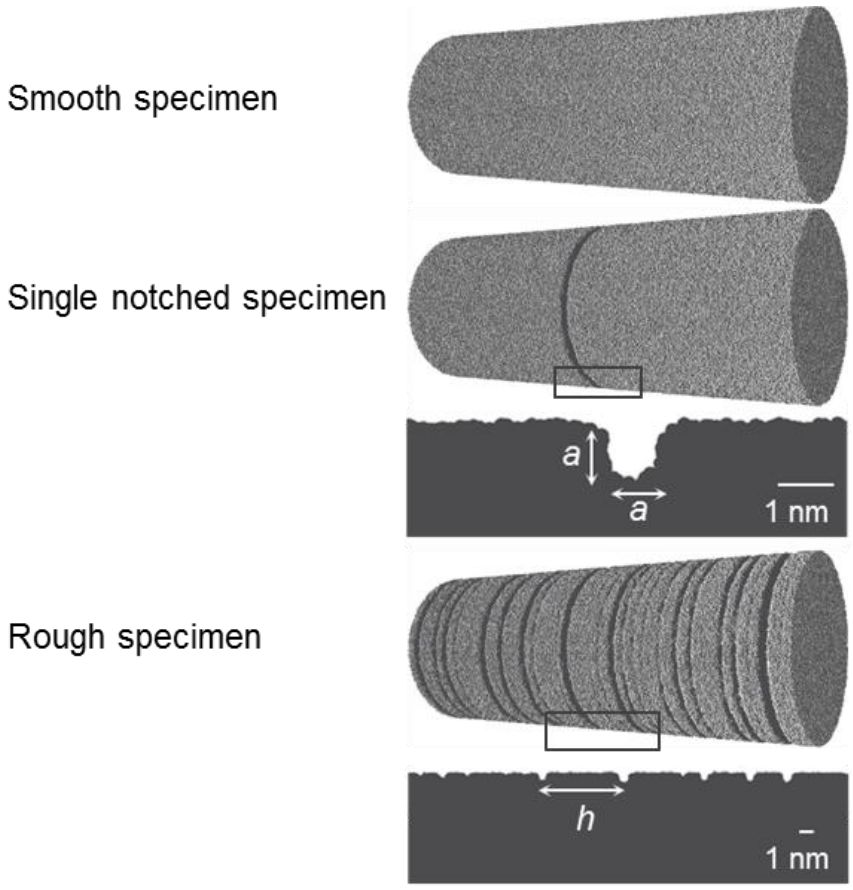

Figure 3-10 Schematic illustration of the cylindrical nanopillars with a smooth surface, a U-shape notch around the circumference of the nanopillars (characteristic dimension *a*) and surface roughness composed of randomly placed U-shaped, circumferential notches along the nanopillars. For a rough specimen *a* represents the maximum single notched size in the sample. *h* is a random number in the range of 3*a to* 5*a* and represents the distance between neighbor notches.

Figures 3-11a-e show the evolution of the plastic deformation in rough MG specimens as a function of surface roughness. Unlike the case of single-notched

specimens where we varied the diameter while keeping the notch size fixed, here we kept the diameter fixed ($d = 25$ nm) and varied the notch sizes. As described above, the circumferential notches along the nanopillar axis are randomly distributed with a maximum notch depth a and mean notch spacing, h = 3a to 5a. Despite these differences, the results for rough nano-specimens follow the same trend as those for the single notched specimens. It can be seen that for $d = 25$ nm and roughness $0.25 \leq a \leq 2$ nm (Fig. 3-11a), instability occurs in the form of a sharp SB. With increasing roughness amplitude (decreasing d/a) a clear transition from SB to necking is observed, akin to the single notched specimens with increasing notch size. The transition occurs somewhere at $1 \leq a \leq 2$ nm for this diameter. We also conducted a similar set of simulations for specimens with $d = 15$ nm (see Fig. 3-12), where a similar transition occurs at $0.25 \leq a \leq 0.75$ nm**.**

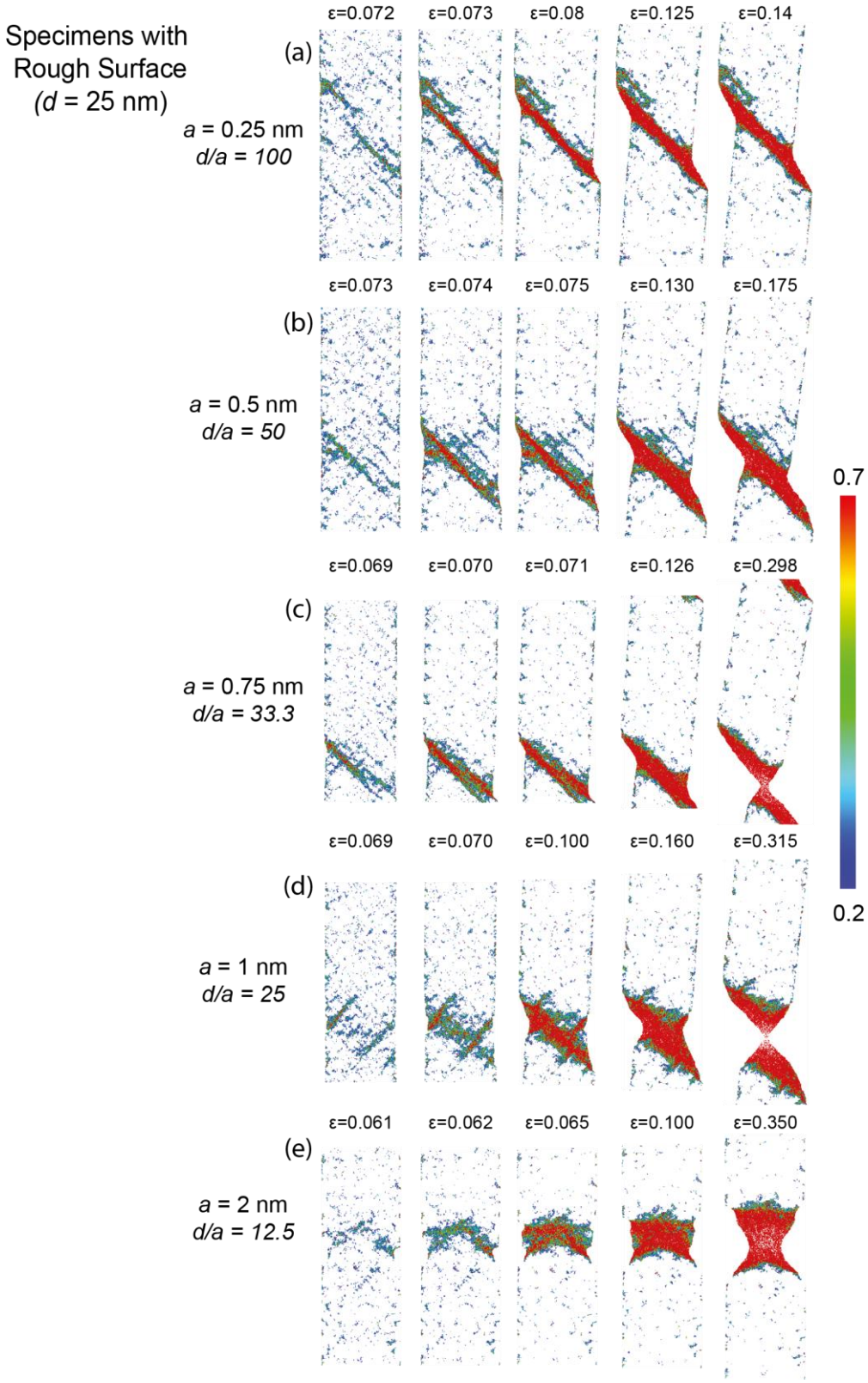

Figure 3-11 Roughness size effects on the deformation and failure mode of MG nanopillars with rough surfaces. Only atoms with local atomic shear strain higher than 0.2 are shown. Nanopillars are deformed at 4×10^{7} s^{-1}. *a* represents the maximum surface roughness in rough nanopillars.

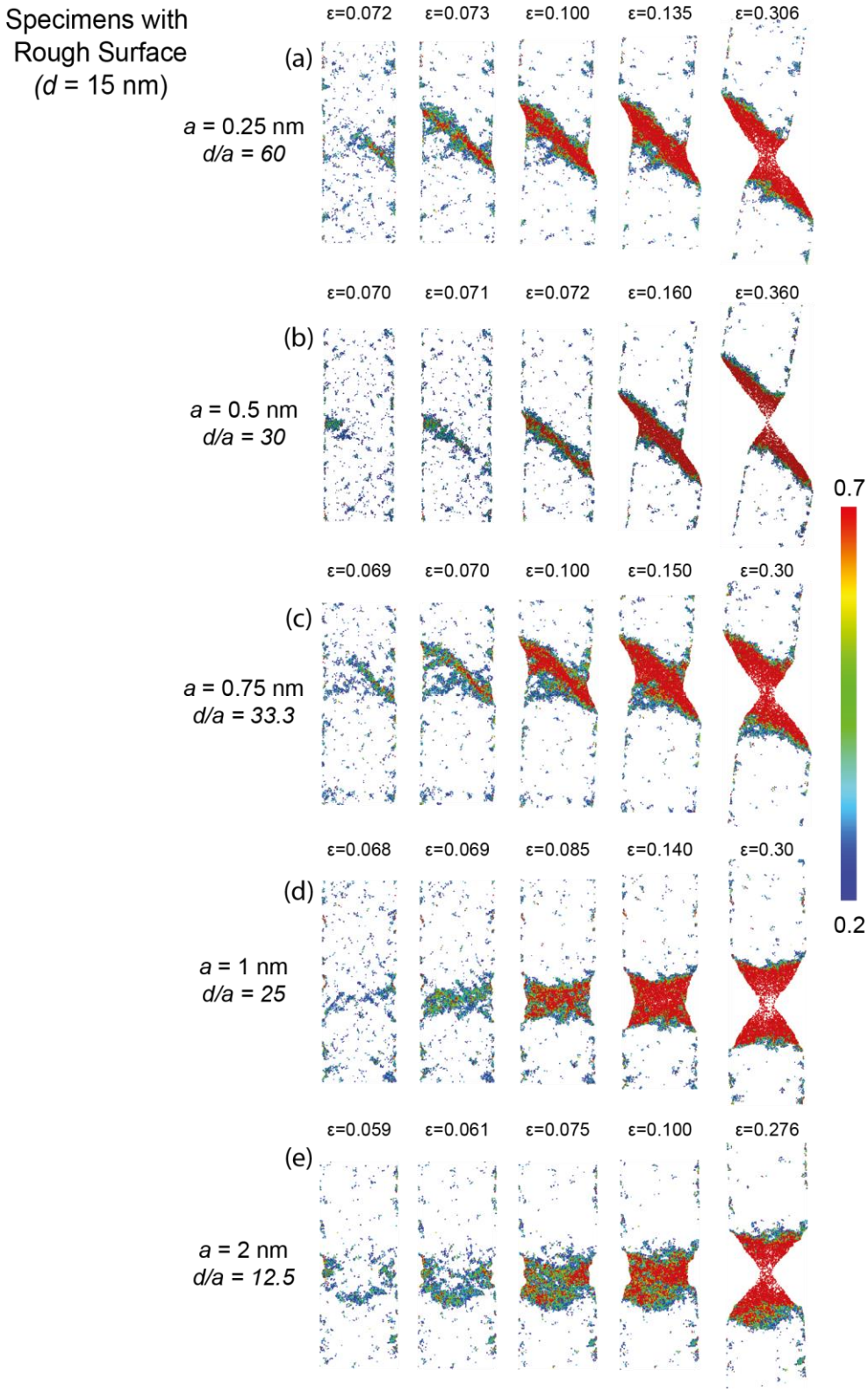

Figure 3-12 (color online): Diameter effects on the deformation and failure mode of MG nanopillars with roughness surfaces. Nanopillars are colored according to the calculated local atomic shear strain. Only atoms with local atomic shear strain higher than 0.2 are shown. Nanopillars are deformed at 4×10^{7} s^{-1}. *a* represents the maximum surface roughness in rough nanopillars.

The results clearly show that there is a transition from SB to necking with increasing surface roughness (for fixed d) or decreasing d (for fixed roughness amplitude). The dependence of the transition on both the surface roughness and the nanopillar diameter suggests that there may well be a combination of these parameters which is key, e.g., a ratio d/a. Interestingly, we observe from figs. 3-7, 3-11 and 3-12 that the threshold $\left(\frac{d}{a}\right)_t$ for the transition in failure behavior consistently falls in the range $0.04 \leq d/a \leq 0.05$. Essentially, over the range of d/a ratios that we considered for this scenario, the conclusion of SB-necking transition is consistent with that of the single-notched specimen results. A noteworthy feature of the present results is that the roughness-induced transition at $\left(\frac{d}{a}\right)_t \sim 0.04$ applies equally well to "smooth" specimens where the roughness is only associated with the discreteness of the amorphous atomic structure, $a \sim 0.2$ nm (Fig. 3-7a-f). Based on this latter observation, we should expect a SB-induced brittle failure at any diameter if the surface roughness could theoretically be completely eliminated (i.e., $a \approx 0$ nm). Indeed, the former seems to be the case as revealed by recent MD simulations of MG specimens prepared by "simulated casting", which fail via catastrophic shear under tensile loading even for $d < 5$ nm (Shi, 2010). Likewise, one should expect necking behavior $d/a \geq \left(\frac{d}{a}\right)_t$, which is indeed observed in experiments on macro-scale specimens (Qu et al., 2013; Wang et al., 2013). The existence of a critical value of the roughness ratio therefore explains a diversity of experimental and simulation results in nano-scale and beyond.

3.7 Summary

The primary objective of this chapter was to report the investigation of the mechanical properties and deformation mechanisms of MGs in the nanoscale via MD simulations. The effect of different nanoscale factors, such as nanopillar diameter, aspect ratio, applied strain rate, as well as surface imperfection were investigated. The results show evidence for a transition in MG failure mode with the applying strain rate. At low strain rates, irreversible deformation of the nanopillars is generated at the yield point by nucleation and propagation of one dominant SB. On the other hand, at high strain rates the failure occurs by formation of multiple shear banding and necking along the nanopillars. MG nanopillars with larger aspect ratio fail at smaller strains while those with smaller aspect ratio fail at larger total strain. A possible explanation is that, longer nanopillars can store more elastic energy for a given strain, while the elastically stored energy in small nanopillar volumes does not match the energy required to expand the area of an SB traversing the nanopillar. Simulations with defect free nanopillars with diameter in the range of 10 nm to 100 nm show essentially the same stress-strain curves, plastic behaviour, and failure implying no relevant diameter effects. However, experiments show a BDT on size reduction on MG nanopillars. Results for nanopillars with smooth surface show brittle failure by SB propagation. On the other hand, nanopillars with a 1 nm U-shape notch along its circumference have a BDT transition. We further found that the BDT crossover characteristic size can be tuned by adjusting the dimension of the surface notch. For CuZr MG nanopillars, as long as the ratio of nanopillar diameter to notch depth is equal or less than 25, we observed necking. For larger ratios, localization of SB is the failure mode. This is related

to the competition between the hydrostatic stress and von Mises stress in the vicinity of the notch. For $d/a < 25$, the triaxiality peak magnitude increased to ~1 and shifted closer to the nanopillar center between the notch roots. The increase in the triaxiality lead to the hydrostatic stress and correspondingly voids growth. This, in turn, induced necking in the nanopillars. Our results indicate the experimentally reported transition of failure mode in MG nanopillars from SB to necking is intrinsically linked to surface imperfections. That is, the nanopillars surface imperfections induce necking below a certain diameter dictated by the magnitude of the surface imperfection.

Part III

NANOGLASSES

4. Nanoglasses: Novel Metallic Glass Microarchitectures with Large Tensile Ductility

4.1 Background

As mentioned in Chapter 1, a possible route to mitigate catastrophic failure of MGs by shear banding is to incorporate a dense network of amorphous interfaces with mean spacing between interfaces in the nanometer scale range (Adibi et al., 2013; Albe et al., 2013; Gleiter, 2008; Ritter et al., 2011; Şopu et al., 2009). Such architecture would topologically resemble a conventional polycrystalline microstructure, except that the grains and interfaces are both amorphous. We refer to it as *nanoglass* (NG), which comprises *glassy grains* separated by *glass/glass interfaces (GGI)*. To enable a systematic design approach toward engineered NG architectures for strength and ductility, an in-depth understanding of the effect of glassy grain size and the GGIs on the mechanical properties of NG is necessary. It is also reasonable to postulate that

apart from grain size, the properties of NGs will depend on the composition and processing conditions.

In this chapter, we investigate the effect of the glassy grain size (d_g) on the mechanical characteristics of NGs by performing systematic MD simulations on $Cu_{64}Zr_{36}$, $Cu_{50}Zr_{50}$ and $Cu_{36}Zr_{64}$ NG samples under uniaxial tensile-loading. We analyse the role GGIs play in mediating the deformation mechanisms by investigating in detail the evolution of their internal structures. In particular, we address the statistics of atomic VPs at grains and GGI, GGI thickness, and the fraction of the bulk and interfacial regions as a function of NG composition and grain size. For each composition, d_g is the control parameter and is systematically varied between 3 to 15 nm.

4.2 Methods

MG and NG samples of $Cu_{64}Zr_{36}$, $Cu_{50}Zr_{50}$ and $Cu_{36}Zr_{64}$ compositions are generated in a thin system geometry with dimensions of ~ 5.4 nm × 54 nm ×135 nm in the *x*-, *y*- and *z*-directions, respectively, resulting in approximately 2.4 million atoms per simulation cell. MD simulation set up and the interatomic potential used in the simulations are the same as that described in section 2.3.

4.2.1 Constructing NG Systems

The NG samples are constructed using the Poisson-Voronoi tessellation method (Brostow et al., 1978; Finney, 1979; Tanemura et al., 1983). For a given composition, individual NG grains are generated from the corresponding

original MG structure. [7] In constructing the MG samples, the same method as the one explained in section 3.2.1 is employed. However, it should be noted that the T_g for MGs is composition-dependent and for our systems using the current interatomic potential the value of T_g is; 800 K for $Cu_{64}Zr_{36}$, 670 K for $Cu_{50}Zr_{50}$, and 600 K for $Cu_{36}Zr_{64}$. These values are in good agreement with experimentally reported values for CuZr MG (Cheng et al., 2008a; Duan et al., 2005). Fig. 4-1 shows a schematic of the procedure to generate the MG and NG samples. As we can see in Fig. 4-1a, in the generation procedure, an MG system is used to generate an NG system of identical dimensions. Grains in the NG sample are filled up with the corresponding volume of material of the MG system. To produce interfaces in the NG sample, all atoms in the original periodic MG system are translated by applying a random shift to atomic positions after each grain is filled up. To avoid overlapping of atoms at interfaces grains are filled up till 1 Å from the mathematically defined interfaces. In addition, after the NG sample is produced atoms in interfaces are removed to ensure that no pair of atoms is closer than 2.2 Å, based on the fact that in CuZr MG bulk structure the average nearest neighbour distances are Cu-

[7] Using MD simulation two main methods can be used to produce nanostructured samples. One may generate spherical like grains and produce a final microstructure by applying temperature, pressure and running the simulation until the system is fully densified, and porosity is mostly eliminated (simulated sintering). Typically, that is a very time consuming procedure required several ns of run time. Alternatively, one may generate a final microstructure with the same average grain size using the Poisson-Voronoi tessellation method. In essence, both methods should generate similar structures even though the latter is much less time consuming. The final microstructure generated in both methods is expected to have plain interfaces between grains and sharp triple junctions if the samples are fully densified and porosity is residual. That is the reason we used in this work the Poisson-Voronoi method.

Cu 2.7 Å, Cu-Zr 3 Å, and Zr-Zr 3.1 Å. Subsequently, the NG architectures are sintered by applying an external hydrostatic pressure of 3 GPa at 50 K for 0.04 ns in order to relax the atomic structure of the GGIs and minimize the initial porosity. The sintering is followed by relaxation of the system at zero pressure and 50 K for 0.04 ns. Because of the thin sample geometry, we adopt a two-dimensional grain structure. Therefore, all grains are columnar along the sample short dimension, that is, *x* direction. For all the cases, traction-free surface condition is imposed in the *y* direction to allow surface effects, e.g. generations and evolution of surface defects and shear offset (Cao et al., 2009). Free surfaces in the MG and NG samples are relaxed using Langevin dynamics for 0.02 ns.

As it is shown in Fig. 4-1b, an independent NG sample with two grains, is constructed from an MG system of dimensions 5.4 (*x*) ×10.8 (*y*) × 102.6 (*z*) nm^3 using a similar procedure as described above. However, the replication process is explicitly avoided to improve the statistics of the structural analysis. The two-grain NG system is designed to investigate in detail the structure of the NG interfacial region.

Figs 4-2a-e show the Voronoi-tessellated architectures of NGs with d_g = 15, 10, 7.5, 5 and 3 nm, respectively. Fig. 4-2f illustrates the two-grain NG system. Different grains in the NGs are shown in different colours to highlight the nanostructures at different average grain sizes.

All samples are simulated under uniaxial tensile stress at the strain rate of 4×10^7 s^{-1}. PBCs are imposed in the *z*-direction (the loading direction), and

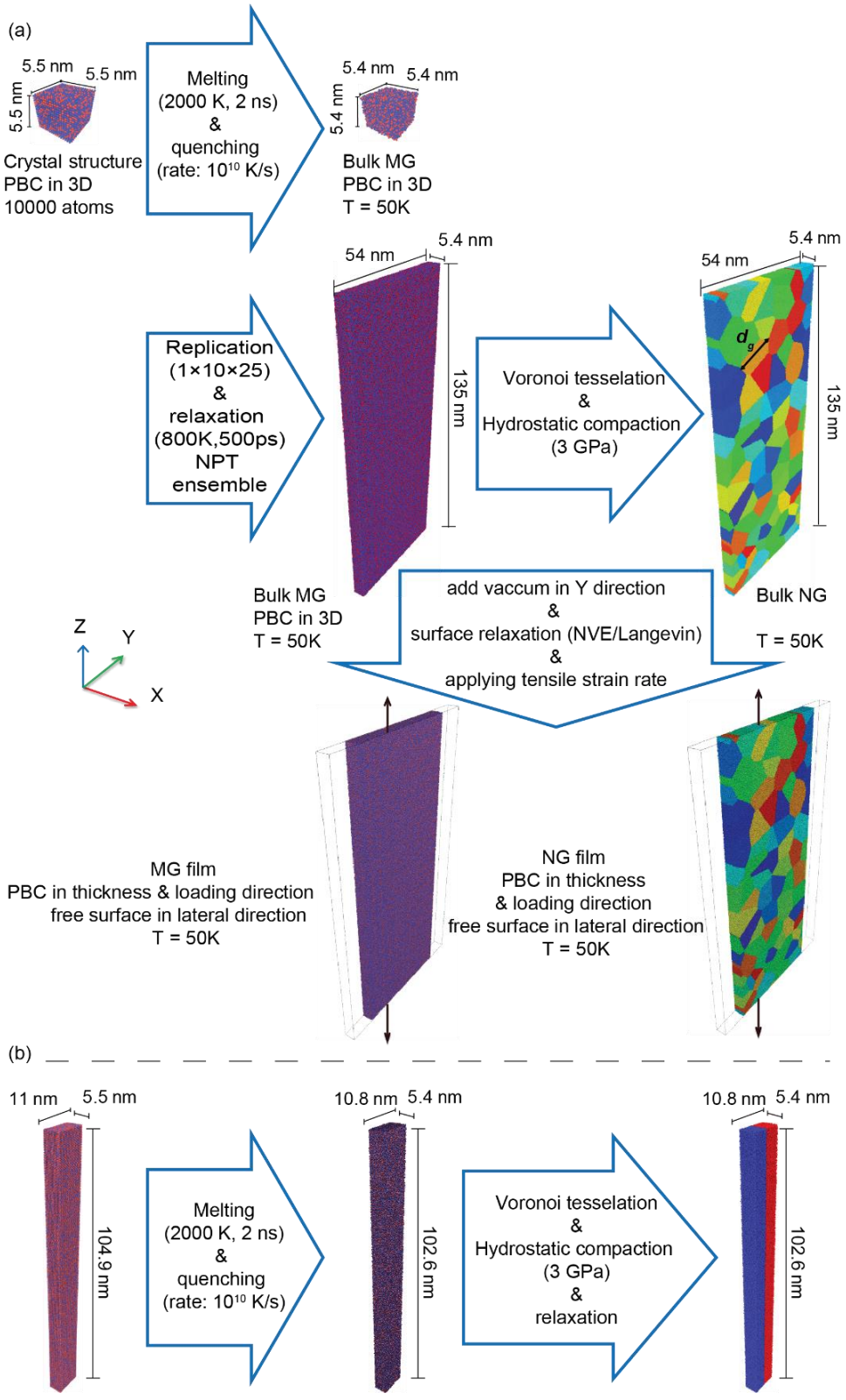

Figure 4-1 Schematic of the process to generate a NG specimens. (a) Schematic of the process to generate a NG films with different columnar grain sizes. (b) Schematic of the process to generate controlled NG system, NG film with two planar grains separated by a single grain boundary.

along the sample short dimension (*x*- direction), while free surfaces are used in the *y*-direction. During the loading, the temperature is maintained at 50 K and a zero stress condition is maintained along the *x*-direction to ensure uniaxial stress condition. Engineering stress is calculated as the average atomic stress in the system based on the Virial stress definition using the initial volume of the system (Branicio and Srolovitz, 2009).

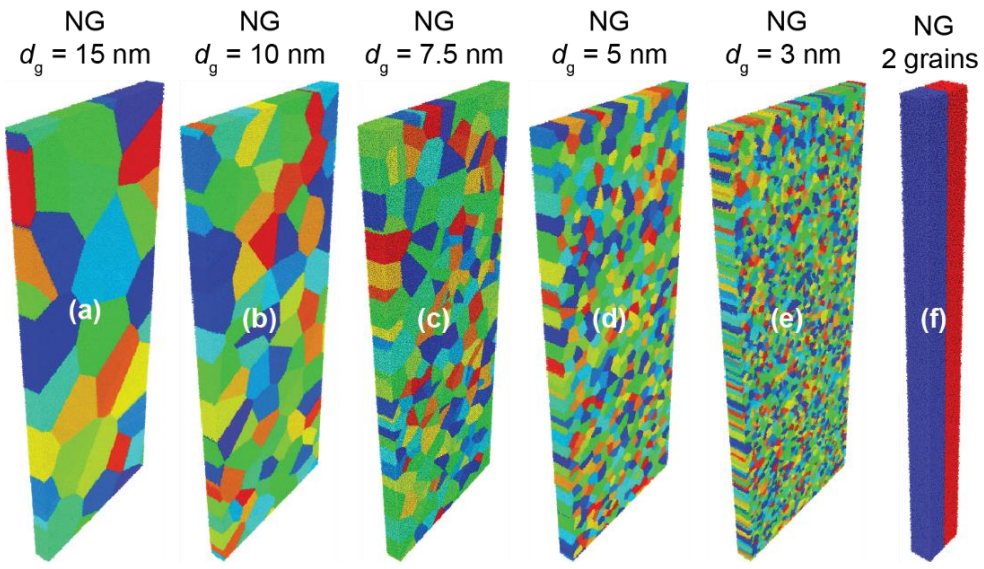

Figure 4-2 NG structures investigated. (a)-(e) represent the atomic configurations of NGs with average grain sizes d_g = 15, 10, 7.5, 5 and 3 nm. (f) NG model with two grains used to investigate interfacial properties. Grains are shown in different colours to highlight the nanostructure.

4.3 Grain Size Effect

We choose $Cu_{64}Zr_{36}$ glass as a model system, and consider multiple NG architectures with the grain sizes in the range d_g ~ 3 to 15 nm, (cf. figs 4-1a-e). We compare the behaviours of NG architectures with its conventional MG counterpart.

Fig. 4-3 depicts the tensile engineering stress-strain curves for the NG specimens together with the MG specimen. It can be seen that beyond initial

linear elastic responses, all the specimens exhibit non-linear behaviour before reaching the peak strengths. Note that the NG peak strengths are lower than the MG and are a function of the grain size (Fig. 4-3 inset). For MG, a sharp drop in stress occurs immediately upon reaching the strength of the material (peak stress), which corresponds to a rapid localization of plastic strain into a single dominant SB (Cao et al., 2009; Falk and Langer, 1998). Akin to this, the NG with d_g = 15 nm and d_g = 10 nm architectures also exhibit a significant stress drop indicating SB formation, albeit from lower peaks compared to the MG and also at a somewhat slower rate. However, the scenario changes appreciably for NG with d_g = 5 nm and d_g = 3 nm. In NG with d_g = 5 nm the deformation induced stress softening resulting in a stress drop, which is smooth rather than abrupt. For NG with d_g = 3 nm, the stress drop essentially disappears and the specimen carries a macroscopic strain over 0.4 with no indication of failure during the course of the simulation. In other words, NGs exhibit a dramatic transition from localized shear banding to extended ductile behaviour, typical of superplasticity, (Zhang et al., 2013) which is intimately tied to the glassy grain size d_g.

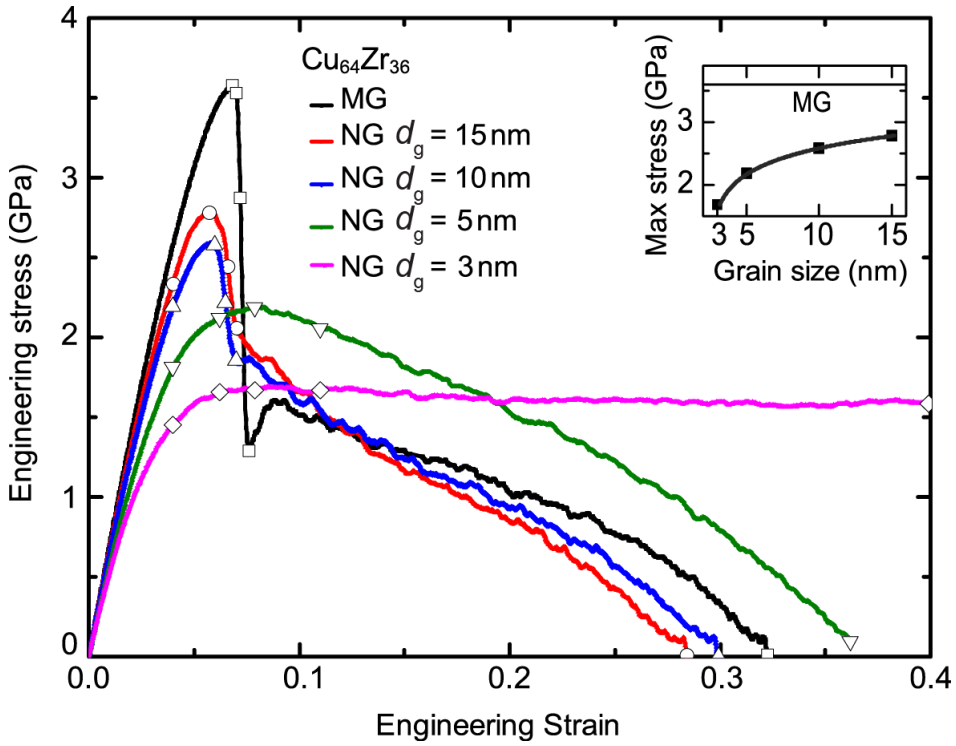

Figure 4-3 Engineering tensile stress-strain curves for NG with d_g = 15, 10, 5 and 3 nm, as well as for the MG. A drastic change in the mechanical response of NG (from localized shear banding to homogeneous plastic deformation failure) is observed by decreasing d from 15 to 3 nm. The large strain (> 0.4) attained by d_g = 3 nm NG indicates superplasticity. The symbols making the strains in each stress−strain curve correspond to the snapshots shown

To understand this transition, we probe the atomic-scale deformation processes by examining the atomic local shear strain η^{Mises} for each atom, (Li, 2003; Shimizu et al., 2007) with respect to the relaxed samples prior to the tensile loading. The presence of regions with relatively large atomic shear strain η^{Mises} imply that they have undergone large localized shear strain and host a high density of STZs (Cao et al., 2009). Fig. 4-4 shows a sequence of snapshots that capture the deformation process for the MG and NG. The nominal strains indicated in the snapshots are marked in each corresponding stress−strain curve, as shown in Fig. 4-2. For the MG specimen (Fig. 4-4a), several embryonic regions with high η^{Mises} emerge. We refer to such a well-defined region with

high local shear strain as a shear transformation zone cluster, or shear cluster (SC) for short. But the deformation in MG quickly localizes into a single dominant SB that propagates rapidly across the sample, ultimately causing the failure of the material. The SB propagation follows the direction of maximum shear stress, which is ~ 45^0 relative to the loading axis.

In contrast to the MG where only a single SB dominates the entire plasticity landscape, for the NG it can be seen from the strain motifs in figs 4-4b-c that at the onset of loading, multiple conjugate SBs initiate and decorate the GGIs. For NG with d_g = 10 nm and d_g = 15 nm (figs 4-4b-c), SCs are primarily activated in the softer GGIs, which is consistent with previous MD simulation results (Şopu et al., 2011a). Consistent with this behaviour, the macroscopic stress drop in NG with d_g = 10 nm and d_g = 15 nm beyond the peak stress is less abrupt compared to the MG case. We note that more SBs are formed in the NG with d_g = 10 nm sample compared to the NG with d_g = 15 nm, which clearly highlights the role of GGI fraction. In both samples, at strain of ~ 0.07, a single SB from the network of SBs develops into a mature predominant SB and as a result, the other SBs do not participate in the plasticity process, leading to a continuous drop in the stress and strain localization albeit in a relatively graceful manner compared to the MG case. Again, the importance of grain size is demonstrated in this strain localization with the NG with d_g = 10 nm architecture exhibiting delayed localization compared to NG with d_g = 15 nm. Indeed, the abrupt drop is smaller for smaller d_g and does not exist at all for $d_g \leq$ 5 nm. A salient feature of these results is that although localization ultimately occurs by propagation of a single, dominant SB across the specimen

through the coalescence of aligned SCs, the occurrence of SB is delayed with decreasing d_g. Further, one observes that the SB tends to be more diffused at smaller d (see e.g. Fig. 4-4d). These figures clearly show that density of SCs is higher for smaller d_g, which corroborates with the higher density of interfaces for the former compared to the latter.

The scenario changes dramatically for the NG with d_g = 3 nm architecture, as shown in Fig. 4-4e. At this grain size, the plastic strain is no longer localized into a single, dominant SB at finite strains. Instead, we observe a colossal network of tiny SBs that decorate GGI regions, indicating that interfacial plasticity is the governing mechanism. While we made a similar observation in the preceding paragraph for larger grain sizes where distributed interfacial plasticity occurred at incipient stages, the remarkable feature here is that the interfacial plasticity is sustained even at large strains. This feature combined with dense distribution of GGIs effectively produces a scenario that mimics homogeneous macroscopic plasticity. Note that even at $\varepsilon > 0.39$ the local effective plastic strains are nearly the same as the applied macroscopic strain. These results explain the nearly constant flow stress observed in Fig. 4-4e for the NGs with the finest grain size.

The result in Fig. 4-4e and the corresponding stress-strain response raise an important question: what is the reason for this grain size-dependent transition from a single dominant SB induced macroscopic softening to superplastic behaviour characterized by nearly homogeneous plasticity? The change in failure modes from brittle to ductile on size reduction was previously understood by considering the competition between localized shear-banding

(brittle fracture) versus homogeneous plastic deformation (cavitation instability) by (Jang and Greer, 2010). However, in our case it is more instructive to consider the deformation and failure in terms of collective operation of SCs, which are the primary carriers of plasticity. It will be shown in section 4.5 that the lower FI fraction results in softer GGIs, which consequently, have a greater propensity to produce an SC and induce plasticity.

It is known that the temporal and spatial correlations of STZs determine the deformation mode in MG (Schuh et al., 2007). In NG with d_g = 15 nm and d_g = 10 nm, although STZs tend to nucleate initially in several GGIs the grain size is large enough to render a weak interaction between them. As a result, the initially developed primary SB continues to dominate the plasticity and effectively halts the development of other SBs. In contrast, in NG with d_g = 3 nm case, the large number of distributed STZs nucleated at GGIs not only remain active as deformation progresses, but new STZs appear, creating an increasingly denser STZs network, as shown in Fig. 4-4e. This indicates that for $Cu_{64}Zr_{36}$, $d_g < 5$ nm is the characteristic length-scale over which the GGIs can interact in a manner such that existing SBs trigger the development of new SBs. In turn, it suggests that over this length scale, STZs in one SB may act cooperatively to trigger STZs in nearby regions (Joshi and Ramesh, 2008; Pan et al., 2008).

At the end of the elastic regime, STZs are activated only in the GGIs. When the tensile loading is further increased, STZs become widespread, indicative of a structural change that occurs both in the soft GGIs as well as in the relatively harder glassy grains. This is distinct from the NG with d_g = 10 nm and d_g = 15

nm architectures, where the structural changes occur only in the GGIs, as shown in figs 4-4b-c.

The driving force for SB propagation is the stored elastic energy (Magagnosc et al., 2013; Nakayama et al., 2010). For NG with d_g = 3 nm, the stored energy is dissipated into the activation and formation of a large number of homogeneously distributed SBs rather than into a localized single SB as in the NG with d_g = 10 nm, d_g = 15 nm and MG scenarios. The homogeneous energy released prevents the drive of an SB propagation. Consequently, NG with d_g = 3 nm deforms homogeneously in contrast to NG with d_g = 10 nm, d_g = 15 nm as well as MG, which all exhibit localized deformation via one major SB propagation.

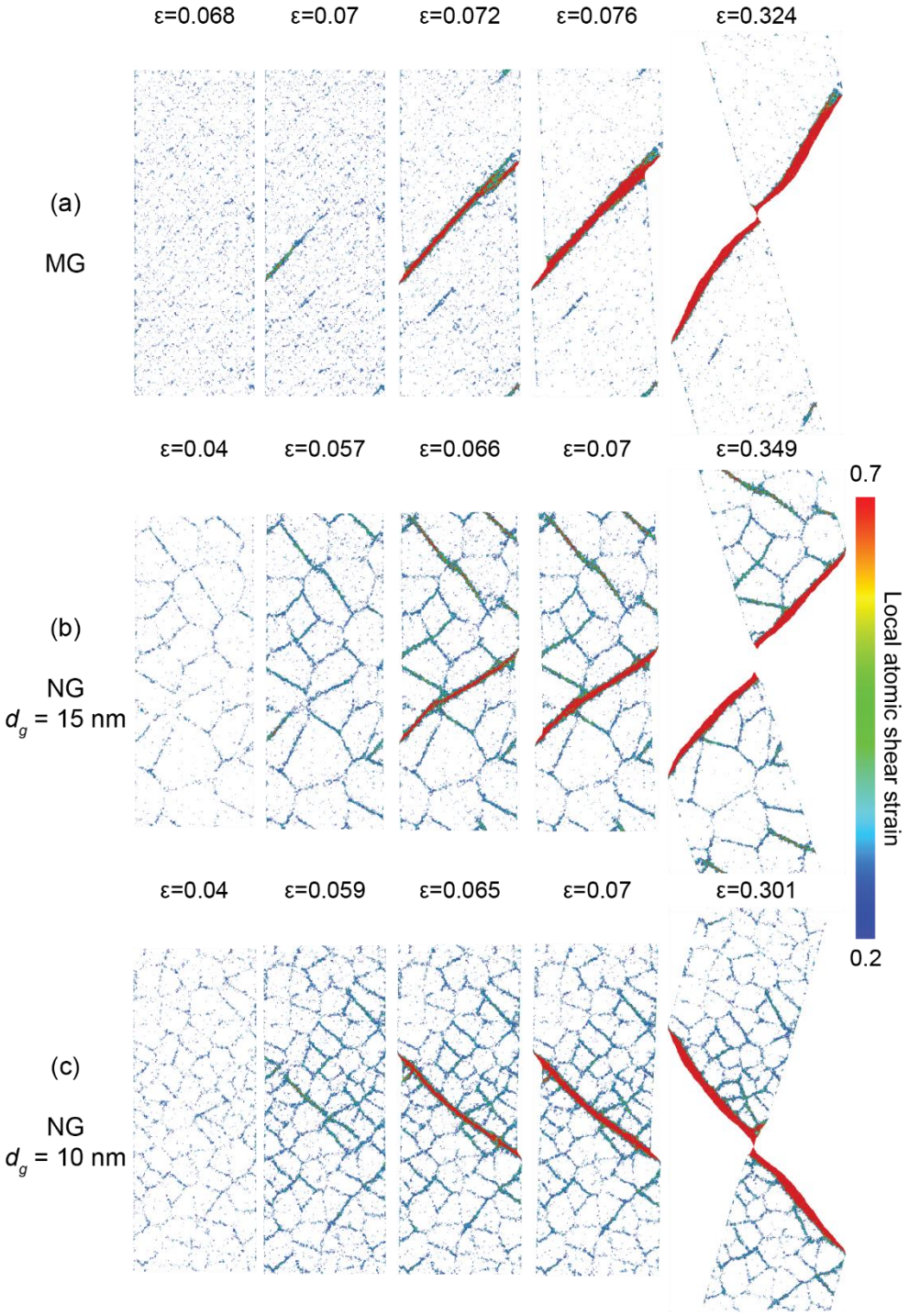

Figure 4-4 Illustrations of the deformation process for the different structures investigated. (a)–(e) Sequence of snapshots capturing the atomic deformation processes for the $Cu_{64}Zr_{36}$ MG and NGs with d_g =15, 10, 5 and 3 nm, respectively. The colours indicate the atomic shear strain. The change in the deformation mode from highly localized shear banding to fully homogeneous plastic flow is clearly observed. For clarity, the atoms with local atomic strain smaller than a criterion value (0.2) are not shown.(continued)

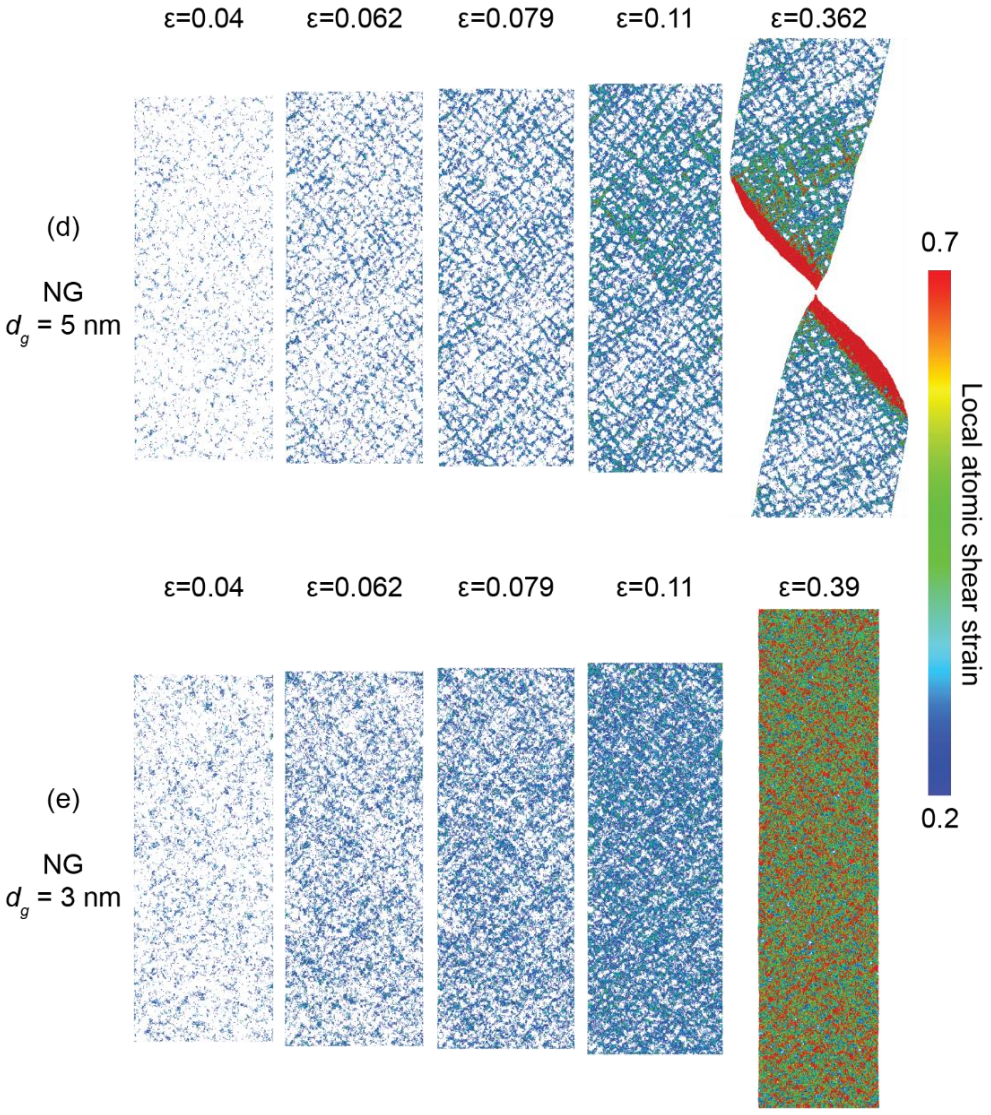

Figure 4-4 Illustrations of the deformation process for the different structures investigated. (a)–(e) Sequence of snapshots capturing the atomic deformation processes for the $Cu_{64}Zr_{36}$ MG and NGs with d_g =15, 10, 5 and 3 nm, respectively. The colours indicate the atomic shear strain. The change in the deformation mode from highly localized shear banding to fully homogeneous plastic flow is clearly observed. For clarity, the atoms with local atomic strain smaller than a criterion value (0.2) are not shown.

4.4 Composition Effect

In this section, we compare simulation results of MG and NG samples composed of $Cu_{36}Zr_{64}$ and $Cu_{50}Zr_{50}$ to those composed of $Cu_{64}Zr_{36}$, which are discussed in the previous section. Preliminary results for the $Cu_{50}Zr_{50}$ case were

recently published (Adibi et al., 2013). For each composition, we consider NGs with average grain size (d_g) ranging from 3 to 15 nm (see Fig. 4-2).

Fig. 4-5 shows the overall engineering stress- engineering strain curves of $Cu_{36}Zr_{64}$ and $Cu_{50}Zr_{50}$ MGs and NGs. As expected, the peak stress (yield stress) for $Cu_{64}Zr_{36}$ MG is higher than the $Cu_{50}Zr_{50}$ MG and both are higher than $Cu_{36}Zr_{64}$ MG. In all cases, the MG stress-strain responses exhibit a large stress drop at $\varepsilon \sim 0.07$, which indicates severe localization of the plastic strain. The stress drop is larger for the $Cu_{64}Zr_{36}$ MG compared to the $Cu_{50}Zr_{50}$ and both are larger than $Cu_{36}Zr_{64}$ MG, denoting that the Cu-rich compositions are inherently more brittle than those which are Zr-rich (Cheng et al., 2008a).

In comparison to the MGs, in all compositions the NGs possess lower yield strengths. Importantly, the yield strength decreases with decreasing grain size as shown in the insets in Fig. 4-3 and Fig. 4-5. As in the case of MGs, for a given d_g, the yield stress of the $Cu_{64}Zr_{36}$ NG is higher than the $Cu_{50}Zr_{50}$ NG and both are higher than $Cu_{36}Zr_{64}$ NG. Further, for all three cases, NGs with d_g = 10 nm and 15 nm also exhibit stress drop, albeit much smaller compared to their MGs. However, the scenario changes dramatically for $d_g < 10$ nm, for the $Cu_{36}Zr_{64}$ NG with d_g =7.5 nm the deformation-induced stress softening beyond initial yield is smooth rather than abrupt, while the same situation occurs at d_g = 5 nm for the $Cu_{64}Zr_{36}$ NG and $Cu_{50}Zr_{50}$ NG. This is likely due to the inherently brittle nature of Cu-rich compositions.

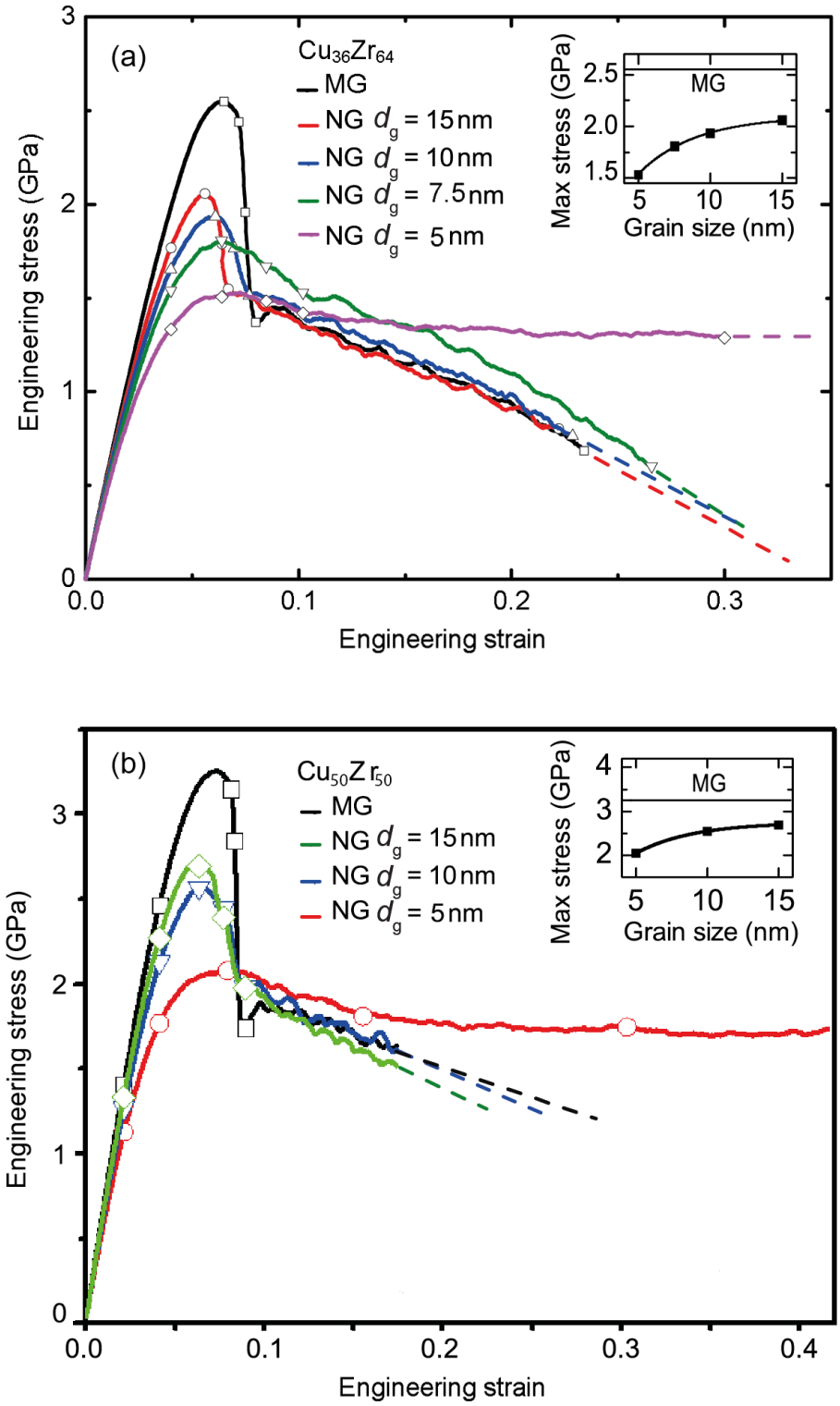

Figure 4-5 Engineering tensile stress vs. strain curves for MG and NG in two compositions. (a) Stress-strain curves for $Cu_{36}Zr_{64}$ MG and NGs with d_g = 15, 10, 7.5 and 5 nm, (b) Stress-strain curves for $Cu_{50}Zr_{50}$ MG and NGs with d_g =15, 10 and 5 nm. The dashed lines indicate the expected continuation of the stress-strain curves (not simulated).

With further decrease in the grain size (at $d_g = 5$ nm for $Cu_{36}Zr_{64}$ and $Cu_{50}Zr_{50}$ and $d_g = 3$ nm for $Cu_{64}Zr_{36}$), the stress drop practically vanishes and instead, the NGs exhibit stable plastic flow up to large strains with no signature of localization. Thus, the macroscopic stress-strain characteristics for a given composition exhibit a clear transition from brittle to ductile response with decreasing grain size. Therefore, the critical average grain size for this transition depends on composition: 5 nm for $Cu_{36}Zr_{64}$ and $Cu_{50}Zr_{50}$ and 3 nm for $Cu_{64}Zr_{36}$. The flow stress of the superplastic NG at different compositions follows the trend of the yield stress of the parent MG, i.e. $Cu_{36}Zr_{64}$ yield/flow stress: 2.54 GPa/1.29 GPa, $Cu_{50}Zr_{50}$ yield/flow stress: 3.25 GPa/1.45 and $Cu_{64}Zr_{36}$ yield/flow stress: 3.57 GPa /1.58 GPa.

Fig. 4-6 and Fig. 4-4 show snapshots of the atomic deformation process for the MG and NGs with compositions $Cu_{36}Zr_{64}$ and $Cu_{64}Zr_{36}$, respectively. In both cases, the MGs fail by the development of an SC, which culminates into an SB that propagates across the whole system. In contrast to the MGs, in NGs with d_g ranging between 7.5 - 15 nm for $Cu_{36}Zr_{64}$ (Figs 4-6b-d) and between 5 - 15 nm for $Cu_{64}Zr_{36}$ (Figs 4-4b-d), multiple SCs are activated and they are primarily located in the GGIs. The generation of deformation-induced SC networks that superpose on to the initial GGI motifs results in a more graceful stress softening beyond yield in NGs (Fig. 4-5 and Fig. 4-3). Indeed, the abrupt drop is smaller for smaller d_g and does not exist at all for $d_g \leq 7.5$ nm for $Cu_{36}Zr_{64}$ and $d_g \leq 5$ nm for $Cu_{50}Zr_{50}$ and $Cu_{64}Zr_{36}$. Further, one observes that the SB tends to be more diffused at smaller d_g (see e.g. Fig. 4-6d and Fig. 4-4d). Although not shown here, a similar situation occurs for $Cu_{50}Zr_{50}$ NG as well over a similar

grain size range (Adibi et al., 2013). These figures clearly show that density of SCs is higher for smaller d_g, which corroborates with the higher density of GGIs for the former compared to the latter. The scenario is dramatically different for $d_g = 5$ nm for $Cu_{36}Zr_{64}$ (Fig. 4-6e) and $d_g = 3$ nm for $Cu_{64}Zr_{36}$ (Fig. 4-4e). At these grain sizes, the plastic strain is no longer localized into a single, dominant SB at finite strain. Instead, we observe a homogeneous network of SCs that decorate GGI regions resulting in large macroscopic plasticity in the form of homogeneous flow, a characteristic signature of superplastic behaviour (Zhang et al., 2013).

Therefore, our results reveal a drastic change in deformation mode from a single SB (d_g ~ 15 – 10 nm), to cooperative shear failure (d_g ~ 10 - 5 nm), to homogeneous superplastic flow ($d_g \leq 5$ nm) for all CuZr compositions. Thus, the results suggest that the composition dependence of the mechanical behaviour of NGs follows that of their parent MGs, e.g. a stronger MG will generate a stronger NG, while the intrinsic tendency for homogeneous deformation occurring at small grain size is not affected by composition.

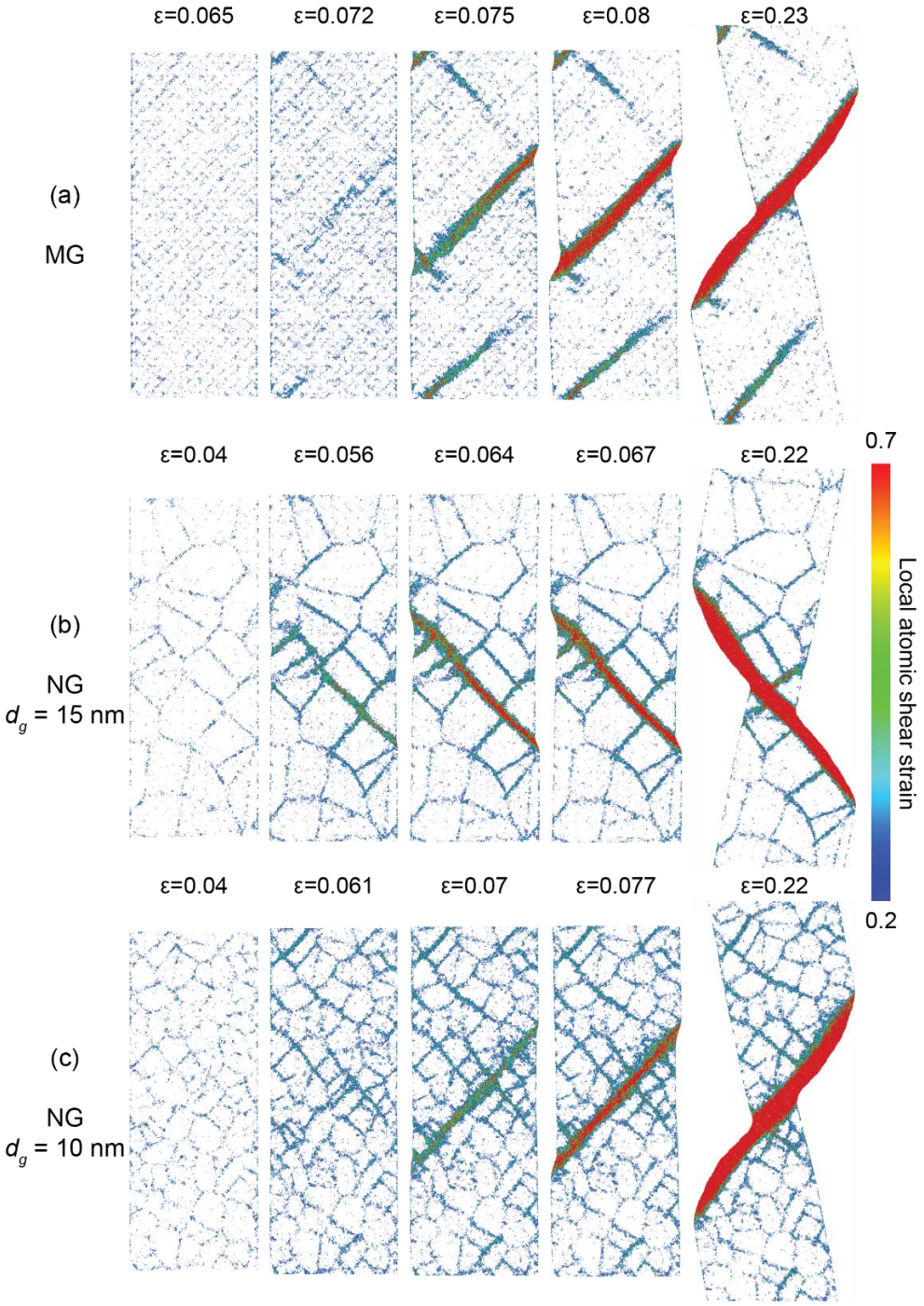

Figure 4-6 Illustrations of the deformation process for the different structures investigated. (a)–(e) Sequence of snapshots capturing the atomic deformation processes for the $Cu_{36}Zr_{64}$ MG and NGs with d_g = 15, 10, 7.5 and 5 nm, respectively. The colours indicate the atomic shear strain. The change in the deformation mode from highly localized shear banding to fully homogeneous plastic flow is clearly observed. (continued)

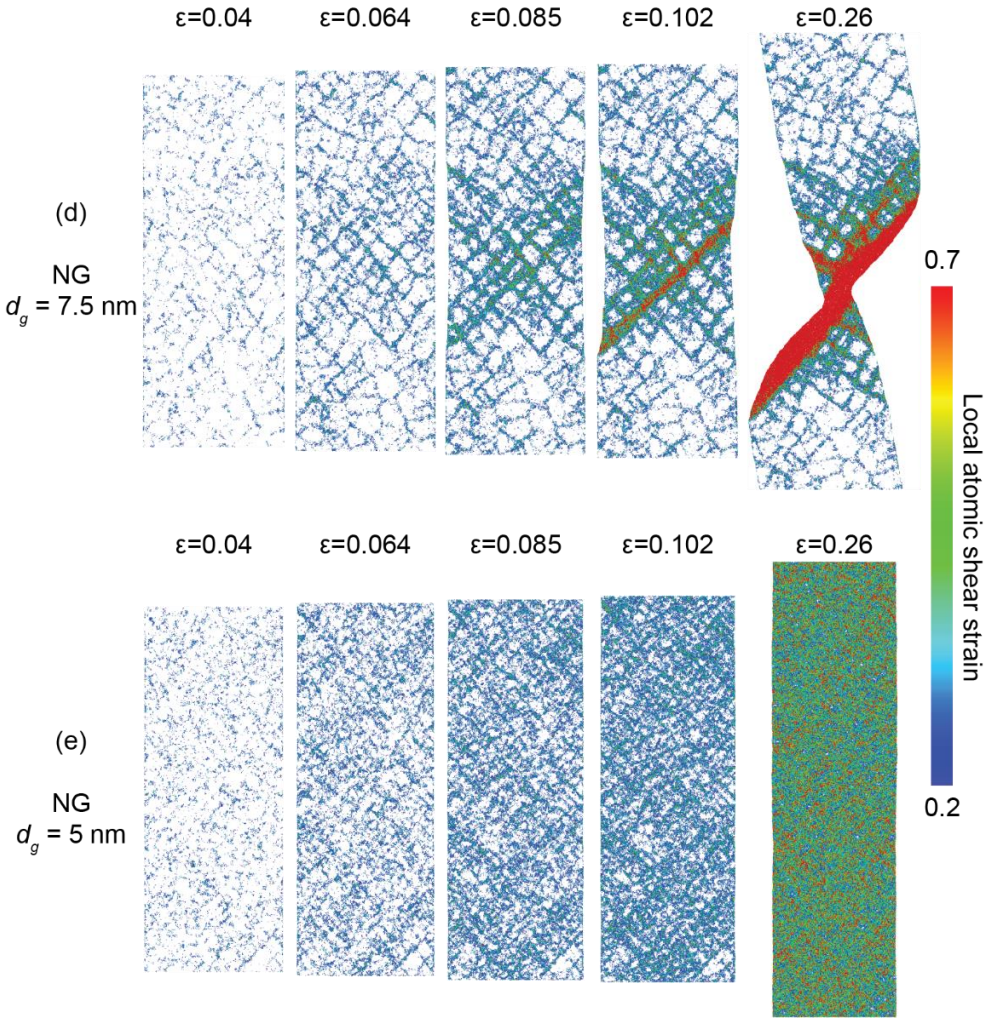

Figure 4-6 Illustrations of the deformation process for the different structures investigated. (a)–(e) Sequence of snapshots capturing the atomic deformation processes for the $Cu_{36}Zr_{64}$ MG and NGs with d_g = 15, 10, 7.5 and 5 nm, respectively. The colours indicate the atomic shear strain. The change in the deformation mode from highly localized shear banding to fully homogeneous plastic flow is clearly observed.

4.5 Structural Characterization

The foregoing results clearly demonstrate that the presence of GGIs in NGs makes their response significantly different from their conventional MG counterparts. Since both bulk and interfacial regions have an amorphous structure, it is essential to characterize the underlying differences in their amorphous atomic bond topologies. A convenient and accurate way to characterize such amorphous structures is by performing a Voronoi tessellation

of the local structure around each atom. A complete characterization of the GGI structure should include an analysis of the atomic VP structures, local density, and so forth. Here, we adopt a simplified NG system, composed of two grains separated by a single flat GB (Fig. 4-2f), referred to hereafter as the controlled NG system. The reason behind adopting this model in lieu of the numerous GGIs in the NG systems is that the large and well-defined GGI enables the calculation of the statistics of atomic Voronoi volume and atomic VPs along the GGI with high accuracy. Furthermore, we do not expect the nature of GGIs in the two-grain model to be fundamentally different from those in the NGs.

Atomic Voronoi volume obtained by an appropriate averaging procedure provides an accurate measure of the local material density (Branicio and Srolovitz, 2009; Quillin and Matthews, 2000). A higher Voronoi volume in a given region indicates the presence of higher local free volume, which relates to a lower local material density in that region. To investigate possible modulation in the local density at the GGIs, we calculate the atomic Voronoi volume for all atoms in the controlled NG system and averaged it in the direction perpendicular to the GGI. Fig. 4-7a shows the average atomic Voronoi volumes across the system for the three compositions ($Cu_{36}Zr_{64}$, $Cu_{50}Zr_{50}$ and $Cu_{64}Zr_{36}$) before (dashed lines) and after (solid lines) relaxation at the GGI. In all the cases, the Voronoi volume at the GGI prior to relaxation is nearly 9-13% higher than the neighbouring bulk glassy region. The thickness of the unrelaxed GGI is about 0.8 nm and is independent of the composition. However, the Voronoi atomic volume of the relaxed systems (solid lines) indicates that the value at the NG interfaces deviates mildly from that of the bulk regions

(respectively, 0.6%, 0.7%, and 1.1% for $Cu_{36}Zr_{64,}$ $Cu_{50}Zr_{50}$ and $Cu_{64}Zr_{36,}$). Even though the differences in the local density at NG interfaces and bulk regions are small, they are very relevant to explain the mechanical properties of NGs.

It is instructive to compare the density at interfaces to that in a typical SB in an MG. Here, we define the atoms to be in an SB within an MG when their local atomic shear strain is higher than 0.3. This threshold value is defined according to the analysis of local atomic shear strain for atoms in the whole system. Fig. 4-7b shows a comparison of the average atomic Voronoi volumes in a relaxed NG interface, an NG grain, and an SB in an MG. The Voronoi volumes in an SB are about 1.2%, 1.5% and 2% higher compared to the grains in $Cu_{36}Zr_{64,}$ $Cu_{50}Zr_{50}$ and $Cu_{64}Zr_{36}$ compositions, respectively. Thus, these results indicate the value of free volume in NG interfaces is about half of that at SB.

Besides differences in local density, it is expected that the topology of the atomic bonds at NG interfaces will be distinct from the MG counterparts. Therefore, it is important to characterize the atomic structure at the NG interfaces and compare it to the structure of the MG. An accurate method to analyse the local atomic structure is to calculate the statistics of the atomic VP. The most prominent VPs have been reported for MGs at different compositions (Cheng et al., 2008a). In particular, the FI centered at Cu are reported to be the most important polyhedron for $Cu_{64}Zr_{36}$ (Ding et al., 2014). With decreasing Cu concentration, the FI has a decreasing presence in the structure (Cheng et al., 2008a). Using the controlled NG system, we evaluated the statistics of all possible polyhedra at the NG interfaces and within the grains for the three compositions. Fig. 4-8 shows the calculated percentage of the ten most

prominent polyhedra at the interfaces and grains of NGs in $Cu_{36}Zr_{64}$, $Cu_{50}Zr_{50}$ and $Cu_{64}Zr_{36}$ compositions. Four indexes are, in general, sufficient to describe all prominent VPs found in CuZr MG or NG. Based on the complete statistics of atomic VPs for CuZr MG with 8 indexes, we find that about 80% of them can be described with only 4 indexes. A common nomenclature for atomic Voronoi polyhedron in an MG, which was followed here, is given by: Cu $< i,j,k,l >$ which indicates that Cu is the central atom of the Voronoi polyhedron that has i faces with 3 edges, j faces with 4 edges, k faces with 5 edges, and l faces with 6 edges. An FI is a polyhedron with k =12 and $i = j = l = 0$ (Cheng et al., 2008a). Comparing figs 4-8a and b with c, we observe that the statistics of VPs for $Cu_{36}Zr_{64}$ and $Cu_{50}Zr_{50}$ are more homogeneous than those for the $Cu_{64}Zr_{36}$, as shown in Fig. 4-8c. It should be noted that Zr-rich compositions have a lower fraction of FI while a high number of five faces still dominate the statistics of most prominent polyhedra. For $Cu_{36}Zr_{64}$, the most prominent polyhedra are Zr<0,2,8,5>, Zr<0,2,8,4>, Cu<0,2,8,2>, Zr<0,1,10,4>, and Cu<0,2,8,2> while for $Cu_{50}Zr_{50}$, they are Cu<0,2,8,2>, Cu<0,0,12,0>, Zr<0,1,10,4>, Cu<0,2,8,1>, and Zr<0,2,8,5>. Similar to the FI, these VPs are characterized by a large number of pentagonal faces, which are indicative of dense atomic packing and arguably high shear resistance (Cheng et al., 2008a). In comparison, from Fig. 4-8c, one can see that the most prominent polyhedron for $Cu_{64}Zr_{36}$ MG is the FI (15.4%), with Voronoi index Cu<0,0,12,0>. We can see from figs 4-8a and b that the FI fraction is much lower in $Cu_{50}Zr_{50}$ MG (5.4%) and it is not even one of the ten most prominent polyhedra for $Cu_{36}Zr_{64}$ MG. These results agree with the previous reports on Voronoi statistics of CuZr MGs (Cheng et al., 2009a; Cheng et al., 2008a; Ritter et al., 2011). It is

instructive to analyse the atomic composition of the FI present at different CuZr compositions to understand why it is prevalent in $Cu_{64}Zr_{36}$ and not in other compositions with higher Zr content. Fig. 4-9a shows that FI in $Cu_{64}Zr_{36}$ has mostly two atomic compositions, i.e., 5 Zr and 7 Cu and 6 Zr and 6 Cu. Arguably, the formation of FI at these atomic compositions is more energetically favoured in CuZr MG. On the other hand, for $Cu_{50}Zr_{50}$ and $Cu_{36}Zr_{64}$, the fraction of FI with these two atomic compositions is significantly reduced due to the lower concentration of Cu in the alloy. For increasing Zr content, we noticed a clear shift in the FI atomic composition to a higher Zr fraction. That suggests the high concentration of Zr prevents the formation of the FI with the most energetically favoured atomic composition, which is present in $Cu_{64}Zr_{36}$. It is also interesting to evaluate the volume of FI as a function of the atomic composition. It can be seen in Fig. 4-9b that in all CuZr MG compositions, the volume of FI has roughly a linear relationship with the number of Zr atoms present in the composition of the FI. This is expected since the atomic mass of Zr, 91, is much larger than that of Cu, 63, which is reflected in the radius of each species in the EAM potential. One can also note that for a given atomic composition, the volume of FI is larger in Zr-rich CuZr compositions. The data shown in Fig. 4-9 therefore indicates that the strong FI encountered in $Cu_{64}Zr_{36}$ have mostly atomic compositions 5Zr-7Cu or 6Zr-6Cu and are compact with a volume under 15 $Å^3$.

From Fig. 4-8 it is clear that the fraction of the most prominent polyhedra is lower at the NG interface as compared to the MG (NG grain). This is expected since glass structure at the interfaces has an overall lower medium range structural order compared to the MG structure generated during the melting and

quenching process. The $Cu_{64}Zr_{36}$ case particularly exemplifies this scenario as the FI fraction drops from 15.4% to 9.2%. Nonetheless, figs 4-8a-b also show a bigger decrease in the most prominent polyhedra, resulting in a more homogeneous distribution of prominent polyhedra. This indicates a reduction in the structure order from MG to interface. It is worth highlighting that overall the structure at NG interfaces has a lower structural order compared to that of the MG, indicating the reasons for the weaker structure. The interfacial structure is clearly composition dependent and the polyhedra statistics of the interface in general follows that of the corresponding MG.

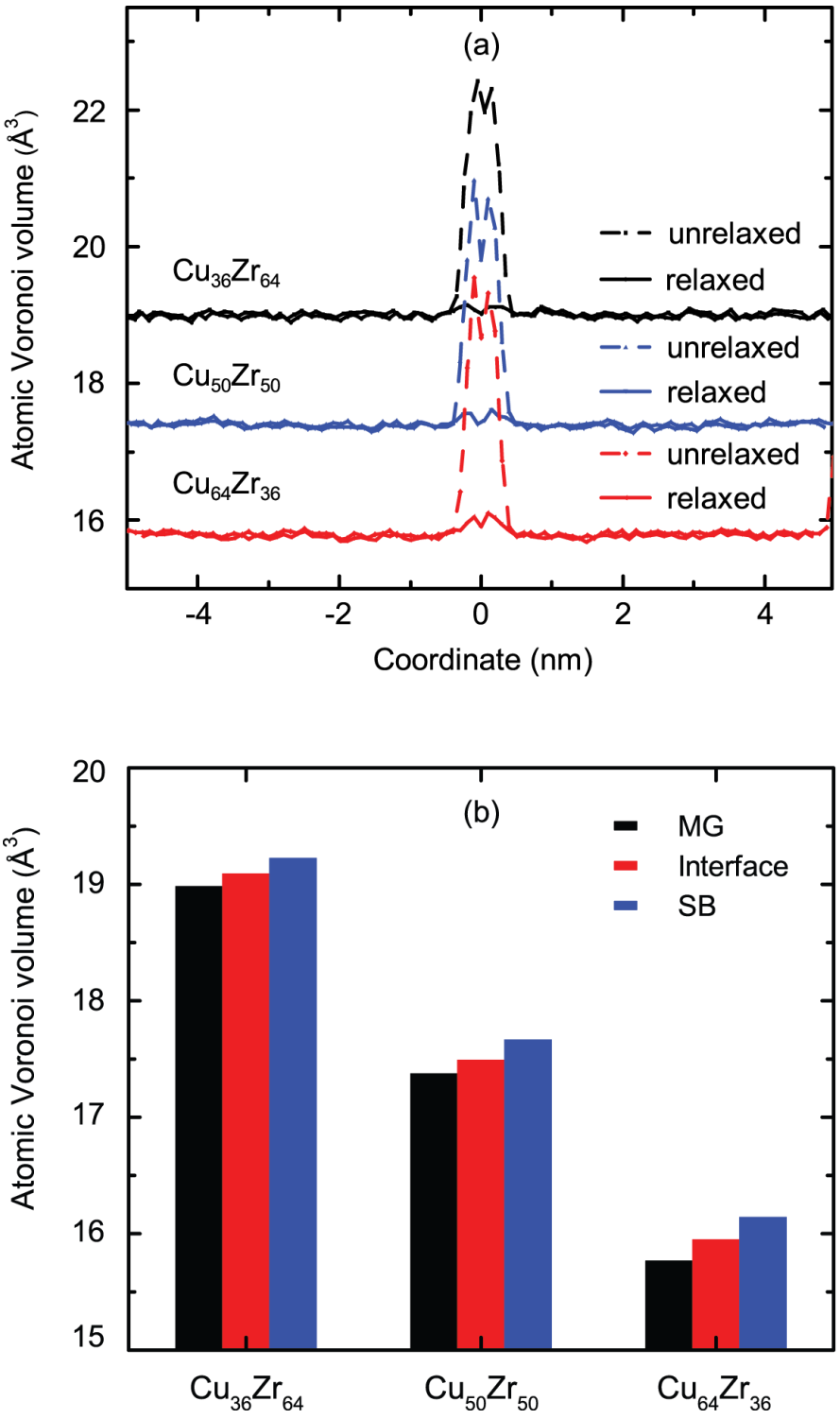

Figure 4-7 Atomic Voronoi volume in MG and NG. (a) Distribution of atomic Voronoi volume along the width of a two grains NG (in the direction perpendicular to the grain interface), (b) Comparison of atomic Voronoi volume in grain, interface, and shear band in three different compositions.

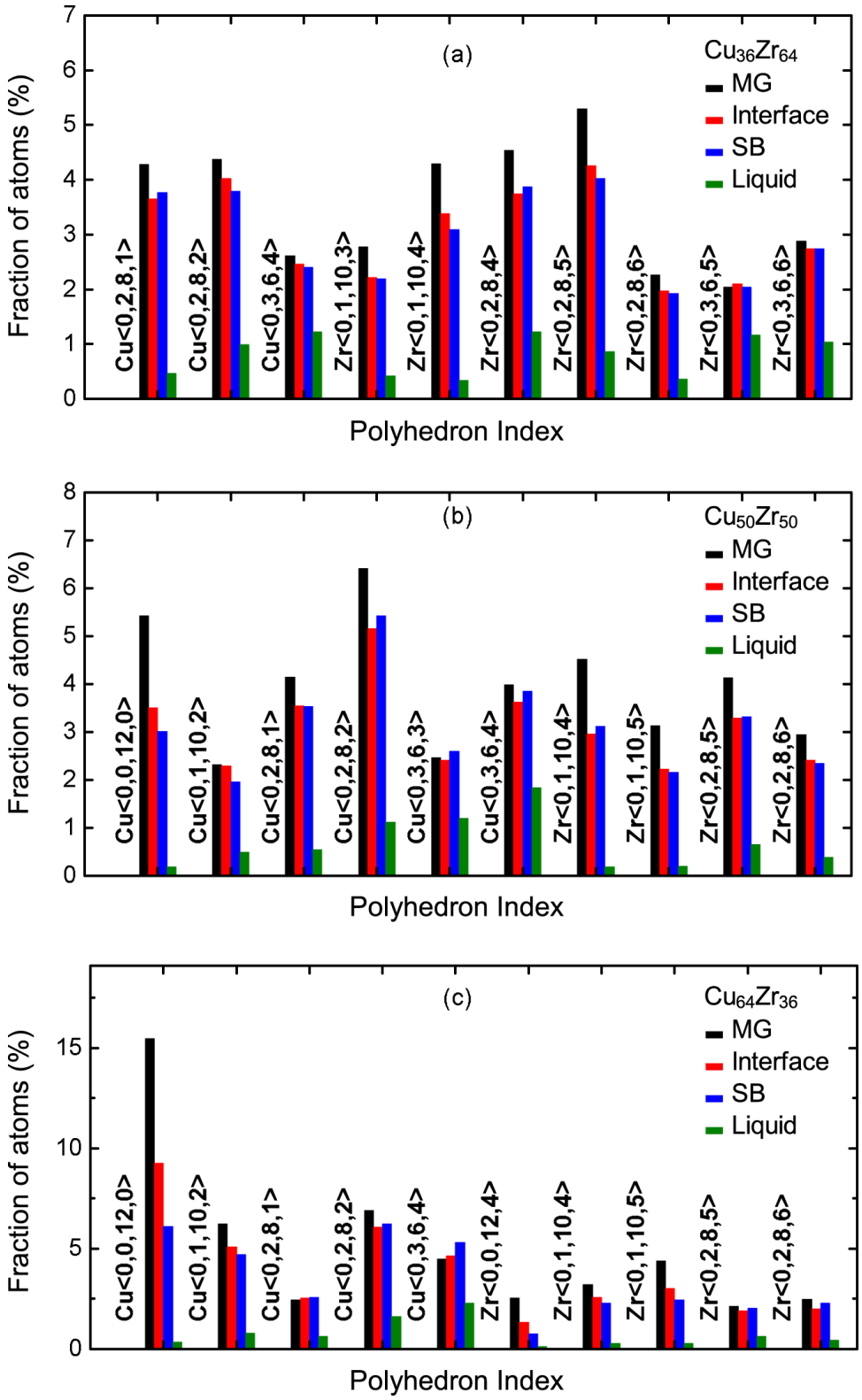

Figure 4-8 Comparison of most prominent atomic Voronoi polyhedra in the MG (grains), shear band, interface and liquid at 2000 K in three compositions of CuZr NGs.

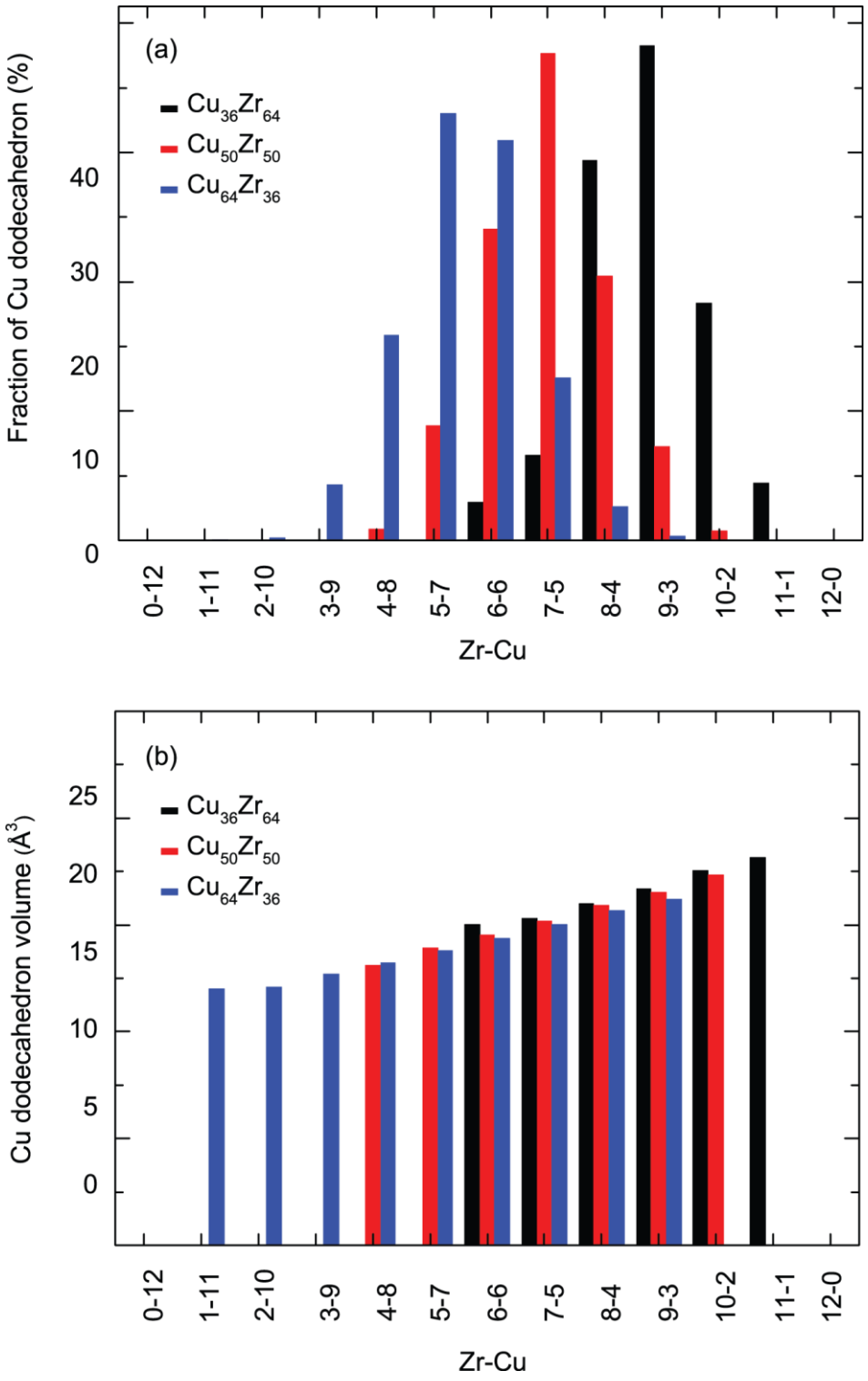

Figure 4-9 Atomic composition and volume of Cu dodecahedra in $Cu_{36}Zr_{64}$, $Cu_{50}Zr_{50}$ and $Cu_{64}Zr_{36}$. (a) Statistics of atomic species in Cu dodecahedra found at different MG compositions. The pair of numbers indicates the number of Zr and the number of Cu atoms that compose the 12 neighbours of the centered Cu dodecahedron. (b) Cu dodecahedron volume as a function of atomic composition at different MGs.

4.6 Discussion

It is instructive to compare the statistics of VPs at NG interfaces and SBs to that in a structure with no structural order, e.g. a liquid. In figs 4-8a-c, we compare the most prominent polyhedra for CuZr at different compositions at NG interfaces, SBs, grains (MG), to that present in a CuZr liquid at 2000 K. The primary highlight of these results is that the polyhedra statistics for the SB and the NG interfaces for both the compositions are nearly identical. This remarkable structural similarity between the NG interface and an SB implies that NG interfaces generate paths conducive for plastic deformation throughout the NG architecture. In addition to this observation, we note that the SB and NG interface statistics are fundamentally different from the homogeneous statistics of the liquid structure.

An important parameter to consider in the nanostructure is the thickness of NG interfaces (loosely referred here as GBs). It is particularly critical for NG architectures with average grain sizes below 10 nm. To evaluate the thickness of the interface for NGs of different compositions, we made use of the corresponding prominent Voronoi polyhedron that indicated the largest difference between the MG and NG for a given composition. The density of each Voronoi polyhedron is evaluated for the two-grain relaxed NG system in the direction perpendicular to the GB interface. Figs 4-10a-c show the calculated densities of Zr<0,1,10,4> for $Cu_{36}Zr_{64}$ NG, Cu<0,0,12,0> for $Cu_{50}Zr_{50}$ NG, and Cu<0,0,12,0> for $Cu_{64}Zr_{36}$ NG. From Fig. 4-10, it is seen that the estimated GB thicknesses based on the region that surround the significant drop of the densities of the respective polyhedra are 1.67 nm for $Cu_{36}Zr_{64}$ NG,

and 1.16 nm for $Cu_{50}Zr_{50}$ NG and 1.38 nm for $Cu_{64}Zr_{36}$ NG. Thus, the GB thicknesses for NGs with different compositions are in the range of ~ 1.1 - 1.7 nm.

In the preceding discussion, we establish that the structure of the NG interfaces resembles that of an SB and is distinct from the structure of the grains (bulk). Therefore, it is useful to calculate the fraction of interfacial material in the NG as a function of grain size. An ingredient for the calculation of the fraction of the interfacial material is the GB thickness. Based on the values estimated from the results shown in Fig. 4-10, we calculate the fraction of atoms in the bulk and at the NG interfaces as a function of grain size for each composition. The results are shown in figs 4-11a and b indicate a crossover between the bulk and interface fractions at about 7 nm for $Cu_{36}Zr_{64}$ NG and 6 nm for $Cu_{64}Zr_{36}$ NG. These results correlate well with the trends highlighted in figs 4-5a and 4-3b, which indicate that the $Cu_{36}Zr_{64}$ NG has the transition from localized to homogeneous deformation at the grain size slightly larger than the $Cu_{64}Zr_{36}$ NG.

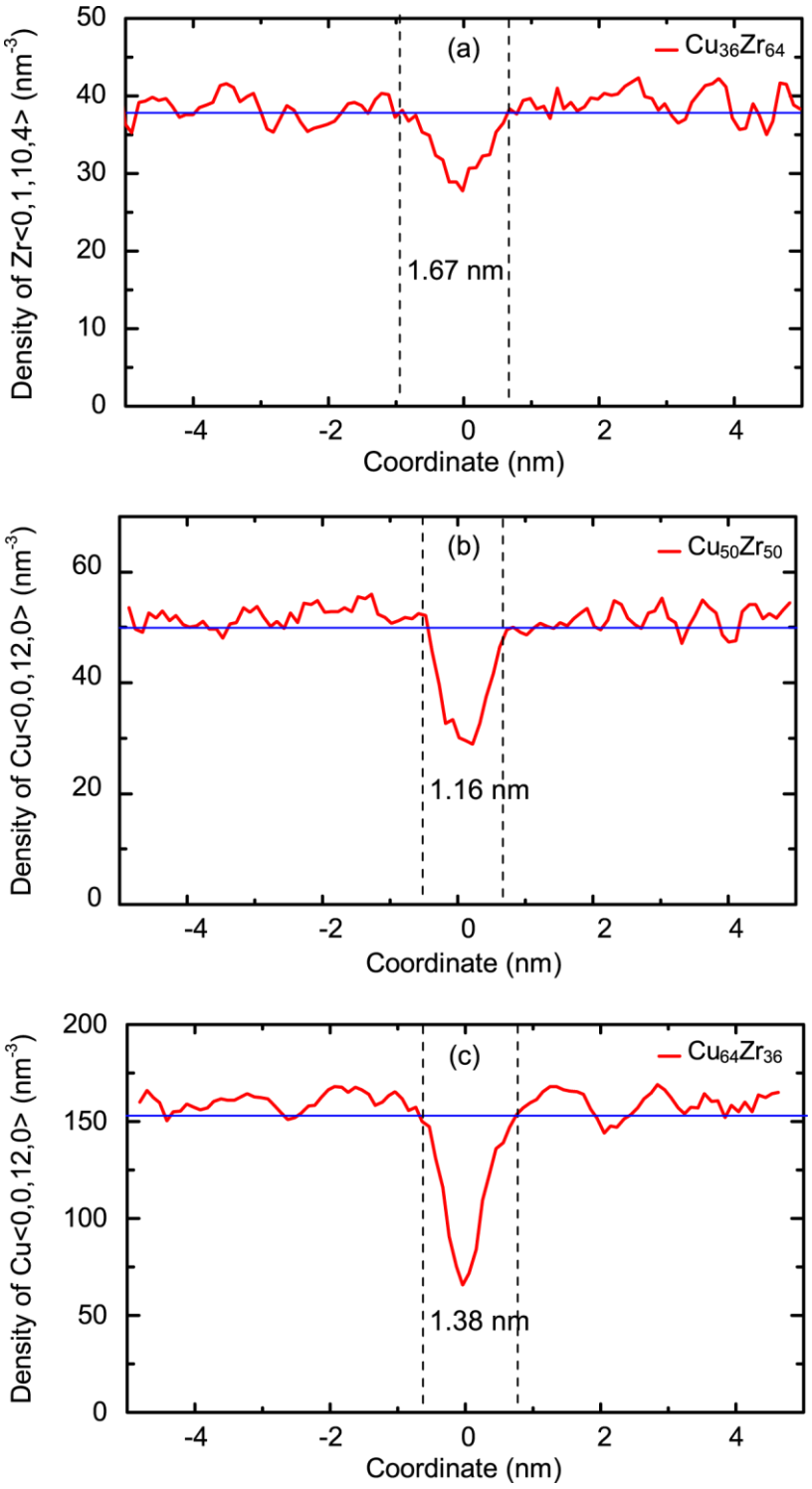

Figure 4-10 Estimation of the grain boundary thickness for the different NGs based on the spatial variation of the density of the most prominent polyhedron. (a) Density of the Zr<0,1.10,4> polyhedron across a flat grain boundary in $Cu_{36}Zr_{64}$, (b) Density of the Cu<0,0.12,0> across a flat grain boundary in $Cu_{50}Zr_{50}$, (c) Density of the Cu<0,0.12,0> across a flat grain boundary in $Cu_{64}Zr_{36}$.

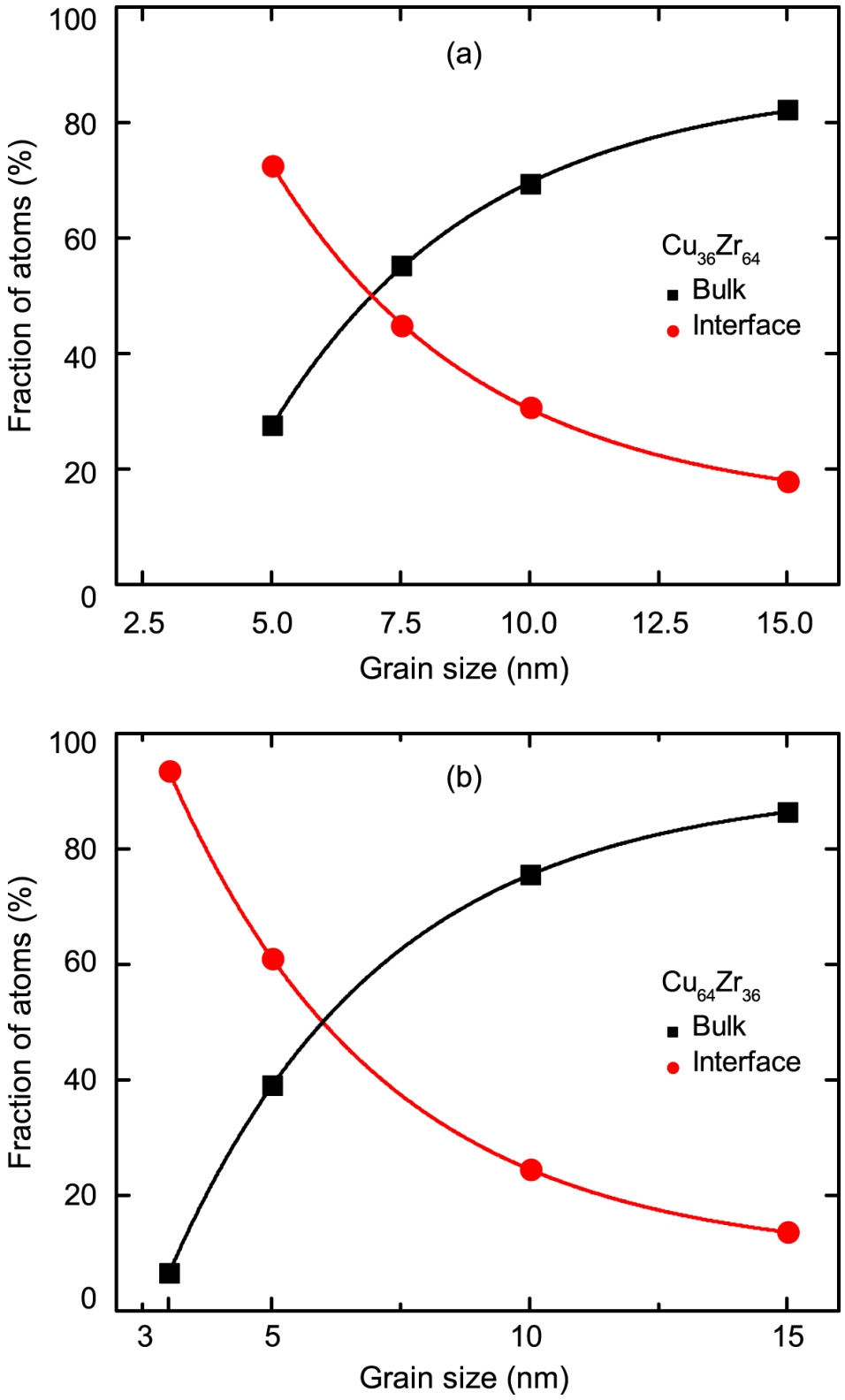

Figure 4-11 Fraction of MG (grain) and interface for (a) $Cu_{36}Zr_{64}$, and (b) $Cu_{64}Zr_{36}$ NGs with different grain sizes at two compositions.

Our results (Fig. 4-7) indicate that the increase in the atomic Voronoi volume from the bulk to the interfaces is 0.6%, 0.7%, and 1.1% in $Cu_{36}Zr_{64}$ NG,

$Cu_{50}Zr_{50}$ NG, and $Cu_{64}Zr_{36}$ NG, respectively. That is the value calculated for relaxed NG interfaces. However, if we consider unrelaxed interfaces, the atomic Voronoi volume increases are much larger, i.e. 9.3%, 10.8%, and 12.4%, respectively. (Ritter et al., 2011) reported excess free volume for interfaces in $Cu_{64}Zr_{36}$ NG of 1-2%. Although our procedure to construct the NG interfaces is distinct from the one used in (Ritter et al., 2011), the reported excess free volume agrees very well with our calculated relaxed value for the same composition. This suggests that the properties of the interfaces in NGs are not dependent on the exact procedure used to relax the NG structure. Essentially, the relaxation procedure should involve cold compression. The relaxation temperature should be lower than the glass transition temperature so as to preserve the interfaces. In this work, we used a relaxation temperature of 50 K. On the other hand, the relaxation pressure should be high, in order to allow a quick heal of the unrelaxed interfacial structure. As a rule of thumb, the relaxation pressure should be a reasonable fraction of the yield stress of the material. In this work, we used 3 GPa for the relaxation pressure.

The results (Fig. 4-7) show that the calculated excess atomic Voronoi volume (~ 1.1%) at interfaces in $Cu_{64}Zr_{36}$ NG is roughly twice the value found for $Cu_{36}Zr_{64}$ NG, which is ~ 0.6%. Recent reports suggest that an increase in the excess atomic Voronoi volume in MGs is directly related to a decrease in the strength of the material (Avchaciov et al., 2013; Raghavan et al., 2010). This implies that, for a given average grain size (d_g), the reduction in the yield stress $(\Delta\sigma = \sigma_{NG} - \sigma_{MG})$ for the $Cu_{64}Zr_{36}$ NG should be larger than for the $Cu_{36}Zr_{64}$ NG, keeping the grain size fixed (i.e. similar interfacial fraction). Indeed, from

figs 4-5 and 4-3, we note that $\Delta\sigma$ for $Cu_{36}Zr_{64}$ is ~ 1.2 GPa for d_g = 5 nm, while for $Cu_{64}Zr_{36}$ with $d_g = 3$ nm, $\Delta\sigma \sim 2$ GPa. Although the grain sizes in the two cases are different, the amount of interfacial material in these two NG compositions is much larger than that in the bulk (Fig. 4-11).

As has been shown, the differences in atomic Voronoi volume between grains and interfaces in NGs are important. In addition, the contrasting atomic VP statistics between these two regions are also crucial. The amorphous structure of MGs is characterized by a clear degree of short and medium range order, as quantified by the calculation of the atomic VP statistics. Fig. 4-8 shows that the statistics are composition-dependent and in contrast with those of the corresponding liquid structure, which has no medium- or long-range order. The interfaces in an NG considerably preserve the medium range order of the corresponding MG (grains), as shown by Fig. 4-8. Interestingly, these interfaces exhibit nearly identical structural order as that in SB, with fewer (and similar) fractions of most prominent atomic VP as compared to the corresponding MG as shown in figs 4-8a-c. Notably, the atomic Voronoi volume is also very similar in NG interfaces and SBs, and is higher than that in MGs (Fig. 4-7a). Thus, we may conclude that it is possible to induce a dense SB-like substructure in MGs by simply introducing interfaces in the structure generating an NG (Cao et al., 2009; Ritter et al., 2011).

The introduction of SBs in MG in order to improve their plasticity has been an active research topic (Cao et al., 2010; He et al., 2008; Lee et al., 2010; Lu et al., 2013; Yokoyama, 2003). Traditionally, this has been achieved by pre-deforming MG samples to generate a certain density of SBs in the material (He

et al., 2008; Lee et al., 2010). The induced plasticity is directly related to the density of SBs introduced and therefore the method is limited by the amount of the possible density of SBs that can be generated. Our results suggest that the use of NG architectures can, in principle, replace the generation of SBs by pre-deformation since the interfaces act, for all practical purposes, as SB-like regions. As demonstrated here, the amount of plasticity that can be induced is only limited by the ability to produce very fine MG powder to generate the corresponding NG. Fortunately, by using inert gas condensation technique particles with average size in the range 3 – 12 nm can be readily produced (Jing et al., 1989), allowing the realization of the NG architectures simulated here.

Compared to the grain size, the role of composition in the properties of NGs is more subtle. The main results of this work, shown in figs 4-3 and 4-5, indicate a direct relationship between grain size and induced plasticity. Eventually, all NGs at any compositions become superplastic at sufficiently small grain sizes. However, the composition defines the strength of the MG and as a consequence the strength of the resulting NG. It is known that for CuZr MGs Cu-rich compositions are stronger but more brittle than Zr-rich compositions (Cheng et al., 2008a), as observed in figs 4-3 and 4-5. The strength of the NG follows that of the MG with the corresponding composition. For example, the yield strength for $Cu_{36}Zr_{64}$ NG for d_g = 10 nm is 1.9 GPa while that for $Cu_{64}Zr_{36}$ NG with the same grain size is 2.6 GPa. Most importantly, the flow stress for the NGs within the superplastic regime is 1.29 GPa for the $Cu_{36}Zr_{64}$ NG with d_g = 5 nm and 1.58 for $Cu_{64}Zr_{36}$ NG with d_g = 3 nm.

Recently, (Franke et al., 2014) have reported an experimental investigation on the thermal and plastic behaviour of FeSc NGs. Their results show that NG interfaces are not only stable at room temperature, but also that they favourably influence the mechanical properties by suppressing shear localization in the form of macroscopic SBs. Frank et al. work follow up the pioneer investigation of the mechanical properties of FeSc NGs by Fang et al. (Fang et al., 2012). In that work micro-compression tests of micropillars composed of MG, synthesized by melt spinning, and NG, synthesized using inert gas condensation, were compared. The results indicate a clear induction of plasticity in the NG micropillars from the yield point. Although the NG investigated in those two experimental works are not CuZr alloys, and the mechanical properties are evaluated by nanoindentation/micro-compression tests, their main results align well with the prediction of this and previous modelling work on NGs.

4.7 Summary

In summary, we performed MD simulations on $Cu_{36}Zr_{64}$, $Cu_{50}Zr_{50}$, and $Cu_{64}Zr_{36}$ NGs with different grain sizes under tensile loading. The primary objective of this work was to characterize the structural and mechanical properties of NGs at different compositions and grain sizes. Our results demonstrate that CuZr NG not only becomes ductile, but can also deform superplastically provided that the glassy grain size is reduced to 3 nm in $Cu_{64}Zr_{36}$ and 5 nm in $Cu_{50}Zr_{50}$ and $Cu_{36}Zr_{64}$. The origin of the transition in failure mode from localized shear banding to superplastic with decreasing glassy grain size d_g is related to the uniformly distributed SCs and the homogeneous elastic energy release with

decreasing grain size. CuZr NG with small d_g introduces a substantial fraction of structural changes that facilitate homogeneous plastic flow, which in turn give rise to the observed superplastic-like behaviour. The present work demonstrates that the glassy grain size can be effectively used as a design parameter for tuning the mechanical properties of metallic glassy materials. Analysis indicates that the strength of an NG is directly related to the fraction of the interfacial material present. The calculated atomic Voronoi volume indicates a small but well-defined excess free volume at NG interfaces at all compositions. The analysis of the statistics of the most prominent atomic VPs indicates that the NG interfaces at each composition preserve the medium range order of the corresponding MG. The analysis also indicates that structurally the NG interfaces are nearly identical to the SB in the corresponding MG. That implies that an NG is structurally similar to an MG pre-deformed to generate a high density of SBs. However, the induced plasticity in an NG is only limited by the ability to produce very fine MG powders, which in turn can be used to generate NG with small average grain size. The results indicate that it may be possible to design ductile MGs using NG architectures by tuning the grain size and/or the Cu concentration in the CuZr parent MG. One may envision an MG composite with enhanced properties by combining MG powders of different grain sizes and different compositions. For example, it would be interesting to evaluate the mechanical behaviours of NGs comprising a judicious combination of different CuZr compositions and grain sizes that are arranged in various architectures, for example, nano-laminates or multi-modal inclusion composites.

5. Damage and Failure Mechanisms of Nanoglass Nanopillars under Tensile Loading

5.1 Background

In Chapter 4, we showed that the macroscopic deformation mode in NG samples transitions from localized SB to a homogeneous flow below a critical grain size. Importantly, this observation holds for all the three compositions considered, although the transition grain sizes are somewhat different. Recent MD simulations on NGs, including that in Chapter 4, have focused on thin-like models comprising columnar grain structures with PBCs along the short dimension (Adibi et al., 2013; Albe et al., 2013; Şopu et al., 2009; Şopu et al., 2011a). That is an ideal geometry to investigate the intrinsic deformation and failure mechanisms in NGs. However, it is of particular interest to characterize the deformation and failure in an NG sample geometry, which could be

compared directly with nanoscale experimental samples. As has been widely reported recently nanopillars offer a convenient experimental platform to investigate the intrinsic mechanical properties of MGs. In this Chapter, we therefore simulate nanoscale CuZr NG specimens with circular cylindrical geometries. To make the samples as realistic as possible we use 3D grain structures of different grain sizes and subjected the samples to uniaxial tensile loading using the same procedure as detailed in Chapter 4. Since the composition effects are well understood from the results of Chapter 4 we restrict our attention to the $Cu_{64}Zr_{36}$ composition and study only the grain size effect. We also keep the specimen diameter ($d = 50$ nm) and the aspect ratio ($\xi = 2.5$) fixed. The particular choice of $Cu_{64}Zr_{36}$ stems from the observations in preceding chapters and literature (Cheng and Ma, 2011) that reveal the propensity of this system to behave in a brittle manner compared to those with lower Cu concentration.

5.2 Methodology

For the given specimen size, the simulation sample comprises approximately 16 million atoms. Fig. 5-1 shows a schematic of the procedure to generate the MG and NG nano-scale cylindrical specimens. Bulk NG samples are constructed from original bulk MG using the Poisson-Voronoi tessellation method (section 4.2). Following this, NG cylinders are curved from the bulk NG sample. Free surfaces are relaxed using Langevin dynamics for 0.02 ns. Residual stress along the nano-scale cylinder axis (z direction) is relaxed using the NPT ensemble for 0.02 ns before loading. Samples are simulated under uniaxial tensile loading. PBC are applied along the cylinders axis (z direction), which is set as the

deformation loading axis, while free surfaces are used in the lateral, *x* and *y* directions. The traction-free lateral surfaces ensure that the specimens experience a uniaxial stress state.

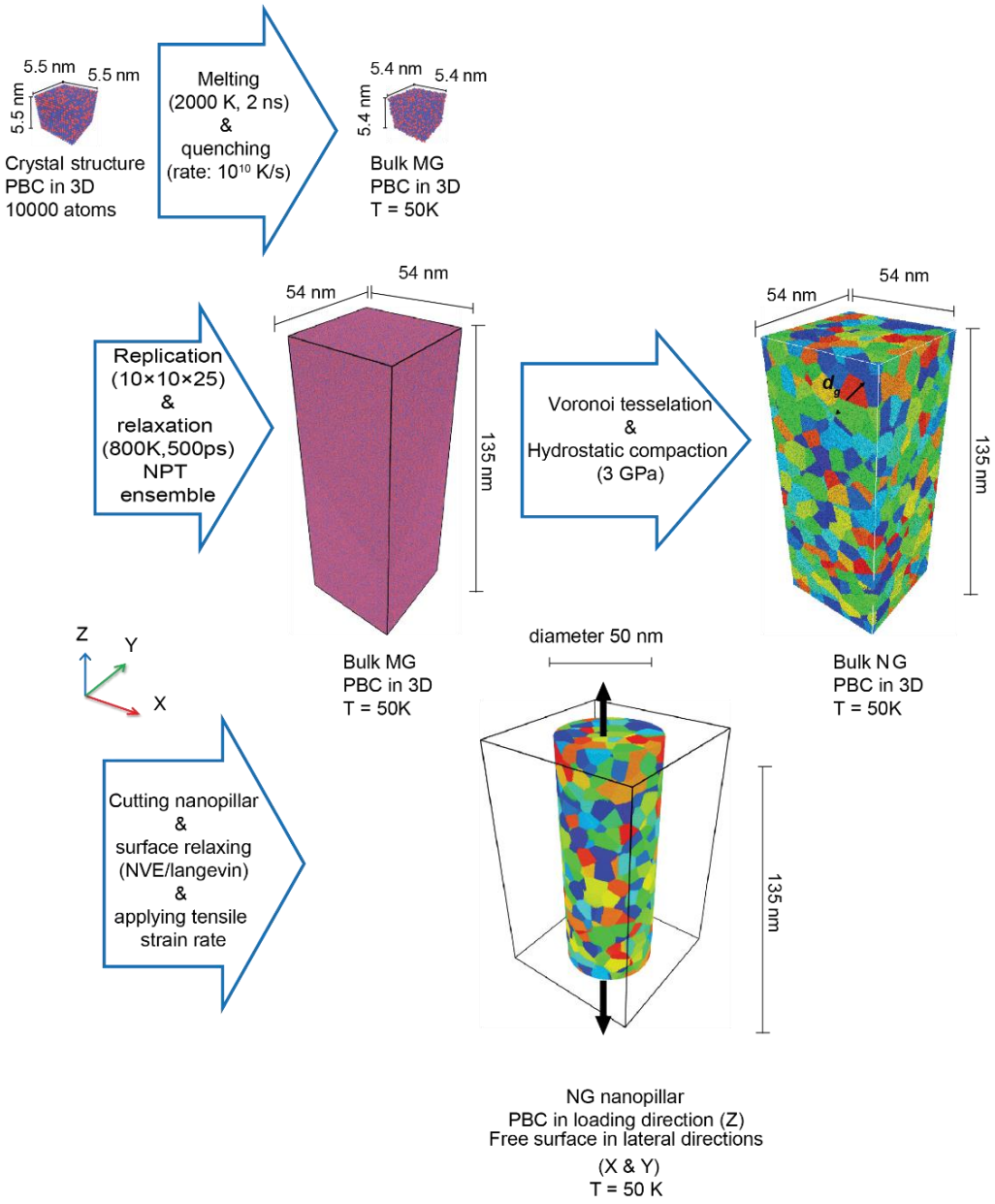

Figure 5-1 Schematic of the process to generate a NG nanopillar sample.

Simulations are based on the EAM potential as in the case discussed in Chapter 4. Engineering stress is calculated as the average atomic Virial stress in the

system. The generation and evolution of local inelastic deformation is calculated using the atomic local von Mises shear strain (Shimizu et al., 2007).

For NGs, we consider average grain sizes (d_g) in the range between 3 to 20 nm (figs 5-2a-e). Different grains in the NGs are shown in different colors to highlight the nanostructures. In addition to these NG architectures, we also consider a conventional $Cu_{64}Zr_{36}$ MG with the same dimension as a reference. Given the large size of the computational models, we perform simulations at a tensile strain rate of 4×10^8 s^{-1} which has been shown not to introduce any significant strain rate effects on the results while keeping the computational cost realisable (see section 3.3).

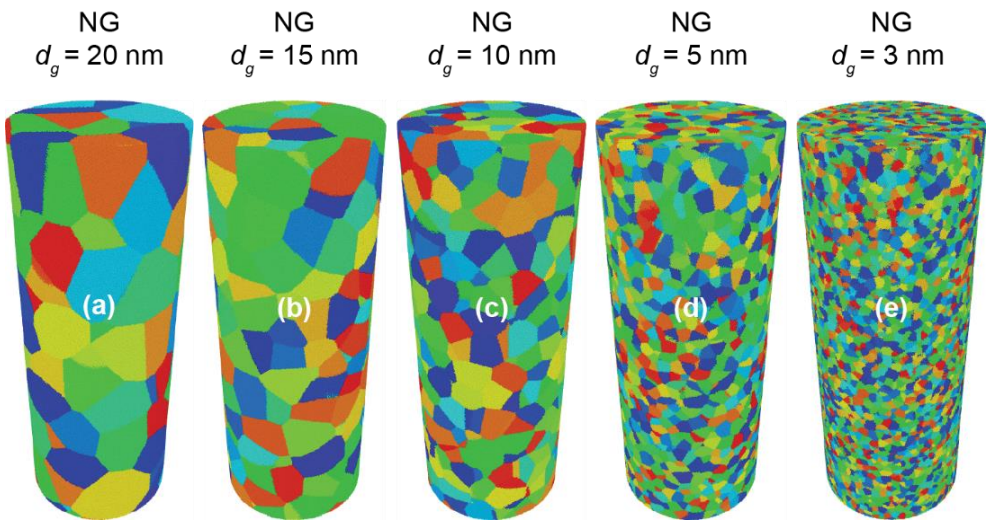

Figure 5-2 NG nanopillars used in the simulations. (a)-(e) illustrations of nanopillars with 50 nm diameter and average grain sizes d_g = 20, 15, 10, 5 and 3 nm. Grains are shown in different colours to highlight the nanostructure.

5.3 Grain Size Effect on the Stress-Strain Responses

The engineering stress-strain curves calculated from the simulations of each NG nanopillar are plotted in Fig. 5-3a. As a reference the stress-strain curve for the

MG nanopillar is also plotted and shows a typical sharp stress drop at strain ~ 0.07, which is an indication of brittle failure by initiation and propagation of an SB. It should be noted that the finite stress drop at the yield point is an effect of the use of fixed strain rate deformation and a low, 2.5, aspect ratio (see section 3.4). An aspect ratio of 13 or larger allows the full propagation of a 45° SB across a nanopillar causing a full stress drop to zero (see section 3.4). In contrast to MG nanopillar, the curves for NG nanopillars show a smooth stress drop from the yield point, suggesting the onset of plastic deformation. The curves show that decreasing the grain size induces both a lower yield stress and a smoother drop from it. For the extreme case of the NG with d_g = 3 nm, the data indicates that the stress from the yield point even increase mildly before start to drop from ε = 0.3, suggesting a distinguished deformation and failure mechanism compared to the MG nanopillar. Therefore, the results indicate a clear change in damage and failure mechanism on grain size reduction. Fig. 5-3b shows the dependence of the maximum stress on NG grain size. As a reference, the maximum stress for the MG nanopillar is also shown with a solid line. Since the maximum stress is an indication of the material strength Fig. 5-3b shows clearly that the strength decreases with grain size. The reduction of strength in the grain size range considered is between 23% for d_g = 20 nm to 58% for d_g = 3 nm. Fig. 5-3c shows the true stress-strain curve of the NG with d_g = 3 nm. It can be seen that the nanopillar shows hardening after the yield point. It is interesting to note that similar hardening of MG under intensive plastic deformation and necking have been reported recently in experiments where the generation of SBs is explicitly avoided by controlling the stress loading state (Wang et al., 2013).

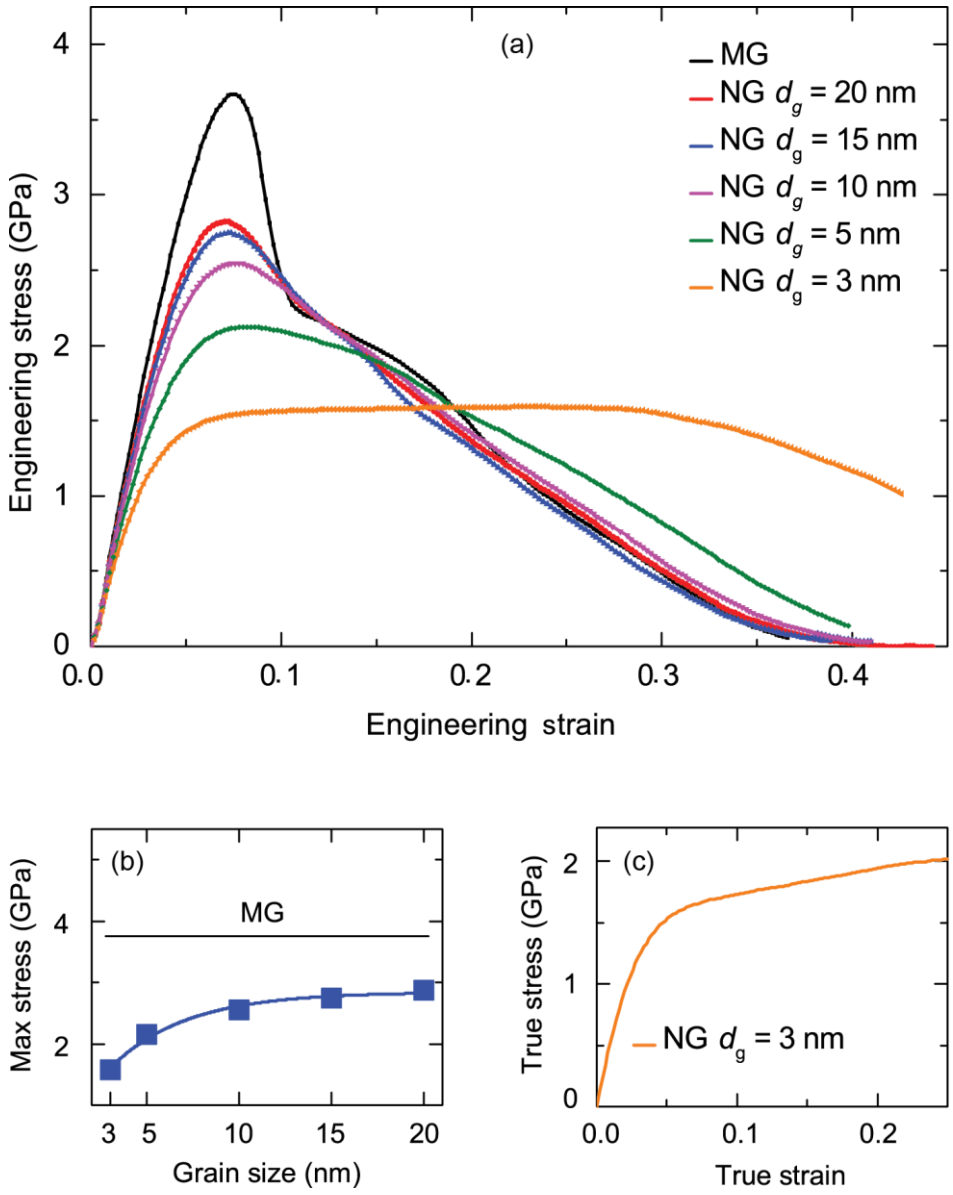

Figure 5-3 Grain size effect on tensile stress-strain curves of $Cu_{64}Zr_{36}$ MG and NG nanopillars. (a) Engineering stress- strain curves for MG nanopillar and NG nanopillars with d_g = 20, 15, 10, 5 and 3 nm. (b) Maximum stress vs. grain size from the curves shown in (a). The value of the maximum stress for MG is also shown for reference. (c) True stress-strain curve for NG nanopillar with d_g = 3 nm.

In order to understand the change in the deformation mechanism experienced by NG nanopillars with different d_g, we examine the atomic deformation processes by analyzing the distribution of atomic local shear strain, which is calculated with respect to the relaxed configurations prior to loading. Fig. 5-4 shows a sequence of images at increasing applied axial strain, with the specimen

sectioned parallel to the loading axis. It illustrates the atomic deformation processes for the MG nanopillar as well as the NG nanopillars with d_g = 20, 15, 10, 5, and 3 nm, respectively. It can be seen in Fig. 5-4 that while MG demonstrates plastic flow in the form of SB, NGs demonstrate a combination of SB and homogeneous flow. In MG nanopillar at ε ~ 0.08, the formation of a plane with highly localized shear strain is apparent. With progressive straining, a thickening of the strain localization region and shear surface offsets can be observed. Eventually, this localized shear strain plane fully propagates across the system causing catastrophic brittle failure of the MG nanopillar. In contrast, for NG nanopillars shown in figs 5-4b-f, shear strain is found predominantly at the interfaces. The results show clearly that NG interfaces act as a favorable channel to carry on plasticity in the nanopillars following a delocalized pattern. In addition, in contrast with the MG nanopillar, NG nanopillars at all grain sizes fail by necking. A direct consequence of necking is the smoother decay of stress from the yield point, as illustrated in Fig. 5-3a. It can be seen that by decreasing d_g from 20 to 3 nm, the denser interface network makes the plastic deformation increasingly more delocalized and the final failure by necking more pronounced. For the extreme case of NG nanopillar with d_g = 3 nm the very dense interface network generates a nearly homogeneous deformation of the nanopillar till ε = 0.33.

In order to investigate changes in the grains shape during deformation, in Fig. 5-5 we show the evolution of the grains during the deformation of NG nanopillars with d_g = 20 nm and 5 nm. The strain localization region is denoted by dashed black lines. It can be seen in figs 5-5a and b that within the

localization region, grains become highly elongated. The grains shape remains stable away from this highly strained region. It can be observed that near the top and bottom of the samples, where plastic strain is low, the grain shape is similar to the as-prepared structure. It should be noted that while the grains shape change significantly there is no grain *growth*, since the local density remains at about the same value. To recapitulate, highly elongated grains are observed in the strain localization/necking region for both grain sizes probed here (d_g = 20 nm and 5 nm). However, away from this region of high plastic strain, the grain structure is unaffected by the applied loading.

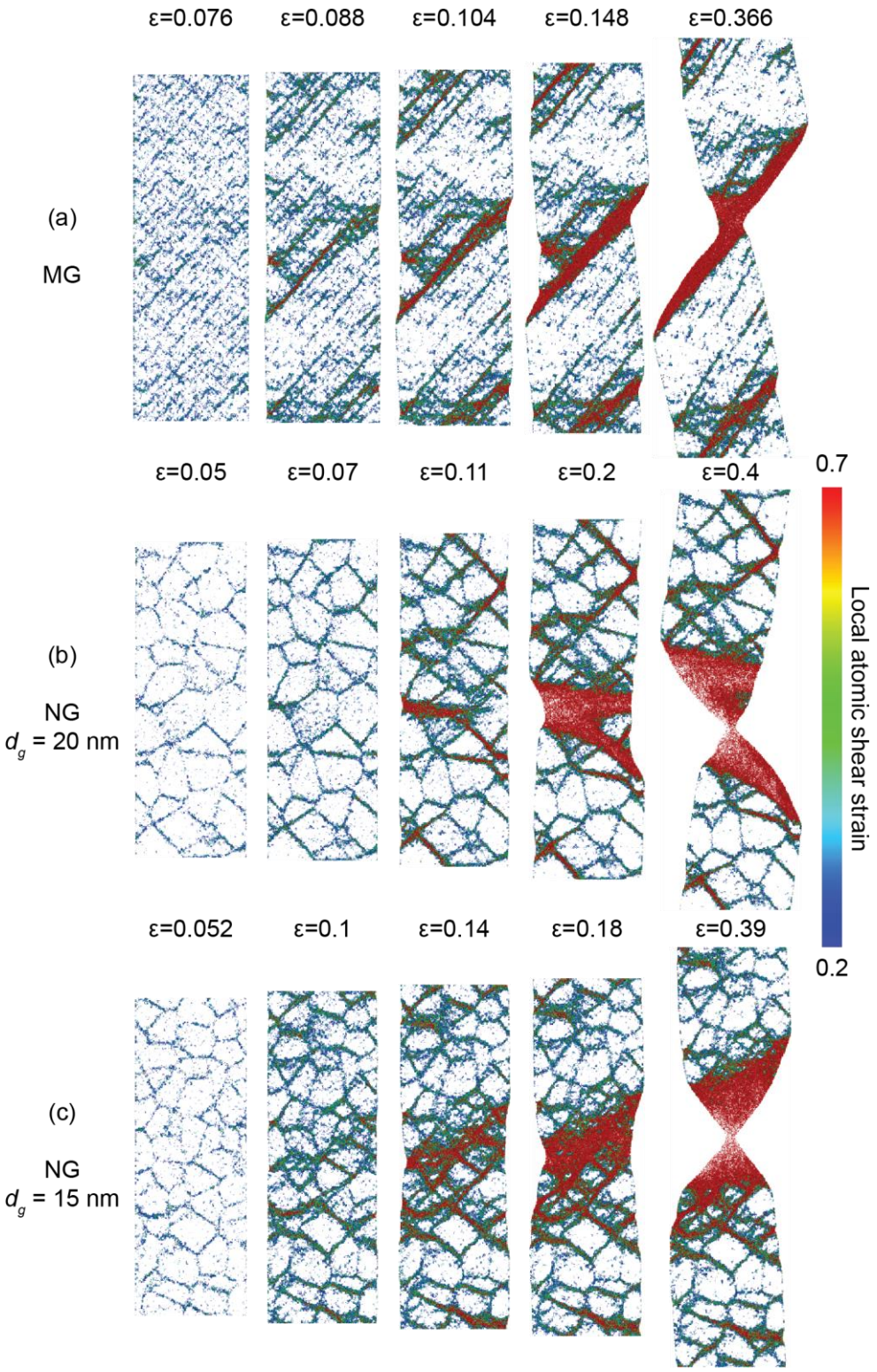

Figure 5-4 Illustrations of the deformation and failure of MG and NG nanopillars (taken from a slice of nanopillars). (a)–(f) Sequence of snapshots capturing the atomic deformation processes for MG nanopillar and NG nanopillars with d_g = 20, 15, 10, 5 and 3 nm, respectively. The colour indicates the local atomic shear strain. For clarity, only atoms with local atomic shear strain higher than 0.2 are shown. (continued)

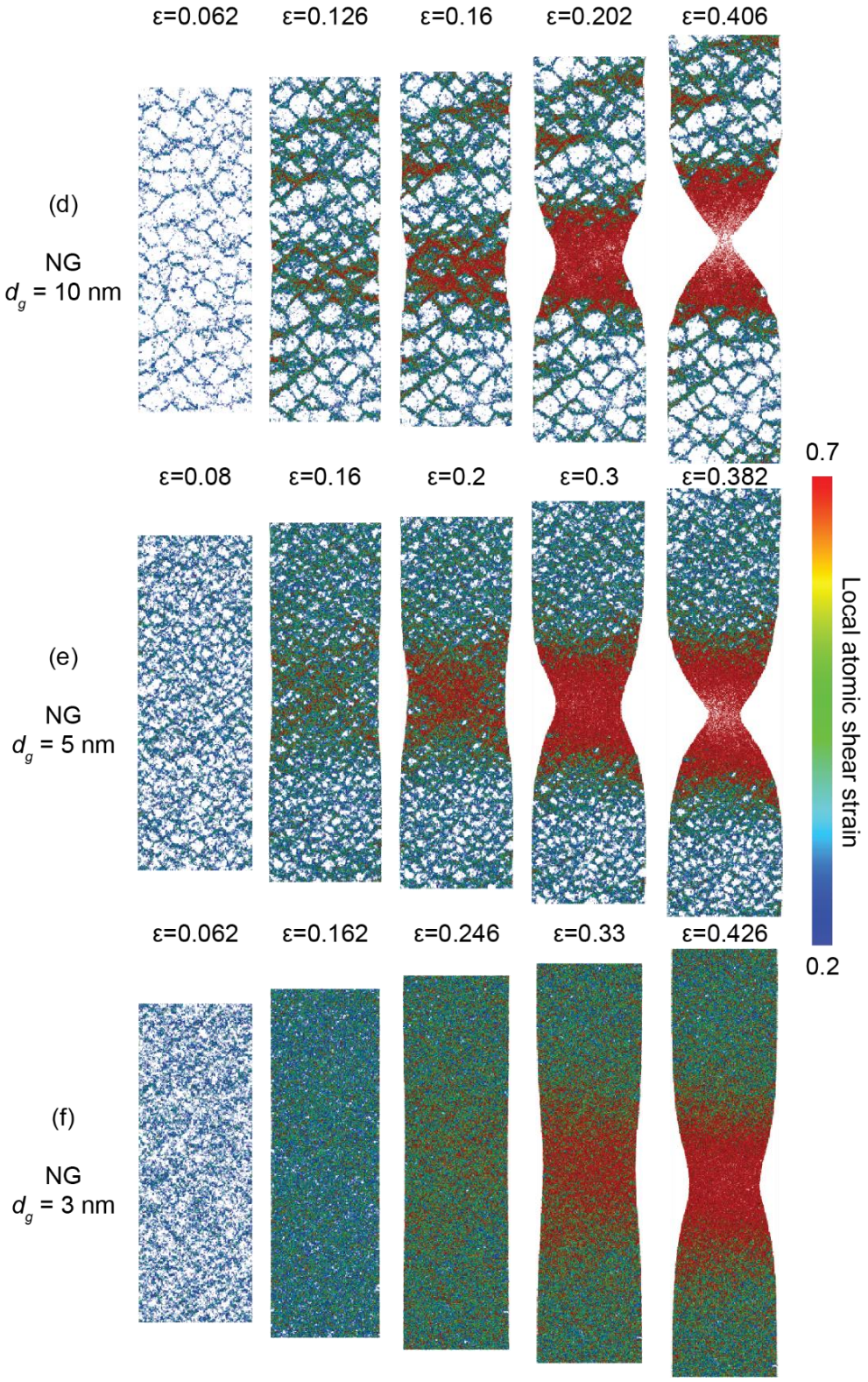

Figure 5-4 Illustrations of the deformation and failure of MG and NG nanopillars (taken from a slice of nanopillars). (a)–(f) Sequence of snapshots capturing the atomic deformation processes for MG nanopillar and NG nanopillars with d_g = 20, 15, 10, 5 and 3 nm, respectively. The colour indicates the local atomic shear strain. For clarity, only atoms with local atomic shear strain higher than 0.2 are shown.

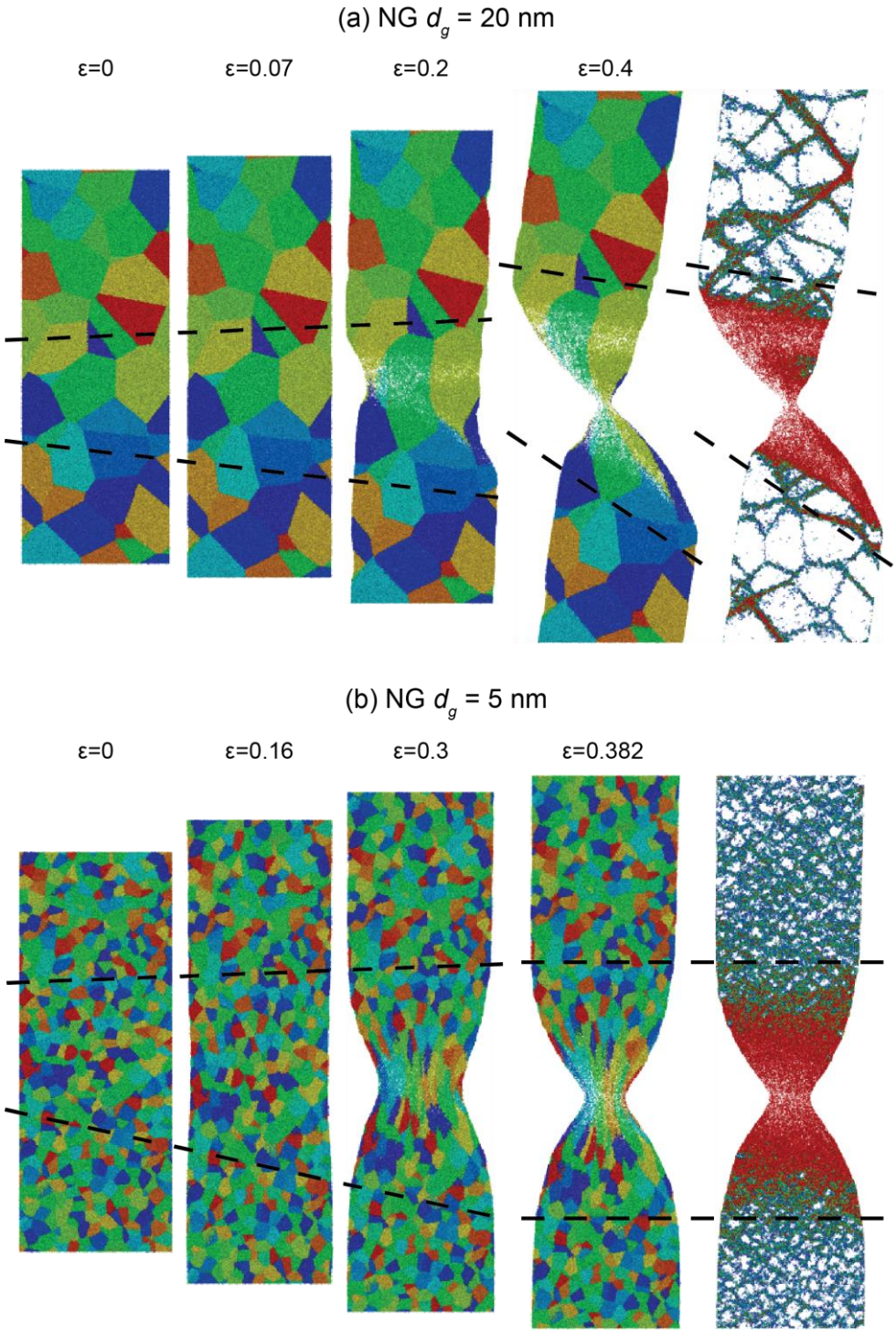

Figure 5-5 The grain structure of the NG with (a) d_g = 20 nm and (b) 5 nm during loading. Coarsened grains are observed in the strain localization region marked by dashed black lines.

In order to further improve upon the visual cues of deformation mechanism in MG and NGs, we quantify the normalized distribution of atoms at different local atomic shear strain. Figs 5-6a and b show the normalized distribution of atoms according to their local atomic shear strain at engineering strains of 0.11 and 0.35, respectively. In the calculation, we use bins 0.01 wide. For each grain size, the corresponding histogram exhibits a characteristic unimodal function with its peak at atomic shear strains less than or near applied macroscopic strain. The width of the atomic shear strain distribution decreases with increasing grain size. In other words, as the grain size increases, a greater proportion of atoms exhibit the shear strain value of the peak, leading to a narrower histogram distribution peaking at progressively lower strain. Figs 5-6a and b show that for NG with d_g = 3 nm the peak in the fraction of atoms are at the strain near to the macroscopic applied strain, which indicates a near-homogeneous shear strain distribution in the sample.

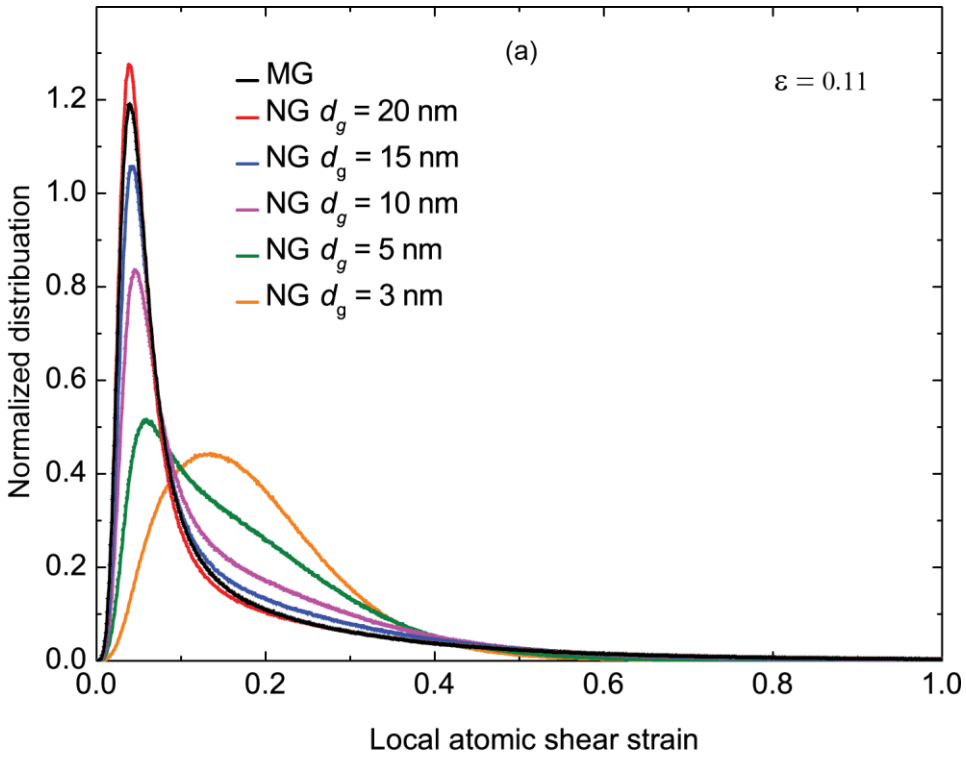

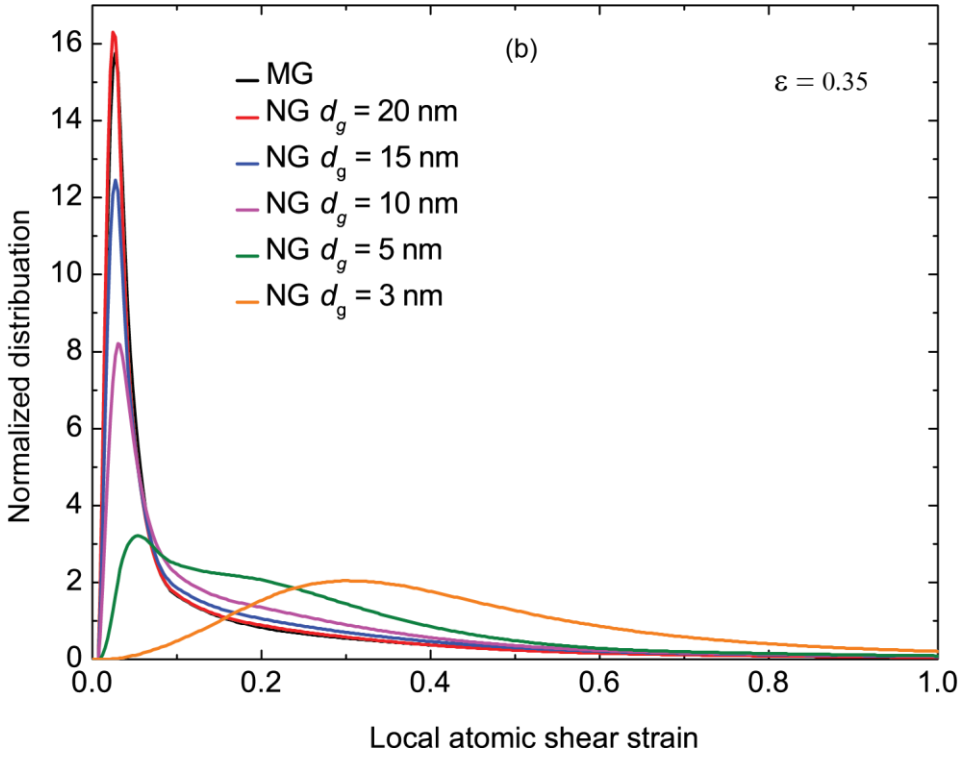

Figure 5-6 Normalized distribution of local atomic shear strain at (a) ε = 0.11, and (b) ε = 0.35. Values are calculated using a histogram of bin size 0.01 and normalized by the total number of atoms. The threshold value, 0.2, is chosen to select the atoms with high local atomic shear strain..

Next, we calculate the fraction of atoms with relatively high local atomic shear strain. Fig. 5-7 shows the deformation distribution for MG and NGs with d_g = 20, 15, 10, 5 and 3 nm. Fig. 5-7a shows the fraction of atoms with $\eta_{\text{Mises}} > 0.2$, during deformation. Compared to MG, NG possesses a higher fraction of atoms that undergo shear strain or structural changes due to the presence of the GGI. In addition, with decreasing the grain size, the proportion of atoms with high shear strain increases. This is the case because, the decrease in glassy grain size results in an increasing GGI fraction thereby increasing of the volume that is able to carry higher shear strain. During deformation, the fraction of atoms undergoing large shear deformation reaches nearly 90% for NG with d_g = 3 nm, implying that a substantial fraction of the material experiences structural changes that facilitate homogeneous plastic flow.

In order to quantify the degree of strain localization in MG and NG specimens, we calculate the Deformation Participation Ratio (DPR), (Shi and Falk, 2005) defined as the fraction of atoms that undergo a local atomic shear strain higher than the nominal engineering strain of the entire material. Fig. 5-7b show the DPR values during deformation. For homogeneous deformation, the DPR ≈ 1 while for a highly localized deformation the DPR tends to zero. As shown in the figure, for a given d_g the DPR is generally a decreasing function of applied strain, which results from the fact that the plastic deformation localizes in the necking region. However, for NGs with d_g = 5 nm and 3 nm the DPR remains constant over a reasonable strain range before it drops. This indicates that at sufficiently small grain sizes one may expect an extended regime of near-homogeneous deformation.

Fig. 5-7b, also reveals that the DPR decreases with increasing grain size. At the macroscopic strain of ε = 0.11 and for d_g = 3 nm, DPR is close to 0.8, which indicates a nearly homogeneous NG deformation. For MG and NG with d_g = 20 nm, however, the DPR values are close to 0.35 indicating a localized deformation. The observed deformation in the MG nanopillar is mostly localized in one SB, while that for the NG nanopillar is mostly in the form of a necking region. It should be noted that the DPR highlights one important result of this work. The presence of grains and interfaces in an MG induces plasticity and graceful failure by necking. This motif occurs at any value of d_g simulated here. However, reducing $d_g$to the finest grain size an independent phenomenon is activated. The dense pattern of grain boundaries increase the homogeneous deformation, resulting in increase in overall ductility of the sample. While for d_g = 3 nm the NG specimen still fails by necking it shows strikingly large overall plastic deformation.

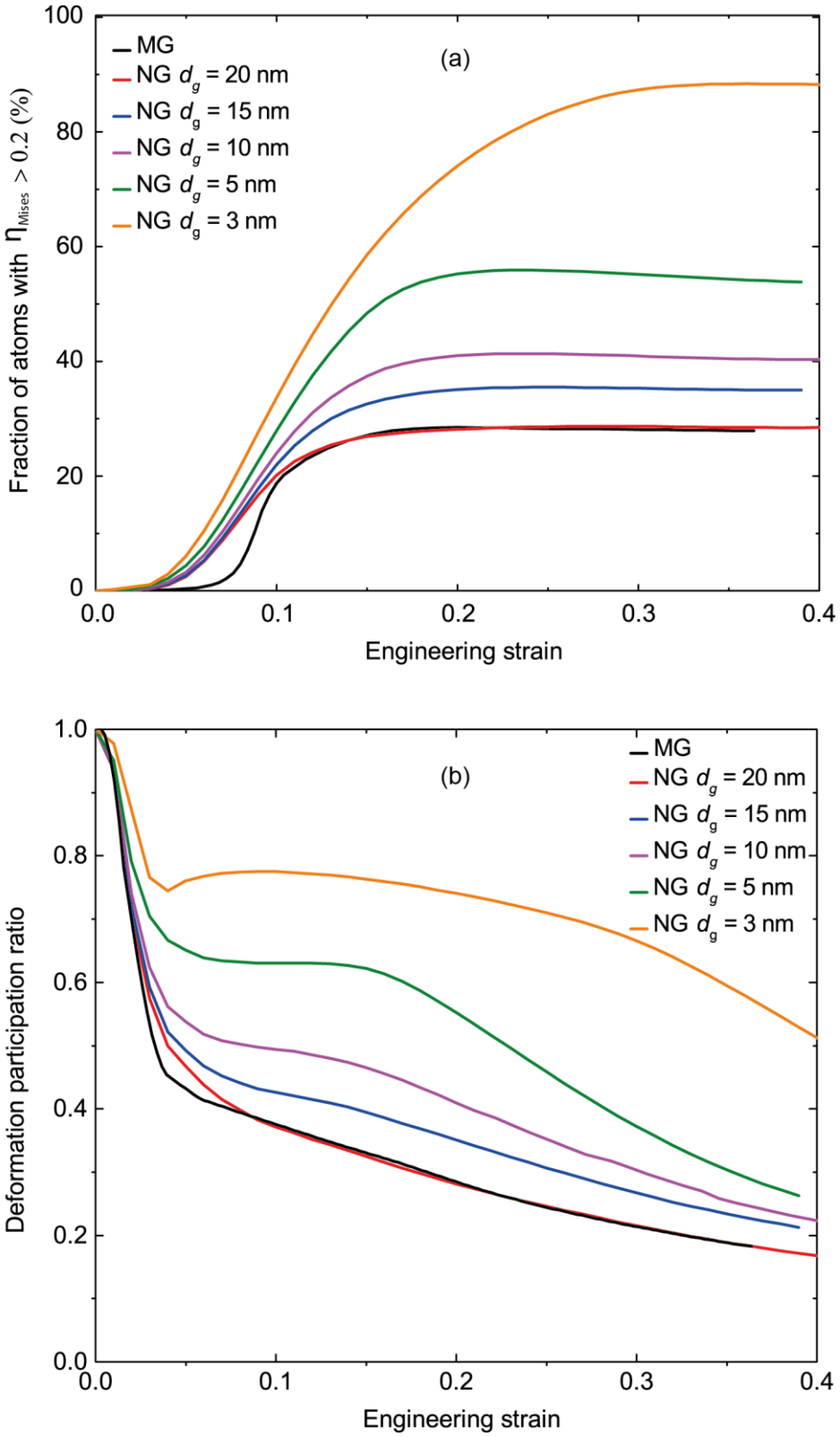

Figure 5-7 Deformation Participation for MG and NG nanopillars with d_g = 20, 15, 10, 5 and 3 nm. (a) The fraction of atoms with relatively large atomic shear strain $\eta_{Misses} \geq 0.2$ during deformation for the MG and NG nanopillars. (b) DPR during deformation for the MG and NG nanopillars.

To show the strain distribution along the nanopillar samples, we divide each pillar in wide segments along its length (i.e., the loading *z*-axis) and calculate the average value of the 1% atoms with the highest local atomic shear strain. The calculated values, in bins 0.01 wide (normalized *z*-axis units), are plotted as a function of the normalized position along the *z*-axis in Fig. 5-8a. This normalisation allows comparing the NGs with different grain sizes on the same graph. Figs 5-8a and b show distribution of the local atomic shear strain along the loading axis for the macroscopic engineering strain of ε = 0.11 and ε = 0.35, respectively. Figs 5-8c-h illustrate the distribution of the local atomic shear strain for ε = 0.35 to highlight areas with high local atomic shear strain. In can be seen in figs 5-8a and b that for both macroscopic strains, MG and NG with d_g = 20 nm exhibits clear peaks in the average shear strain highlighting the spatial localization of the plasticity. However, it is shown in Fig. 5-4 that localization occurs in the form of localized SB in MG and defuse necking in NG with d_g = 20 nm. The height of the peak in average shear strain decreases to the intermediate value as the grain size decrease, and then the strain profile appears nearly flat for the finest grain size d_g = 3 nm. It indicates that changing the deformation mechanism from localized SB to necking decrease the peaks spontaneously by generation of homogeneous deformation in the samples. Therefore, the transition to more spatially homogeneous strain occurs at finer grain size. For NG with d_g = 3 nm (Fig. 5-8h), although necking occurs at the either end of the sample, it is of low shear strain (amber curve in Fig. 5-8b).

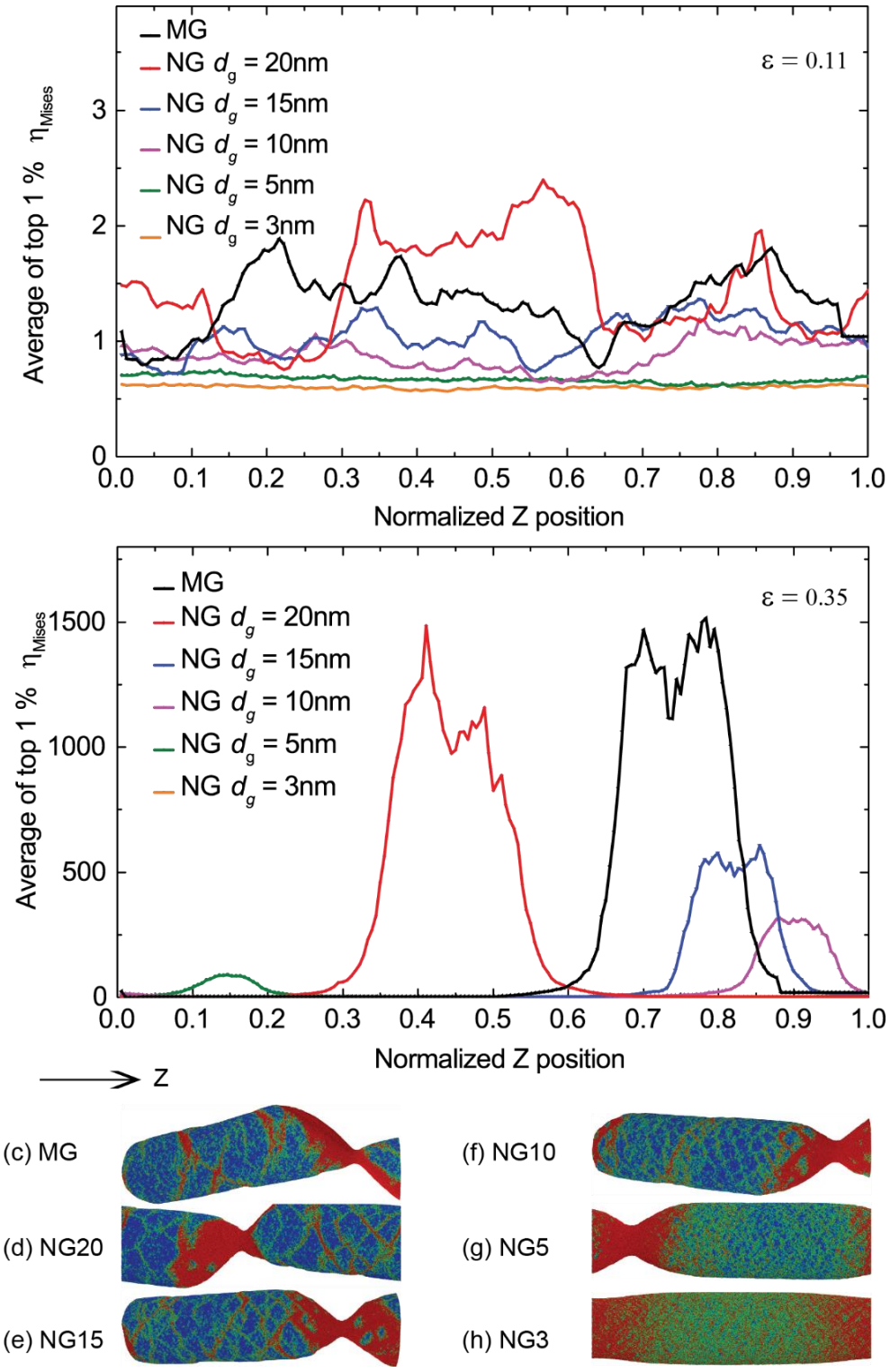

Figure 5-8 The average of top 1 % of local atomic shear strain (η_{Misses}) as a function of position along the pillar length at macroscopic strain of (a) ε = 0.11, and (b) ε = 0.35. (c)-(h) Illustration of deformed MG and NG nanopillars at macroscopic strain of ε = 0.35 are shown as a reference to show region with high local atomic shear strain along nanopillar length.

Comparing figs 5-8a and b with figs 5-8c-h, indicate that the peaks in the shear stress along the nanopillar length correspond to regions with high local atomic shear strain (reddish areas in figs 5-8c-h). Furthermore, an increase in shear strain is observed at the site of deformation. The local atomic shear strain at the deformation site increases with the applied macroscopic shear strain.

In section 4.5, we show that the structure of the NG interfaces is different from the structure of the grains (bulk), and interfaces play a very important role in initiation of SBs. It is, thus, important to quantify the fraction of interfacial material (GB and triple and higher junction) in the three dimensional grain structure of NG nanopillars as a function of grain size. To calculate the fraction of atoms at interface and grains as a function of grain size, the interface thickness is derived from previous simulations on NG with two grains (see section 4.5). Based on the estimated interface thickness in the NG nanopillars, 1.38 nm, we calculate the fraction of material at bulk, interfaces, GBs, and triple and higher junctions as a function of grain size. The results are shown in Fig. 5-9. It can be seen that the interface fraction is ~ 91% in NG with d_g = 3 nm, while for d_g = 20 nm, it is ~ 21%. It can be seen that the interface fraction increase as the grain size decrease, while the GB fraction does not have the same trend. The data show that GB fraction increase by decreasing grain size till ~6 nm and then starts to decline. This trend shows the importance of triple and higher junctions at finer grain sizes. In addition, it can be seen that the crossover between the bulk and interface fractions occurs at d_g ~ 8 nm while the crossover of bulk, GBs, and triple and higher junctions occurs at d_g ~ 5.5 nm. These results correlate well with the trends observed in Fig. 5-3, which indicate that by

decreasing the grain size the fraction of interfaces and hence activated SCs are increasing.

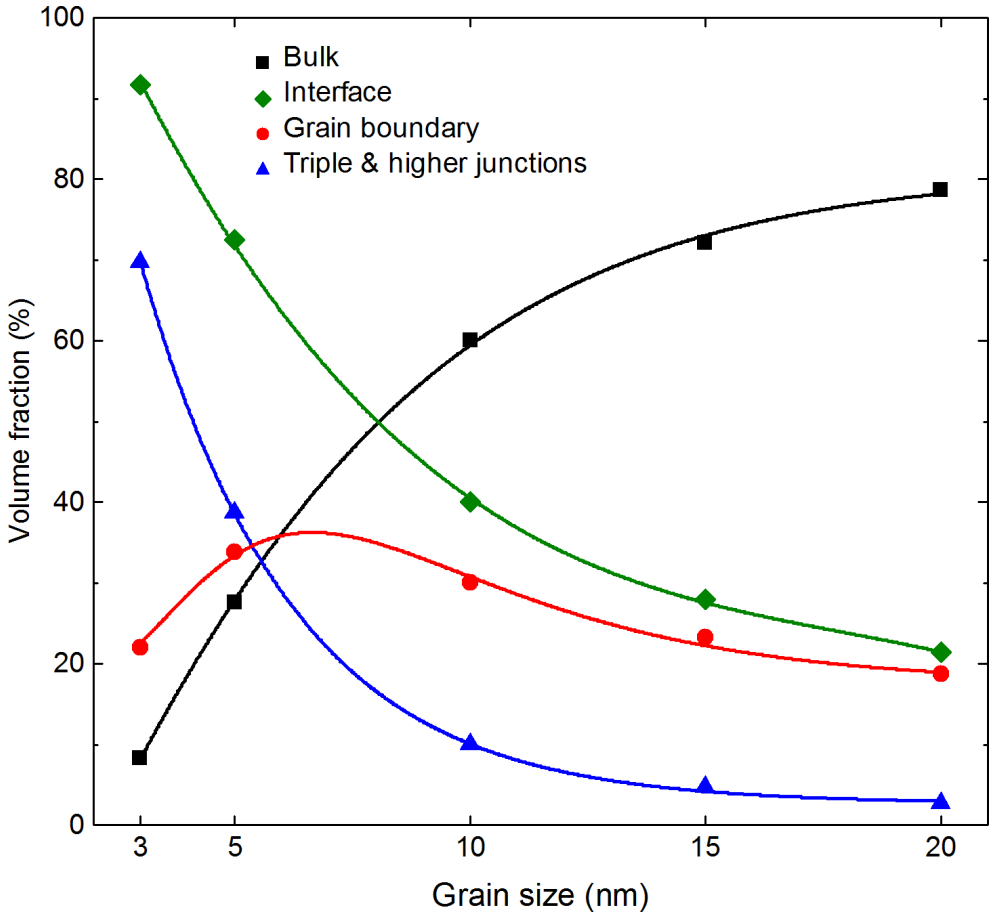

Figure 5-9 Fraction of atoms in MG grains (bulk) and NG interfacial regions as a function of grain size. Atoms in interfaces include those in grain boundaries and triple and higher junctions.

5.4 Nanopillar Design Effect

In this section, we investigate the differences in deformation and failure characteristics introduced by the use of an NG nanopillar geometry compared to the reference NG samples investigated in Chapter 4. Section 4.3 presents the results for NG samples at strain rate of 4×10^{7} s^{-1}. As explained in Section 3.3 SB activities in MGs can be altered by applied strain rate. At high strain rates,

a single shear localization event cannot release all the shear strain built up in the system and many plastic events are generated, which leads to a more uniform strain distribution in MGs. It is expected that the strain rate dependence of strain localization in NGs appears to be similar to that observed in MGs. Therefore, to have a fair comparison between the deformation of NG samples and those of NG nanopillars discussed in this Chapter, we recalculate the result for NG samples at strain rate of 4×10^{8} s^{-1}.

Fig. 5-10 shows the stress-strain response of the NG samples. It can be seen that NG samples with $d_g \geq 10$ nm show the typical stress drop after yield point. However, NG with $d_g = 5$ nm shows a very gradual decay in the stress-strain curve. NG with $d_g = 3$ nm shows the flat stress-strain plot after yield point which is an indication of homogeneous deformation in the sample. In contrast, Fig. 5-3a that for NG nanopillars at all grain sizes a graceful decay in stress-strain occur after yield point and the stress drop disappear entirely. In addition, a transition in deformation mechanism from localized necking to homogeneous flow is observed at NG nanopillar with $d_g = 3$ nm. That clearly show that the use of nanopillar shape introduce significant effects in the deformation of NG systems, in particular the induced NG ductility is enhanced.

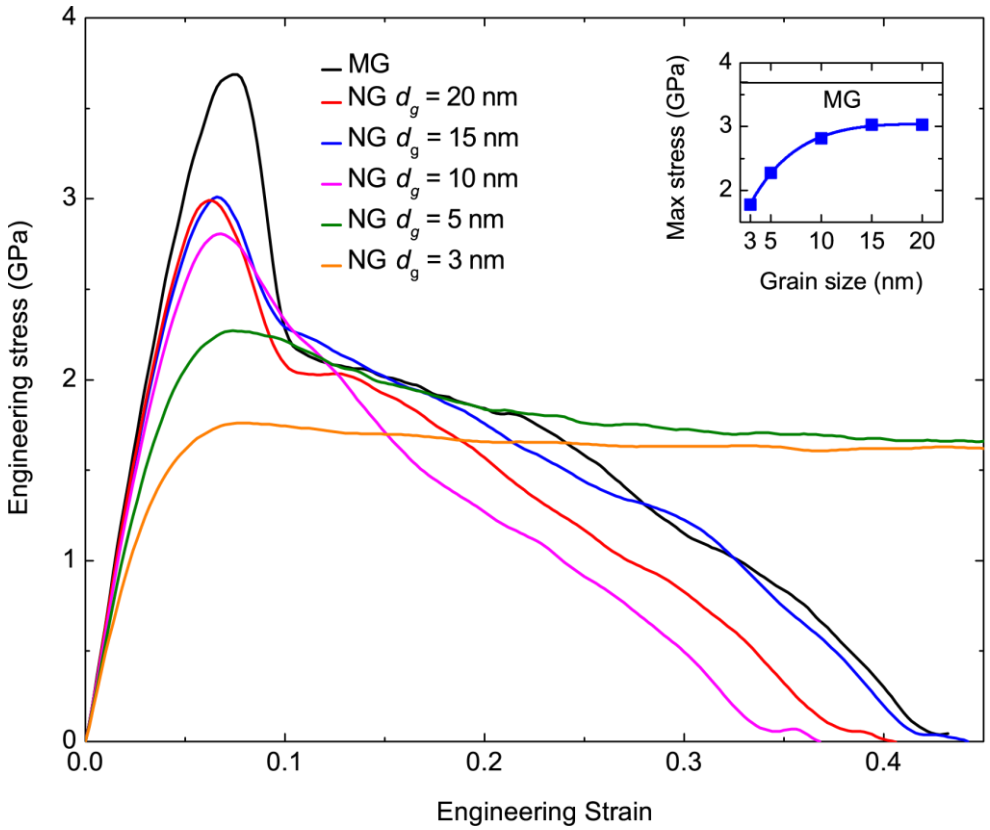

Figure 5-10 Engineering stress- strain curves for MG sample and NG samples with d_g = 20, 15, 10, 5 and 3 nm.

In order to investigate the deformation mechanism in NG samples, images of the MG and NG samples, sliced to view the interior, are shown in Fig. 5-11. Atoms are colored according to the local von Mises shear strain. At strain ~ 0.07, immediately after a major stress drop in the stress-strain plot (see Fig. 5-10), a path of high strain is percolating across the NG samples with $d_g \geq 10$ nm width. This localization path is created through percolation of high strain in GB regions. The strain along this path intensifies with progressive straining, with the colors in Fig. 5-11shifting from light blue to dark red. This also appears as a thickening of the GB strain path. Secondary SBs conduit in the samples, but the highest strain occurs along the initial path. However, at $d_g \leq 5$ nm a discrete distribution of plastic deformation in the samples are observed. This discrete

plastic deformation leads to the homogeneous deformation of the NGs. From previous analysis of atomic fractions at interfaces, it is clear that a smaller grain size indicates that a larger volume fraction of the sample is interfacial material, making it easier to spread the plastic strain in the sample. Therefore, the simulation on NG samples (see Fig. 5-11) show a transition from localized SB formation to homogeneous deformation at d_g = 5 nm.

In comparison, it can be seen in Fig. 5-4 that for NG nanopillar samples during the early stage of plastic deformation, high shear strain occur at GBs that are evenly dispersed throughout the sample. However, in the three dimensional grain structure of NG nanopillars, the random orientation of grains offer no easy path for the strain accommodation along their GBs. NG samples of all grain sizes beyond 5 nm fail by generation and propagation of a single SB. In contrast, the results for NG nanopillars shown in Fig. 5-4 indicate that while the initial deformation takes place at NG interfaces they do not form a convenient path for propagation of an SB across the system since the nanopillars grains have a 3D random orientation. That is true even for large grains at d_g = 20 nm, see Fig. 5-4b. The induced necking for the NG nanopillars is a consequence of the suppression of SB propagation coming from the 3D grain structure and the presence of free surfaces throughout the whole circumference of the nanopillars. Therefore, it should be noted that while the reference NG samples show a transition from localized SB to homogeneous deformation on grain size reduction, NG nanopillars show a complex transition from localized SB, to necking, to homogeneous deformation.

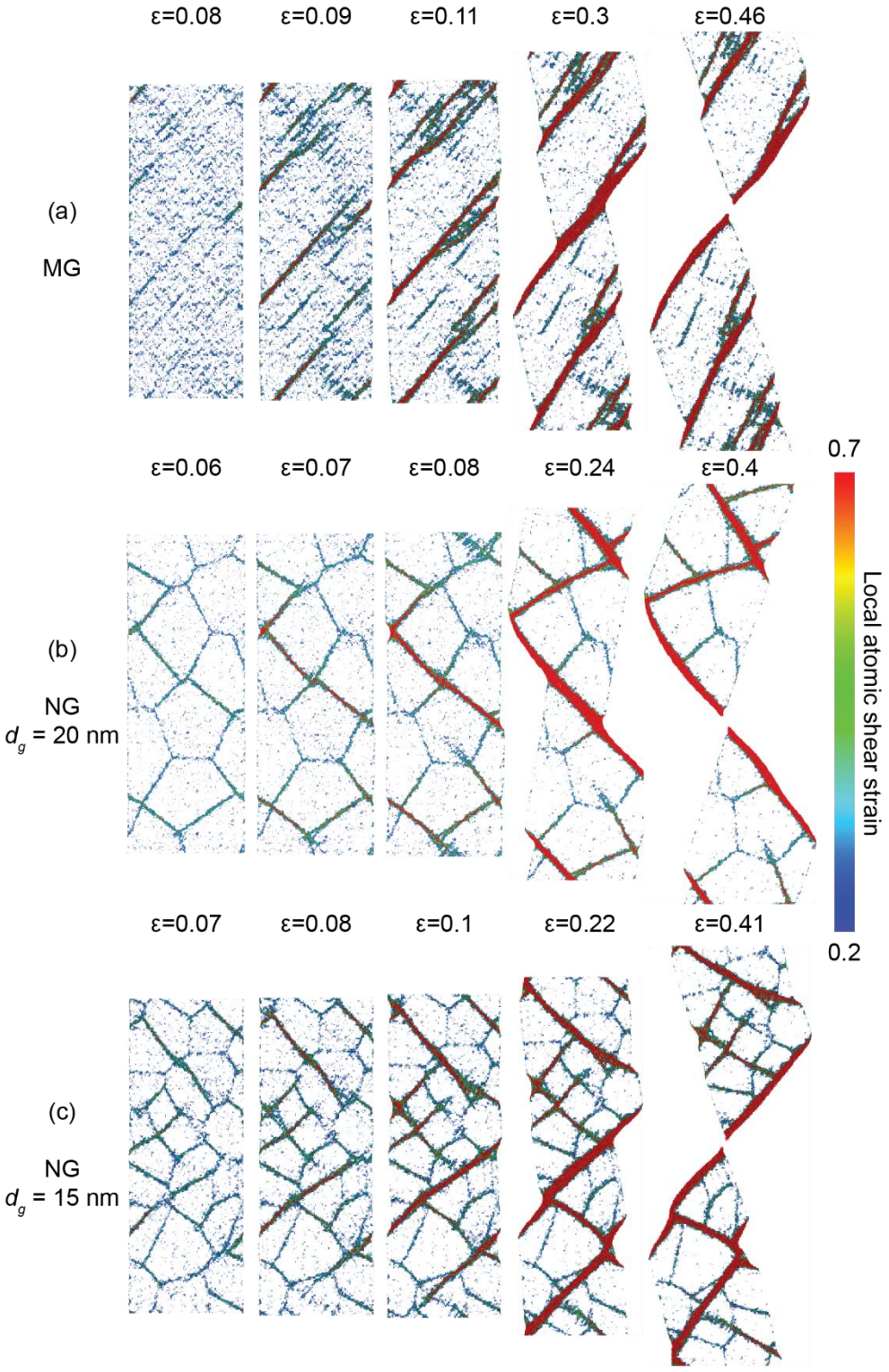

Figure 5-11 Illustrations of the deformation and failure of MG and NG samples. (a)–(f) Sequence of snapshots capturing the atomic deformation processes for MG and NG samples with d_g = 20, 15, 10, 5 and 3 nm, respectively. The colour indicates the local atomic shear strain. For clarity, only atoms with local atomic shear strain higher than 0.2 are shown. (continued)

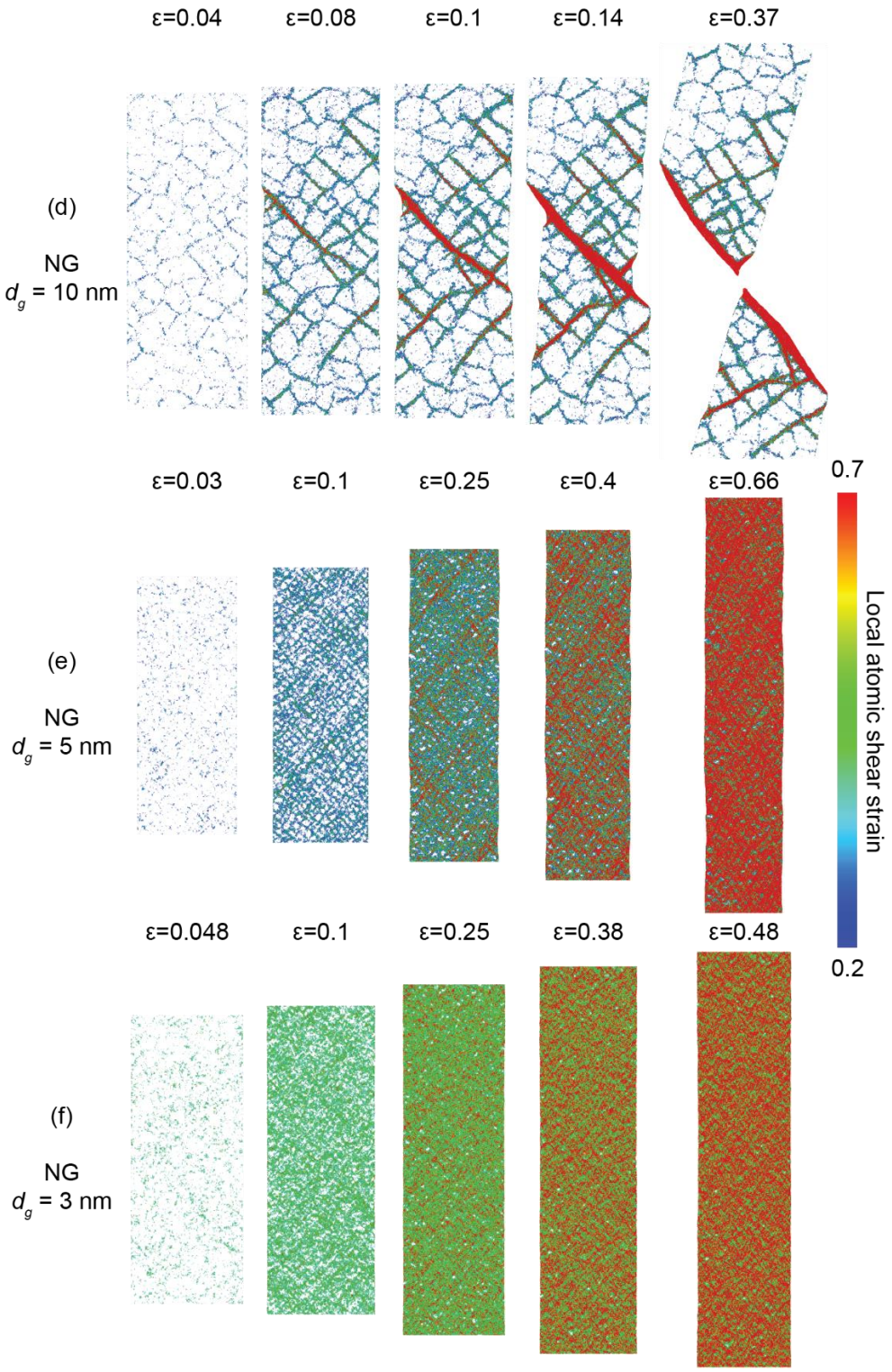

Figure 5-11 Illustrations of the deformation and failure of MG and NG samples. (a)–(f) Sequence of snapshots capturing the atomic deformation processes for MG sample and NG samples with d_g = 20, 15, 10, 5 and 3 nm, respectively. The colour indicates the local atomic shear strain. For clarity, only atoms with local atomic shear strain higher than 0.2 are shown.

It is also instructive to highlight the differences in strain localization in MG and NG nanopillars and those in the reference samples by using the DPR. The DPR calculated at different grain sizes and $\varepsilon = 0.11$ and $\varepsilon = 0.35$ in shown in Fig. 5-12. The DPR values calculated for the NG nanopillars are plotted in Fig. 5-12a and those for the MG and NG reference systems in Fig. 5-12b. One of the contrasting features of the curves is at $d_g = 5$ nm. One can see at $\varepsilon = 0.11$ that the DPR values for both cases are ~ 0.6 which indicates homogeneous deformation in early stage of deformation. However, at $\varepsilon = 0.35$ the DPR for NG nanopillar decrease to ~ 0.3, which can be explained by accumulation of plastic deformation in necking area (see Fig. 5-4e). For $d_g \geq 10$ nm, DPR values decrease in both cases. The higher DPR values for NG nanopillar samples with $d_g \geq 10$ nm, compared to those of the NG reference system, indicate a lower degree of localization in nanopillars. That is a direct consequence of the necking in NG nanopillars as compared to localized SB in the reference system.

Another aspect to be discussed is the amount of interfacial material in an NG nanopillar as compared to the reference system. It was demonstrated that interfacial regions play a very important role in the induced plasticity in NGs. Therefore, the higher plasticity shown in NG nanopillars maybe related to the fraction of interfacial material. The fraction of interfaces in NG nanopillar samples are shown in Fig. 5-9 and for reference NG samples in Fig. 4-11b. It can be seen that for $d_g = 3$ nm the interfacial fraction is ~90% for both NG sample and pillar geometry. However, the values diverge quickly for larger grain sizes. NG nanopillars have larger interfacial fractions compared to reference NG samples by ~ 19%, 63% and 100% at grain sizes 5, 10, and 15 nm, respectively. These differences in the interfacial fraction explain the higher

degree of plasticity in the nanopillars at these grain sizes. In particular, nanopillars have a higher percentage of triple and higher junctions due to the 3D grain structure.

One may notice that the formation of an easy shear path across the NG sample is essential for strain localization. This path can be formed through induced plasticity in GBs. When the strain path is shaped, it is accompanied by rapid strain localization along that same plane and significant stress driven grain growth. However, These GB localization mechanisms is limited by grain size and structure and connectivity of the GB network, hence limits the localization path in MGs. Based on the above observation one of the potential methods for suppressing strain localization in NGs is by breaking up the GB percolation path. It can be done by 3D grain structure of NGs, similar to the one shown in NG nanopillars. The significance of an interfacial path for strain localization shows that GB engineering, the designed modification of the interfacial network topology and character might be an effective way for strain localization prevention.

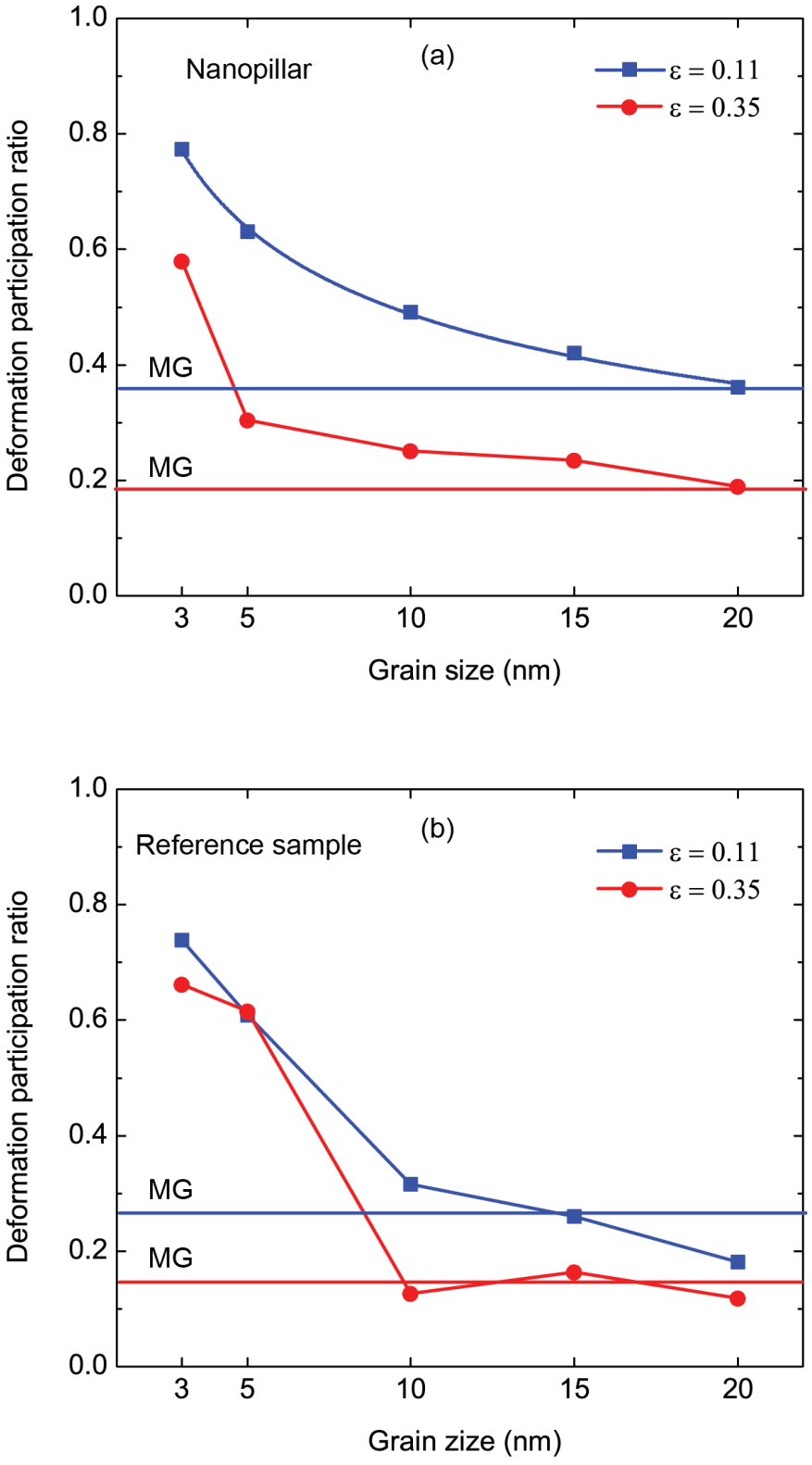

Figure 5-12 DPR for MG and NG (a) nanopillars, and (b) reference sample at different grain sizes at macroscopic strain of ε = 0.11 and ε = 0.35. Solid lines indicate the DPR values for MG samples and nanopillars.

5.5 Summary

Our results reveal induced NG ductility and failure by necking at all grain sizes in NG nanopillars with d_g = 3 – 20 nm, in contrast to brittle failure by SB propagation in MG nanopillars. In addition, we observe a continuous increase in homogeneous ductility on grain size reduction resulting in nearly superplastic flow at d < 5 nm in NG nanopillars. Ductility is generated at interfacial regions, which act as preferred channels for plasticity, causing a generation of an interconnected motif of localized shear deformation zones. The degree of deformation homogeneity and the corresponding overall ductility is directly dependent on the nanostructure characteristic size and structure and connectivity of the GB network. The 3D grain structure in NG nanopillar can breakdown the localized SB path along the NG interfaces. Necking and induced plasticity occur in NG nanopillars at all grain sizes. Given the experimentally realisable NG nanopillars geometry with a 3D distribution of grains, we conclude that they offer meaningful results to guide the development of MGs with enhanced mechanical properties. The results highlight the surprising effects of NG architectures in amorphous metallic alloys and indicate that grain size, structure, and connectivity of GB network are effective design parameter to tune the ductility of MGs.

Part IV

CONCLUSIONS

6. Conclusion and Future Directions

As the primary objective of the present thesis, we characterized the structure, mechanical properties, and deformation mechanism of MGs and NGs in the nano size scale through large-scale MD simulations. A summary of the key results follows:

- We quantified the extrinsic effects of nanoscale geometrical factors (diameter and aspect ratio) as well as the applied strain rate on the mechanical response and deformation mechanism of nanoscale MG samples. For these quantifications, we performed large-scale tensile loading MD simulations of $Cu_{64}Zr_{36}$ MG nanopillars. Our results provided evidence for a transition in MG failure mode with the loading strain rate. At low strain rate regime ($10^7 s^{-1}$), the plastic deformation in the nanopillars was generated at the yield point by nucleation of one dominant SB. Increasing strain rate from $10^7 s^{-1}$ to $10^9 s^{-1}$ led to a transition in deformation

mode from a single SB to multiple SBs, and increased the plastic flow and necking. Longer MG nanopillars failed at smaller strains, in contrast with smaller ones. This can be explained in terms of the capacity of nanopillars with high aspect ratio to store more elastic energy for a given strain. This allows the full propagation of SBs across the pillars at the yield point. Simulations of smooth nanopillars with diameters in the range of 10 nm to 100 nm showed similar stress-strain curves, plastic behavior, and failure, implying little dependence on diameter.

- We studied the role of surface imperfection on the failure mechanism of nanoscale MGs. We focused on the MG nanopillars with diameters ranging from 5 to 100 nm, and with a 1 nm U-shape notch carved along their circumference. The simulations indicated that the presence of surface imperfection on the surface of MG nanopillars induces brittle to necking transition in their failure mode. This transition occurs below a certain diameter relative to the notch depth ratio ($d/a < 25$). We concluded that the specimen size and surface imperfections are key parameters that effectively modulate the macroscopic characteristics of MG nano-scaled specimens.
- We introduced the NG microstructure as an alternative to enhance the ductility of MGs. We quantified the mechanical properties and deformation mechanism of NGs, in particular, their plasticity, for different grain sizes, and then we compared these results with those of MGs. While conventional MG samples fail catastrophically through localization – due to formation of a single dominant SB, – NG architectures exhibited a homogenized plastic deformation as the grain size decrease. This can be explained by the

fact that NG grain boundaries act as hot spots for heterogeneous generation of SBs, changing drastically the observed deformation profile.

- We then furthered the analysis to the effects of NG composition on the mechanical and structural properties and deformation mechanism of $Cu_{36}Zr_{64}$, $Cu_{50}Zr_{50}$, and $Cu_{64}Zr_{36}$ NGs with different grain sizes under tensile loading. All compositions showed the localized to near homogeneous deformation transition. The corresponding grain size to this transition depends on the NG compositions. The statistics of atomic Voronoi polyhedral at grains and grain boundaries, the grain boundary thickness, and the fraction of the bulk and interfacial regions are key parameters, which determined the transition grain size in NG compositions.
- Additionally, we expanded the analysis to the effect of the design and topology of NG grains on their failure mechanism. We observed that the three dimensional grain structure in NG nanopillars break down the localized path along the NG interfaces and induce necking for all grain sizes. We demonstrated that the grain size, its structure, and the connectivity of grain boundaries are key parameters in controlling the localization path along NG interfaces, and hence, determining the failure mode.

One of the key contributions of this study is the comprehensive analysis on the effect of different extrinsic parameters on the mechanical properties and deformation mechanisms of nanoscale MGs. The corresponding results provide insight into the intrinsic failure mechanisms in nanoscale MGs, and shed light on the unclear aspects of the BDT in nanoscale MGs. Additionally, our results expanded the current knowledge on the deformation mechanism of the novel MGs with enhanced plasticity (NGs). We characterized the effect of the design

and composition of these materials' microstructure on their deformation mechanism. The simulation results of the present study predict that MGs with exceptional plasticity may be conveniently generated by using the NG design. That suggests novel and wide spread application of MG in different fields such as space and automobile industry.

6.1 Future work

Here I enumerate a number of ongoing and future directions of this research.

- In studying the effect of surface imperfection, we simulated nanopillars with a U-shape notch along the nanopillar circumference. A notch was chosen as a basic unit of surface imperfection. It provided a good model for studying and understanding the experimentally observed BDT in MGs. However, a more realistic representation for the experimental roughness surface would naturally be a combination of multiple surface notches. Further simulations to understand and characterize the induced deformations by a *rough* nanopillar surface model are currently in progress.
- We showed that multiple SB formation enhances plasticity in MGs. However, the extent to which other mechanisms such as hardening and cavitation in the intersection of SBs may contribute to the deformation is not clear. Further experiments are required in order to identify the contribution of these mechanisms. Experimental results show the evidence of hardening in MG pillars with a deep notch. A further step is the investigation of the contribution of hardening mechanisms through structural characterization of the simulated necked area in notched nanopillars.

- We showed that for the diameter to notch depth ratio less than 25, BDT occurs in nanoscale MGs with surface imperfection. It is an open question whether this pattern occurs at micro- and macro- scale regimes. The methodology to probe this is through modeling MGs at a larger scale by phase field or finite element methods.
- NGs have been studied for a very limited number of alloy systems. Future research should attempt to study the effect of chemical composition on the mechanical properties and deformation mechanism of NGs.
- Here we studied the mechanical properties of chemically homogeneous NGs. The extent to which NGs composites comprising glassy grains of different composition (or grain sizes) exhibit a homogeneous plastic deformation similar to chemically homogeneous NGs is still unknown. Do compacting soft and hard glassy grains yield NGs as strong as the hard glassy alloy while exhibiting an improved plasticity provided by the soft alloy? It is also interesting to investigate the mechanical properties and plasticity of multi-layer NG composites.
    - Studying the thermodynamic and physical properties of NGs pave the way for better understanding of NGs and their deformation mechanism to enhance the plasticity. Additionally, this opens avenues towards finding new approaches to improve mechanical properties of NGs.

List of Publication

Journals:

Sara Adibi, Paulo S Branicio, Yong-Wei Zhang, Shailendra P Joshi. (2014) Composition and grain size effects on the structural and mechanical properties of CuZr Nanoglasses. Journal of Applied Physics, 116, 4, 043522.

Sara Adibi, Zhen-Dong Sha, Paulo S. Branicio, Shailendra P. Joshi, Zi-Shun Liu, Yong-Wei Zhang. (2013) A transition from localized shear banding to homogeneous superplastic flow in nanoglass. Applied Physics Letters, 103, 211905.

Prakash Thamburaja, Benjamin Klusemann, **Sara Adibi,** and Swantje Bargmann. (2015) The plastic yield and flow behavior in metallic glasses. Appl. Phys. Lett. 106, 051903.

Sara Adibi, Paulo S. Branicio, Shailendra P. Joshi. (2014) Harnessing surface imperfections to impart tensile ductility in metallic glass, to be submitted.

Sara Adibi, Paulo S. Branicio, Shailendra P. Joshi. (2014) Nanostructure induced tunable ductility in metallic glasses, to be submitted.

Sara Adibi, Paulo S. Branicio, Shailendra P. Joshi. (2014) Molecular dynamics simulation of nanoglass-metallic galss composites, to be submitted.

Conferences:

Sara Adibi, Paulo S. Branicio, Shailendra P. Joshi. (2013) Molecular dynamics simulations of metallic nanoglasses. 5th Asia Pacic Congress on Computational Mechanics (APCOM2013) and ISCM 2013, 11th-14th December, Singapore. Oral presentation.

Sara Adibi, Paulo S. Branicio, Shailendra P. Joshi. (2013) Tuneable tensile ductility in nanoengineered metallic glass architecture: An atomistic investigation. The 23rd International Workshop on Computational Mechanics of Materials (IWCMM 23), 2th-4th October, Singapore. Oral presentation.

Sara Adibi, Paulo S. Branicio, Shailendra P. Joshi. (2013) Atomistic investigations of size and strain rate dependence on the mechanical response of nanoscale metallic glass structures. The 3rd LAMMPS workshop and symposium, 6th-8th August, Albuquerque, New Mexico, United States. Poster presentation.

Sara Adibi, Paulo S. Branicio, Shailendra P. Joshi. (2013) Molecular dynamics simulations of metallic nanoglasses. SES 50th Annual Technical Meeting and

ASME- AMD Annual Summer Meeting, 28th-31th July, Brown University, Providence-Rode Island, United States. Oral presentation.

Sara Adibi, Paulo S. Branicio, Shailendra P. Joshi. (2013) Molecular dynamics simulation of size and strain rate dependent mechanical response of metallic glass nano-rods. 12th U.S. National Congress on Computational Mechanics (USNCCM12), 22th-25th July, Raleigh, North Carolina, United States. Oral presentation.

Sara Adibi, Paulo S. Branicio, Shailendra P. Joshi. (2013) Atomistic tensile loading simulations of metallic glass and nanoglass nanofilms. The 12th U.S. National Congress on Computational Mechanics (USNCCM12), 22th-25th July, Raleigh, North Carolina, United States. Poster presentation.

Sara Adibi, Paulo S. Branicio, Shailendra P. Joshi. (2013) Size and Strain Rate effects on the mechanical response of nanopillar metallic glasses: A molecular dynamics study. International Conference on Materials for Advanced Technologies (ICMAT 2013), 30th June-5thJuly, Singapore. Poster presentation.

Sara Adibi, Paulo S. Branicio, Shailendra P. Joshi. (2013) Molecular dynamics simulations of metallic nanoglasses. International Conference on Materials for Advanced Technologies (ICMAT 2013), 30th June-5thJuly, Singapore. Poster presentation. **Winner of Best poster award competition**.

Paulo S. Branicio, **Sara Adibi**, Yong Wei Zhang, Shailendra P. Joshi. (2014) Composition and Grain Size Effects on the Structural and Mechanical Properties of CuZr Nanoglasses. Nano2014, 13th-17th July, Russia. Oral presentation.

References

Adibi, S., Sha, Z.-D., Branicio, P.S., Joshi, S.P., Liu, Z.-S., Zhang, Y.-W., 2013. A transition from localized shear banding to homogeneous superplastic flow in nanoglass. Applied Physics Letters 103, 211905.

Albe, K., Ritter, Y., Şopu, D., 2013. Enhancing the plasticity of metallic glasses: Shear band formation, nanocomposites and nanoglasses investigated by molecular dynamics simulations. Mechanics of Materials 67, 94-103.

Ali, M.Y., Hung, N.P., Yuan, S., 2002. Surface Roughness of FIB Sputtered Silicon, in: Inasaki, I. (Ed.), Initiatives of Precision Engineering at the Beginning of a Millennium. Springer US, pp. 147-151.

Allen, M.P., Tildesley, D.J., 1989. Computer simulation of liquids. Clarendon Press.

Allen, P., Tildesley, D.J., 1987. Computer simulation of liquids. Clarendon Press.

Alpas, A.T., Embury, J.D., 1988. Flow localization in thin layers of amorphous alloys in laminated composite structures. Scripta Metallurgica 22, 265-270.

Andersen, H.C., 1980. Molecular dynamics simulations at constant pressure and/or temperature. The Journal of Chemical Physics 72, 2384-2393.

Ansari, R., Momen, A., Rouhi, S., Ajori, S., 2014. On the Vibration of Single-Walled Carbon Nanocones: Molecular Mechanics Approach versus Molecular Dynamics Simulations. Shock and Vibration 2014, 8.

Argon, A.S., 1979. Plastic deformation in metallic glasses. Acta Metallurgica 27, 47-58.

Berendsen, H.J.C., Postma, J.P.M., van Gunsteren, W.F., DiNola, A., Haak, J.R., 1984. Molecular dynamics with coupling to an external bath. The Journal of Chemical Physics 81, 3684-3690.

Berendsen, H.J.C., van der Spoel, D., van Drunen, R., 1995. GROMACS: A message-passing parallel molecular dynamics implementation. Computer Physics Communications 91, 43-56.

Bharathula, A., Lee, S.-W., Wright, W.J., Flores, K.M., 2010. Compression testing of metallic glass at small length scales: Effects on deformation mode and stability. Acta Materialia 58, 5789-5796.

Bletry, M., Guyot, P., Brechet, Y., Blandin, J.J., Soubeyroux, J.L., 2004. Homogeneous deformation of bulk metallic glasses in the super-cooled liquid state. Materials Science and Engineering: A 387–389, 1005-1011.

Boudreaux, D.S., Frost, H.J., 1981. Short-range order in theoretical models of binary metallic glass alloys. Physical Review B 23, 1506-1516.

Branicio, P.S., Kalia, R.K., Nakano, A., Vashishta, P., 2010. Nanoductility induced brittle fracture in shocked high performance ceramics. Applied Physics Letters 97, 111903.

Branicio, P.S., Kalia, R.K., Nakano, A., Vashishta, P., Shimojo, F., Rino, J.P., 2008. Atomistic damage mechanisms during hypervelocity projectile impact on AlN: A large-scale parallel molecular dynamics simulation study. Journal of the Mechanics and Physics of Solids 56, 1955-1988.

Branício, P.S., Rino, J.-P., 2000. Large deformation and amorphization of Ni nanowires under uniaxial strain: A molecular dynamics study. Physical Review B 62, 16950-16955.

Branicio, P.S., Srolovitz, D.J., 2009. Local stress calculation in simulations of multicomponent systems. Journal of Computational Physics 228, 8467-8479.

Brooks, B.R., Bruccoleri, R.E., Olafson, B.D., States, D.J., Swaminathan, S., Karplus, M., 1983. CHARMM: A program for macromolecular energy, minimization, and dynamics calculations. Journal of Computational Chemistry 4, 187-217.

Brostow, W., Dussault, J.P., B.L. Fox, 1978. Construction of Voronoi polyhedra. J. Comput. Phys. 29, 81-92.

Brothers, A.H., Dunand, D.C., 2006. Amorphous metal foams. Scripta Materialia 54, 513-520.

Bruck, H.A., Christman, T., Rosakis, A.J., Johnson, W.L., 1994. Quasi-static constitutive behavior of Zr41.25Ti13.75Ni10Cu12.5Be22.5 bulk amorphous alloys. Scripta Metallurgica et Materialia 30, 429-434.

Bruck, H.A., Rosakis, A.J., Johnson, W.L., 1996. The dynamic compressive behavior of beryllium bearing bulk metallic glasses. J Mater Res 11, 503-511.
Cahn, R., Greer, A., 1996. Metastable states of alloys. Physical metallurgy 2, 1723.

Campbell, T.J., 1998. Nanostructure modelling in oxide ceramics using large scale parallel molecular dynamics simulations, The Department of Physics and Astronomy. Louisiana State University.

Cao, A.J., Cheng, Y.Q., Ma, E., 2009. Structural processes that initiate shear localization in metallic glass. Acta Materialia 57, 5146-5155.
Cao, Q.P., Liu, J.W., Yang, K.J., Xu, F., Yao, Z.Q., Minkow, A., Fecht, H.J., Ivanisenko, J., Chen, L.Y., Wang, X.D., Qu, S.X., Jiang, J.Z., 2010. Effect of

pre-existing shear bands on the tensile mechanical properties of a bulk metallic glass. Acta Materialia 58, 1276-1292.

Cao, Q.P., Ma, Y., Wang, C., Wang, X.D., Jiang, J.Z., 2013. Effect of temperature and strain rate on deformation behavior in metallic glassy films. Thin Solid Films, 10.1016/j.tsf.2013.1005.1176.

Chen, C.Q., Pei, Y.T., De Hosson, J.T.M., 2010. Effects of size on the mechanical response of metallic glasses investigated through in situ TEM bending and compression experiments. Acta Materialia 58, 189-200.

Chen, C.Q., Pei, Y.T., Kuzmin, O., Zhang, Z.F., Ma, E., De Hosson, J.T.M., 2011. Intrinsic size effects in the mechanical response of taper-free nanopillars of metallic glass. Physical Review B 83, 180201.

Chen, D.Z., Jang, D., Guan, K.M., An, Q., Goddard, W.A., Greer, J.R., 2013. Nanometallic Glasses: Size Reduction Brings Ductility, Surface State Drives Its Extent. Nano Letters, 130830114009009.

Chen, H., He, Y., Shiflet, G.J., Poon, S.J., 1994. Deformation-induced nanocrystal formation in shear bands of amorphous alloys. Nature 367, 541-543.

Chen, H.S., 1974. Thermodynamic considerations on the formation and stability of metallic glasses. Acta Metallurgica 22, 1505-1511.

Chen, H.S., Turnbull, D., 1969. Formation, stability and structure of palladium-silicon based alloy glasses. Acta Metallurgica 17, 1021-1031.

Chen, H.S., Wang, T.T., 1970. Mechanical properties of metallic glasses of pdsingle bond signsi-based alloys. Journal of Applied Physics 41, 5338-5339.

Cheng, S., Wang, X.-L., Choo, H., Liaw, P.K., 2007. Global melting of $Zr_{57}Ti_5Ni_8Cu_{20}Al_{10}$ bulk metallic glass under microcompression. Applied Physics Letters 91, 201917.

Cheng, Y.Q., Cao, A.J., Ma, E., 2009a. Correlation between the elastic modulus and the intrinsic plastic behavior of metallic glasses: The roles of atomic configuration and alloy composition. Acta Materialia 57, 3253-3267.

Cheng, Y.Q., Cao, A.J., Sheng, H.W., Ma, E., 2008a. Local order influences initiation of plastic flow in metallic glass: Effects of alloy composition and sample cooling history. Acta Materialia 56, 5263-5275.

Cheng, Y.Q., Han, Z., Li, Y., Ma, E., 2009b. Cold versus hot shear banding in bulk metallic glass. Physical Review B 80, 134115.

Cheng, Y.Q., Ma, E., 2008. Indicators of internal structural states for metallic glasses: Local order, free volume, and configurational potential energy. Applied Physics Letters 93, 051910.

Cheng, Y.Q., Ma, E., 2011. Atomic-level structure and structure–property relationship in metallic glasses. Progress in Materials Science 56, 379-473.

Cheng, Y.Q., Sheng, H.W., Ma, E., 2008b. Relationship between structure, dynamics, and mechanical properties in metallic glass-forming alloys. Physical Review B 78, 014207.

Choi, Y.C., Hong, S.I., 2009. Enhancement of plasticity in Zr-base bulk metallic glass by soft metal plating. Scripta Materialia 61, 481-484.

Chu, J.P., Greene, J.E., Jang, J.S.C., Huang, J.C., Shen, Y.-L., Liaw, P.K., Yokoyama, Y., Inoue, A., Nieh, T.G., 2012. Bendable bulk metallic glass: Effects of a thin, adhesive, strong, and ductile coating. Acta Materialia 60, 3226-3238.

Cohen, M.H., Turnbull, D., 1959. Molecular Transport in Liquids and Glasses. The Journal of Chemical Physics 31, 1164-1169.

Cyrot-Lackmann, F., 1980. Elastic properties of a metallic glass relative to the crystal. Physical Review B 22, 2744-2748.

Delogu, F., 2009. Molecular dynamics study of size effects in the compression of metallic glass nanowires. Physical Review B 79.

Deng, Q., Cheng, Y., Yue, Y., Zhang, L., Zhang, Z., Han, X., Ma, E., 2011. Uniform tensile elongation in framed submicron metallic glass specimen in the limit of suppressed shear banding. Acta Materialia 59, 6511-6518.

Dieter, G.E., Bacon, D.J., 1988. Mechanical Metallurgy. MCGRAW-HILL Higher Education.

Ding, J., Cheng, Y.-Q., Ma, E., 2014. Full icosahedra dominate local order in Cu64Zr34 metallic glass and supercooled liquid. Acta Materialia 69, 343-354.

Dong, W., Zhang, H., Sun, W., Wang, A., Li, H., Hu, Z., 2011. Zr-Cu-Ni-Al-Ta glassy matrix composites with enhanced plasticity. J Mater Res 21, 1490-1499.

Donovan, P.E., 1989. A yield criterion for Pd40Ni40P20 metallic glass. Acta Metallurgica 37, 445-456.

Drehman, A.J., 1982. Bulk formation of a metallic glass: Pd40Ni40P20. Applied Physics Letters 41, 716.

Duan, G., Lind, M.L., Demetriou, M.D., Johnson, W.L., Goddard, W.A., Çağin, T., Samwer, K., 2006. Strong configurational dependence of elastic properties for a binary model metallic glass. Applied Physics Letters 89, 151901.

Duan, G., Xu, D., Zhang, Q., Zhang, G., Cagin, T., Johnson, W.L., Goddard, W.A., 2005. Molecular dynamics study of the binary $Cu_{46}Zr_{54}$ metallic glass motivated by experiments: Glass formation and atomic-level structure. Physical Review B 71, 224208.

Dubach, A., Raghavan, R., Loffler, J., Michler, J., Ramamurty, U., 2009. Micropillar compression studies on a bulk metallic glass in different structural states. Scripta Materialia 60, 567-570.

Dürr, M., Höfer, U., 2013. Hydrogen diffusion on silicon surfaces. Progress in Surface Science 88, 61-101.

Eckert, J., Schultz, L., Hellstern, E., Urban, K., 1988. Glass-forming range in mechanically alloyed Ni-Zr and the influence of the milling intensity. Journal of Applied Physics 64, 3224.

Falk, M.L., 1999. Molecular-dynamics study of ductile and brittle fracture in model noncrystalline solids. Physical Review B 60, 7062-7070.

Falk, M.L., Langer, J.S., 1998. Dynamics of viscoplastic deformation in amorphous solids. Physical Review E - Statistical Physics, Plasmas, Fluids, and Related Interdisciplinary Topics 57, 7192-7205.

Fan, C., Li, C., Inoue, A., Haas, V., 2000. Deformation behavior of Zr-based bulk nanocrystalline amorphous alloys. Physical Review B 61, R3761-R3763.

Fang, J.X., Vainio, U., Puff, W., Würschum, R., Wang, X.L., Wang, D., Ghafari, M., Jiang, F., Sun, J., Hahn, H., Gleiter, H., 2012. Atomic Structure and Structural Stability of Sc75Fe25Nanoglasses. Nano Letters 12, 458-463.

Finney, J.L., 1970. Random Packings and the Structure of Simple Liquids. I. The Geometry of Random Close Packing. Proceedings of the Royal Society A: Mathematical, Physical and Engineering Sciences 319, 479-493.

Finney, J.L., 1979. A procedure for the construction of Voronoi polyhedra. J. Comput. Phys. 32, 137-143.

Flores, K.M., Dauskardt, R.H., 1999. Enhanced toughness due to stable crack tip damage zone in bulk metallic glass. Scr. Mater. 41, 937.

Flores, K.M., Dauskardt, R.H., 2001. Mean stress effects on flow localization and failure in a bulk metallic glass. Acta Materialia 49, 2527-2537.

Foiles, S.M., Baskes, M.I., Daw, M.S., 1986. Embedded-atom-method functions for the fcc metals Cu, Ag, Au, Ni, Pd, Pt, and their alloys. Physical Review B 33, 7983-7991.

Franke, O., Leisen, D., Gleiter, H., Hahn, H., 2014. Thermal and plastic behavior of nanoglasses. J Mater Res 29, 1210.

Ghafari, M., Hahn, H., Gleiter, H., Sakurai, Y., Itou, M., Kamali, S., 2012a. Evidence of itinerant magnetism in a metallic nanoglass. Applied Physics Letters 101, 243104.

Ghafari, M., Kohara, S., Hahn, H., Gleiter, H., Feng, T., Witte, R., Kamali, S., 2012b. Structural investigations of interfaces in Fe90Sc10 nanoglasses using high-energy x-ray diffraction. Applied Physics Letters 100, 133111.

Gleiter, H., 1991. Nanocrystalline solids. Journal of Applied Crystallography 24, 79-90.

Gleiter, H., 2008. Our thoughts are ours, their ends none of our own: Are there ways to synthesize materials beyond the limitations of today? Acta Materialia 56, 5875-5893.

Gleiter, H., 2009. Nanoscience and Nanotechnology: The Key to New Studies in Areas of Science Outside of Nanoscience and Nanotechnology. Mrs Bulletin 34, 456-464.

Greer, A.L., 1995. Metallic Glasses. Science 267, 1947-1953.

Greer, A.L., Cheng, Y.Q., Ma, E., 2013. Shear bands in metallic glasses. Materials Science and Engineering: R: Reports 74, 71-132.

Greer, A.L., Ma, E., 2007. Bulk Metallic Glasses: At the Cutting Edge of Metals Research. Mrs Bulletin 32, 611-619.

Greer, J.R., De Hosson, J.T.M., 2011. Plasticity in small-sized metallic systems: Intrinsic versus extrinsic size effect. Progress in Materials Science 56, 654-724.

Gu, X., Jiao, T., Kecskes, L.J., Woodman, R.H., Fan, C., Ramesh, K.T., Hufnagel, T.C., 2003. Crystallization and mechanical behavior of (Hf, Zr)–Ti–Cu–Ni–Al metallic glasses. J Non-Cryst Solids 317, 112-117.

Gu, X.W., Jafary-Zadeh, M., Chen, D.Z., Wu, Z., Zhang, Y.-W., Srolovitz, D.J., Greer, J.R., 2014. Mechanisms of Failure in Nanoscale Metallic Glass. Nano Letters 14, 5858-5864.

Gu, X.W., Loynachan, C.N., Wu, Z., Zhang, Y.-W., Srolovitz, D.J., Greer, J.R., 2012. Size-Dependent Deformation of Nanocrystalline Pt Nanopillars. Nano Letters 12, 6385-6392.

Guo, H., Yan, P.F., Wang, Y.B., Tan, J., Zhang, Z.F., Sui, M.L., Ma, E., 2007. Tensile ductility and necking of metallic glass. Nat Mater 6, 735-739.

H. Gleiter, T.S., H. Hahn, 2014. Nanostructured solids — From nano-glasses to quantum transistors.

Haile, J.M., 1997. Molecular Dynamics Simulation: Elementary Methods. Wiley.

Hays, C.C., Kim, C.P., Johnson, W.L., 2000. Microstructure Controlled Shear Band Pattern Formation and Enhanced Plasticity of Bulk Metallic Glasses Containing *in situ* Formed Ductile Phase Dendrite Dispersions. Physical Review Letters 84, 2901-2904.

Hays, C.C., Kim, C.P., Johnson, W.L., 2001. Improved mechanical behavior of bulk metallic glasses containing in situ formed ductile phase dendrite dispersions. Materials Science and Engineering: A 304–306, 650-655.

He, G., Eckert, J., Löser, W., Schultz, L., 2002. Novel Ti-base nanostructure–dendrite composite with enhanced plasticity. Nature Materials 2, 33-37.

He, L., Zhong, M.B., Han, Z.H., Zhao, Q., Jiang, F., Sun, J., 2008. Orientation effect of pre-introduced shear bands in a bulk-metallic glass on its "work-ductilising". Materials Science and Engineering A 496, 285-290.

Heck, D., Schl, T., Deussen, O., 2013. Blue noise sampling with controlled aliasing. ACM Trans. Graph. 32, 1-12.

Heggen, M., Spaepen, F., Feuerbacher, M., 2005. Creation and annihilation of free volume during homogeneous flow of a metallic glass. Journal of Applied Physics 97, 033506.

Henann, D.L., Anand, L., 2009. Fracture of metallic glasses at notches: Effects of notch-root radius and the ratio of the elastic shear modulus to the bulk modulus on toughness. Acta Materialia 57, 6057-6074.

Hess, P.A., Poon, S.J., Shiflet, G.J., Dauskardt, R.H., 2011. Indentation fracture toughness of amorphous steel. J Mater Res 20, 783-786.

Hofmann, D.C., Suh, J.Y., Wiest, A., Duan, G., Lind, M.L., Demetriou, M.D., Johnson, W.L., 2008. Designing metallic glass matrix composites with high toughness and tensile ductility. Nature 451, 1085-1089.

Hoover, W.G., 1985. Canonical dynamics: Equilibrium phase-space distributions. Physical Review A 31, 1695-1697.

Hoover, W.G., 1988. Reversible mechanics and time's arrow. Physical Review A 37, 252-257.

Huang, L., Wang, C.Z., Hao, S.G., Kramer, M.J., Ho, K.M., 2010. Short- and medium-range order in amorphous Zr_2Ni metallic alloy. Physical Review B 81, 094118.

Hufnagel, T.C., Brennan, S., 2003. Short- and medium-range order in $(Zr_{70}Cu_{20}Ni_{10})_{90-x}Ta_xAl_{10}$ bulk amorphous alloys. Physical Review B 67, 014203.

Humphrey, W., Dalke, A., Schulten, K., 1996. VMD: Visual molecular dynamics. Journal of Molecular Graphics 14, 33-38.

Inoue, A., 2000. Stabilization of metallic supercooled liquid and bulk amorphous alloys. Acta Materialia 48, 279-306.

Inoue, A., Takeuchi, A., 2002. Recent progress in bulk glassy alloys. Materials Transactions 43, 1892-1906.

Inoue, A., Zhang, T., Masumoto, T., 1990. Production of Amorphous Cylinder and Sheet of $La_{55}Al_{25}Ni_{20}$ Alloy by a Metallic Mold Casting Method. Materials Transactions, JIM 31, 425-428.

Jang, D., Greer, J.R., 2010. Transition from a strong-yet-brittle to a stronger-and-ductile state by size reduction of metallic glasses. Nat Mater 9, 215-219.

Jang, D.C., Gross, C.T., Greer, J.R., 2011. Effects of size on the strength and deformation mechanism in Zr-based metallic glasses. Int. J. Plasticity 27, 858-867.

Jing, J., Kramer, A., Birringer, R., Gleiter, H., Gonser, U., 1989. Modified atomic-structure in Pd-Fe-Si nanoglass- A Mossbauer study. J Non-Cryst Solids 113, 167-170.

Jinghan Wang, J.L., and Sidney Yip 1995. Mechanical instabilities of homogeneous crystals. Physical Review B 52, 12627.

Johnson, W., Samwer, K., 2005. A Universal Criterion for Plastic Yielding of Metallic Glasses with a (T/Tg)2/3 Temperature Dependence. Physical Review Letters 95.

Johnson, W.L., 1999. Bulk glass-forming metallic alloys: science and technology. MRS Bulletin 24, 42-56.

Jones, J.E., 1924. On the Determination of Molecular Fields. II. From the Equation of State of a Gas. Proceedings of the Royal Society A: Mathematical, Physical and Engineering Sciences 106, 463-477.

Joshi, S.P., Ramesh, K.T., 2008. Stability map for nanocrystalline and amorphous materials. Phys. Rev. Lett. 101, 025501.
Kato, H., Kawamura, Y., Inoue, A., Masumoto, T., 1997. Bulk glassy Zr-based alloys prepared by consolidation of glassy alloy powders in supercooled liquid region. Materials Science and Engineering: A 226–228, 458-462.

Kawamura, Y., Nakamura, T., Inoue, A., 1999. Superplasticity in Pd40Ni40P20 metallic glass, in: Sakuma, T., Aizawa, T., Higashi, K. (Eds.), Towards Innovation in Superplasticity Ii. Transtec Publications Ltd, Zurich-Uetikon, pp. 349-354.

Khonik, S.V., Granato, A.V., Joncich, D.M., Pompe, A., Khonik, V.A., 2008. Evidence of Distributed Interstitialcy-Like Relaxation of the Shear Modulus due to Structural Relaxation of Metallic Glasses. Physical Review Letters 100, 065501.

Kim, J.Y., Jang, D.C., Greer, J.R., 2011. Nanolaminates Utilizing Size-Dependent Homogeneous Plasticity of Metallic Glasses. Adv. Funct. Mater. 21, 4550-4554.

Kipp, M.E., Grady, D.E., 1985. Dynamic fracture growth and interaction in one dimension. Journal of the Mechanics and Physics of Solids 33, 399-415.

Klement, W., Willens, R.H., Duwez, P., 1960. Non-Crystalline Structure in Solidified Gold-Silicon Alloys. Nature 187, 869-870.

Koh, S., Lee, H., Lu, C., Cheng, Q., 2005. Molecular dynamics simulation of a solid platinum nanowire under uniaxial tensile strain: Temperature and strain-rate effects. Physical Review B 72, 085414.

Kohn, W., Sham, L.J., 1965. Self-Consistent Equations Including Exchange and Correlation Effects. Physical Review 140, A1133-A1138.

Kui, H.W., Greer, A.L., Turnbull, D., 1984. Formation of bulk metallic glass by fluxing. Applied Physics Letters 45, 615.

Kumar, G., Desai, A., Schroers, J., 2011. Bulk Metallic Glass: The Smaller the Better. Advanced Materials 23, 461-476.

Kuzmin, O.V., Pei, Y.T., Chen, C.Q., De Hosson, J.T.M., 2012. Intrinsic and extrinsic size effects in the deformation of metallic glass nanopillars. Acta Metall. 60, 889-898.

Kuzmin, O.V., Pei, Y.T., De Hosson, J.T.M., 2011. In situ compression study of taper-free metallic glass nanopillars. Applied Physics Letters 98, 233104.

Lai, Y.H., Lee, C.J., Cheng, Y.T., Chou, H.S., Chen, H.M., Du, X.H., Chang, C.I., Huang, J.C., Jian, S.R., Jang, J.S.C., Nieh, T.G., 2008. Bulk and microscale compressive behavior of a Zr-based metallic glass. Scripta Materialia 58, 890-893.

Lao, J., Naghdi Tam, M., Pinisetty, D., Gupta, N., 2012. Molecular Dynamics Simulation of FCC Metallic Nanowires: A Review. Jom 65, 175-184.

Leamy, H.J., Wang, T.T., Chen, H.S., 1972. Plastic flow and fracture of metallic glass. MT 3, 699-708.

Lee, C.J., Huang, J.C., Nieh, T.G., 2007a. Sample size effect and microcompression of Mg65Cu25Gd10 metallic glass. Appl. Phys. Lett. 91, 161913.

Lee, J.C., Park, K.W., Kim, K.H., Fleury, E., Lee, B.J., Wakeda, M., Shibutani, Y., 2007b. Origin of the plasticity in bulk amorphous alloys. J. Mater. Res. 22, 3087-3097.

Lee, M.H., Lee, K.S., Das, J., Thomas, J., Kühn, U., Eckert, J., 2010. Improved plasticity of bulk metallic glasses upon cold rolling. Scripta Materialia 62, 678-681.

Lee, S., Lu, W., 2014. Controlling the number of graphene sheets exfoliated from graphite by designed normal loading and frictional motion. Journal of Applied Physics 116.

Lemons, D.S., Gythiel, A., 1997. Paul Langevin's 1908 paper "On the Theory of Brownian Motion" American Journal of Physics 65, 1079-1081.

Leng, Y., Courtney, T.H., 1991. Multiple shear band formation in metallic glasses in composites. J Mater Sci 26, 588-592.

Lewandowski, J.J., 2001. Effects of Annealing and Changes in Stress State on Fracture Toughness of Bulk Metallic Glass. Materials Transactions 42, 633-637.

Lewandowski, J.J., Greer, A.L., 2006. Temperature rise at shear bands in metallic glasses. Nat Mater 5, 15-18.

Lewandowski, J.J., Wang, W.H., Greer, A.L., 2005. Intrinsic plasticity or brittleness of metallic glasses. Philosophical Magazine Letters 85, 77-87.

Li, J., 2002. AtomEye: an efficient atomistic configuration viewer. Modelling Simul. Mater. Sci. Eng. 11, 173.

Li, J., 2003. AtomEye: an efficient atomistic configuration viewer. Modelling Simul. Mater. Sci. Eng. 11, 173-177.

Li, J., 2005. Basic Molecular Dynamics. Handbook of Materials Modeling, ISBN 978-1-4020-3287-5. Springer Science+ Business Media BV, 2005, p. 565 1, 565.

Li, J.H., Dai, X.D., Liang, S.H., Tai, K.P., Kong, Y., Liu, B.X., 2008. Interatomic potentials of the binary transition metal systems and some applications in materials physics. Physics Reports 455, 1-134.

Li, J.X., Shan, G.B., Gao, K.W., Qiao, L.J., Chu, W.Y., 2003. In situ SEM study of formation and growth of shear bands and microcracks in bulk metallic glasses. Materials Science and Engineering: A 354, 337-343.

Li, Q.-K., Li, M., 2005. Effects of surface imperfections on deformation and failure of amorphous metals. Applied Physics Letters 87, 031910.

Li, Q.-K., Li, M., 2006. Molecular dynamics simulation of intrinsic and extrinsic mechanical properties of amorphous metals. Intermetallics 14, 1005-1010.

Li, Q.-K., Li, M., 2008. Surface structure and properties of NiZr model metallic glasses: A molecular dynamics simulation. J Non-Cryst Solids 354, 2060-2065.

Liebermann, H.H., Graham, C.D., 1976. Production of amorphous alloy ribbons and effects of apparatus parameters on ribbon dimensions. Magnetics, IEEE Transactions on 12, 921-923.

Lind, M.L., Duan, G., Johnson, W.L., 2006. Isoconfigurational Elastic Constants and Liquid Fragility of a Bulk Metallic Glass Forming Alloy. Physical Review Letters 97, 015501.

Liu, A.C.Y., Paganin, D.M., Bourgeois, L., Nakashima, P.N.H., Ott, R.T., Kramer, M.J., 2011. Quantitative microscopic measurement of void distribution in shear bands in $Zr_{66.7}Cu_{33.3}$ metallic glass. Physical Review B 84, 094201.

Liu, C.T., Heatherly, L., Horton, J.A., Easton, D.S., Carmichael, C.A., Wright, J.L., Schneibel, J.H., Yoo, M.H., Chen, C.H., Inoue, A., 1998. Test environments and mechanical properties of Zr-base bulk amorphous alloys. Metall and Mat Trans A 29, 1811-1820.

Liu, L., Hasan, M., Kumar, G., 2014. Metallic glass nanostructures: fabrication, properties, and applications. Nanoscale 6, 2027.

Liu, L.F., Dai, L.H., Bai, Y.L., Wei, B.C., Eckert, J., 2005a. Behavior of multiple shear bands in Zr-based bulk metallic glass. Materials Chemistry and Physics 93, 174-177.

Liu, L.F., Dai, L.H., Bai, Y.L., Wei, B.C., Yu, G.S., 2005b. Strain rate-dependent compressive deformation behavior of Nd-based bulk metallic glass. Intermetallics 13, 827-832.

Louzguine-Luzgin, D.V., Yavari, A.R., Xie, G., Madge, S., Li, S., Saida, J., Greer, A.L., Inoue, A., 2010. Tensile deformation behaviour of Zr-based glassy alloys. Philosophical Magazine Letters 90, 139-148.

Lu, J., Ravichandran, G., Johnson, W.L., 2003. Deformation behavior of the Zr41.2Ti13.8CU12.5Ni10Be22.5 bulk metallic glass over a wide range of strain-rates and temperatures. Acta Materialia 51, 3429-3443.

Lu, X.L., Lu, Q.H., Li, Y., Lu, L., 2013. Gradient confinement induced uniform tensile ductility in metallic glass. Sci Rep 3, 3319.

Luo, J.H., Wu, F.F., Huang, J.Y., Wang, J.Q., Mao, S.X., 2010. Superelongation and Atomic Chain Formation in Nanosized Metallic Glass. Physical Review Letters 104, 215503.

Ma, W., Kou, H., Li, J., Chang, H., Zhou, L., 2009. Effect of strain rate on compressive behavior of Ti-based bulk metallic glass at room temperature. Journal of Alloys and Compounds 472, 214-218.

Magagnosc, D.J., Ehrbar, R., Kumar, G., He, M.R., Schroers, J., Gianola, D.S., 2013. Tunable Tensile Ductility in Metallic Glasses. Sci. Rep. 3, 1096.
Mahmoudinezhad, E., Ansari, R., 2013. Vibration analysis of circular and square single-layered graphene sheets: An accurate spring mass model. Physica E: Low-dimensional Systems and Nanostructures 47, 12-16.

Masumoto, T., Maddin, R., 1971. The mechanical properties of palladium 20 a/o silicon alloy quenched from the liquid state. Acta Metallurgica 19, 725-741.

Mauro, N.A., Wessels, V., Bendert, J.C., Klein, S., Gangopadhyay, A.K., Kramer, M.J., Hao, S.G., Rustan, G.E., Kreyssig, A., Goldman, A.I., Kelton, K.F., 2011. Short- and medium-range order in $Zr_{80}Pt_{20}$ liquids. Physical Review B 83, 184109.

Mayr, S.G., 2006. Activation energy of shear transformation zones: a key for understanding rheology of glasses and liquids. Phys Rev Lett 97, 195501.

Miracle, D.B., Greer, A.L., Kelton, K.F., 2008. Icosahedral and dense random cluster packing in metallic glass structures. J Non-Cryst Solids 354, 4049-4055.

Mukai, T., Nieh, T.G., Kawamura, Y., Inoue, A., Higashi, K., 2002a. Dynamic response of a Pd40Ni40P20 bulk metallic glass in tension. Scripta Materialia 46, 43-47.

Mukai, T., Nieh, T.G., Kawamura, Y., Inoue, A., Higashi, K., 2002b. Effect of strain rate on compressive behavior of a Pd40Ni40P20 bulk metallic glass. Intermetallics 10, 1071-1077.
Murali, P., Guo, T.F., Zhang, Y.W., Narasimhan, R., Li, Y., Gao, H.J., 2011. Atomic Scale Fluctuations Govern Brittle Fracture and Cavitation Behavior in Metallic Glasses. Physical Review Letters 107.

Murali, P., Narasimhan, R., Guo, T.F., Zhang, Y.W., Gao, H.J., 2013. Shear bands mediate cavitation in brittle metallic glasses. Scripta Materialia 68, 567-570.

Murali, P., Ramamurty, U., 2005. Embrittlement of a bulk metallic glass due to sub-Tg annealing. Acta Materialia 53, 1467-1478.

Nakayama, K.S., Yokoyama, Y., Ono, T., Chen, M.W., Akiyama, K., Sakurai, T., Inoue, A., 2010. Controlled Formation and Mechanical Characterization of Metallic Glassy Nanowires. Advanced Materials 22, 872-875.

Nelson, M.T., Humphrey, W., Gursoy, A., Dalke, A., Kale, L.V., Skeel, R.D., Schulten, K., 1996. NAMD: a Parallel, Object-Oriented Molecular Dynamics

Program. International Journal of High Performance Computing Applications 10, 251-268.

Nieh, T.G., Schuh, C., Wadsworth, J., Li, Y., 2002. Strain rate-dependent deformation in bulk metallic glasses. Intermetallics 10, 1177-1182.

Nieh, T.G., Wadsworth, J., Liu, C.T., Ohkubo, T., Hirotsu, Y., 2001. Plasticity and structural instability in a bulk metallic glass deformed in the supercooled liquid region. Acta Materialia 49, 2887-2896.

Nørskov, J.K., Lang, N.D., 1980. Effective-medium theory of chemical binding: Application to chemisorption. Physical Review B 21, 2131-2136.

Nosé, S., 1984. A unified formulation of the constant temperature molecular dynamics methods. The Journal of Chemical Physics 81, 511.

Pampillo, C., 1975. Flow and fracture in amorphous alloys. J Mater Sci 10, 1194-1227.

Pampillo, C.A., Davis, L.A., Li, J.C.M., 1972. The effective modulus interpretation of the strength-differential effect in ferrous alloys. Scripta Metallurgica 6, 765-768.

Pan, D., Inoue, A., Sakurai, T., Chen, M.W., 2008. Experimental characterization of shear transformation zones for plastic flow of bulk metallic glasses. Chen, Proc. Natl. Acad. Sci. 105, 14769.

Park, J.M., Chang, H.J., Han, K.H., Kim, W.T., Kim, D.H., 2005. Enhancement of plasticity in Ti-rich Ti–Zr–Be–Cu–Ni bulk metallic glasses. Scripta Materialia 53, 1-6.

Park, M., Lee, I.-H., Kim, Y.-S., 2014. Lattice thermal conductivity of crystalline and amorphous silicon with and without isotopic effects from the ballistic to diffusive thermal transport regime. Journal of Applied Physics 116.

Parrinello, M., Rahman, A., 1980. Crystal Structure and Pair Potentials: A Molecular-Dynamics Study. Physical Review Letters 45, 1196-1199.

Pearlman, D.A., Case, D.A., Caldwell, J.W., Ross, W.S., Cheatham Iii, T.E., DeBolt, S., Ferguson, D., Seibel, G., Kollman, P., 1995. AMBER, a package of computer programs for applying molecular mechanics, normal mode analysis, molecular dynamics and free energy calculations to simulate the structural and energetic properties of molecules. Computer Physics Communications 91, 1-41.

Peker, A., Johnson, W.L., 1993. A highly processable metallic glass: Zr41.2Ti13.8Cu12.5Ni10.0Be22.5. Applied Physics Letters 63, 2342-2344.
Plimpton, S., 1995. Fast Parallel Algorithms for Short-Range Molecular-Dynamics. J. Comput. Phys. 117, 1-19.

Polk, D.E., Turnbull, D., 1972. Flow of melt and glass forms of metallic alloys. Acta Metallurgica 20, 493-498.

Qiao, J.W., Zhang, Y., Liaw, P.K., Chen, G.L., 2009. Micromechanisms of plastic deformation of a dendrite/Zr-based bulk-metallic-glass composite. Scripta Materialia 61, 1087-1090.

Qu, R.T., Zhang, Q.S., Zhang, Z.F., 2013. Achieving macroscopic tensile plasticity of monolithic bulk metallic glass by surface treatment. Scripta Materialia 68, 845-848.

Quillin, M.L., Matthews, B.W., 2000. Accurate calculation of the density of proteins. Acta Crystallographica Section D 56, 791-794.

Raabe, D., 2004. Molecular Dynamics, Computational Materials Science. Wiley-VCH Verlag GmbH & Co. KGaA, pp. 87-110.

Rahman, A., 1964. Correlations in the Motion of Atoms in Liquid Argon. Physical Review 136, A405-A411.

Ramamurty, U., Lee, M.L., Basu, J., Li, Y., 2002. Embrittlement of a bulk metallic glass due to low-temperature annealing. Scripta Materialia 47, 107-111.

Refson, K., 2000. Moldy: a portable molecular dynamics simulation program for serial and parallel computers. Computer Physics Communications 126, 310-329.

Reger-Leonhard, A., Heilmaier, M., Eckert, J., 2000. Newtonian flow of $Zr_{55}Cu_{30}Al_{10}Ni_5$ bulk metallic glassy alloys. Scripta Materialia 43, 459-464.
Ritter, Y., Albe, K., 2012. Chemical and topological order in shear bands of Cu64Zr36 and Cu36Zr64 glasses. Journal of Applied Physics 111, 103527.

Ritter, Y., Şopu, D., Gleiter, H., Albe, K., 2011. Structure, stability and mechanical properties of internal interfaces in Cu64Zr36 nanoglasses studied by MD simulations. Acta Materialia 59, 6588-6593.

Roth, J., Stadler, J., Brunelli, M., Bunz, D., Gähler, F., Hahn, J., Hohl, M., Horn, C., Kaiser, J., Mikulla, R., Schaaf, G., Stelzer, J., Trebin, H.-R., 2000. IMD — A Massively Parallel Molecular Dynamics Package for Classical Simulations in Condensed Matter Physics, in: Krause, E., Jäger, W. (Eds.), High Performance Computing in Science and Engineering '99. Springer Berlin Heidelberg, pp. 72-81.

Rupert, T.J., 2013. Strain localization in a nanocrystalline metal: Atomic mechanisms and the effect of testing conditions. Journal of Applied Physics 114, 033527.

Salimon, A.I., Ashby, M.F., Bréchet, Y., Greer, A.L., 2004. Bulk metallic glasses: what are they good for? Materials Science and Engineering: A 375–377, 385-388.

Schlick, T., 2010. Molecular Modeling and Simulation: An Interdisciplinary Guide: An Interdisciplinary Guide. Springer.

Schroers, J., Johnson, W., 2004. Ductile Bulk Metallic Glass. Physical Review Letters 93.

Schuh, C.A., Hufnagel, T.C., Ramamurty, U., 2007. Mechanical behavior of amorphous alloys. Acta Materialia 55, 4067-4109.

Schuh, C.A., Lund, A.C., Nieh, T.G., 2004. New regime of homogeneous flow in the deformation map of metallic glasses: elevated temperature nanoindentation experiments and mechanistic modeling. Acta Materialia 52, 5879-5891.

Schuster, B.E., Wei, Q., Ervin, M.H., Hruszkewycz, S.O., Miller, M.K., Hufnagel, T.C., Ramesh, K.T., 2007. Bulk and microscale compressive properties of a Pd-based metallic glass. Scripta Materialia 57, 517-520.

Schuster, B.E., Wei, Q., Hufnagel, T.C., Ramesh, K.T., 2008. Size-independent strength and deformation mode in compression of a Pd-based metallic glass. Acta Metall. 56, 5091-5100.

Scudino, S., Surreddi, K.B., Eckert, J., 2010. Mechanical properties of cold-rolled Zr60Ti5Ag5Cu12.5Ni10Al7.5 metallic glass. physica status solidi (a) 207, 1118-1121.
Sergueeva, A.V., Mara, N.A., Kuntz, J.D., Branagan, D.J., Mukherjee, A.K., 2004. Shear band formation and ductility of metallic glasses. Materials Science and Engineering: A 383, 219-223.

Sha, Z.-D., Pei, Q.-X., Sorkin, V., Branicio, P.S., Zhang, Y.-W., Gao, H., 2013. On the notch sensitivity of CuZr metallic glasses. Applied Physics Letters 103, 081903.

Shan, Z.W., Li, J., Cheng, Y.Q., Minor, A.M., Syed Asif, S.A., Warren, O.L., Ma, E., 2008. Plastic flow and failure resistance of metallic glass: Insight from in situ compression of nanopillars. Physical Review B 77.

Sharma, P., Yubuta, K., Kimura, H., Inoue, A., 2009. Brittle metallic glass deforms plastically at room temperature in glassy multilayers. Physical Review B 80, 024106.

Shekhar, A., Nomura, K.-i., Kalia, R.K., Nakano, A., Vashishta, P., 2013. Nanobubble Collapse on a Silica Surface in Water: Billion-Atom Reactive Molecular Dynamics Simulations. Physical Review Letters 111.

Sheng, H.W., Luo, W.K., Alamgir, F.M., Bai, J.M., Ma, E., 2006. Atomic packing and short-to-medium-range order in metallic glasses. Nature 439, 419-425.

Shi, Y., 2010. Size-independent shear band formation in amorphous nanowires made from simulated casting. Applied Physics Letters 96, 121909.

Shi, Y., Falk, M., 2005. Strain Localization and Percolation of Stable Structure in Amorphous Solids. Physical Review Letters 95.

Shi, Y., Falk, M.L., 2006. Atomic-scale simulations of strain localization in three-dimensional model amorphous solids. Physical Review B 73, 214201.

Shi, Y., Falk, M.L., 2008. A computational analysis of the deformation mechanisms of a nanocrystal–metallic glass composite. Acta Materialia 56, 995-1000.

Shimizu, F., Ogata, S., Li, J., 2007. Theory of Shear Banding in Metallic Glasses and Molecular Dynamics Calculations. Materials Transactions 48, 2923-2927.

Smith, W., Forester, T.R., 1996. DL_POLY_2.0: A general-purpose parallel molecular dynamics simulation package. Journal of Molecular Graphics 14, 136-141.

Smith, W., Yong, C.W., Rodger, P.M., 2002. DL_POLY: Application to molecular simulation. Molecular Simulation 28, 385-471.

Şopu, D., Albe, K., Ritter, Y., Gleiter, H., 2009. From nanoglasses to bulk massive glasses. Applied Physics Letters 94, 191911.

Şopu, D., Ritter, Y., Gleiter, H., Albe, K., 2011a. Deformation behavior of bulk and nanostructured metallic glasses studied via molecular dynamics simulations. Physical Review B 83, 100202.

Şopu, D., Ritter, Y., Gleiter, H., Albe, K., 2011b. Deformation behavior of bulk and nanostructured metallic glasses studied via molecular dynamics simulations. Physical Review B 83.

Spaepen, F., 1977. A microscopic mechanism for steady state inhomogeneous flow in metallic glasses. Acta Metallurgica 25, 407-415.

Srolovitz, D., Vitek, V., Egami, T., 1983. An atomistic study of deformation of amorphous metals. Acta Metallurgica 31, 335-352.

Steif, P.S., Spaepen, F., Hutchinson, J.W., 1982. Strain localization in amorphous metals. Acta Metallurgica 30, 447-455.

Stukowski, A., 2010. Visualization and analysis of atomistic simulation data with OVITO–the Open Visualization Tool. Modelling and Simulation in Materials Science and Engineering 18, 015012.

Tanemura, M., Ogawa, T., Ogita, N., 1983. A new algorithm for three-dimensional Voronoi tesselation. J. Comput. Phys. 51, 191-207.

Telford, M., 2004. The case for bulk metallic glass. Materials Today 7, 36-43.
Tersoff, J., 1988. New empirical approach for the structure and energy of covalent systems. Physical Review B 37, 6991-7000.

Tian, L., Shan, Z.-W., Ma, E., 2013. Ductile necking behavior of nanoscale metallic glasses under uniaxial tension at room temperature. Acta Materialia 61, 4823-4830.

Tsai, D.H., 1979. The virial theorem and stress calculation in molecular dynamics. The Journal of Chemical Physics 70, 1375-1382.

Tsuzuki, H., Rino, J.P., Branicio, P.S., 2011. Dynamic behaviour of silicon carbide nanowires under high and extreme strain rates: a molecular dynamics study. Journal of Physics D: Applied Physics 44, 055405.

Volkert, C.A., Donohue, A., Spaepen, F., 2008. Effect of sample size on deformation in amorphous metals. Journal of Applied Physics 103, 083539.

Wada, T., Inoue, A., Greer, A.L., 2005. Enhancement of room-temperature plasticity in a bulk metallic glass by finely dispersed porosity. Applied Physics Letters 86.
Wang, C.C., Ding, J., Cheng, Y.Q., Wan, J.C., Tian, L., Sun, J., Shan, Z.W., Li, J., Ma, E., 2012. Sample size matters for Al88Fe7Gd5 metallic glass: Smaller is stronger. Acta Materialia 60, 5370-5379.

Wang, S.Y., Wang, C.Z., Li, M.Z., Huang, L., Ott, R.T., Kramer, M.J., Sordelet, D.J., Ho, K.M., 2008. Short- and medium-range order in a $Zr_{73}Pt_{27}$ glass: Experimental and simulation studies. Physical Review B 78, 184204.

Wang, X.L., Jiang, F., Hahn, H., Li, J., Gleiter, H., Sun, J., Fang, J.X., 2014. Plasticity of a scandium-based nanoglass. Scripta Materialia.

Wang, Z.T., Pan, J., Li, Y., Schuh, C.A., 2013. Densification and Strain Hardening of a Metallic Glass under Tension at Room Temperature. Physical Review Letters 111, 135504.

Wen, Y.-H., Zhu, Z.-Z., Zhu, R.-Z., 2008. Molecular dynamics study of the mechanical behavior of nickel nanowire: Strain rate effects. Computational Materials Science 41, 553-560.

Wendt, H.R., Abraham, F.F., 1978. Empirical Criterion for the Glass Transition Region Based on Monte Carlo Simulations. Physical Review Letters 41, 1244-1246.

Wessels, V., Gangopadhyay, A.K., Sahu, K.K., Hyers, R.W., Canepari, S.M., Rogers, J.R., Kramer, M.J., Goldman, A.I., Robinson, D., Lee, J.W., Morris, J.R., Kelton, K.F., 2011. Rapid chemical and topological ordering in supercooled liquid $Cu_{46}Zr_{54}$. Physical Review B 83, 094116.

Witte, R., Feng, T., Fang, J.X., Fischer, A., Ghafari, M., Kruk, R., Brand, R.A., Wang, D., Hahn, H., Gleiter, H., 2013. Evidence for enhanced ferromagnetism in an iron-based nanoglass. Applied Physics Letters 103, 073106.

Wright, W.J., Schwarz, R.B., Nix, W.D., 2001. Localized heating during serrated plastic flow in bulk metallic glasses. Materials Science and Engineering: A 319–321, 229-232.

Wu, F.F., Zhang, Z.F., Jiang, F., Sun, J., Shen, J., Mao, S.X., 2007a. Multiplication of shear bands and ductility of metallic glass. Appl. Phys. Lett. 90, 191909.

Wu, F.F., Zhang, Z.F., Mao, S.X., 2009a. Size-dependent shear fracture and global tensile plasticity of metallic glasses. Acta Materialia 57, 257-266.

Wu, F.F., Zhang, Z.F., Mao, S.X., Eckert, J., 2009b. Effect of sample size on ductility of metallic glass. Philosophical Magazine Letters 89, 178-184.

Wu, F.F., Zhang, Z.F., Mao, S.X., Peker, A., Eckert, J., 2007b. Effect of annealing on the mechanical properties and fracture mechanisms of a $Zr_{56.2}Ti_{13.8}Nb_{5.0}Cu_{6.9}Ni_{5.6}Be_{12.5}$ bulk-metallic-glass composite. Physical Review B 75, 134201.

Wu, G.Y., Jiang, J.Z., Lin, X.P., 1999. Nanoglass Fe79B21 powders prepared by chemical reduction: A low-temperature Mossbauer study. Nanostructured Materials 12, 843.

Wu, H.A., 2006. Molecular dynamics study on mechanics of metal nanowire. Mechanics Research Communications 33, 9-16.

Wu, W.F., Han, Z., Li, Y., 2008a. Size-dependent “malleable-to-brittle” transition in a bulk metallic glass. Applied Physics Letters 93, 061908.

Wu, W.F., Zhang, C.Y., Zhang, Y.W., Zeng, K.Y., Li, Y., 2008b. Stress gradient enhanced plasticity in a monolithic bulk metallic glass. Intermetallics 16, 1190-1198.

Wu, X.L., Guo, Y.Z., Wei, Q., Wang, W.H., 2009c. Prevalence of shear banding in compression of Zr41Ti14Cu12.5Ni10Be22.5 pillars as small as 150 nm in diameter. Acta Metall. 57, 3562-3571.

Wu, Y., Li, H.X., Jiao, Z.B., Gao, J.E., Lu, Z.P., 2010. Size effects on the compressive deformation behaviour of a brittle Fe-based bulk metallic glass. Philosophical Magazine Letters 90, 403-412.

Wu, Z., Zhang, Y.-W., Jhon, M.H., Gao, H., Srolovitz, D.J., 2012. Nanowire Failure: Long = Brittle and Short = Ductile. Nano Letters 12, 910-914.

Wu, Z.X., Zhang, Y.W., Jhon, M.H., Greer, J.R., Srolovitz, D.J., 2013. Nanostructure and surface effects on yield in Cu nanowires. Acta Materialia 61, 1831-1842.

Wu, Z.X., Zhang, Y.W., Srolovitz, D.J., 2011. Deformation mechanisms, length scales and optimizing the mechanical properties of nanotwinned metals. Acta Materialia 59, 6890-6900.

Xi, X., Zhao, D., Pan, M., Wang, W., Wu, Y., Lewandowski, J., 2005. Fracture of Brittle Metallic Glasses: Brittleness or Plasticity. Physical Review Letters 94.

Xiao, X., Fang, S., Xia, L., Li, W., Hua, Q., Dong, Y., 2003. Effect of strain rates on the fracture morphologies of Zr-based bulk metallic glasses. J Non-Cryst Solids 330, 242-247.

Xie, S., George, E.P., 2008. Size-dependent plasticity and fracture of a metallic glass in compression. Intermetallics 16, 485-489.

Xue, Y.F., Cai, H.N., Wang, L., Wang, F.C., Zhang, H.F., 2008. Effect of loading rate on failure in Zr-based bulk metallic glass. Materials Science and Engineering: A 473, 105-110.

Yang, Y., Ye, J., Lu, J., Wang, Q., Liaw, P.K., 2011a. Revelation of the effect of structural heterogeneity on microplasticity in bulk metallic-glasses. J Mater Res 25, 563-575.

Yang, Y., Ye, J.C., Lu, J., Liaw, P.K., Liu, C.T., 2010. Characteristic length scales governing plasticity/brittleness of bulk metallic glasses at ambient temperature. Applied Physics Letters 96, 011905.

Yang, Y., Ye, J.C., Lu, J., Liu, C.T., 2011b. Dual character of stable shear banding in bulk metallic glasses. Intermetallics 19, 1005-1013.

Yavari, A.R., Georgarakis, K., Botta, W.J., Inoue, A., Vaughan, G., 2010. Homogenization of plastic deformation in metallic glass foils less than one micrometer thick. Physical Review B 82, 172202.

Yavari, A.R., Nikolov, N., Nishiyama, N., Zhang, T., Inoue, A., Uriarte, J.L., Heunen, G., 2004. The glass transition of bulk metallic glasses studied by real-time diffraction in transmission using high-energy synchrotron radiation. Mat Sci Eng a-Struct 375, 709-712.

Yip, S., 2005. Handbook of materials modeling: Models. Springer.

Yip, S., 2007. Handbook of Materials Modeling. Springer.

Yokoyama, Y., 2003. Ductility improvement of Zr-Cu-Ni-Al glassy alloy. J Non-Cryst Solids 316, 104-113.

Zhang, B., Wang, R.J., Zhao, D.Q., Pan, M.X., Wang, W.H., 2004. Properties of Ce-based bulk metallic glass-forming alloys. Physical Review B 70, 224208.

Zhang, C., Kalia, R.K., Nakano, A., Vashishta, P., Branicio, P.S., 2008. Deformation mechanisms and damage in α-alumina under hypervelocity impact loading. Journal of Applied Physics 103, 083508.

Zhang, J., Park, J.M., Kim, D.H., Kim, H.S., 2007. Effect of strain rate on compressive behavior of Ti45Zr16Ni9Cu10Be20 bulk metallic glass. Materials Science and Engineering: A 449–451, 290-294.

Zhang, J.Y., Sha, Z.D., Branicio, P.S., Zhang, Y.W., Sorkin, V., Pei, Q.X., Srolovitz, D.J., 2013. Superplastic Nanocrystalline Ceramics at Room Temperature and High Strain Rates. Scripta Mater. 69, 525.

Zhang, Y., Stelmashenko, N.A., Barber, Z.H., Wang, W.H., Lewandowski, J.J., Greer, A.L., 2011. Local temperature rises during mechanical testing of metallic glasses. J Mater Res 22, 419-427.

Zhang, Y., Xu, W., Tan, H., Li, Y., 2005. Microstructure control and ductility improvement of La–Al–(Cu, Ni) composites by Bridgman solidification. Acta Materialia 53, 2607-2616.

Zhang, Z.F., Eckert, J., Schultz, L., 2003. Difference in compressive and tensile fracture mechanisms of Zr59Cu20Al10Ni8Ti3 bulk metallic glass. Acta Materialia 51, 1167-1179.

Zhao, J.X., Wu, F.F., Qu, R.T., Li, S.X., Zhang, Z.F., 2010. Plastic deformability of metallic glass by artificial macroscopic notches. Acta Mater. 58, 5420-5432.

Zheng, Q., Cheng, S., Strader, J.H., Ma, E., Xu, J., 2007. Critical size and strength of the best bulk metallic glass former in the Mg–Cu–Gd ternary system. Scripta Materialia 56, 161-164.

Zhou, F., Molinari, J.-F., 2004. Stochastic fracture of ceramics under dynamic tensile loading. International Journal of Solids and Structures 41, 6573-6596.

APPENDIX

A Grady-Kipp model

Fig. A-1 shows the strain rate effects on the final failure strain and strength of MG nanopillars with 15 nm diameter and aspect ratio, ξ = 13 and 50. Rate dependency of the tensile strength of the MG nanopillars can be contemplated by two forms of related inertia, structural inertia and the inertia associated with micro cracking (Zhou and Molinari, 2004). Fig. A-1a shows a noticeable rate hardening of the MG nanopillars at high strain rates; e.g., a strength of 6 GPa at strain rate of 4×10^{10} s^{-1} compared to a strength of 3.42 GPa at the lower strain rate of 10^{7} s^{-1}. This observation can be explained due to the propagation of stress waves throughout the pillars. Fracture in nanopillars at high strain rates, might occur before a uniform stress distribution throughout the pillars. The reason is that the stress waves cannot propagate within the whole nanopillar length before the fracture occurs. Accordingly, the abrupt increase of the nanopillars strength is a consequence of the non-uniform stress distribution within the nanopillar at the failure time. Fig. A-1b shows the rate dependency of the number of localized plastic zones and SB/necking in the nanopillars. The number of SB/necks throughout the nanopillar increases with strain rate. This is also evident as in the deformed nanopillar at the failure point with the aspect ratio ξ = 13 and 50, as shown in the figs 3-2b-i and figsA-1c-i respectively. The extension of the SBs/necking within the nanopillars has a characteristic time. During a fast deformation of the nanopillars, other SBs/necking might be activated before a neighbouring activated SB/necking reaches the required time to extend and release the stress state. As a result, the nanopillars break with an increasing

number of SBs/necking at higher loading rates. At lower rates, however, a single main SB/necking event cause the catastrophic MG nanopillar failure (Zhou and Molinari, 2004).

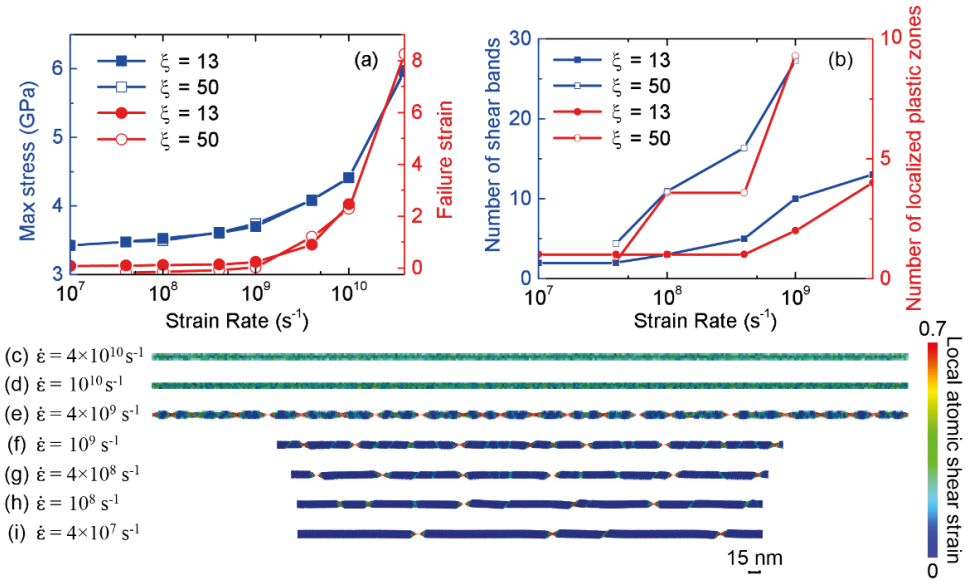

Figure A-1 Strain-rate effects on the failure strain, strength, and deformation of MG nanopillars. (a) Failure strain and maximum stress for strain rate from 10^7 s^{-1} to 4×10^{10} s^{-1}, for nanopillars with 15 nm diameter and aspect ratio ξ = 13 and 50. (c) Number of total shear bands in the nanopillar and the number of localized plastic zones with applying strain rate from 10^7 s^{-1} to 4×10^{10} s^{-1}, for nanopillars with 15 nm diameter and aspect ratio ξ = 13 and 50. (c)-(i) Illustration of the deformed nanopillars simulated highlighting the failure mode. Nanopillars are coloured according to the calculated local atomic shear strain. All nanopillars have a diameter of 15nm and an aspect ratio of, ξ = 50.

Mott analysis is one of the methods for modelling the stress release wave propagation in materials, and hence, it is used to describe the mechanical behaviour of the MG nanopillars with dynamic fracture. Grady-Kip model uses Mott analysis besides considering local energy dissipation due to fracture growth, in order to derive the strain rate effects on dynamic crack propagation in one dimensional rod (Kipp and Grady, 1985). Figure A-2 illustrates the diagram of the model. In Grady-Kip model, the fragmentation length and time

for dynamic crack propagation is derived based on rigid-plastic behaviour of crack propagation and the law of linear displacement of the unloading crack opening. Therefore, in the vicinity of the crack tip, the stress release wave generates an elastic-plastic boundary between the unloading elastic behaviour and the plastic behaviour. The Grady-Kip model considers this elastic regime in front of the fracture as a rigid area with the same velocity distribution in this region. The displacement of the rigid-plastic boundary is derived by applying balance of momentum on the rod at each time interval. It is assumed that with a distance -twice of the plastic boundary, no other fragment can propagate. Therefore, at the time of fracture, twice of the distance of the plastic boundary is represents the fragmentation size, and accordingly, the number of fragmentation along the rod can be determined. In this way, the Grady-Kip model draws a relationship between fracture size and strain rate with the applied strain rate. This relationship is formulated in Eq. A-1.

$$x_f = \left(\frac{24\Upsilon}{\rho\dot{\varepsilon}^2}\right)^{\frac{1}{3}}$$
$$N_f = \frac{L}{x_f} \qquad \text{A-1}$$

where x_f represent the fragment size, N_f denotes the number of fragments throughout the rod, ρ is the initial material density per unit length, L is the rod length, and γ denotes the fracture energy. According to Eq. A-1, the number of fragments increases with the strain rate, and this, in turn, leads to smaller fragmentation sizes of the rod (Kipp and Grady, 1985). By considering MG nanopillars as a one-dimensional rod, Grady-Kipp model predicts the finding that the number of SB/necking points increases at higher strain rates (see Fig.

A-1b). Therefore, stress wave induced communication between SBs/neckings, and set up a length scale and a time scale for MG nanopillar failure.

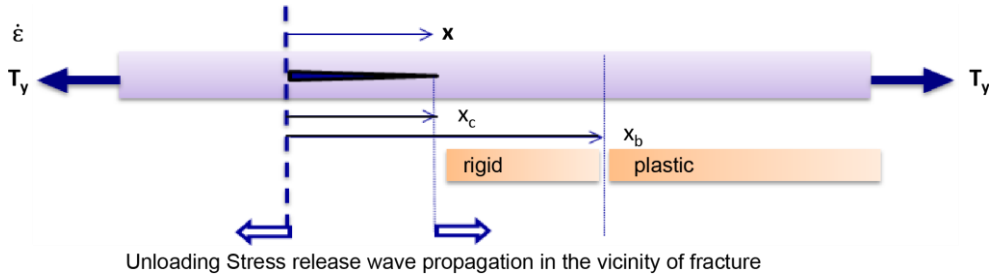

Figure A-2 Schematic of one dimensional rod considered in Grady-Kip model to investigate realising stress wave propagation. x_c denotes displacement of fracture boundary, x_b: displacement of plastic boundary (elastic-plastic interface) and T_y flow tension on rod.